FACULTY OF SCIENCES



READING THE (SUB-)SURFACE: A GEOMORPHOLOGICAL, STRATIGRAPHIC AND SEDIMENTOLOGICAL INVESTIGATION OF THE AXIAL CHANNEL (SOUTHERN NORTH SEA)

MORGAN VERVOORT

Supervisor: Prof. Dr. Marc De Batist
Co-supervisor: Dr. Ruth Plets

Academic year: 2026-2027

Submitted to the Faculty of Science of Ghent University in fulfilment of the requirements for the degree of Doctor of Science: Geology

GHENT UNIVERSITY

Reading the (sub-)surface: a geomorphological, stratigraphic and sedimentological investigation of the Axial Channel (southern North Sea)

Morgan Vervoort

Supervisor: Prof. dr. Marc De Batist

Co-supervisor: Dr. Ruth Plets

Dissertation submitted to the Faculty of Science of Ghent University in fulfilment of the requirements for the degree of Doctor of Science: Geology

Academic Year: 2026-2027

Ghent University

Members of the examination committee:

Prof. Dr. Marc De Batist (Ghent University, BE)	Supervisor
Dr. Ruth Plets (Flanders Marine Institute, BE)	Supervisor
Prof. Dr. David Van Rooij (Ghent University, BE)	Chair
Prof. Dr. Maarten Van Daele (Ghent University, BE)	Jury member
Prof. Dr. Vera Van Lancker (Institute of Natural Sciences, Ghent University BE)	Jury member
Prof. Dr. David Hodgson (University of Leeds, UK)	Jury member
Dr. Freek Busschers (Geological Survey of the Netherlands, NL)	Jury member

This research was carried out by Morgan Vervoort with the financial support of the Belgian Science Policy Office (BELSPO), project no. RV/21/WALDO. Shiptime on the RV *Belgica II* was provided through the same project.

The author and the supervisors give the authorisation to consult and copy parts of this work for personal use only. Every other use is subjected to copyright laws. Permission to reproduce any material contained in this work should be obtained from the author. MS Copilot (UGent license) and ChatGPT were used as spelling and grammar check. No confidential data has been entered into AI tools.

Cover image: Picture taken onboard the RV *Belgica II* during the September 2022 campaign (BE2022-22).

Back image: Picture taken at sunset onboard the RV *Belgica II* during transit for the August 2022 DynaMOD II campaign (BE2022-18).

ACKNOWLEDGEMENTS

Numerous people have contributed to this PhD in various ways, and I would like to express my sincere appreciation to all of you. First and foremost, to my supervisors Marc and Ruth: Marc, I remember the day I knocked at the door of your office to ask for information regarding the new PhD position as part of the WALDO project. You encouraged me to apply, and here we are. I am very grateful to both you and Ruth, to be given this opportunity. Without your guidance, support and trust in me, I wouldn't have come this far. You've allowed me to learn and grow at my own pace, while also providing the occasional gentle nudge in the right direction. One thing I can say for sure is that my curiosity in Quaternary research for the North Sea has only been growing since the moment I started. I would further like to thank all the members of the examination committee for the insightful discussions and constructive feedback. To all the co-authors who contributed to the publications resulting from this research: your expertise and insights have all been invaluable. I further express my gratitude to BELSPO that funded the WALDO-project.

Over the last 4,5 years I have met many people at UGhent and VLIZ, but also at the various conferences I had the opportunity to attend and during the different research surveys with the RV *Belgica* and RV *Simon Stevin*. It would be a long list naming all of you, but I'm sure while you're reading this, you know who you are! Most importantly, I would like to thank my other PhD-half, Despina Kyriakoudi: Darling, I could not have asked for a better companion throughout the WALDO journey. I'll especially cherish all the fun moments on the PhD-related trips, from our little mouse-friend in Texel (what did we name him again?) to the pants/trousers discussion on the Belgica. I'm not surprised we went from 'the WALDO ladies' to being called 'the happily married couple'! A big thank you to everyone else from the SPF team (Victor, Tine, Thomas, Hakan and Warre) for the inspiring discussions in the office, as well as for the many fun and memorable moments we shared onboard, during the writing retreats or during afterwork drinks/dinners. A special shout-out to Thomas and Hakan for your help with seismic data processing, without you the data would not have looked this good!

As I spent most of the time at the office in Ghent, I would also very much like to thank my fellow RCMG members and all the other people from the geology department I've crossed paths with in S8. Especially Loic, Matthias, Rikza, Kimberly and Warre — with whom I had the privilege of sharing the office with — but also Lotte, Alice, Piet, Stijn, Katleen and everyone else from the B-wing: Thank you for the science-related chats in the office or hallway, the help in the lab, but also for our typical resto S5 lunches, the countless Delhaize trips, the lovely and memorable moments during conferences (including the sprite-incident) and afterwork get-togethers.

Lastly, I would like to thank my family and all the friends that I made during my (bachelor, master and PhD) studies in Ghent. Either meeting up for drinks or dinners, the board game nights, bike rides, Rock Werchter, Gentse Feesten, summer holidays and so much more. All these moments provided a welcome distraction from my PhD work. To my family; Mama, Papa en Dorianne: dankjewel om in mij te geloven en om me te blijven steunen gedurende mijn tijd op den univ. En toch ook wel een kleine sorry dat ik gaandeweg mijn Antwerps accent verloren ben. Finally, to Anaïs: You are the one person that was there for me every step of the way. You always listened to my (over-enthusiastic) stories about my research to the point where I must have annoyed you. And thus, by now, you probably know more about the Quaternary geology of the North Sea than you ever signed up for (sorry-not-sorry!). But I'm so grateful for everything you've done for me throughout the last few years, whether directly or indirectly related to my work.

SUMMARY

Studying past landscapes that occur nowadays submerged or buried beneath the seafloor is not only important for archaeological purposes and the offshore industry (such as wind-farm developments), but also for understanding past environmental and climatic changes. Particularly, knowledge of past sea-level fluctuations and resulting changes in coastline positions and fluvial systems are important in the context of present-day climate change. In the last decades, studies have shown that integrated analysis of various datasets, such as bathymetric, seismic/acoustic and ground-truth data, offer a valuable tool for palaeoenvironmental reconstructions.

In the Southern Bight (the southernmost region of the southern North Sea Basin) a prominent geomorphological feature known as the Axial Channel is visible in the present-day bathymetry. This 150 km-long depression extends from the Norfolk Banks in the north to the Strait of Dover in the south. It is believed to be a remnant of a large drainage system that existed during the Middle (c. 780 - 130 ka BP) and Late (c. 130 - 11.7 ka BP) Pleistocene, when ice sheets (British-Irish and Fennoscandian Ice Sheets – BIIS and FIS) occupied parts of the southern North Sea during three successive, major glaciations: the Elsterian/Anglian (MIS12; c.420 - 370 ka BP), Saalian/Wolstonian (MIS6; c. 170-130 ka BP) and Weichselian/Devensian (MIS5d-2; c. 116 – 11.7 ka BP) glaciations. The presence of these ice sheets was accompanied by a large fall in global sea level, causing the southern North Sea region to emerge and become isolated from the Atlantic Ocean. As a drainage route towards the north was blocked by coalescing ice sheets during their maximum expansion, both glacial meltwater and river water from the major NW European rivers (e.g. Meuse-Rhine, Thames, Scheldt) followed a southern drainage route towards the Strait of Dover. Even though the Axial Channel is believed to have acted as an important, confluent drainage system for NW European rivers and glacial meltwater, it has been understudied. In this dissertation, both the present-day seafloor and subsurface of the Southern Bight were investigated to assess the origin and evolution of the Axial Channel system using available offshore bathymetry data and newly acquired seismic, acoustic and vibrocore data.

The bathymetric datasets of the Southern Bight and Axial Channel system studied in Chapter 3 revealed that the associated geomorphological features primarily indicate a fluvial origin, linked to a sea-level lowstand and terrestrial landscape. However, evidence was also found for a glacial, a short-lived high-energy fluvial drainage, and a tidal dominated marine phase. Based on the erosional relationships between the mapped features, these phases were placed in a relative chronology. The initial glacial phase is evidenced by features interpreted as subglacial tunnel valleys, as well as depressions and lineations that resemble other subglacial landforms, including kettle holes and mega-scale lineations, respectively. A subsequent long-term fluvial phase which likely reflects multiple stages of landscape evolution, is characterised by fluvial channels, terraces and streamlined landforms. Geomorphological features that may reflect a short-lived, high-energy drainage event include linear features preserved on top of a plateau and streamlined island. The youngest landforms are marine depositional features, including sand waves, ridges, and tidal furrows, which indicate a transition to a marine environment. These observations demonstrate landscape changes associated with climatic and sea-level fluctuations throughout the Pleistocene and provide a first relative chronology for the evolution of the Axial Channel system.

In Chapter 4, newly acquired high-resolution sparker seismic data (penetration depth of c. 100 m; vertical resolution c. 0.5-1.5 m) were investigated to reassess the current stratigraphic

framework and geological map of the Southern Bight. In total nine seismic units, six generations of incisions and three major regional-scale erosional surfaces were identified and placed within an updated stratigraphic framework. These findings were further placed within the context of the Quaternary evolution of the southern North Sea Basin and highlight the transition from a deltaic and fluvial environment to a landscape increasingly influenced by glacial processes. The identified Plio-Pleistocene and Lower Pleistocene deposits include the Red Crag, Westkapelle Ground, Smith's Knoll and Yarmouth Roads Formations, which are described in unprecedented detail. The Red Crag Formation is identified as four prominent incisions, interpreted as dynamic (inter-)tidal channel systems connected to a more northerly positioned North Sea. The Westkapelle Ground and Smith's Knoll Formations reflect progradational deltaic systems, linked to an increase in accommodation space towards the northeast and accompanied by a northwards migration of the coastline. While the lower part of the Yarmouth Roads Formation likely reflects a continuation of these deltaic depositional systems, the upper part marks a major change in basin configuration. Here, multiple incisional phases were identified and interpreted as remnants of a large, braided river system. This system was interpreted as reflecting a fluvial dominated, relatively flat, low-lying landscape at the end of the Cromerian Stage (Middle Pleistocene). Evidence for a widespread erosional surface was identified at the top of the Yarmouth Roads Formation. Based on its stratigraphic position and the identification of deep incisions tentatively interpreted as subglacial tunnel valleys, this surface was linked to the Elsterian glacial advance (MIS12). The overlying unit was therefore also linked to the Elsterian glaciation, but also the following Holsteinian interglacial, and correlated with the Swarte Bank and Egmond Ground Formations. However, uncertainties remain regarding the exact depositional environment. Based on their stratigraphic position and location in relation to the MIS6 maximum ice extent Younger, isolated incisional remnants were correlated with the late Saalian ice advance (MIS6). Two large-scale Late Pleistocene erosional surfaces were further identified, marking the base and top of the confidently identified Brown Bank Formation. The basal surface likely reflects a preserved late Saalian topography whereas the upper, younger surface records multiple erosional phases linked to base-level changes during the Weichselian (including at MIS4 and MIS2). This detailed stratigraphic study builds on existing stratigraphic frameworks and highlights the need for a continually refined, transnational stratigraphic framework. The identification of Elsterian, Saalian and Weichselian deposits and/or erosional surfaces represent an important step towards improving our understanding of the Middle to Late Pleistocene glacial history.

The Late Pleistocene erosional surface identified in Chapter 4, which was interpreted to record base-level changes during the Weichselian, displays notable similarities to the present-day bathymetry and consequently the morphology of the Axial Channel system. This observation highlighted the need for detailed lithological and chronological investigations. Accordingly, Chapter 5 presents a detailed subregional investigation of the central Axial Channel system using higher-resolution acoustic systems and sediment core data. By integrating sub-bottom profiler data with sedimentological core analyses, including palaeoenvironmental proxies (pollen, foraminifera and molluscs) and chronological data (optically stimulated luminescence; OSL), a Middle to Late Pleistocene chronostratigraphic framework and palaeogeographic reconstruction of the study area were established. Marine deposition was evidenced by the identification of the first *in-situ*, open-marine sediments of the Eem Formation (MIS5e), overlain by shallow-marine deposits of the Brown Bank Formation (MIS5a). Both formations cover a widespread erosional surface. Where this surface is directly overlain by the Eem Formation, OSL ages and the presence of Eemian shell species indicate that it records the Eemian transgression. Where it is overlain by the Brown Bank Formation, shell assemblages and OSL ages indicate cooler conditions and

marine reworking during MIS5c-b. Subsequent relative sea-level fall during MIS4 marks the transition from a marine to a terrestrial landscape, evidenced by an incision restricted to the western Axial Channel. This incision was interpreted to result from glaciofluvial drainage associated with an advancing northern ice margin. A subsequent phase of incision, located c. 10 km north of the established Axial Channel system, was interpreted as an (inter-)tidal channel infilled by reworked deposits of the Brown Bank Formation (based on a reworked MIS5a microfossil assemblage) dated to early MIS3. This incision therefore provides evidence for a renewed marine incursion in the present-day central Axial Channel area. These shallow-marine conditions were followed once again by terrestrial conditions, marked by renewed incision in the western Axial Channel area. This phase corresponds to late MIS3, as the overlying deposits were dated to c. 29 ka (MIS3-2 transition). The infilling deposits represent a proglacial lacustrine environment, characterised by rhythmically laminated sediments and a pollen assemblage indicative of cold (glacial) conditions, and are linked to the development of an extensive ice lobe along the Norfolk Coast (UK). The identification of these proglacial lacustrine sediments indicates that an enclosed basin existed in the western Axial Channel system, although its full extent remains unknown. A final, regionally extensive erosional surface was identified and linked to large-scale glaciofluvial drainage during MIS2 associated with the retreat of the BIIS and FIS. This event likely established the present-day morphology of the Axial Channel.

By integrating geomorphological, seismic/acoustic, sedimentological, palaeoenvironmental and chronological datasets, we were able to assess and update the Quaternary stratigraphic framework and demonstrate that the Axial Channel (1) has a multi-phased origin and (2) acted as an important (glacio-)fluvial drainage pathway during the Middle to Late Pleistocene. The identification of previously unrecognised deposits and incisional stages highlights the complex geology of the Southern Bight and the rapid environmental changes that occurred throughout glacial-interglacial cycles. Additionally, we demonstrated the need for a continually refined, transnational stratigraphic framework that forms the basis for both research and offshore industry purposes.

SAMENVATTING

Het bestuderen van verdronken of begraven paleolandschappen is niet alleen van belang voor archeologisch onderzoek en de offshore-industrie (bv. de aanleg van windmolenparken), maar ook voor een beter begrip van vroegere klimaatveranderingen. In het bijzonder is inzicht in vroegere zeespiegelschommelingen en daarmee samenhangende veranderingen in kustlijnposities en fluviatiele systemen essentieel om de gevolgen van de huidige klimaatverandering beter te begrijpen. In de voorbije decennia hebben talrijke studies aangetoond dat een geïntegreerde analyse van verschillende datasets, zoals bathymetrische, seismische en akoestische gegevens, en boorkernen, een waardevolle basis vormt voor de reconstructie van paleolandschappen.

In de Zuidelijke Bocht (het zuidelijkste deel van de zuidelijke Noordzee) is op de huidige bathymetrie een opvallende geomorfologische structuur zichtbaar, beter bekend als het Axiaal Kanaal. Deze ca. 150 km lange depressie strekt zich uit van de Norfolk Zandbanken in het noorden tot het Nauw van Calais in het zuiden. Het kanaal wordt beschouwd als een restant van een grootschalig drainagesysteem dat actief was tijdens het Midden- (ca. 780 - 130 ka BP) en Laat-Pleistoceen (ca. 130 - 11.7 ka BP), toen de Brits-Ierse en Scandinavische ijskappen (BIIS en FIS) delen van de zuidelijke Noordzee bedekten tijdens drie opeenvolgende glaciaties: het Elsteriaan (MIS12; ca. 420 - 370 ka BP), het Saaliaan (MIS6; ca. 170 - 130 ka BP) en het Weichseliaan (MIS5d-2; ca. 116 - 11,7 ka BP). De groei van deze en andere noordelijke ijskappen ging gepaard met een sterke daling van de globale zeespiegel, waardoor het zuidelijke Noordzeegebied droog kwam te liggen, geïsoleerd van de Atlantische Oceaan. Tijdens de maximale uitbreiding en samensmelting van de ijskappen werd een noordelijke drainage route geblokkeerd, waardoor smeltwater en rivierwater van grote NW-Europese rivieren, zoals de Rijn-Maas, Theems en Schelde, via een zuidelijke afvoerroute naar het Nauw van Calais werden geleid. Ondanks het feit dat het Axiaal Kanaal beschouwd wordt als een belangrijk, samengesteld drainagesysteem voor zowel smelt- als rivierwater, is het tot op heden relatief weinig bestudeerd. In deze studie werden zowel de huidige bathymetrie als de geologie van de Zuidelijke Bocht onderzocht om de oorsprong en evolutie van het Axiaal Kanaal te reconstrueren. Hiervoor werd gebruikgemaakt van bestaande bathymetrische datasets, aangevuld met nieuwverworven seismische en akoestische gegevens, en sedimentkernen (‘vibrocores’).

De analyse van de bathymetrie van de Zuidelijke Bocht en het Axiaal Kanaal (Hoofdstuk 3) toont aan dat de meeste geomorfologische structuren een fluviatiele oorsprong hebben, gerelateerd aan perioden met een lage zeespiegel en terrestrische omstandigheden. Daarnaast werden ook een glaciale fase, een kortstondige hoogenergetische fluviatiele fase en een door getijden gedomineerde mariene fase onderscheiden. Op basis van de erosieve relaties tussen de verschillende gekarteerde geomorfologische landvormen konden deze fasen in een relatieve chronologische volgorde worden geplaatst. De initiële glaciale fase wordt gekenmerkt door structuren die werden geïnterpreteerd als subglaciale tunnelvalleien, evenals door depressies en lineaties die sterke gelijkenissen vertonen met andere subglaciale landvormen, zoals ‘kettle holes’ en ‘mega-scale lineations’. De daaropvolgende langdurige fluviatiele fase, die vermoedelijk meerdere ontwikkelingsstadia omvatte, wordt gekenmerkt door kanaalsystemen, terrassen en gestroomlijnde landvormen. Geomorfologische kenmerken die mogelijk wijzen op een kortstondige hoogenergetische drainagefase omvatten lineaire structuren op een bewaard plateau en een gestroomlijnd eiland. De jongste landvormen bestaan onder meer uit zandgolven, zandruggen en getijden- ‘furrows’, die wijzen op een overgang naar een mariene omgeving in het studiegebied. Deze observaties illustreren de ingrijpende Pleistocene landschapsveranderingen

als gevolg van klimaat- en zeespiegelschommelingen. Op basis van onze resultaten kon een eerste relatieve chronologie voor de evolutie van het Axiaal Kanaal worden opgesteld, waaruit blijkt dat de huidige morfologische expressie van het kanaal het resultaat is van meerdere ontwikkelingsfasen.

In Hoofdstuk 4 werden nieuwverworven hoge-resolutie sparker seismische data (penetratiediepte ca. 100 m, verticale resolutie ca. 0.5-1.5 m) geanalyseerd om zowel het bestaande stratigrafisch kader als de geologische kaart van de Zuidelijke Bocht te herzien. Daarbij werden negen seismische eenheden, zes generaties van insnijdingen en drie grootschalige regionale erosieoppervlakken geïdentificeerd en opgenomen in een vernieuwd stratigrafisch kader. Vervolgens werden deze resultaten geïnterpreteerd binnen de Kwartaire evolutie van het zuidelijke Noordzeebekken. Ze tonen een geleidelijke overgang van een deltaïsch en fluviatiel systeem naar een landschap dat in toenemende mate door glaciale processen werd beïnvloed. De Plio-Pleistocene en Vroeg Pleistocene afzettingen omvatten onder meer de Formaties van Red Crag, Westkapelle Ground, Smith's Knoll en Yarmouth Roads, die in deze studie in het hoogste detail werden beschreven. De Formatie van Red Crag bevat vier grote insnijdingen, die worden geïnterpreteerd als dynamische getijdengeulen die in verbinding stonden met een destijds noordelijker gelegen Noordzee. De Formaties van Westkapelle Ground en Smith's Knoll weerspiegelen prograderende deltaïsche systemen die geassocieerd zijn met een toename van de accommodatieruimte in het noordoosten en een gelijktijdige noordwaartse migratie van de kustlijn. Hoewel het onderste deel van de Formatie van Yarmouth Roads waarschijnlijk een voortzetting vormt van deze deltaïsche systemen, wijst het bovenste deel op een belangrijke wijziging in de configuratie van het Noordzeebekken. Hier werden meerdere insnijdingsfasen onderscheiden, die werden geïnterpreteerd als resten van een uitgestrekt vlechtend riviersysteem. Dit systeem weerspiegelt een overwegend fluviatiel landschap aan het einde van het Cromeriaan (Midden-Pleistoceen). Aan de top van de Formatie van Yarmouth Roads werd een regionaal erosieoppervlak onderscheiden. Op basis van de stratigrafische positie, maar vooral vanwege de aanwezigheid van diepe insnijdingen die mogelijk subglaciale tunnelvalleien vertegenwoordigen, werd dit oppervlak toegeschreven aan het Elsteriaan (MIS12). De bovenliggende afzettingen werden eveneens aan deze glaciatie, maar ook het daaropvolgende interglacial (Holsteiniaan) toegeschreven en gecorreleerd met de Formaties van Swarte Bank en Egmond Ground, hoewel onzekerheid blijft bestaan over de exacte afzettingsomstandigheden. Jongere verspreide insnijdingen werden gekoppeld aan het late Saaliaan (MIS6). Daarnaast werden twee grootschalige Laat Pleistocene erosieoppervlakken onderscheiden, die respectievelijk de basis en de top van de Formatie van Brown Bank markeren. Het onderste erosievlak vertegenwoordigt vermoedelijk een bewaard reliëf uit het late Saaliaan (MIS6), terwijl het bovenste erosieoppervlak meerdere erosieve fasen weerspiegelt die verband houden met zeespiegelschommelingen tijdens het Weichseliaan (o.a. gedurende MIS4 en MIS2). Deze resultaten bouwen voort op bestaande stratigrafische kaders maar benadrukken ook de noodzaak tot het opstellen van een voortdurend verfijnd transnationaal stratigrafisch kader. Daarbovenop vormt de identificatie van afzettingen en/of erosieoppervlakken gelinkt aan het Elsteriaan, Saaliaan en Weichseliaan een belangrijke vooruitgang omtrent de glaciale geschiedenis van het Midden- en Laat-Pleistoceen.

Gezien de sterke gelijkenissen tussen het Laat-Pleistocene erosievlak en de huidige bathymetrie (Hoofdstuk 4), richtte Hoofdstuk 5 zich op de bovenste 20 m van de ondergrond. Aan de hand van hoge-resolutie akoestische gegevens en sedimentkernen werd het centrale deel van het Axiaal Kanaal op subregionale schaal in detail onderzocht. Op basis van sedimentologische, chronologische ('optically stimulated luminescence', OSL) en paleomilieugegevens (pollen, foraminifera en schelpen) werd een chronostratigrafisch kader opgesteld. Mariene

afzettingsomstandigheden werden aangetoond door de identificatie van de eerste *in-situ*, open-mariene sedimenten van de Formatie van Eem (MIS 5e), evenals de bovenliggende ondiep-mariene afzettingen van de Formatie van Brown Bank (MIS 5a). Beide eenheden bedekken een regionaal erosieoppervlak. OSL-datering en schelpen wijzen erop dat dit oppervlak de Eemiaan transgressie vertegenwoordigt, daar waar het rechtstreeks wordt bedekt door de Formatie van Eem. Waar het erosieoppervlak wordt bedekt door de Formatie van Brown Bank, wijzen zowel de schelpassociaties als de OSL-dateringen op koelere omstandigheden en mariene herwerking tijdens MIS 5c-b. Een erosieve insnijding in het westelijke deel van het Axiaal Kanaal toont aan dat het studiegebied tijdens MIS4 een terrestrisch landschap werd als gevolg van een dalende zeespiegel. Een daaropvolgende insnijdingsfase gedateerd tot vroeg MIS3 werd geïnterpreteerd als een getijdengeul, opgevuld met herwerkte afzettingen van de Formatie van Brown Bank, zoals blijkt uit de aanwezigheid van herwerkte MIS5a microfossielen. Dit wijst op een hernieuwde (ondiep-)mariene fase in het studiegebied. Tijdens laat MIS3 maakten deze omstandigheden opnieuw plaats voor een terrestrisch landschap, zoals blijkt uit een hernieuwde insnijding in het westelijke deel van het Axiaal Kanaal, waarvan de sedimentopvulling werd gedateerd tot ca. 29 ka (overgang MIS3-2). Deze afzettingen bestaan uit ritmisch gelamineerde sedimenten met een pollenassemblage die wijst op koude, glaciale afzettingsomstandigheden. Daarom werden ze geïnterpreteerd als proglaciale lacustriene sedimenten, die gelinkt kunnen worden aan een groeiende ijslob langs de kust van Norfolk (UK). Deze afzettingen wijzen op het bestaan van een afgesloten meer in het Axiaal Kanaal, al kon de exacte omvang hiervan niet worden bepaald. Tenslotte werd een grootschalig erosieoppervlak onderscheiden dat wordt gekoppeld aan glaciofluviatiele drainage tijdens MIS2, geassocieerd met de terugtrekking van de BIIS en FIS. Deze erosiefase heeft vermoedelijk geleid tot de huidige morfologische expressie van het Axiaal Kanaal.

Door de integratie van geomorfologische, geofysische (seismische/akoestische), sedimentologische en paleomilieugegevens kon een vernieuwd Kwartair stratigrafisch kader worden opgesteld. Hieruit blijkt dat het Axiaal Kanaal (1) een meerfasige ontstaansgeschiedenis heeft en (2) heeft gefungeerd als een belangrijk (glacio-)fluviatiel drainagesysteem gedurende het Midden- en Laat-Pleistoceen. De identificatie van nieuwe afzettingen en insnijdingsfasen benadrukt zowel de complexe geologie van de Zuidelijke Bocht als de snelle landschapsveranderingen tijdens glaciale-interglaciale cycli. Daarnaast toont deze studie het belang aan van een voortdurend verfijnd transnationaal stratigrafisch kader als basis voor zowel wetenschappelijk onderzoek als voor toepassingen binnen de offshore-industrie.

TABLE OF CONTENTS

Acknowledgements i

Summary ii

Samenvatting v

CHAPTER 1. Introduction 2

1.1 North Sea Basin 2

1.2 Middle to Late Pleistocene 3

1.3 Research aim and objectives 8

1.4 Dissertation outline 9

CHAPTER 2. Methodology 12

2.1 Seismic reflection datasets and processing 13

2.2 Sediment cores 17

2.2.1 Sedimentological analysis 17

2.2.2 Optically stimulated luminescence (OSL) 19

2.2.3 Environmental analysis 20

CHAPTER 3. Geomorpology of the Axial Channel (Southern Bight, North Sea) 22

3.1 Introduction 23

3.2 Study area 23

3.3 Methodology 24

3.4 Geomorphological features 25

3.4.1 The Axial Channel 25

3.4.2 Lobourg Channel 27

3.4.3 Smaller channels connected to the Axial and Lobourg Channel 28

3.4.4 Deeps and depressions on the UK Plateau 30

3.4.5 Linear features in the Southern Bight 30

3.4.6 Depositional bedforms: sand waves and sand ridges 32

3.4.7 Depositional bedforms: transverse ridges 32

3.5 Interpretation and conclusions 32

CHAPTER 4. Reassessment of the Quaternary seismic stratigraphy of the western sector of the Southern Bight (2°-3°E), North Sea 36

4.1 Introduction 37

4.2 Geological background – current state of knowledge 38

4.3 Methodology 43

4.4 Results and interpretation 44
4.4.1 Seismic-stratigraphic units 44
4.4.2 Revised geological map 56
4.4.3 Incisions and channel features 56
4.5 Discussion 59
4.5.1 New light on the Upper Pliocene to Middle Pleistocene stratigraphy (U1-U4) 59
4.5.2 Deposits of the Middle to Upper Pleistocene (U5-U7) 61
4.5.3 New light on the Upper Pleistocene stratigraphy (U8 and U9) 63
4.5.4 Regional-scale environmental reconstruction throughout the Pleistocene 65
4.6 Conclusions 68
CHAPTER 5. New chronostratigraphic insights into the evolution of the Axial Channel (southern North Sea) from preserved Upper Pleistocene deposits 70
5.1 Introduction 71
5.2 Regional setting 73
5.3 Methods 74
5.3.1 High-resolution acoustic data 74
5.3.2 Sediment cores 74
5.3.3 Sedimentological analysis 75
5.3.4 Palaeoenvironmental analysis 76
5.3.5 OSL dating 77
5.4 Results and interpretations 78
5.4.1 Acoustic record 78
5.4.2 Sedimentary record 80
5.5 Discussion 91
5.5.1 Pre-MIS6 deposits 91
5.5.2 Marine deposits of MIS5 93
5.5.3 Filling the gap: deposits correlated with MIS4-3 95
5.5.4 Evolution of the Axial Channel system 97
5.6 Conclusions 102
CHAPTER 6. Synthesis and outlook 104
6.1 Stratigraphy of the Axial Channel 52°-53°N 104
6.2 Role of the Axial Channel throughout the Middle to Late Pleistocene 109
6.2.1 (Pre-) Elsterian glaciation 109

6.2.2 Holsteinian interglacial and early Saalian glacial 111
6.2.3 Late Saalian (Drenthe) glaciation 111
6.2.4 Eemian interglacial 113
6.2.5 Weichselian glaciation 113
6.2.6 Holocene 115
6.3 Final thoughts, wider implications and future perspectives 115
6.3.1 Data specific perspectives 117
6.4 Conclusional remarks 118
List of Abbreviations **119**
List of Figures **121**
List of Tables **126**
Supplementary Material **127**
References **147**



Picture taken at sunrise onboard the RV *Belgica II* during the August 2022 DynaMOD II survey (BE2022-18).

CHAPTER 1. INTRODUCTION

1.1 North Sea Basin

The present-day North Sea Basin is a shallow, continental sea situated on the European shelf. To the south, it is connected to the Atlantic Ocean via the Strait of Dover and the English Channel (Figure 1-1). The North Sea is subdivided in a northern, central and southern sector, with the southernmost part of the southern North Sea referred to as the Southern Bight (Figure 1-1a). The Southern Bight has an average depth of -50 m relative to lowest astronomical tide (LAT). It is characterised by extensive sandbanks, which are grouped into several distinct sandbank fields: the Dutch Banks, Zeeland Banks, Flemish Banks, Hinder Banks, Thames Banks and the Norfolk Banks (Figure 1-1b; e.g. Johnson et al., 1982).

The North Sea Basin developed in an intratectonic setting, centred above a Mesozoic rift structure (Arfai et al., 2018; Lamb et al., 2018). Throughout the Neogene and Quaternary, basin evolution and sediment accumulation were primarily controlled by long-term tectonic subsidence (Cameron et al., 1992; Lamb et al., 2018; Thorne and Watts, 1989). Over the last 1.8 Ma, mean background subsidence rates in the southern North Sea, including the combined effects of tectonic subsidence, compaction and sediment loading, have remained below c. -0.25 m/kyr (Cohen et al., 2022; Hijma et al., 2025). The main Quaternary depocenter is confined to a NNW-SSE zone in the northern and central North Sea ("Central Graben", purple contour; Figure 1-1a), where Quaternary deposits attain a maximum thickness of c. 1200 m (Arfai et al., 2018; Lamb et al., 2018). In the Southern Bight, the thickest Quaternary succession (800-900 m) occurs in a depocenter in the Dutch sector of the North Sea ("Southern Bight Basin", purple contour; Figure 1-1a; Busschers et al., 2025). The Quaternary sedimentary infill of this depocenter was predominantly supplied by the Eridanos or Baltic River system, which transported sediment from the Baltic region and Central Uplands of Germany into the North Sea Basin (Gibbard and Lewin, 2016). During the late Pliocene and Early Pleistocene (c. 2.6 Ma - 0.8 Ma), the Eridanos system, together with other major NW European river systems, developed extensive (pro-)deltaic complexes across the basin (Gibbard and Lewin, 2016).

At the onset of the Middle Pleistocene (c. 800 ka), sedimentation became increasingly controlled by glacial-interglacial cycles and associated changing sea levels (see Section 1.2). Progressive climatic cooling promoted the expansion of major ice sheets in the Alps, the British Isles and Scandinavia. The growth of the Scandinavian Ice Sheet ultimately disrupted the Eridanos River System, fundamentally altering sediment supply in the North Sea Basin (Cohen et al., 2017; Gibbard and Lewin, 2016). Throughout the Middle and Late Pleistocene (c. 800 – 11.7 ka), repeated glaciations caused major rerouting of NW European river systems leading to substantial reconfiguration of regional coastlines. These changes not only influenced the palaeogeography of the southern North Sea but also controlled the depositional evolution, resulting in alternating phases of sediment accumulation and erosion (e.g. Cohen et al., 2014).

The Quaternary geology of the Southern Bight has been mapped based on extensive datasets collected during the 1960s-1980s as part of a joint British, Dutch, and Belgian mapping effort (Laban et al., 1984), and subsequently compiled by the British Geological Survey (BGS, 2000). The principal map sheets covering most of the Southern Bight include the East Anglia, Flemish Bight, Thames Estuary and Ostend sheets (Figure 1-1b; Balson and D'Olier, 1990; Cameron et al., 1984a; Harrison and Hopson, 1991; Laban et al., 1992).

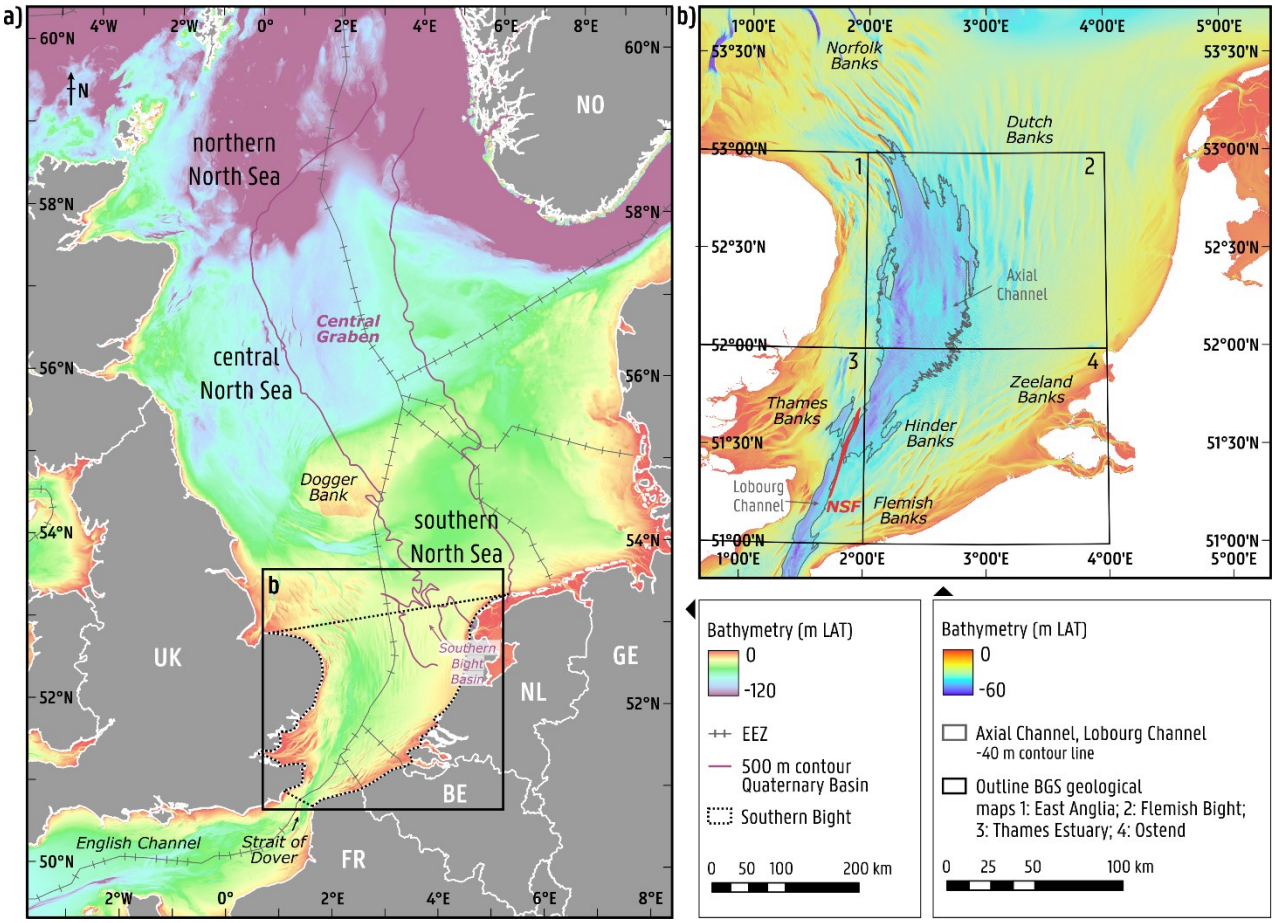


Figure 1-1. (a) Overview bathymetric map (in m to lowest astronomical tide; LAT) of the North Sea with Southern Bight area (black dotted line) and Quaternary depocenters (Central Graben and Southern Bight Basin; purple line) indicated. The Dogger Bank, Strait of Dover and English Channel are indicated for geographical reference. (b) Bathymetric map (in m LAT) of the Southern Bight, with linear sandbank fields, North-South Falls sandbank (red; NSF), Axial Channel, Lobourg Channel indicated for geographical reference.

The most prominent geomorphological feature in the present-day bathymetry of the Southern Bight is the Axial Channel (Liu et al., 1992; Mathys, 2009). This large depression extends from the Norfolk Banks in a general northeast-southwest direction towards the Lobourg Channel and the Strait of Dover, making this a c. 200 km-long feature (Figure 1-1). The Axial Channel is situated in between the extensive tidal sandbank fields of the Southern Bight, with the North-South Falls sandbank separating the Axial Channel from the Lobourg Channel in the south (Figure 1-1b; Balson and D'Olier, 1990). The Axial Channel has an average depth of c. -50 m LAT, locally reaching depths of up to -65 m LAT. It is widest in its central part, between 52° N and 52°30' N, where it reaches a width of c. 55 km, and narrows to a width of c. 10 km towards both the north and the south (Figure 1-1b).

1.2 Middle to Late Pleistocene

The Pleistocene (c. 2.6 Ma - 11.7 ka) is characterised by periodic glacial-interglacial oscillations. $\delta^{18}O$ values from global deep-sea records are commonly used as a proxy for global ice volume, sea-level fluctuations and temperature, with high $\delta^{18}O$ values indicating large ice volumes during cold periods (Figure 1-2; Lisiecki and Raymo, 2005). This isotope record forms the basis for the subdivision of the Quaternary into Marine Isotope Stages (MIS), with even numbers corresponding to glacial periods and uneven numbers to interglacial periods (Lisiecki and Raymo, 2005). An overall intensification of glacial-interglacial oscillations occurred from the Plio-Pleistocene transition onwards (c. 2.6 Ma), but the periodicity changed drastically during the Middle Pleistocene. This shift involved a transition from cycles with relatively short glacials and long interglacials to cycles with longer glacials and shorter

interglacials (Lisiecki and Raymo, 2005). This interval, between c. 1.2 and 0.7 Ma, is known as the Mid Pleistocene Revolution (MPR) and is characterised by the transition from 41-kyr climatic cycles to 100-kyr cycles (Figure 1-2; Clark et al., 2006). In addition to recording the advance and retreat of continental ice sheets, glacial-interglacial cycles are closely linked to eustatic sea-level fluctuations (Spratt and Lisiecki, 2016). From the Middle Pleistocene onwards, global sea level fluctuated between c. -130 m and +10 m, with a mean sea level of c. -55 m below mean sea level (bmsl) (Figure 1-2; Spratt and Lisiecki, 2016). Given that the southern North Sea has an average depth of c. -50 m LAT (green line; Figure 1-2), this implies that the area was a terrestrial landscape during most of the Pleistocene, alternated by intervals of shallow-marine to open-marine conditions.

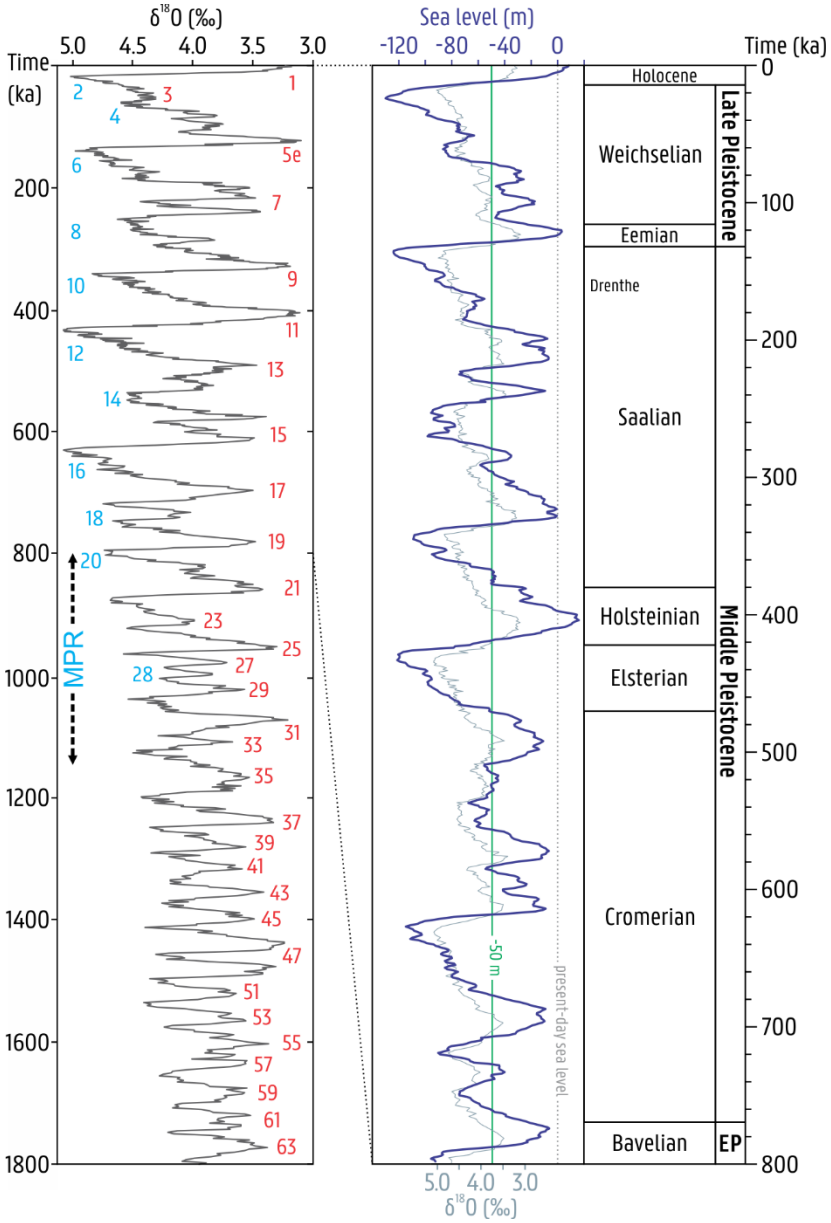


Figure 1-2. Oxygen isotope sequence for the last 1800 ka, with Marine Isotope Stages (MIS; red – interglacial stages; blue – glacial stages) and sea-level stack for the last 800 ka (superimposed on oxygen isotope sequence) adapted from Lisiecki and Raymo (2005) and Spratt and Lisiecki (2016). Average depth of southern North Sea (-50 m LAT) indicated by green line. Subdivision of the Early Pleistocene (EP) to Holocene after Cohen and Gibbard (2019).

During the Late Pliocene and Early Pleistocene, the difference between sea-level minima and maxima did not exceed 100 m (Spratt and Lisiecki, 2016). Despite these fluctuations, the palaeogeography of NW Europe remained relatively stable and the major river systems repeatedly occupied similar positions (e.g. Cohen et al., 2014). During this period, the North Sea Basin formed an embayment

connected to the Atlantic Ocean in the north, into which major river systems, including the Eridanos, Thames and Rhine formed an extensive delta plain (Figure 1-3). To the south, the Weald-Artois Anticline formed a land bridge that connected Britain to mainland Europe (Figure 1-3). Consequently, even during interglacial sea-level highstands, no southern marine connection to the Atlantic Ocean existed (e.g. Cohen et al., 2017; Gibbard and Lewin, 2016; Hijma et al., 2012).

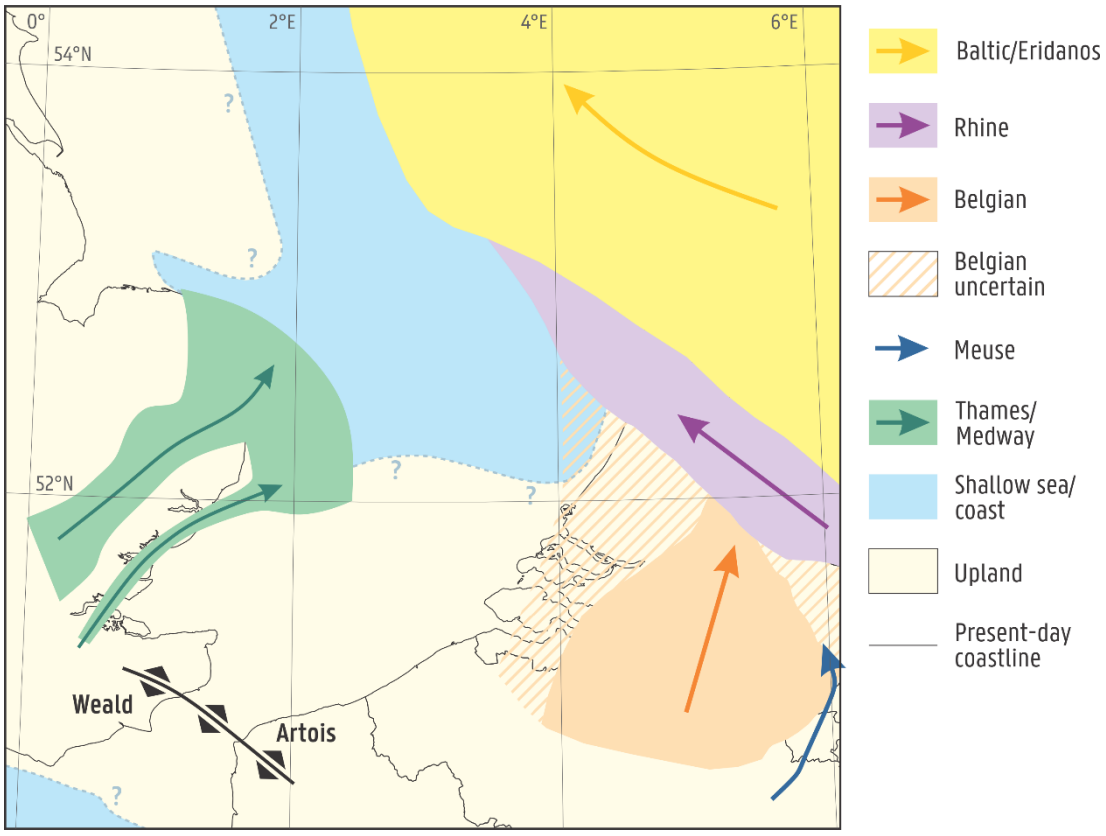


Figure 1-3. Palaeogeographic setting during the Early Pleistocene (Calabrian) adapted from Busschers et al. (2025) and Hijma et al. (2012).

Throughout the Middle and Late Pleistocene, cold climatic conditions caused the British-Irish and Scandinavian Ice Sheets (BIIS and FIS, respectively) to advance across the North Sea Basin during three consecutive major glaciations: the Elsterian/Anglian, Saalian/Wolstonian and Weichselian/Devensian (NW European/British nomenclature; the European terminology is adopted throughout this dissertation) (e.g.Graham et al., 2011). The most recent reconstructions of the Elsterian and Saalian ice-sheet are presented by Batchelor et al. (2019), based on compiled empirical datasets and numerical modelling, and subsequently refined by Busschers et al. (2025) using additional onshore evidence from the Netherlands (Figure 1-4). According to these reconstructions, the Elsterian maximum ice margin extended from the Dutch coast at c. 53°N in a southwestern direction towards the Suffolk and Essex Coast (UK), forming a distinctive 'W'-pattern at the British-Dutch border in the southern North Sea (Figure 1-4). The maximum Saalian ice margin extended further south over the Netherlands and its adjacent offshore areas, forming a distinctive lobe at the height of c. 4° E. Offshore, the reconstructed margin abruptly bends northwards to c. 53°30'N before turning southwest towards the Norfolk Coast (Figure 1-4). The most up-to-date reconstruction of the Weichselian ice-sheet extent was produced as part of the BRITICE-CHRONO project (Clark et al., 2022). During the Weichselian, the ice margin did not advance south of c. 53°N in the southern North Sea, following a line that connects the Norfolk Coast with the southern edge of Dogger Bank (Figure 1-1a, Figure 1-4).

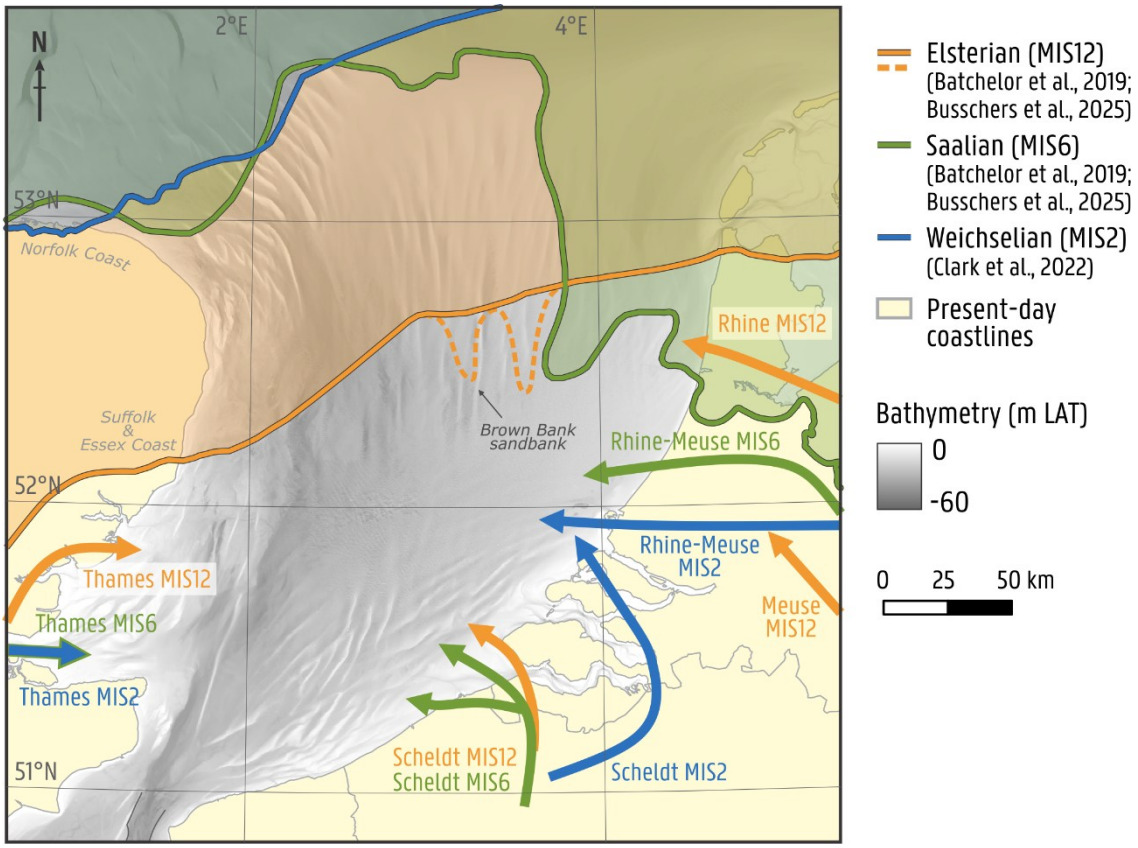


Figure 1-4. Middle to Late Pleistocene ice limit reconstructions after Batchelor et al. (2019); Busschers et al. (2025); Clark et al. (2022). Reconstructions of the courses of major NW European river systems (Thames, Rhine, Meuse, Scheldt) at MIS12 (orange arrows), MIS6 (green arrows) and MIS2 (blue arrows) are adapted from Busschers et al. (2025); De Clercq et al. (2018); Hijma et al. (2012); Rose (2009).

The Elsterian glaciation is assigned to MIS12 (c. 480 - 420 ka; Figure 1-2; Cohen and Gibbard, 2019; Lisiecki and Raymo, 2005). It is widely regarded as a key phase in the evolution of the southern North Sea landscape (e.g. Cohen et al., 2014). It represents the most extensive Pleistocene glaciation in the North Sea Basin (Figure 1-4), evidenced by the widespread occurrence of buried subglacial tunnel valleys (e.g. Graham et al., 2011; Kirkham et al., 2024; Praeg, 2003). The advance of the ice sheet blocked a northern drainage route, forcing rivers such as the Thames and Scheldt to be deflected towards the south (Figure 1-4; Gibbard et al., 1988; Gibbard and Lewin, 2016; Hijma et al., 2012). Also the Rhine and Meuse must have deflected southwards, where they merged with proglacial drainage systems south of the ice margin (Figure 1-4; Busschers et al., 2025). The presence of the ice margin to the north combined with the Weald-Artois land bridge to the south has led to the hypothesis that a large proglacial lake may have developed within the present-day southern North Sea Basin (e.g. Gibbard et al., 1988; Gibbard and Lewin, 2016; Hijma et al., 2012). It has been proposed that overspill of this lake at the end of the Elsterian glacial phase breached the Weald-Artois land bridge, opening the Strait of Dover through a catastrophic glacial lake outburst flood (GLOF). Erosional landforms preserved within the Strait of Dover and the English Channel have been interpreted as evidence for such an event (Collier et al., 2015; García-Moreno et al., 2019; Gibbard et al., 1988; Gupta et al., 2007). However, this hypothesis remains debated as no direct sedimentological evidence for such a large proglacial lake has been identified in the southern North Sea (Cohen et al., 2014). Furthermore, the erosional landscape preserved in the Strait of Dover and English Channel could also be linked to a prolonged phase (>200 kyr) and/or repeated episodes of high-energy fluvial erosion (Arosio et al., 2021; García-Moreno et al., 2021; Mellett et al., 2013). Regardless of the precise mechanism, sedimentary records from the Bay of Biscay indicate that a southern drainage route was established during MIS12, confirming that the Strait of Dover had been breached and that a southern connection

between the North Sea Basin and the English Channel existed by the end of the Elsterian glacial period (Toucanne et al., 2009b, 2009a).

The Saalian glaciation is generally correlated with MIS10 to MIS6 (c. 380-130 ka; Figure 1-2; Cohen and Gibbard, 2019; Lisiecki and Raymo, 2005). Due to limited empirical evidence, the extent of the ice sheets during the early and middle Saalian remains poorly constrained (Batchelor et al., 2019). Loess deposits onshore in the Netherlands indicate cold periglacial conditions during MIS10, 8 and 6, alternated with warmer periods characterised by soil formation during MIS9 and 7 (Meijs et al., 2013). Offshore, c. 80 km north of the Wadden Islands, a diamicton has been attributed to an early Saalian phase (most-likely corresponding to MIS8) based on the MIS7 age correlation of the overlying deposits (Beets et al., 2005). The late Saalian (Drenthe) glaciation, within MIS6 (c. 160-150 ka; Figure 1-2), is considerably better constrained. Coalescing of the BIIS and FIS in the southern North Sea Basin during this phase is evidenced by tills (diamictons; Davies et al., 2011) and subglacial tunnel valleys north of 53°N (e.g. Huuse and Lykke-Andersen, 2000; Moreau et al., 2012). Based on the location of late Saalian ice-pushed ridges onshore the central Netherlands and in adjacent areas offshore (Hollandse Kust West wind farm), this glaciation is identified as the most extensive glaciation in the Netherlands (Figure 1-4; Bakker and Van Der Meer, 2003; Busschers et al., 2025; Cartelle et al., 2021). The ice margin and associated ice-pushed ridges forced the Rhine to adopt a westward course, with the Meuse as its principal tributary (Figure 1-4; Busschers et al., 2008). For a second time, a large proglacial lake is believed to have formed in the present-day southern North Sea Basin, impounded between the Saalian ice margin to the north and the last vestiges of the Weald-Artois land bridge to the south (Busschers et al., 2008; Gibbard et al., 1988; Hijma et al., 2012; Murton and Murton, 2012). Overspill of this lake has been proposed as the mechanism responsible for further breaching of the Strait of Dover (Gupta et al., 2017; Murton and Murton, 2012). However, the absence of direct offshore evidence for a large proglacial lake has led to continued debate regarding its existence (Cartelle et al., 2021; Cohen et al., 2014; Mellett et al., 2013). Regardless of the mechanism that further shaped the preserved erosional landscape in and south of the Strait of Dover (e.g. García-Moreno et al., 2019; Mellett et al., 2013), sedimentary records from the Bay of Biscay indicate repeated episodes of southern drainage during MIS10, 8 and 6 (Toucanne et al., 2009b, 2009a).

The Weichselian glaciation corresponds to MIS5d-2 (c. 116-11.7 ka; Figure 1-2; Cohen and Gibbard, 2019; Lisiecki and Raymo, 2005). In the southern North Sea Basin, two major glacial advances have been correlated with MIS4 and MIS2 (Batchelor et al., 2019; Toucanne et al., 2023). However, uncertainties remain regarding the coalesce and formation of a vast, grounded ice sheet during the Early Pleniglacial (MIS4; Toucanne et al., 2023). During the Last Glacial Maximum (LGM), the southernmost ice-margin position was reached between c. 27 and 21 ka (Figure 1-4; Clark et al., 2022). Sedimentary evidence for the LGM ice advance is concentrated around Dogger Bank (Figure 1-1a) and includes glaciolacustrine deposits, till sheets and ice-pushed ridges (Cotterill et al., 2017; Emery et al., 2019; Phillips et al., 2018; Roberts et al., 2018). Southern drainage through the Strait of Dover has been inferred during both MIS4 and MIS2. However, the absence of a distinct northern European geochemical signature (i.e. Baltic-type of Nd isotopes) in the Bay of Biscay suggests additional drainage activity to the north (Toucanne et al., 2023). During MIS2, the Rhine adopted a course south of the Saalian ice-pushed ridges and became confluent with the Meuse (Figure 1-4; Busschers et al., 2007; Peeters et al., 2016). However, also the Scheldt changed its course during late MIS3, merging with the Rhine-Meuse system near today's city of Rotterdam (Figure 1-4; Busschers et al., 2025; Heyse and Demoulin, 2018; Slupik et al., 2013). Renewed and intensified drainage through the Strait of Dover between c. 20 and 17 ka has been recorded by an increased input of sediment (with a Baltic-type geochemical signature) and linked to the onset of deglaciation of the BIIS and FIS (Clark et al., 2022; Mellett et al., 2013; Toucanne et al., 2010).

1.3 Research aim and objectives

The previous section demonstrates that there are still many uncertainties surrounding the Middle and Late Pleistocene glaciations in the southern North Sea, including the positions of former ice margins and the evolution of fluvial drainage pathways. This dissertation focuses on the Axial Channel to assess whether this feature can provide new insights into the glacial history of the southern North Sea, particularly concerning the interactions between ice-sheet dynamics and (glacio-)fluvial systems.

Previous studies proposed that the Axial Channel originated as an eastward branch of the Thames-Medway system during the Early to Middle Pleistocene, draining northwards into a more northernly positioned North Sea (Balson and D'Olier, 1990; Gibbard and Lewin, 2016). More recent publications suggested that the Axial Channel acted as a major drainage system that incorporated several NW European river systems, before ultimately discharging southwards through the Strait of Dover during the Middle and Late Pleistocene (De Clercq et al., 2018; Hijma et al., 2012). Given its alignment with the Lobourg Channel, the Strait of Dover and the English Channel, whose evolution has been linked to major drainage events during the Elsterian (MIS12), Saalian (MIS10, 8 and 6) and Weichselian (MIS4 and 2) (see Section 1.2), the evolution of the Axial Channel may be related to one or more of these glaciofluvial drainage phases. An initial bathymetric and seismic investigation of the Axial Channel was conducted by García-Moreno (2017), who identified six escarpments, including four prominent NE–SW-oriented scarps, that were interpreted as resulting from successive incisional phases during the late Saalian and/or Weichselian. One of these escarpments, located on the Belgian Continental Shelf has been interpreted as a river terrace of the late Saalian (MIS6) deflected Rhine-Meuse system (De Clercq et al., 2018; Hijma et al., 2012). During MIS2, the Rhine-Meuse-Scheldt system is believed to have merged with the Axial Channel, which likely functioned as a glaciofluvial drainage system connected to the Weichselian ice margin in the north (Busschers et al., 2025; De Clercq et al., 2018). However, most of these interpretations remain largely hypothetical as they are solely based on the present-day bathymetric expression and lack direct chronological constraints. Consequently, both the timing and mechanisms of the formation and evolution of the Axial Channel is still unknown. The **aim of this dissertation** is therefore to reconstruct the formation and evolution of the Axial Channel system throughout the Middle and Late Pleistocene. To achieve this, both the present-day bathymetry and subsurface geology of the Axial Channel and wider Southern Bight were investigated.

A detailed analysis of the present-day bathymetry, including preserved geomorphological features associated with the Axial Channel, is needed to test the current hypothesis that the Axial Channel represents a remnant of a large-scale drainage system. Studies of the Strait of Dover and English Channel have demonstrated that detailed bathymetric mapping can substantially improve our understanding of the geomorphic processes involved in their evolution (Arosio et al., 2021; García-Moreno et al., 2019; Gupta et al., 2017). These studies have also shown that preserved geomorphological evidence can be used to establish a relative sequence of events. Similarly, analysing the bathymetry of the Southern Bight may therefore not only clarify the evolution of the Axial Channel, but also provide the basis for establishing a relative chronology (**Objectives 1 & 2**).

A robust stratigraphic framework is essential for constraining both the origin and evolution of the Axial Channel. Existing offshore stratigraphic frameworks have been developed for the Dutch (Rijsdijk et al., 2005) and British (Stoker et al., 2011) sectors of the southern North Sea, primarily using seismic interpretation and lithological data from boreholes. More recent studies have demonstrated that detailed analysis of higher-resolution seismic and sub-bottom profiler data, combined with extensive lithological investigations (including sedimentological, palaeontological and chronological analyses) can significantly improve Quaternary stratigraphic reconstructions (e.g. Cotterill et al., 2017; Eaton et al., 2020; Waajen-Labee et al., 2025). As such, a comprehensive reassessment of the stratigraphy and geology of the Southern Bight is needed before it can be used to constrain the formation and evolution

of the Axial Channel system (**Objectives 3 & 4**). Busschers et al. (2025) recently published an updated stratigraphic framework for the Dutch onshore and offshore sectors. And although Dakin et al. (2026) substantially improved the British framework using offshore wind-farm (OWF) data, the latter remains geographically restricted and lacks a regional perspective. Despite previous attempts at regional correlations between the different frameworks, an integrated transnational stratigraphic framework for the southern North Sea is still missing.

Developing an integrated stratigraphic framework is fundamental to palaeolandscape reconstructions. In recent years, integrated analyses of geophysical and lithological datasets have enabled increasingly detailed reconstructions of the Late Quaternary palaeogeography of the southern North Sea (e.g. Amkreutz and Vaart-Verschoof, 2021; De Clercq et al., 2018; Emery et al., 2020; Gaffney et al., 2007; Mellett et al., 2013; Waajen-Labee et al., 2025). Reassessing the stratigraphy of the Southern Bight, together with detailed lithological investigations, will therefore not only provide chronological constraints on the Axial Channel system, but also enable detailed palaeogeographic reconstructions (**Objective 5 & 6**). Such reconstructions are archaeologically significant as they improve our understanding of how climate and landscape changes influenced human occupation and evolution during the Palaeolithic (i.e. prehistoric period largely corresponding with the Pleistocene) (Cohen et al., 2014; Hijma et al., 2012). Palaeolandscape reconstructions are also highly relevant in the context of modern climate change. Understanding processes such as the formation or reoccupation of glaciofluvial drainage systems, postglacial sea-level rise and coastal inundation under natural conditions provides valuable analogues that can help refine predictions of future environmental and sea-level change (e.g. Hijma et al., 2025). As the Axial Channel is believed to be a remnant of a major glaciofluvial drainage system, reconstructing its evolution is essential for understanding both the Late Quaternary evolution of the southern North Sea and its broader palaeoenvironmental significance.

From an applied perspective, the reassessment of the stratigraphy and development of an integrated stratigraphic framework (**Objective 3- 6**) are crucial for the Offshore Renewable Energy (ORE) sector, including offshore windfarm (OWF) developments. Such projects play a key role in meeting the European Union's energy and climate targets, while at the same time reducing dependence on energy imports (European Comission, 2020). As geology exerts a primary control on seabed and subsurface properties, a robust geological characterisation is essential for sustainable offshore developments. Seismic and lithological dataset interpretations in particular give valuable insights into the geometry and heterogeneity of geological units, and geotechnical properties of the (shallow) subsurface, respectively, which in turn provide a baseline for geoengineering considerations and thus the development of offshore infrastructures (e.g. Dakin et al., 2026).

1.4 Dissertation outline

This dissertation consists of three main research chapters that address the objectives and overarching aim outlined in the previous section. A schematic overview of the dissertation structure, including the different chapters and their corresponding objectives (two per chapter), is shown in Figure 1-5. Prior to the main research chapters, an overview chapter of the methodologies used throughout this dissertation is provided (**Chapter 2**).

Chapter 3 investigates and maps preserved geomorphological features associated with the Axial Channel (Objective 1). Publicly available bathymetric datasets, including EMODnet bathymetry and high-resolution bathymetry blocks provided by the UK Hydrographic Office, were compiled and incorporated in a Geographic Information System (GIS) software. Morphological analysis and the assessment of erosional relationships were used to interpret the origin of these features (marine, fluvial or glacial) and to reconstruct a relative chronology of the development of the Axial Channel

system and associated landforms (Objective 2). This chapter has been published in *Journal of Maps* as Vervoort et al. (2026).

Chapter 4 analyses an extensive high-resolution sparker seismic dataset covering a large part of the Southern Bight. The seismic interpretation enabled the development of a regional seismostratigraphic framework (Objective 3), which provides the basis for comparing and reassessing the existing Quaternary stratigraphic frameworks (Objective 4). This reassessment offers new insights into the Late Quaternary evolution of the southern North Sea Basin. This chapter has been submitted to *Quaternary Science Reviews* and is under review.

Chapter 5 integrates high-resolution SBP data and vibrocore data to investigate preserved Upper Pleistocene deposits within the Axial Channel system. These data are used to establish a chronostratigraphic framework (Objective 5), which in turn enables the reconstruction of the Late Pleistocene palaeogeography of the Axial Channel and wider southern North Sea region (Objective 6). The resulting reconstruction is correlated with published palaeogeographic reconstructions of the major NW European river systems. This chapter will be submitted to *Journal of Quaternary Science*.

Finally, **Chapter 6** synthesises the principal findings of the preceding research chapters and discusses their broader implications for understanding the Late Quaternary evolution of the southern North Sea Basin. As the research chapters are based on published or (soon to be) submitted peer-reviewed journal articles, some repetition is expected, particularly within the Introduction, Study area and Methodology sections. Each chapter uses a different numbering system for the interpretation of seismic/acoustic units and their basal surfaces. For an overview and additional guidance, the reader is referred to Table 6-1.

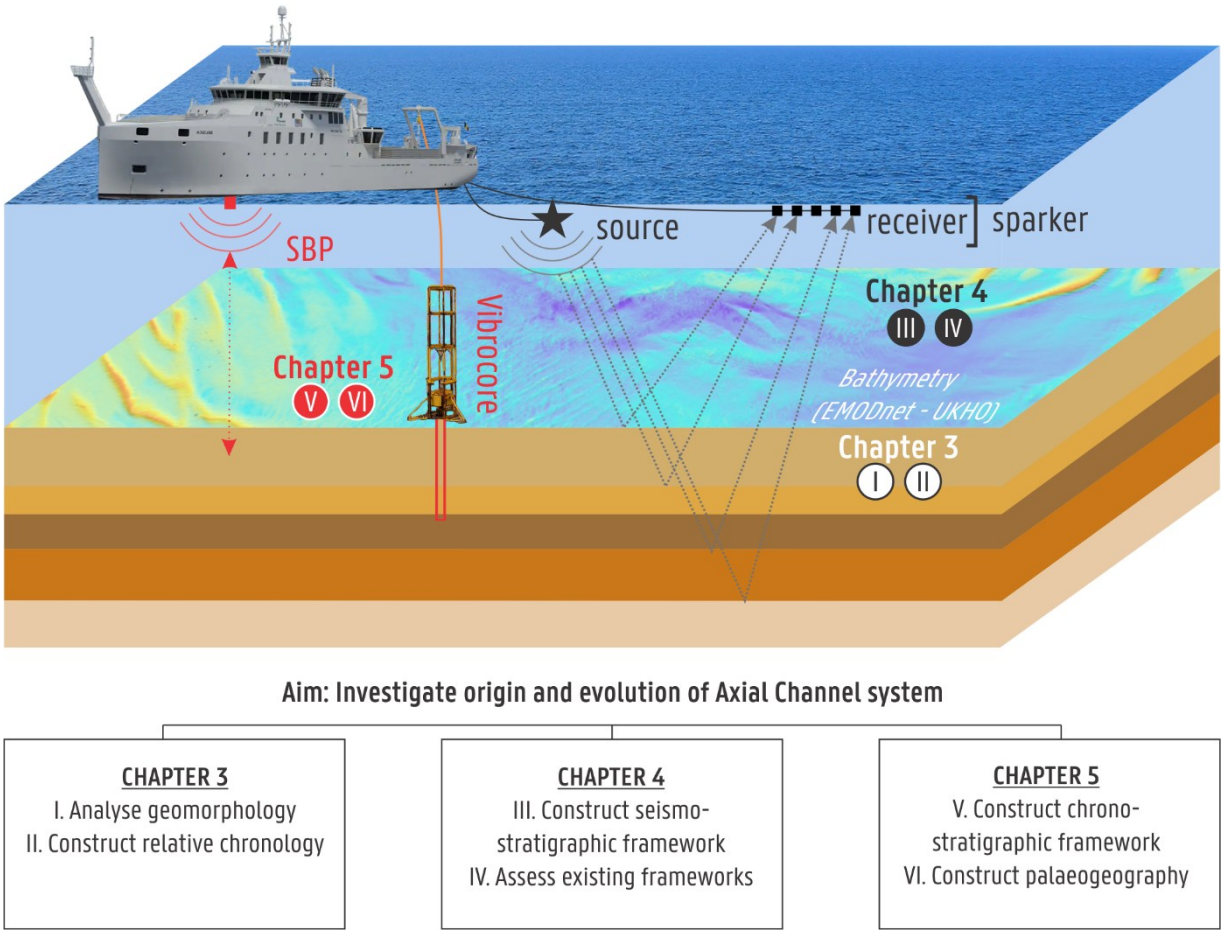


Figure 1-5. Schematic representation of the research aim, objectives and dissertation outline. It further includes the four main datasets: bathymetric, seismic sparker, sub-bottom profiler (SBP) and vibrocore data.

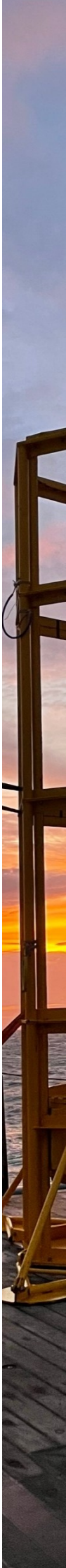
This dissertation forms part of the Belgian Science Policy Office (BELSPO) WALDO-project (project no. RV/21/WALDO), led by the Flanders Marine Institute (VLIZ) and the Renard Centre of Marine Geology (RCMG) of Ghent University. WALDO is an acronym for "**W**here are **a**ll the (proglacial) **l**ake se**d**iments in the N**o**rth Sea Basin?". This project commenced on 15 December 2021 and ran until 30 September 2026. A follow-up committee was established to provide scientific guidance and oversight, comprising of Dr. Natasha Barlow, Dr. Sarah Bradley, Dr. Sytze van Heteren (substitute: Dr. Freek Busschers), Gareth Carter (substitute: Dayton Dove), Prof. Dr. Sanjeev Gupta and Prof. Dr. Vince Gaffney. As the acronym suggests, the WALDO-project aims to test the hypothesis that proglacial lakes were important landscape features in the southern North Sea Basin. Existing lithostratigraphic and seismostratigraphic frameworks have provided insufficient evidence to confirm their presence (Section 1.2). Consequently, one of the project's principal objectives was to acquire extensive new geophysical and sedimentological datasets. These datasets are intended to refine the existing stratigraphic frameworks and facilitate more detailed palaeogeographic reconstructions of the southern North Sea. The research presented in this dissertation contributes directly to these objectives.

CHAPTER 2. METHODOLOGY

ABSTRACT

This chapter provides an overview of the research techniques employed throughout this dissertation, together with the theoretical background and other methodological considerations relevant to the interpretation of the results. As Chapters 3, 4 and 5 are adapted from published or (soon to be) submitted peer-reviewed journal articles, they each contain a study-specific methodology section. Some overlap in methodological descriptions therefore occurs.

The research is primarily based on the interpretation of marine geophysical and geological datasets. These comprise newly acquired seismic reflection and sub-bottom profiler data, and vibrocores collected between 2022 and 2025 onboard the research vessels RV *Belgica II* and RV *Simon Stevin*. In addition, previously acquired geophysical data collected by VLIZ and RCMG between 2018 and 2021 were incorporated, together with several publicly available datasets, including those provided by the EMODnet consortium, UK Marine Data Exchange, UK Offshore GeoIndex, UK Hydrographic Office and DINOloket. Data processing, analyses, interpretation and visualisation were performed using a range of specialised software packages and include the S&P Global Software Geoscience package (Kingdom Version 2019), Geographic Information System software (ArcGISPro and Global Mapper), RadExPro, Grapher (Golden Software), RStudio and CorelDRAW.



2.1 Seismic reflection datasets and processing

Seismic reflection surveying is a geophysical technique used to image subsurface sediments and geological structures. Although various seismic sources and receivers can be deployed, all seismic reflection systems operate according to the same principle. A seismic source generates compressional waves (P-waves) that propagate through the water column, seafloor and underlying sediments. The acoustic impedance, which is the product of seismic velocity and density, changes at the interface between two media. At that interface, part of the seismic energy is reflected back to the water surface, while the remaining energy travels through the underlying medium and is refracted according to the contrast in acoustic properties. The reflected waves are recorded by one or more receivers. The time at which the seismic wave propagates through the water column and subsurface (two-way travel time) is measured and used to construct a vertical image of the subsurface. The velocity and amplitude of the reflected waves depend on the elastic properties and densities of the subsurface materials, allowing geological boundaries and sedimentary structures to be displayed in the resulting vertical profile (Nanda, 2021; Reynolds, 2011).

The seismic reflection datasets acquired specifically for this dissertation in 2022, 2023 and 2025 consist of high-resolution sub-bottom profiler (SBP) data (Kongsberg TOPAS PS18 from RV *Belgica II* and Innomar SES-2000 Quattro from VLIZ) and both single-channel and multi-channel sparker data (GSO 360 multi-tip from VLIZ or Centipede multi-tip from Ghent University) (Figure 2-1; Table 2-1). The complete survey coverage acquired as part of the WALDO-project is presented in Supplementary Figure S1. In addition to these newly acquired datasets, previously collected data from surveys conducted between 2018 and 2021 were also incorporated in this dissertation. These include parametric echosounder, single-channel sparker and multi-channel sparker datasets (Figure 2-1). An overview of all seismic reflection datasets and the acquisition systems used is shown in Table 2-1, while the characteristics and operating principles of the individual systems are described in the following sections.

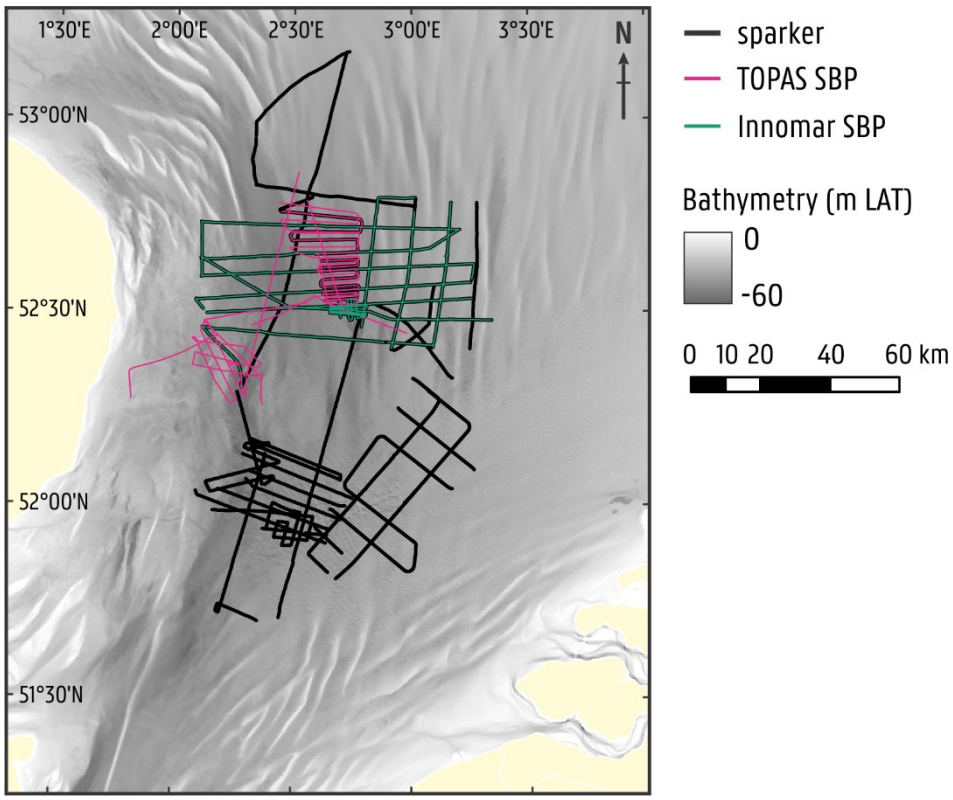


Figure 2-1. Overview of seismic and sub-bottom profiler (SBP) data used in this study. See Supplementary Figure S1 for the complete survey coverage acquired as part of the WALDO-project.

The sparker system is a high-resolution seismic system consisting of a separate source (i.e. the sparker *sensu strictu*) and a receiver, both towed behind the research vessel (Figure 1-5). The centre frequency varied between 350 and 1200 depending on the survey and sparker source used, resulting in a vertical resolution of c. 0.3-1.2 m (Table 2-1). The sparker source consists of a series of electrodes. A high-voltage electrical discharge is generated between the electrode tips, ionising the seawater and producing rapidly expanding bubbles. Once these bubbles implode, an acoustic pressure pulse is created which propagates through the water column, where it is reflected by the seabed as well as the underlying sediments (at interfaces with contrasting acoustic impedance). The returning reflections are recorded by hydrophones, positioned in either a single-channel or multi-channel streamer. Two different sparker sources were deployed depending on the survey: the GSO-360 multi-tip sparker and the Centipede multi-tip sparker. The GSO-360 multi-tip sparker consists of clustered electrodes in a compact frame, whereas the Centipede multi-tip sparker consists of a linear electrode array (Geophysical Services Offshore BV, n.d.). Surveys conducted aboard the RV *Belgica II* utilised a SIG multi-channel streamer with 24 channels. During the other surveys, a single-channel streamer (or dual-channel streamer with only one channel activated) was deployed (Table 2-1). Compared with single-channel acquisition, multi-channel seismic survey provides an improved signal-to-noise ratio and enhanced data quality (Reynolds, 2011). This improvement is achieved through the Common Depth Point (CDP) processing method, which combines multiple traces from different source-receiver pairs that reflect off the exact same subsurface reflection point (Nanda, 2021).

The Kongsberg TOPAS PS18 SBP is a high-resolution acoustic system consisting of a hull-mounted transducer (Figure 1-5). This hull-mounted configuration allows less interference from waves as opposed to towed systems, permitting higher surveying speeds for similar data results. Depending on the required penetration depth, water depth and desired resolution, the system can transmit different signal waveforms (chirps or pulses). During surveys conducted onboard the RV *Belgica II*, a secondary frequency of 2-4 kHz was used, resulting in a decimetric vertical resolution (Table 2-1; Kongsberg Geoacoustics ltd., 2019). With these acquisition settings, the top c. 50 m of the subsurface can be imaged.

The Innomar SES-2000 Quattro is a dual-frequency SBP consisting of four transducers that transmit two slightly different high frequency signals (i.e. primary frequencies). The interaction of these primary frequencies in the water column generates by interference a new low-frequency signal, which is the secondary or difference frequency. During the different surveys this secondary frequency ranged from 6 to 8 kHz, resulting in a vertical resolution of c. 5-10 cm (Table 2-1). The pulse repetition rate ranged between 0.075 and 0.1 s (Table 2-1). On average, a penetration depth of up to 15 m below the seafloor was achieved. The transducers were pole-mounted and attached to the side of the survey vessel, allowing this system to be lowered 20-30 cm below the water surface during measurements (Innomar Technologie GmbH, n.d.; Missiaen, 2010).

Table 2-1. Overview of settings for the different sparker seismic and SBP datasets used for this dissertation.

SPARKER					
Survey	**Source**	**Streamer**	**Centre frequency**	**Shot interval**	**Vertical resolution**
RV *Belgica* BE2018-09	Centipede multi-tip	SIG single channel	1.1-1.2 kHz	1 s	c. 0.3-0.4 m
RV *Belgica* BE2019-13	GSO 360 multi-tip	SIG single channel	800 Hz	1 s	c. 0.5 m

RV *Belgica II* BE2022-22	GSO 360 multi-tip	SIG 24 multi channel	350-450 Hz	0.5 s	c. 0.9-1.2 m
RV *Simon Stevin* SS23-490	Centipede multi-tip	SIG dual channel (only 1 channel used)	900 Hz	0.5 s	c. 0.5 m
RV *Belgica II* BE2023-19	GSO 360 multi-tip	SIG 24 multi channel	350-450 Hz	0.5 s	c. 0.9-1.2 m
RV *Simon Stevin* SS25-430	GSO 360 multi-tip	SIG dual channel (only 1 channel used)	350-450 Hz	0.5 s	c. 0.9-1.2 m

TOPAS PS18 SBP			
Survey	**Secondary frequency**	**Ping interval**	**Vertical resolution**
RV *Belgica II* BE2022-22	4 kHz	0.2 s	c. 10 cm
RV *Belgica II* BE2023-19	2 kHz	0.2 s	c. 20 cm

INNOMAR SBP			
Survey	**Secondary frequency**	**Pulse repetition interval**	**Vertical resolution**
RV *Belgica* BE2018-09	6-8 kHz	0.075 – 0.1 s	c.5-10 cm
RV *Belgica* BE2019-13	6-8 kHz	0.075 – 0.1 s	c.5-10 cm
RV *Simon Stevin* SS23-490	6 kHz	0.075 – 0.1 s	c.10 cm
RV *Simon Stevin* SS25-430	6 kHz	0.075 – 0.1 s	c.10 cm

Numerous processing steps are required to convert the raw seismic reflection data to interpretable profiles. The specific processing workflow differs depending on the acquisition systems. All datasets were processed using the RadExPro 2022.4 software. The processing workflow for the newly acquired multi-channel sparker data comprises of twelve different steps, which is summarised in Table 2-2.

Table 2-2. Overview of processing steps for the multi-channel sparker data in the RadExPro software.

Step	**RadExPro module**
1. Navigation correction: UTM zone 31N (+ CDP binning)	Marine Geometry Input
2. Smoothen/flatten seafloor (handpicked or shot domain)	Swell Filter
3. Bandpass filtering	Butterworth filter

4.	Increase amplitudes at greater depth (= later arrivals) compared to amplitudes close to the seafloor (= earlier arrivals)	Amplitude Correction
5.	Deconvolution to surpass or remove unwanted signals originating from convolution process (e.g. reverberation, ghosting, diffractions, multiples or noise)	Nonstationary Predictive Deconvolution
6.	Deghosting (not applied when shot domain seafloor picking was performed)	SharpSeis Deghosting
7.	Velocity analysis (every 1000 CDP)	Super Gather; Interactive Velocity Analysis
8.	Normal move-out (NMO) correction	NMO/NMI
9.	Stacking of all traces from the same CDP	Ensemble Stack
10.	Migration to restore geometric relationships	Pre/Post-Stack Kirchhoff Time Migration
11.	Tide correction: achieved by the summation of the sea surface height above the geoid (SHH; European Union-Copernicus Marine Service, 2019) with the lowest astronomical tide (LAT) values (constant value for each location): NL and BE (Agentschap Maritieme Dienstverlening en Kust, 2024; Royal Netherlands Navy, Hydrographic Service, 2023) and UK Hydrographic Office (©British Crown Copyright 2024)	Tides Import*; Apply Statics; Subtract static
12.	Post-stack processing	Burst Noise Removal; Amplitude Correction; 2D Spatial Filtering; Bandpass Filtering

Processing of the single-channel sparker data was limited to the 'Swell Filter' (step 2), tidal corrections (step 11) and the processing modules described in step 12 (Table 2-2). The TOPAS SBP data require the least processing steps. Aside from tidal corrections (step 11), only the modules 'Burst Noise Removal', 'Amplitude Correction', 'Nonstationary Predictive Deconvolution' and 'Bandpass filtering' were applied. For this last module, a Butterworth filter with 10 % tapering was set. With the tidal correction step of the TOPAS data, however, an additional 'Apply Statics' module needed to be applied to account for the 4.8 m height offset of the hull-mounted transducer.

The sparker and Innomar SBP datasets acquired during the BE2018-09 and BE2019-13 surveys had already been processed by Oscar Zurita Hurtado.

2.2 Sediment cores

During the WALDO-project sediment cores were retrieved using an OSIL VC4000 vibrocorer. This system consists of a steel housing containing the core barrel, three support legs and a vibrocorer motor installed within a hexagonal top frame. The barrel is designed to hold a PVC liner with an external diameter of 100 mm and internal diameter of 96 mm. During the BE2022-22, BE2022-30 and SS23-490 surveys, 3.5 m-long liners were used. For the BE2023-19 survey, an extension was added to the housing, allowing the use of 4.5 m-long liners. A core catcher was fitted at the base of the barrel to retain the sediments during core recovery. A vibration period of 30 s to 2 min was generally sufficient to achieve full penetration. In harder substrates, however, penetration depth was usually less. All recovered cores were cut into 1 m sections (in addition to a ≤ 1 m top section). Each section was subsequently split lengthwise into two halves (archive and work half), either onboard the vessel or at the VLIZ Marine Station (MSO). Core splitting was always performed in dark conditions, to allow potential future optically stimulated luminescence analysis (OSL; see Section 2.2.2).

An overview of all sediment cores collected within the study area during the different surveys, including their location and type of performed analysis, is provided in Supplementary Table S2.

2.2.1 Sedimentological analysis

Multi-Sensor Core Logger

High-resolution true colour line-scan images were acquired of the complete core surface using the GEOTEK Multi-Sensor Core Logger (MSCL) of Ghent University or the AvaaTech core scanner ('CORA') of the Royal Netherlands Institute for Sea Research. The resulting image resolutions were 50 x 50 µm and 70 x 70 µm, respectively. Crossed polarizers were used to minimise reflections on the wet core surface. For the line scans acquired with the MSCL, an aperture of 8 and exposure time of 20 s were used. The same aperture but shorter exposure time (5 s) was applied during scanning with the AvaaTech core scanner. A histogram equalisation filter was applied to all line-scan images to enhance colour contrasts (e.g. Gonzalez and Woods, 2002).

In addition, the MSCL is equipped with a gamma-ray source and detector, a thickness sensor, a magnetic susceptibility (MS) sensor and a colour spectrophotometer (Geotek Ltd., n.d.). Measurements with these sensors were conducted but were not further used in this study.

X-Ray Computed Tomography

X-ray computed tomography (CT) is a non-destructive imaging technique used to visualize the internal structure of sediment cores based on variations in X-ray attenuation (expressed in Hounsfield Units, HU). These variations are primarily controlled by the composition and density of the sediment (Cnudde et al., 2004). Higher HU values correspond to materials or sediment with a higher radiodensity, whereas lower HU values indicate lower radiodensity. As all sediment cores had already been split prior to analysis, CT scanning was performed on the work halves using a medical CT-scanner (Siemens SOMATOM Definition Flash of Siemens AG) at Ghent University Hospital. The settings used for scanning are: 120 kV energy, 1 s rotation time, craniocaudal directionality, centre X of 1 mm and field of view of 100 mm. The resulting CT volumes have a vertical (downcore) resolution of 0.3 mm and x-y resolution of c. 0.2 mm. CT image visualisation and analysis were achieved using the VGStudio software (Volume Graphics, Hexagon).

X-Ray Fluorescence

X-ray fluorescence (XRF) core scanning is a rapid, high-resolution and non-destructive technique to analyse the elemental composition of the surface of split sediment cores. Incoming primary X-rays

iridate this surface, leading to the emission of characteristic secondary (fluorescent) X-rays. The spectral signature of this secondary radiation is element-specific and intensity of the emitted radiation is proportional to the concentration of that element (Richter et al., 2006). The acquired spectra are processed through background removal, peak identification and corrections for peak overlap to calculate element intensities, expressed in counts-per-second (cps). Element intensities are not quantitative; consequently, direct comparison between the intensities of different elements is not possible. Instead, only relative changes in elemental abundance can be estimated from downcore variations in the intensities of individual elements. These variations may be affected by downcore changes in physical properties of the sediment, absorption and/or attenuation by air or water, non-linear XRF absorption and matrix effects (Bertrand et al., 2024).

XRF measurements were conducted on the working halves of the sediment cores at a resolution of ≤ 1 cm using the Avaatech XRF Core Scanner "DEX" at the Royal Netherlands Institute for Sea Research (NIOZ). Prior to scanning, the core surface was covered with a 4 µm thick Ultralene cover foil (from Instrument Solutions) to prevent contamination. Measurements were conducted in three separate scanning runs, each using different voltage settings to optimise the detection of specific groups of elements (Table 2-3).

Table 2-3. Settings of the Avaatech XRF Core Scanner "DEX" at the Royal Netherlands Institute for Sea Research (NIOZ).

Elements	Energy (kV)	Voltage (µA)	Measuring time (s)	Filter	Slit size (mm)
Mg-Fe	10	300	5	No	1x12
Mn-Rh	30	200	5	Pd thin	1x12
Nb-Ba	50	175	10	Cu	1x12

Several strategies exist for the analysis of XRF core-scanning data. In this dissertation, centred log-ratio (clr) transformation was applied, as it enables the assessment of downcore variations in individual elements. The clr values were calculated by dividing the intensity of each element by the geometric mean of the intensities of all selected elements within a single measurement, followed by logarithmic transformation. An automated script was written in R (RStudio software) to calculate these clr values. During core scanning, replicate measurements were acquired to assess the robustness and reproducibility of the XRF dataset. This reproducibility was evaluated by calculating the Pearson correlation coefficient (r) between replicate measurements. Only the elements with a coefficient of ≥ 0.75 were included for further analysis (e.g. Verweirder et al., 2026). For the dataset used in this study, the elements include Mg, Al, Si, S, K, Ca, Ti, Mn, Fe, Zn, Rb, Sr, Zr and Ba.

Hierarchical cluster analysis was subsequently applied to identify groups of samples with similar geochemical compositions. The clr-values of the previously listed elements were used as input for Ward's hierarchical clustering analysis, following the methodology after Martin-Puertas et al. (2017). Clustering was performed in R using the hclust() function from the stats package with the ward.D2 option, which implements Ward's minimum variance method. This method aims to find compact, spherical clusters by minimising the increase within cluster variance at each clustering step. As the hclust() function requires a dissimilarity matrix as input argument, Euclidian distances were first calculated using the dist() function from the stats package. The Euclidian methodology is used to determine the appropriate number of clusters that best explain the geochemical variability within the dataset, while maintaining a meaningful sedimentological interpretation (e.g. Martin-Puertas et al.,

2017; McGuire, 2020; Waajen-Labee et al., 2025). Cluster results, including hierarchical dendrograms, were visualised in R using functions from the factoextra package.

Grain-Size Analysis

Grain-size analysis was performed using the Malvern Mastersizer 3000 (Malvern Panalytical) at Ghent University (RCMG). This instrument determines particle-size distributions based on the principle of laser diffraction. It measures the angular variation of scattered light when the laser passes through a dispersed particulate sample: large particulates scatter light at smaller angles, whereas smaller particulates scatter light at larger angles. Using the Mie theory of light scattering, the angular scattering pattern is converted into a particle-size distribution, with particle sizes reported as volume-equivalent sphere diameters. An important measurement parameter is the obscuration, defined as the percentage of laser light blocked by the sample. When the laser light is diffracted by multiple grains, it will result in increased scattering angles which will be interpreted as an apparent higher number of finer grains. To minimise this effect, the obscuration should generally be maintained below 20%. For finer grained sediment samples even lower obscuration values are required. Measurements on a single sample are achieved three consecutive times to assess analytical reproducibility. Stable results between successive measurements are considered as reliable measurements.

The sampling interval ranged from 2 to 3 mm. The required sediment mass for a single sample was determined by a few test samples checking the required obscuration levels, and ultimately ranged between 50 and 80 mg. Prior to grain-size measurements, samples were chemically pretreated following the procedure described by Van Daele et al. (2016). The pretreatment consists of three steps and includes the removal of the organic matter, carbonate and biogenic silica content. In the first step, sediment samples were placed in 100 ml glass beakers filled with 10 ml of distilled water. By adding 2 ml of 30% H2O2 and heating the samples on a hotplate until the reaction stopped, the fine-grained organic matter content was removed. After setting the samples aside to cool down, 1 ml of 10 % HCl was added to dissolve calcium carbonate (if present). The samples were reheated for 1 minute, diluted to 100 ml and left untouched for at least 8 hours allowing the fine particles to settle before decanting. This dilution and decantation procedure was repeated twice to ensure complete pH neutralisation of the samples. In the second step, 1 ml of 2N NaOH was added to remove biogenic silica (if present). The mixture was heated for 10 minutes, after which the dilution and decantation procedure was repeated twice to ensure and restore a neutral pH. For the last step, 1 ml of 2% sodium hexametaphosphate (Calgon) was added, and the mixture was briefly heated, to achieve complete disintegration of the sample. The resulting grain-size data were processed and statistics were calculated using GRADISTAT version 8.0 (Blott and Pye, 2001). These statistical results were plotted in Grapher (Golden software, version 23.1) and sediment samples were classified based on the Udden-Wentworth scale (Udden, 1914; Wentworth, 1922).

2.2.2 Optically stimulated luminescence (OSL)

Optically stimulated luminescence (OSL) dating is an absolute geochronological technique that uses quartz or feldspar minerals to calculate the last exposure time to light. These minerals accumulate and store energy achieved from natural occurring radioactivity in their crystal structure. Once the grains are exposed to daylight, the stored energy is released, therefore resetting the luminescence signal through optical bleaching. In other words, this method can measure the last time that mineral grains in sediment were exposed to daylight and thus the time of deposition and burial. The release of the last-stored energy is the luminescence signal measured (Grant and Marshall, 2025; Mahan et al., 2022). Using conventional techniques, luminescence dating is generally applicable to sediments deposited within the last 250 ka, although specialised protocols can extend this age-range (Mahan et al., 2022). Both quartz OSL and polymineral fine-fraction OSL were applied in this dissertation.

Prior to sampling, OSL profiling measurements were performed at VLIZ under safe-light conditions using a SUERC portable OSL reader. This portable reader is programmed with an interleaved measurement sequence comprising system dark count, infrared stimulated luminescence (IRSL) and OSL measurements. Untreated bulk sediment samples (c. 10-15 g per sample) taken at irregular intervals throughout each core were analysed. The resulting proxy data included net IRSL and OSL signal intensities, IRSL and OSL depletion indices and the IRSL:OSL ratio. Based on the profiling results, the actual sample locations for luminescence dating were selected. Samples were analysed by Tim Kinnaird at the School of Earth and Environmental Sciences (SEES), University of St Andrews.

The luminescence age is the quotient of the burial dose (in Gy) over the effective environmental dose rate (in mGy/a). However, a specific set of measurements are needed to calculate the burial or equivalent dose, i.e. total dose received by the sample during burial, and determine the environmental dose, i.e. the amount of energy delivered to the sample per year. The equivalent dose determinations were made on sets of 24 aliquots using the single aliquot regenerative dose (SAR) OSL protocol. For polymineral fine fraction OSL, the quartz-enriched polymineral 4-11µm SAR OSL protocol was followed (Murray and Wintle, 2000). The SAR technique involves making a series of paired OSL intensity measurements: i.e. the natural signal intensity (Ln) and the luminescence from a series of regenerative doses (Lx), and the response to a fixed test dose (Tn and Tx). To compensate for observed changes in sensitivity during the laboratory measurement sequence, each measurement is standardised to the test dose response determined immediately after its readout. The values are subsequently estimated using the corrected OSL intensities Ln/Tn and Lx/Tx and the interpolated dose-response curve (Murray and Wintle, 2000). The central dose estimate model of Galbraith et al. (1999) was used to calculate the equivalent doses and obtain the palaeodose. Environmental dose rates were determined from ^{232}Th, ^{238}U and ^{40}K radionuclide concentrations, achieved by inductively coupled plasma mass spectrometry (ICP-MS) for thorium and uranium and inductively coupled plasma optical emission spectrometry (ICP-OES) for potassium. Water contents were measured for all received samples and the dry infinite-matrix dose rates were calculated using the conversion factors of Cresswell et al. (2018) and corrected for grain-size attenuation and chemical etching using the datasets of Mejdahl (1979) and Bell and Zimmerman (1978), respectively. These dry infinite-matrix dose rate measurements were used in combination with the assumed burial water contents to acquire the total effective dose rates for age estimation.

2.2.3 Environmental analysis

Palynology

The pollen assessment for this dissertation had three main aims: (1) to ascertain whether pollen grains were preserved within the samples; (2) to reconstruct the local environment based upon the pollen assemblages and (3) to provide an indication of the age of these deposits. The assessment was conducted by Micheal Grant at Coastal and Offshore Archaeological Research Services (COARS), University of Southampton and by Tonny Bakker and Irene Waajen-Labee at the Faculty of Geosciences, Utrecht University.

At COARS, samples containing 2-4 cm^3 of sediment were processed following the standard preparation procedure after Moore et al., (1991). One tablet of *Lycopodium* spores (batch 3862) was added to each sample to enable the calculation of pollen concentrations (Stockmar, 1971). All samples received the following chemical pretreatment: 20 ml of 10% KOH (80°C for 30 minutes), 20 ml of 60% HF (80°C for 120 minutes), 15 ml of acetolysis mix (80°C for 3 minutes), stained in 0.2% aqueous solution of safranin and mounted in silicone oil following dehydration with tert-butyl alcohol. Owing to the minerogenic nature of some samples, additional sieving and decanting was undertaken between the KOH and HF treatment stages. Pollen counting was performed using a Nikon Eclipse Ci-L transmitted light microscope at x400 a magnification, with x1000 oil immersion magnification used

for critical identifications. Determinable pollen and spore types were identified to the lowest possible taxonomic level using the COARS reference collection. Taxonomic identifications afollow Bennett (1994) and Bennett et al. (1994) with the exception of *Poaceae* (Küster, 1988), *Cupressaceae* (Moore et al., 1991), and *Betulaceae* (Blackmore et al., 2003). Plant nomenclature follows Stace (2010). A total land pollen (TLP) sum of 100 grains was sought for all samples. In the samples that failed to reach the 100 TLP sum, a minimum of two complete mounted slides were examined, and all identifiable pollen grains were recorded. Pollen diagrams were plotted using Tilia v 3.0.3 (Grimm, 1991). Aside from pollen, also microscopic charcoal was quantified on the pollen slides using a modified method adapted from Clark (1982) whereby a minimum of 200 randomly selected fields of view were examined per slide and all charcoal particles were recorded. *Lycopodium* spores were counted simultaneously, with a minimum of 50 spores counted from each level to permit calculation of microcharcoal concentration.

At the Faculty of Geosciences, Utrecht University, samples (1 cm^3 of sediment) were processed following the procedure described by Waajen et al. (2024). Chemical pretreatment includes removal of carbonates using 5% HCl and removal of organic compounds using 5% KOH (70°C, 60 minutes). The residues were subsequently sieved and dissolved in acetolysis (100°C for 5 minutes), and the remaining organic matter was separated by heavy liquid flotation (sodium polytungstate of 2.0 g/cm^3). Pollen and spore types were identified to the lowest possible taxonomic level using a reference sheet from the Faculty of Geosciences, as well as a reference book (Beug, 1961) and the online reference collection of Martin and Harvey (2017). A sum of 200 pollen grains was sought for each sample. Pollen percentages were calculated relative to the terrestrial pollen sum, and taxa with < 2% occurrences in two or three of the samples were excluded from the diagram to improve readability.

Malacological analysis

Malacological analysis (i.e. analysis of mollusc shells) was undertaken to gain insight into the palaeoenvironment, including water depth (within a marine setting), energy and climate. This is based on the principle that different assemblages are present in different climatic zones (such as boreal or arctic) and/or different depositional settings (fluvial, estuarine, marine). For analysis, samples were taken from different identified lithological units. Either half of a work half section per unit, or the entire unit was sampled. Afterwards, the samples were soaked in warm water for 4 to 8 hours and subsequently wet sieved at multiple grain sizes (1 mm, 500 µm and 250 µm). Following sieving, the residues were dried at 40 °C. The > 500 µm-fraction was analysed by Frank Wesselingh at Naturalis Biodiversity Center (Leiden, the Netherlands).

The samples were examined qualitatively for shell abundance, fragmentation preservation state, dominant taxa and taphonomic characteristics. Based on the ecological preferences of the identified taxa, the depositional environment, salinity, water depth, hydrodynamic energy, and general sea-temperature regime were inferred. Species ecological information was obtained primarily from the Ocean Biodiversity Information System (OBIS, 2026). Within Quaternary units in the southern North Sea Basin reworking by currents and waves, fluvial transport or through bioturbation are common phenomena. Close attention was therefore given to distinguish autochthonous (*in situ*) from allochthonous (reworked) fauna. *In-situ* specimens were identified based on the preservation of delicate shell ornamentation, the absence of abrasion features, the occurrence of articulated bivalves and the ecological consistency of the assemblage. Determination of the potential *in-situ* faunal components was subsequently used to establish palaeoenvironmental reconstructions.

CHAPTER 3. GEOMORPOLOGY OF THE AXIAL CHANNEL (SOUTHERN BIGHT, NORTH SEA)

ABSTRACT

This study presents a transnational geomorphological map of the Southern Bight, North Sea, using bathymetric data (EMODnet – c. 115 m horizontal resolution; UKHO – 4 m horizontal resolution). Based on the erosional and/or depositional relationship of the mapped features, a first step is established towards the reconstruction of the evolution of the Axial Channel, i.e. a major geomorphological feature on the southern North Sea seafloor. It reveals that the present-day Axial Channel reflects four distinct phases that occurred throughout the Pleistocene: a glacial phase, a major, regional scale fluvial dominated phase – that evolved after the glacial phase; a short-lived, high-energy drainage event; and a last, tidal dominated marine phase. These findings contribute to a refined understanding of the Southern Bight's geomorphological evolution and offer a framework for future palaeo-environmental and stratigraphic studies in the region.

This chapter has been published as: Vervoort, M., Plets, R., Kyriakoudi, D., Missiaen, T., & De Batist, M. (2026). Geomorphology of the Axial Channel (Southern Bight, North Sea). JOURNAL OF MAPS, 22(1). https://doi.org/10.1080/17445647.2026.2620910

Author contribution (CRediT): **Morgan Vervoort:** Conceptualisation, methodology, formal analysis, investigation, writing – original draft, writing – review & editing, visualisation. **Ruth Plets:** Conceptualisation, investigation, project administration, writing – review & editing, supervision. **Despina Kyriakoudi:** writing – review & editing. **Tine Missiaen:** project administration, writing – review & editing. **Marc De Batist:** project administration, writing – review & editing, supervision.

3.1 Introduction

The Axial Channel is a prominent geomorphological feature on the present-day southern North Sea seafloor (Main Map; Supplementary Dataset S3), believed to be a remnant of a long-lived, intermittently active, large drainage system. However, its origin and evolution remain unclear. Some studies suggest it formed during the Miocene, as a northern extension of the Lobourg Channel in the Dover Strait (Dingwall, 1975; Liu et al., 1992). Others propose it originated as an eastward branch of the Thames-Medway system during the Early to Middle Pleistocene, draining the uplifted Weald area in the south towards the at that time more northernly positioned North Sea (Balson and D'Olier, 1990; Gibbard and Lewin, 2016). During the Middle to Late Pleistocene, repeated glaciations caused a fall in global sea level, isolating the southern North Sea and leading to the formation of large proglacial lakes in front of the merged British and Fennoscandian ice sheets (e.g. Böse et al., 2012; Graham et al., 2011; Roberts et al., 2018). The West European rivers and glacial meltwater drained into these lakes (e.g. Busschers et al., 2008; Gibbard et al., 1988; Hijma et al., 2012). Indirect evidence for the existence of these lakes are the erosional features still preserved in the Dover Strait, which were created by catastrophic outburst floods at the end of the Elsterian/Anglian and Saalian/Wolstonian, recording the breaching of the land bridge connecting UK to mainland Europe (Collier et al., 2015; Gibbard and Cohen, 2015; Gupta et al., 2007). West European rivers subsequently flowed towards this southern outlet, turning the Axial Channel into a complex, southward running drainage system (Gibbard, 1995; Hijma et al., 2012). Its present-day seabed expression reflects multiple phases of drainage related to glacial and fluvial processes, and tidal erosion and reworking during interglacial periods (Cohen et al., 2017)

Previous studies of the geomorphology of the southern North Sea concentrated on local or national scales (Cohen et al., 2017; De Clercq et al., 2016; Dix and Sturt, 2011; Hijma et al., 2012; Limpenny et al., 2011). Here, we create a transnational geomorphological map of the southern North Sea (the Southern Bight; located roughly between 53° and 51° N, 5° and 1° E; Figure 3-1a). By mapping the bathymetry, we take a first step in re-evaluating the formation and evolution of the Axial Channel and associated geomorphological features, which will form the basis for future investigations into the sub-surface. The overall aim is to: (1) identify major geomorphological features; (2) make a first interpretation of their formation and evolution; (3) create a relative chronology of events that shaped the region of the Axial Channel.

3.2 Study area

The ~200 km long Axial Channel extends from the Norfolk Banks in the north towards the Lobourg Channel in the south. The – 40 m contour line delineates a crescent-shaped deep, curving southwestward towards the Dover Strait (Figure 3-1a). The Southern Bight area is covered by marine sands and gravel up to 5 m thick on the UK Continental Shelf and reaching up to 20 m on the Dutch Continental Shelf (Balson et al., 1991; Cameron et al., 1984b). Locally, these sediments are organised into extensive Holocene tidal sandbanks: the Dutch Banks, Zeeland Banks, Flemish Banks, Hinder Banks, Thames Banks and the Norfolk Banks (Balson et al., 1991; Balson and D'Olier, 1990; Johnson et al., 1982) (Figure 3-1a). The Axial Channel axis is located in between these sand ridge fields. It has an average depth of 50 m below lowest astronomical tide (LAT), locally down to 65 m, and is widest in the centre (around 55 km), between 52° N and 52°30' N, narrowing to ~10 km in the north and south (Figure 3-1a). The western margin of the Axial Channel consists of a plateau, here referred to as the UK Plateau. The (pre-) Quaternary geology of the southern North Sea has been compiled and published by the British Geological Survey (BGS, 2000) (Figure 3-1b). Across the Southern Bight, between East Anglia (UK) and Zeeland (the Netherlands), a clear geological change is observed (Figure 3-1b). In the north, thick packages of Quaternary sediments ranging from the Early to Late Pleistocene dominate (for individual formations see Figure 3-1b). In contrast, pre-Quaternary formations (Eocene-

Paleocene and Cretaceous) are found close to the seabed in the south. Here, Quaternary sediments are discontinuous, concentrated in banks or depressions and valley incisions cut into the Paleogene (Balson and D'Olier, 1990; Cameron et al., 1984a; Harrison and Hopson, 1991; Laban et al., 1992) (Figure 3-1b).

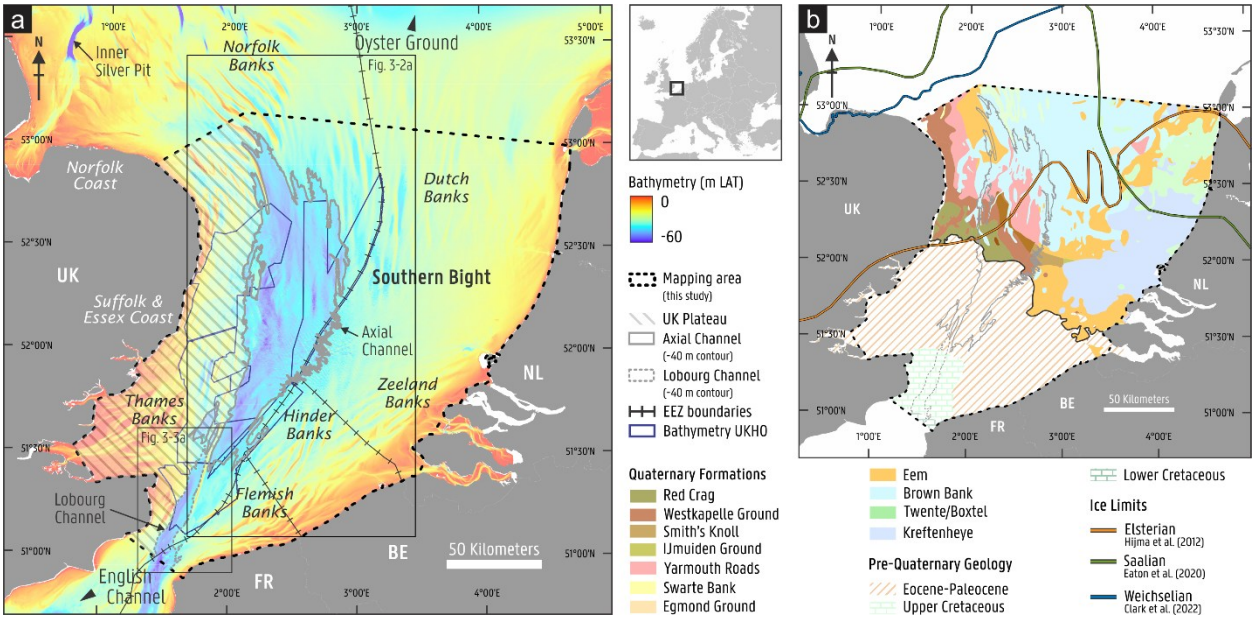


Figure 3-1. (a) Bathymetric map of the Southern Bight, southern North Sea. The mapped area is indicated, as well as the bathymetry blocks obtained from the UK Hydrographic Office (UKHO; ©The Crown). Geomorphological features (the Axial Channel and Lobourg Channel), geographic features (boundaries of the Exclusive Economic Zone (EEZ), Inner Silver Pit, English Channel, Oyster Ground) and tidal sandbanks (Dutch Banks, Zeeland Banks, Flemish Banks, Hinder Banks, Thames Banks and Norfolk Banks) are also indicated; (b) Pre-Holocene Geological map of the Southern Bight, compiled by the BGS (2000). The Pleistocene ice extents by Clark et al. (2022), Eaton et al. (2020) and Hijma et al. (2012) are also shown.

3.3 Methodology

To map the present-day geomorphology of the Axial Channel, the EMODnet Digital Bathymetry data (EMODnet Bathymetry Consortium, 2022) were used. The current digital terrain model (DTM) is available as a gridded raster of c. 115 m with water depths in m below LAT. Additionally, bathymetry blocks from the UK Admiralty Seabed Mapping Service (United Kingdom Hydrographic Office (UKHO) data) were compiled for most of the (south-)western part of the study area. Each block has a different horizontal resolution, ranging from 1 up to 4 m. The blocks were merged, applying the same parameters as the original raster blocks, but reducing the horizontal resolution to a common cell size of 4 m. Subsequently, the EMODnet DTM and UKHO bathymetry blocks were incorporated into ArcGIS Pro and transformed to reference system UTM Zone 31N (WGS84). The mapping was performed on the lower resolution DTM and on the higher resolution UKHO data where available and all depths are expressed in m below sea level. Traditional hillshades (including at 0°, 90°, 180°, 270° azimuth and 20° altitude, no vertical exaggeration) and multidirectional hillshades (no scaling) were created. Slope angles were measured based on a slope map created from the EMODnet DTM. The term 'escarpment' is used to describe features with a slope drop of ≥ 10 m. For drops < 10 m, the term 'slope break' is used. Geomorphological features were subsequently delineated as polyline features and polygons, and their statistics (i.e. mean length, orientation) calculated in the ArcGIS Pro software. In places where too many features were present, the area was delineated and a subsection of features was selected to calculate their statistics. The result of the delineated features (and feature areas) is shown on the Main Map (Supplementary Dataset S3). Topographic profiles were created by adding the EMODnet DTM and merged UKHO blocks as elevation source layers.

3.4 Geomorphological features

3.4.1 The Axial Channel

The full Axial Channel's extent is only partly expressed in the bathymetry, with its northern and southern limits masked by extensive tidal sand banks and wave fields (Figure 3-2a). In the north, the Axial Channel is discernible only to ~53° N, beyond which it becomes buried beneath the Norfolk and Dutch tidal sand banks (Figure 3-2a). There is no bathymetric evidence of a northward connection to the Oyster Ground or Inner Silver Pit (Figure 3-1a; Figure 3-2a). Along the northwestern margin of the Axial Channel, two gentle slopes (< 1°) occur just west of the Dutch sandbanks (ns; Figure 3-2a). In its central and southern sector, the Axial Channel comprises a main branch (MB1) and multiple side branches (Figure 3-2a). The main branch reaches depths of up to 65 m and follows an s-shaped, meandering course (Figure 3-2b, d). Its western margin is defined by an escarpment (W1) that extends intermittently over ~150 km, from the central sector to the southern end of the channel (Figure 3-2a). This escarpment, with an average slope of ~4°, marks the eastern boundary of the UK Plateau, which itself dips gradually northeastward. The plateau sits at 10-15 m in the offshore Thames Estuary, 25-30 m near the Suffolk and Essex Coast, and ~35 m along its eastern margin (Figure 3-1a). Given that the main branch reaches 65 m depth, the height difference between the Axial Channel and the UK Platform is up to 30 m.

In the central sector of the main branch, a teardrop-shaped streamlined island (SI) crops out, with its apex oriented southwestward (Figure 3-2b). The feature is 10 km long and 2.5 km wide, with an average surface depth of 45.5 m, which is ~15 m above the base of the main branch on its western side and ~10 m on its eastern side (Figure 3-2d). At least six terraces are preserved along the western slope of the streamlined island (Figure 3-2b inset). The height difference between the second (T2) and third (T3) terrace is 7 m, while that between T3 and T4 is 5.5 m; the remaining terraces show a relief of 1-3 m. The eastern flank of the streamlined island forms a gradual slope of ~2° (Figure 3-2b inset).

Side branch B1 is separated from the main branch MB1 by a shallow plateau (P; Figure 3-2b, d). This side branch extends for ~70 km and curves broadly parallel to the main branch. Connection to the main branch occurs south of plateau P via three branches (white arrows in Figure 3-2b, c), creating interruptions in the otherwise continuous western escarpment W1. With depths reaching to 50 m, side branch B1 is shallower than the main branch of the Axial Channel.

East of the main branch, a streamlined plateau (SP) is present, preserving evidence of multiple – though less clearly defined – incisional stages resembling an anastomosing fluvial braid plain (Figure 3-2b, d). The plateau measures ~25 km in width and up to 20 km in length, with an average surface depth of 42 m. Its eastern and western flanks are well defined, reaching slopes of up to 3° (Figure 3-2b, d). The plateau is bounded on the east by side branch B2, which attains depths of 62 m. Northeast of B2, two additional, but shallower side branches, B3 and B4, occur at depths of 57 and 52 m, respectively. The eastern slope of B4 defines the easternmost margin of the Axial Channel, beyond which the morphology is obscured by the Dutch Sand banks (Figure 3-2b).

In the southern sector of the Axial Channel, the main branch MB1 is accompanied by three side branches (B5, B6, B7; Figure 3-2c). Two of these (B5, B7) are relatively shallow, reaching a depth of 46 m, whereas B6 is deeper at 54 m. Only B5 connects to the main branch. The western escarpment (W1) remains a prominent morphological feature; however, the Hinder and Flemish Banks prevent identification of a distinct eastern channel margin. A slope break of up to 2° occurs at the eastern edge of the main branch at 44 m (s1; Figure 3-2c). Further southeast, two additional slope breaks occur: one with a gradient of < 1° at a water depth of 35 m (s2; Figure 3-2c), and another with an E-W

orientation and slope of < 1.5° at a depth of 30 m (s3; Figure 3-2c). The latter has previously been mapped by De Clercq et al. (2016).

At the southern end of the Axial Channel, the western escarpment is displaced ~8 km at the location of a depression, here termed Falls Deep (FD; Figure 3-2c). This feature reaches a depth of 49 m, extends ~20 km in length and is less than 5 km wide. South of Falls Deep, the escarpment is again

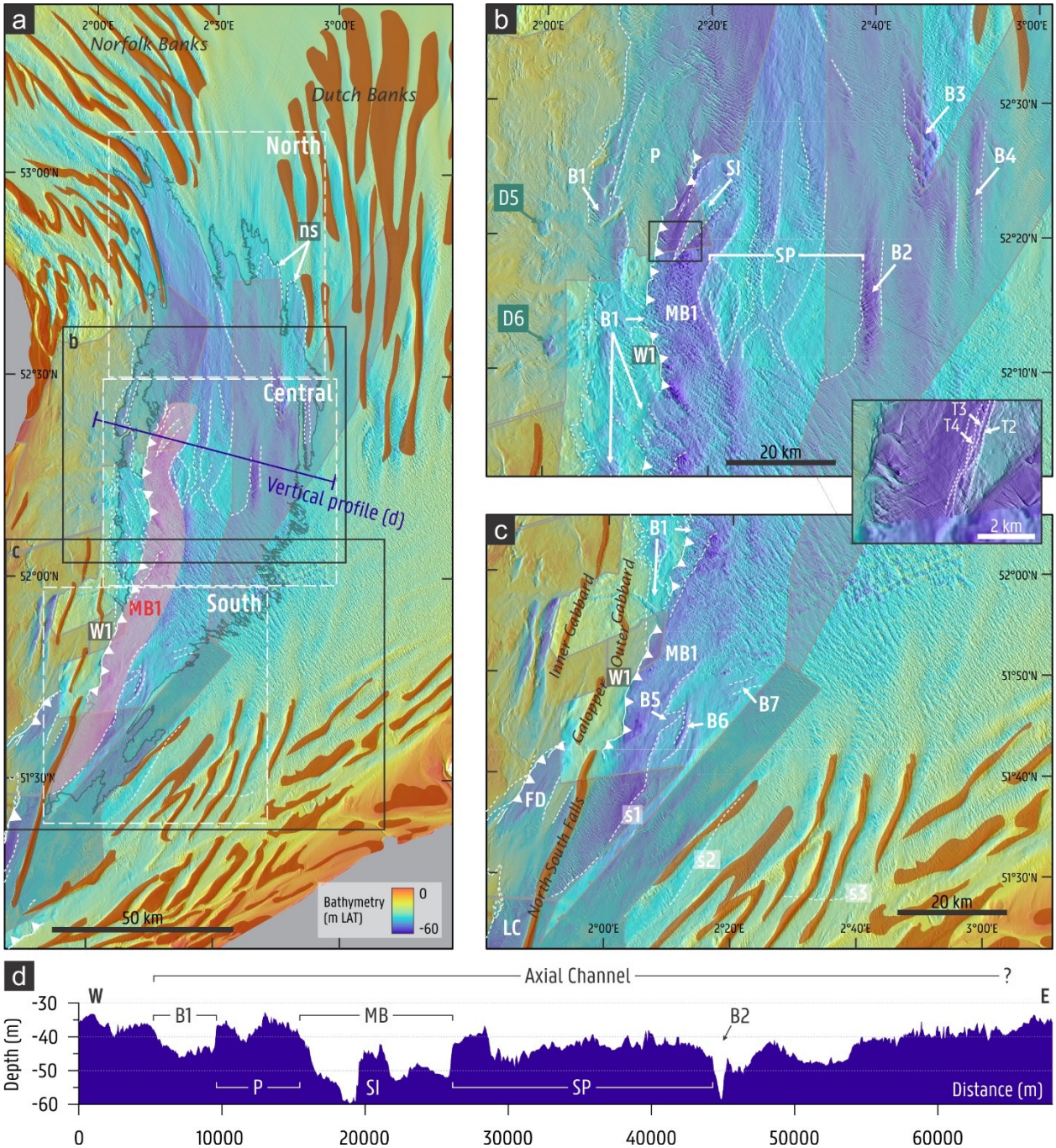


*Figure 3-2. (a) Bathymetric map of the Axial Channel (map location indicated on Figure 3-1a) indicating the northern, central and southern sectors of the Axial Channel (white boxes). UKHO bathymetry data are indicated by the more shaded blocks. Breaks in slope are indicated by white dotted lines, escarpments by a white line with triangles. Tidal sand*banks *are shown in brown and the main branch of the Axial Channel is overlain by red shading; (b) Zoom of the central Axial Channel* sector*; (c) Zoom of the southern Axial Channel* sector*. (d) Vertical profile over the central Axial Channel, location of the profile is shown by a dark blue line in (a). B1-7: side branches, D5-6: depressions, FD: Falls Deep, LC: Lobourg Channel, MB1: main branch, P:* plateau*, s1-3: slope-breaks, SI: streamlined island, SP: streamlined plateau, W1: western escarpment.*

displaced (~18 km southeastwards), marking the northern limit of the Lobourg Channel (Figure 3-2a; Figure 3-3a).

3.4.2 Lobourg Channel

In the south, the Axial Channel is separated from the Lobourg Channel by the North-South Falls tidal sand bank (Figure 3-2c; Figure 3-3a). The southern Axial Channel is < 60 m deep, whereas the Lobourg Channel reaches depths to 65 m (Figure 3-3a).

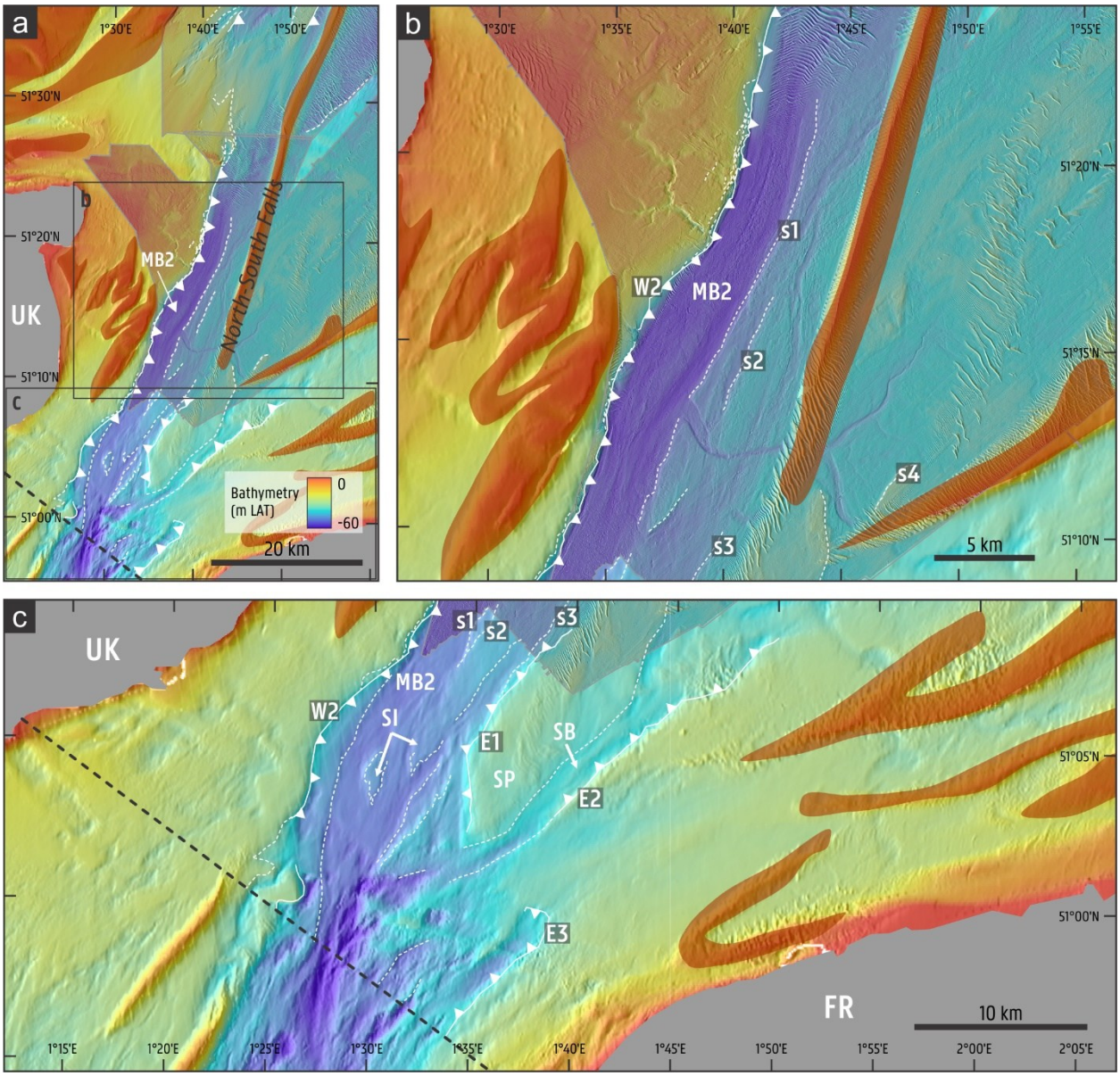


*Figure 3-3. (a) Bathymetric map of the Lobourg Channel, map location indicated on Figure 3-1a. UKHO bathymetry data are indicated by the more shaded blocks. Breaks in slope are indicated by white dotted lines, escarpment by a white line with triangles. Tidal sand*banks *are shown in brown; (b) Zoom of the northern Lobourg Channel valley; (c) Zoom of the southern Lobourg Channel valley. MB2: main branch, SB: side branch, W2: western escarpment, E1-3: eastern escarpments, SP: streamlined plateau, SI: streamlined island, s1-4: slope-breaks.*

The main branch (MB2) of the Lobourg Channel (Figure 3-3a, b) is bounded to the west by a continuous, 50 km-long escarpment (W2) with slopes up to 5°. Within this branch, two teardrop-shaped, streamlined islands (~1 km wide, ~3 km long) occur, with their apex pointing southwestward (SI; Figure 3-3c).

On the eastern margin, four slope breaks and three prominent escarpments are present (s1-4, E1-3; Figure 3-3b, c). The first escarpment (E1), with a slope of 1.5-2°, forms the western boundary of a streamlined plateau (SP: Figure 3-3c). This plateau is ~5 km wide, ~20 km long and separates the side branch (SB) from the main branch. The second escarpment, with a slope of 2.5-3°, defines the eastern slope of the side branch. The third escarpment, farther south in the Dover Strait, also has a slope of 2.5-3°.

3.4.3 Smaller channels connected to the Axial and Lobourg Channel

Several smaller channels connect to the Axial and Lobourg Channels and related geomorphological features (e.g. elongated deeps, see Section 3.4.4). Most occur along the western margin, except for two systems on the eastern margin (Figure 3-4a). Channel depths are reported relative to the surrounding bathymetry.

In the north of the study area, just off the Norfolk coast (UK), a > 30 km-long (palaeo-)channel is preserved on the UK Plateau (p1; Figure 3-4b). Previously described by Limpenny et al. (2011) and Tizzard et al. (2014), this meandering channel is up to 2 km wide and 8 m deep. Small-scale linear bedforms are abundant and point bars occur in the two widest meander bends (PB; Figure 3-4b). At its east-west bend, a streamlined island is present with its apex pointing southeastward (SI; Figure 3-4b). Channel remnants extend eastward towards the western side branch of the Axial Channel (B1; Figure 3-4b). Northeast of the bend, linear bedforms suggest the presence of a tributary channel system (Figure 3-4b, encircled area), while farther northeast, a second channel system is preserved. This latter channel is ~7 km long, ~1.5 km wide, and incised 2 m into the UK Plateau (Figure 3-4b).

Further south on the UK Plateau, two channel systems are present (p3-4; Figure 3-4c), which were previously described by Dix & Sturt (2011), Henriet et al. (1984) and Sturt et al. (2009). P3 is a narrow, east-west-oriented channel, ~20 km long, ~400 m wide and only a few meters deep (Figure 3-4c). Two north-south tributaries join its northern flank: a ~5 km-long tributary at its eastern end and a shorter, ~1 km-long tributary at the west. The channel shows no connection to the western side branch (B1; Figure 3-4c), the Axial Channel to the east or the elongated deeps to the west (see Section 3.4.4). Instead, it is truncated by a north-south oriented elongated deep (see Section 3.4.4; Figure 3-4c). Approximately 10 km to the south, channel p4 extends from the mainland towards the western escarpment of the Axial Channel (Figure 3-4c). Although partly obscured by the Inner and Outer Gabbard sandbanks, the system displays a clear, low-sinuous main channel with multiple tributaries on its southern bank. The main channel is ~50 km long, ~500 m wide, with banks up to 10 m above the channel floor and slopes of ~3°. It widens towards the eastern margin of the UK Plateau, reaching a width of ~2 km at its mouth, where it joins the main branch of the Axial Channel (Figure 3-4c).

Three smaller channels are present further south on the UK Plateau (p5-7; Figure 3-4c). p5 is a north-south-oriented, low-sinuous channel, ~8 km long, that has been previously described by Sturt et al. (2009) and Dix & Sturt (2011). It connects at its southern end to the elongated deep west of the Galloper sandbank (see Section 3.4.4; Figure 3-4c) but shows no connection to the tributaries of p4 to the north (Figure 3-4c). South of the western Inner Gabbard Deep (see Section 3.4.4), channel p7 extends ~15 km southeastward. This complex system displays braided channels and overdeepend sections, reaching depths of up to 12 m, and widths of up to 1 km (Figure 3-4c inset). While connected to the western Inner Gabbard Deep, no clear connection to the Falls Deep (FD; Figure 3-4c) is observed. Approximately 2.5 km to the northeast, on the UK Plateau, a meandering channel (p6)

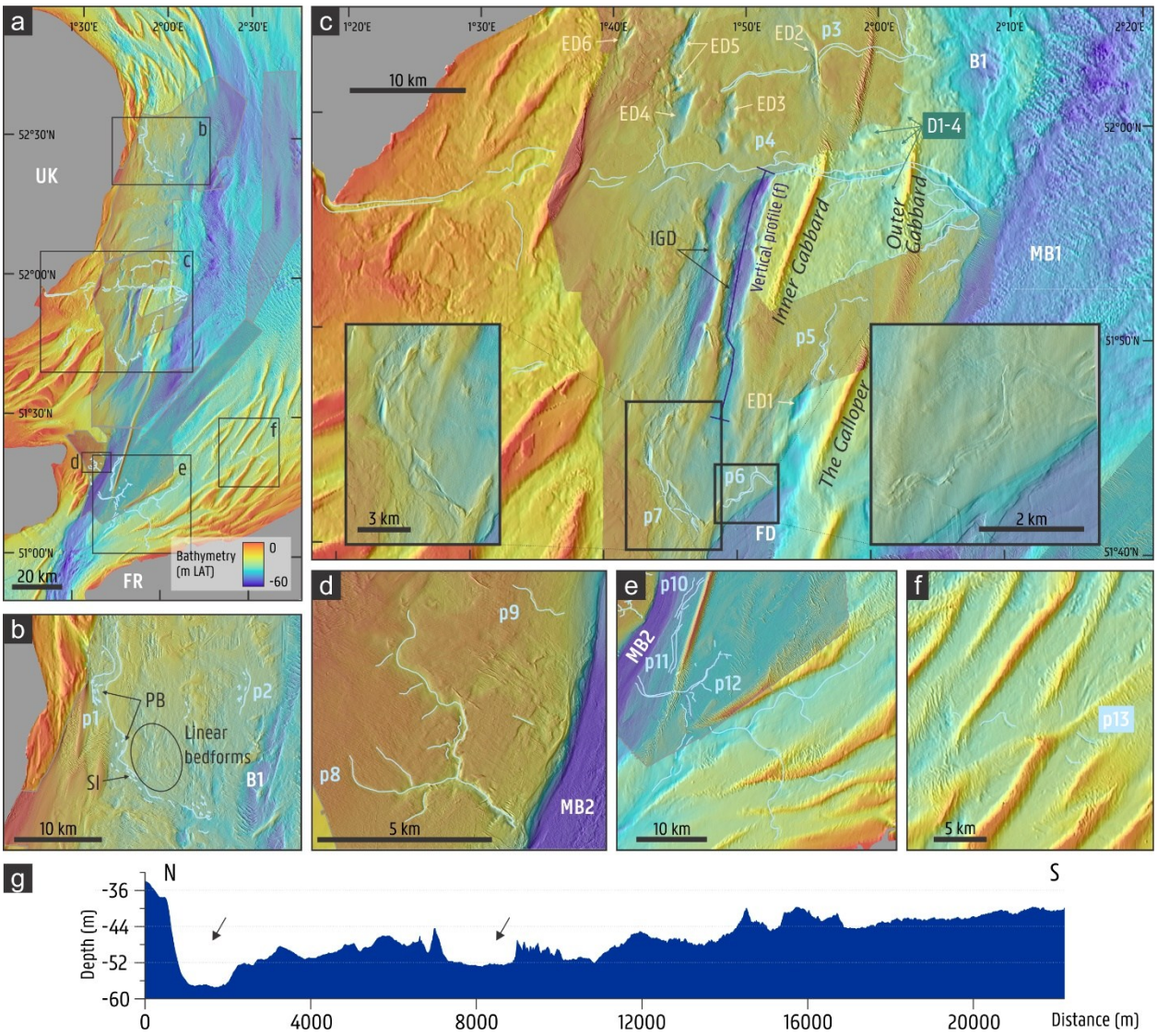


Figure 3-4. (a) Palaeochannels connected to the Axial Channel and Lobourg Channel (indicated in light blue lines). (b) Zoom of palaeochannels p1 and p2; (c) Zoom of palaeochannels p4-7, as well as Inner Gabbard Deeps, elongated deeps and depressions on the UK Plateau; (d) Zoom of palaeochannels p8 and p9; (e) Zoom of palaeochannels p10-12; (f) Zoom of palaeochannel p13; (g) Vertical profile over the eastern Inner Gabbard Deep, location of the profile is shown by a dark blue line in (c), arrows indicate overdeepend areas. UKHO bathymetry data are indicated by the more shaded blocks. B1: western side branch of Axial Channel, D1-4: depressions, ED1-6: Elongated deeps, IGD: Inner Gabbard Deeps, MB1: main branch of Axial Channel, MB2: main branch of Lobourg Channel, PB: point bar, SI: streamlined island.

extends for ~5 km with widths between 80 and 320 m (Figure 3-4c inset). It appears isolated from p7, and any connection to FD remains uncertain due to a lack of high-resolution bathymetry (Figure 3-4c).

On the western margin of the Lobourg Channel, a small dendritic channel system is present (p8; Figure 3-4d). Its sinuous main branch runs NW-SE for 8.8 km and is joined by multiple tributaries. The channel base lies ~6 m below the surrounding plateau. There is no distinct mouth or connection to the Lobourg Channel; instead, the system terminates just before a > 20 m drop into the Lobourg Channel floor. North of this system, a single sinuous channel (p9) extends for ~2 km with a depth of ~2 m. It also lacks any visible connection to the Lobourg Channel (Figure 3-4d).

Parallel to the main branch of the Lobourg Channel, east of slopes s1 and s2 (Figure 3-3b), two additional channel systems are present (p10-11; Figure 3-3b; Figure 3-4e). The northernmost channel (p10) is ~6 km long and up to 700 m wide. It incises and overprints channel p11, which is ~9 km long

and up to 600 m wide. Depths reach ~3 m in p10 and ~4 m in p11. Channel p10 can be traced southwards into the Lobourg Channel, while to the north it disappears beneath the North-South Falls sandbank. Channel p11 displays a braid plain to the north, also partly buried beneath the sandbank, but shows no connection southwards to either the Lobourg Channel or channel system p12.

Approximately 3 km further south, an extensive, intricate channel system (p12) is present, partly buried beneath the Flemish Banks (Figure 3-4a, e), previously described by García-Moreno et al. (2019). Two branches can be discerned – one originating at the French coast and another draining NE-SW from the Belgian Continental Shelf – converge into an E-W channel, ultimately connecting to the Lobourg Channel. A southern tributary extends southwestward towards the English Channel. In total, the system comprises > 60 km of channels, with depths reaching up to 10 m.

Additional remnants are exposed or partly buried beneath the Flemish Banks, representing a larger, now fragmented system (p13; Figure 3-4f).

3.4.4 Deeps and depressions on the UK Plateau

Two parallel, elongated deeps occur on the UK Plateau, west of the Inner Gabbard sandbank (Inner Gabbard Deeps, IGD; Figure 3-4c). Previously described by Sturt et al. (2009) and Dix & Sturt (2011), these NNE-SSW trending features are 21.6 km (eastern IGD) and 16.8 km (western IGD) long, with widths up to 2.2 km. Maximum depths are located at their northern margins, reaching 24 m in the eastern and 21 m in the western deep, with corresponding slopes of ~7° and ~6.5°. Both deeps shallow southwards, their undulating floors containing two distinct overdeepend sections (Figure 3-4c, g).

Five similar, albeit smaller elongated deeps (ED2-6) occur on the UK Plateau north of the IGDs; a sixth deep (ED1) is located east of the IGDs. Although previously mapped (Dix and Sturt, 2011; Sturt et al., 2009), their geomorphology has not yet been described. These roughly N-S oriented features average ~4 km in length, ~900 m in width and 8-18 m in depth. All exhibit an elongated form, except the westernmost, heart-shaped deep (ED6; Figure 3-4c). The deep located ~3 km north of the Inner Gabbard sandbank (ED2; Figure 3-4c) differs in showing shallow slopes at both ends and truncating an E-W channel (p3; Figure 3-4c; see Section 3.4.3). Since 2015, this area is designated as an aggregates site, with associated disturbance features obscuring the original morphology.

Between the Inner and Outer Gabbard sandbanks, on the flanks of channel p4, four irregular depressions are present (D1-4; Figure 3-4c). These features are 5-10 m deep and up to 2.5 km wide. On the southern flank, one depression appears connected to p4 by a ~900 m long, shallow (~2 m deep) channel. The deeps on the northern flank show no clear connection to either p4 or p3. Further north on the UK Plateau, two circular depressions (D5-6; Figure 3-2b) occur, each 1.5-2 km wide and ~15 m deep.

3.4.5 Linear features in the Southern Bight

On the UK Plateau, parallel to the western side branch of the Axial Channel (B1), linear ridges occur (Figure 3-5a, b). Channel p1 incises these ridges (Figure 3-5a). The ridges exhibit a parallel, near N-S orientation (mean: 190°) and range in length from 100 m to 2 km. Intervening scour pits reach depths of up to 10 m and widths of up to 450 m. Smaller-scale linear features with a mean length of 350 m and a comparable orientation are superimposed (mean: 195°; Figure 3-5b). The features are situated in or near aggregates sites, where seabed morphology may have been modified by extraction activities.

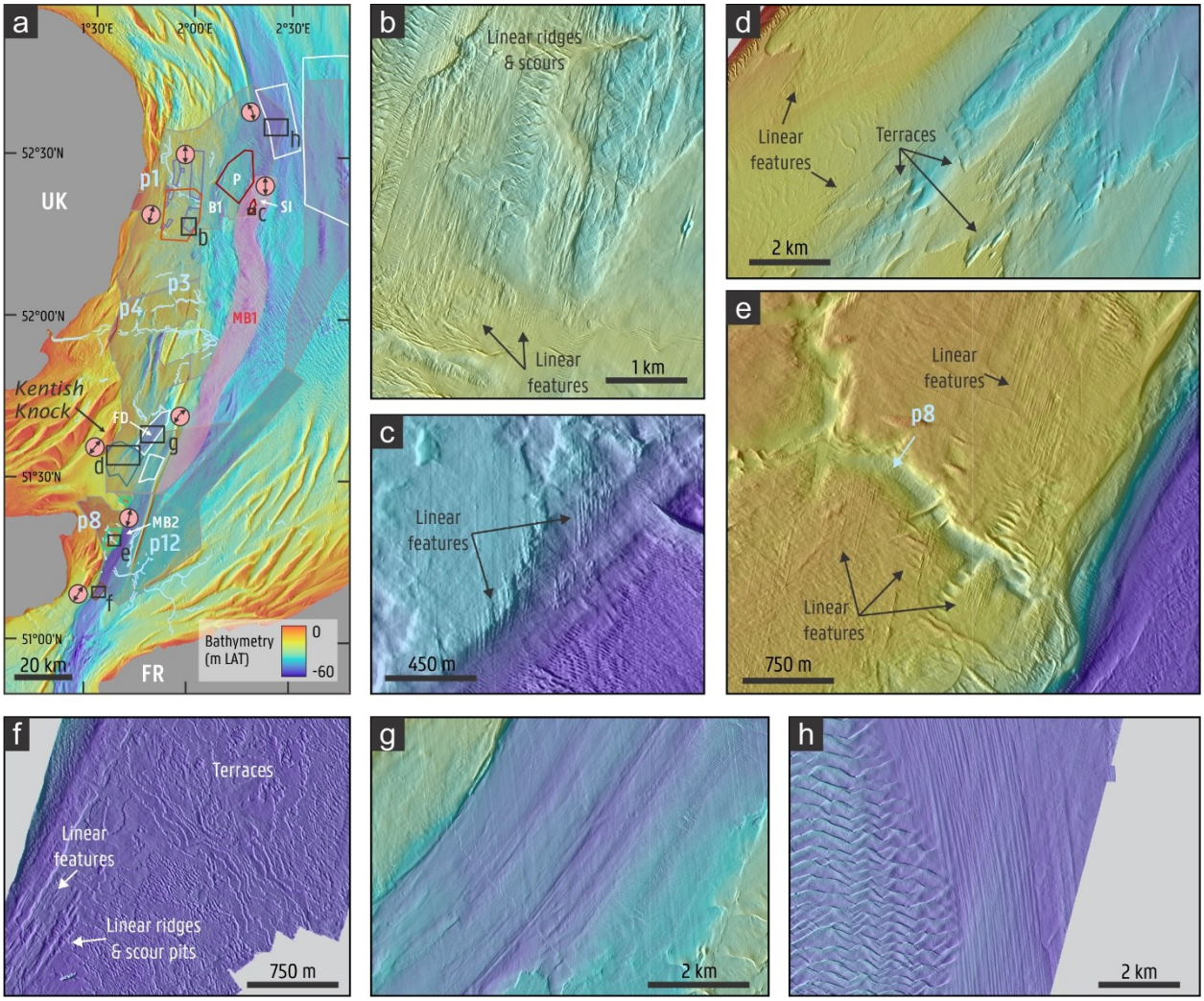


Figure 3-5. (a) Linear feature areas in the Southern Bight (indicated by different coloured polygons), with the orientation of the linear features indicated by arrows. UKHO bathymetry data are indicated by the more shaded blocks; (b) Linear ridges and scour pits on the UK Plateau (a: purple polygons), superimposed by linear features (a: orange polygon); (c) Linear features upstanding from the seabed on the plateau and streamlined island in the central Axial Channel (a: dark red polygons); (d) Linear features in a step-like terraced landscape in the Falls Deep (a: blue polygon); (e) Linear features upstanding from the seabed at the dendritic palaeochannel p8 (a: light green polygons); (f) Linear ridges and scour pits, superimposed by linear features, in a step like terraced landscape, at the base of the main branch of the Lobourg Channel (a: brown polygon); (g, h) Linear features at the base of the Axial Channel valley and Falls Deep (a: white polygons). B1: western side branch of Axial Channel, FD: Falls Deep, MB1: main branch of Axial Channel, MB2: main branch of Lobourg Channel, p1, 3, 4, 8, 12: smaller channels connecting to the Axial and Lobourg Channels, P: plateau, SI: streamlined island.

At the base of the main branch of the Lobourg Channel (MB2), similar linear ridges and scour pits are present, though at smaller scale (Figure 3-5a, f). The ridges average 244 m in length and 10-20 m in width, with a mean orientation of 210°. Intervening scour pits reach depths of up to 2 m and widths of 20-60 m. These features are further superimposed by smaller linear features, averaging 70 m in length and sharing a comparable orientation (mean: 212°; Figure 3-5a, f).

Smaller-scale linear features are also present on the plateau (P) and streamlined island (SI) in the central sector of the Axial Channel (Figure 3-5a, c), east of the Kentish Knock sandbank (Figure 3-5a, d) and at the dendritic channel p8 (Figure 3-5a, e). Their mean lengths are 200 m, 566 m and 240 m, with mean orientations of 179°, 219° and 192°, respectively. It remains unclear whether these features are depositional or represent erosional remnants protruding the surrounding seabed.

Another type of linear feature occurs at the base of Falls Deep (FD), west of the North-South Falls sandbank, and in the Axial Channel (white boxes on Figure 3-5a). The largest lineations are found in

the Axial Channel, particularly towards the Dutch Banks, where they reach 2-3 km in length and 70-200 m in width (Figure 3-5h). These features show slight curvature, following the channel axis (Figure 3-5h). Comparable lineations at the base of Falls Deep are up to five times shorter (~600 m) but exhibit wider spacing (~100 m compared to ~50 m in the Axial Channel; Figure 3-5g).

Southwest of Falls Deep and at the base of the main branch of the Lobourg Channel a terraced, step-like morphology is observed (Figure 3-5d, f). Terrace dimensions vary: those at Falls Deep show height differences of up to 15 m, whereas in the Lobourg Channel they do not exceed 1 m.

3.4.6 Depositional bedforms: sand waves and sand ridges

The occurrence of sand waves in the Southern Bight has been described by e.g. Van Veen (1935), McCave (1971) and Van Der Veen et al. (2006). In this study, six distinct sand-wave fields are described in the Southern Bight (Figure 3-6a). Sand waves in areas 3-6 share a NW-SE orientation (~127°; Figure 3-6b). Area 1 is unique compared to the other areas, as it displays symmetrical sand waves with a contrasting orientation and associated larger sand ridges. The ridges have a mean orientation of 143°, while the sand waves are nearly perpendicular to them (~72° and 80°; Figure 3-6b). In area 2, two orientations are present: sand waves at the base of the Axial Channel trend ~93°, perpendicular to the curvature of the main branch, whereas those on the streamlined plateau align with the general NW-SE orientation (~123°; Figure 3-6b).

3.4.7 Depositional bedforms: transverse ridges

Within the western side branch of the Axial Channel (B1; Figure 3-2b), four ridges are present: one crossing the side branch (R1), one isolated within the channel (R2) and two along its western margin (R3-R4; Figure 3-6c). Ridges R1-R3 were previously described by Limpenny et al. (2011). Despite differences in shape and size, all share an ENE-WSW orientation (~50-60°), contrasting with the N-S orientation of the sandbanks and the NW-SE orientation of the sand waves (see Section 3.4.6). Ridge R1, the southernmost, is narrow and elongated (4.3 km long, ≤ 600 m wide, 15 m high). Its northeastern end is dome-shaped with smooth, near-symmetrical slopes (~3°; Figure 3-6c, d), while the southwestern end has a crest with a steeper NW slope (4°) and a terraced SE slope. Ridge R2 is smaller (1.6 km long, 800 m wide, 13 m high), more circular and contains a summit depression. Its western slope is the steepest (up to 6°), contrasting with the terraced SE slopes (Figure 3-6d). Ridge R3, situated on the margin of the side branch, is the largest (3.5 km long, > 1 km wide, 17 m high). It has a steep southern (up to 7°) and less steep northern slope (up to 4°) and a plateau-like crest bearing small sand waves, with a similar orientation as the ridge itself, to the north (Figure 3-6c, d). A N-S oriented, S-shaped ridge may represent its northern extension, but this is uncertain (Figure 3-6c). Ridge R4, the northernmost, is the smallest (1.2 km long, 700 m wide and 7 m high) with gentle, symmetrical slopes (~2°; Figure 3-6c, d).

3.5 Interpretation and conclusions

The geomorphological mapping of the Southern Bight provides a first step towards reconstructing the evolution of the Axial and Lobourg Channels. Based on cross-cutting and erosional relationships of the mapped features a relative chronological framework is established, while their morphology allows for a tentative depositional and environmental interpretation. These interpretations are illustrated in Figure 3-7. In the absence of absolute chronological constraints, however, this relative timeline cannot yet be placed within the broader Pleistocene evolution of the southern North Sea Basin.

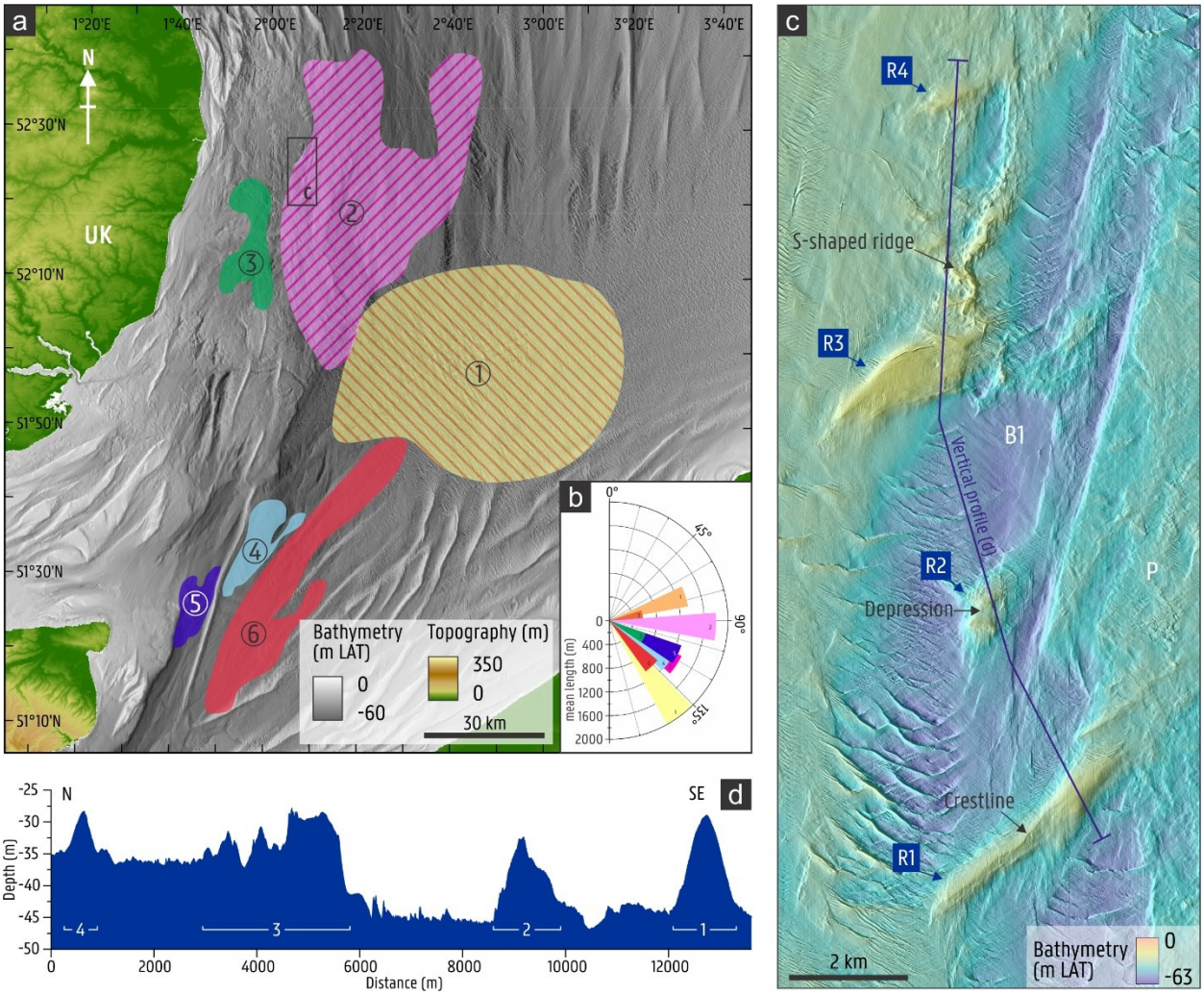


Figure 3-6. Depositional bedforms in the Southern Bight: (a) Sand wave field areas indicated by encircled numbers 1-6; (b) Rose plot with the mean orientation and mean length of the different sand waves. Area 1: yellow, light orange and dark orange, Area 2: dark and light pink, Area 3: green, Area 4: light blue, Area 5: dark blue, Area 6: red; (c) Transverse ridges (R1-4), west of plateau (P) and crossing the western side branch (B1) of the Axial Channel; (d) Vertical profile over the transverse ridges, location of the profile is shown by a dark blue line in (c).

The majority of geomorphological features identified on the UK Plateau – including the Inner Gabbard Deeps (IGDs), elongated deeps (ED1-6) and Falls Deep (FD) – were previously described and interpreted by Sturt et al. (2009). Based on morphological similarities, we here follow the interpretation of Sturt et al. (2009) and suggest that these features are (shallow) subglacial tunnel valleys (e.g. Huuse & Lykke-Andersen, 2000; Kristensen et al., 2007; Ottesen et al., 2020; Praeg, 2003; see also discussion in Sturt et al., 2009). The presence of such subglacial features indicates a glacially influenced landscape. This interpretation is further supported by the morphology of the – in this study identified – depressions (especially D5-6; Figure 3-2b) as well as the parallel linear ridges and scour pits north of the IGDs (purple polygons on Figure 3-5a), which resemble subglacial landforms such as kettle holes (e.g. Bennett & Glasser, 2009; Maizels, 1977) and mega-scale glacial lineations (MSGL's; e.g. Spagnolo et al., 2014), respectively. On the same UK-Plateau, channels p3 and p4 provide evidence for a fluvial landscape, representing a different, terrestrial phase. This phase predates the glacial phase, as demonstrated by the erosional relationship between p3-4 and the IGDs (see Section 3.4.4; see also discussion in Sturt et al., 2009).

The western escarpment (W1) delineates the margin of the UK Plateau, showing the erosional relationship between the plateau and the younger, incised main branch (MB1). Following the earlier phases, a third, more prolonged terrestrial phase is inferred from the fluvially shaped main branch of

the Axial Channel (MB1), its side branches (B1-7) and associated streamlined landforms (SI, SP). This phase may include base level changes and an eastward migration of the Axial Channel, expressed by terrace formation on the streamlined island (SI) and the presence of an anastomosing fluvial braid plain on the streamlined plateau (SP). Although the origin of the transverse ridges R1-4 is unclear, they may be associated with the eastward migration of the system. We tentatively interpret these ridges as (river) dunes formed after the western side branch (B1) was abandoned. The (re-)activation of several channels (p1-7, p13) is tentatively interpreted to indicate additional or renewed fluvial activity.

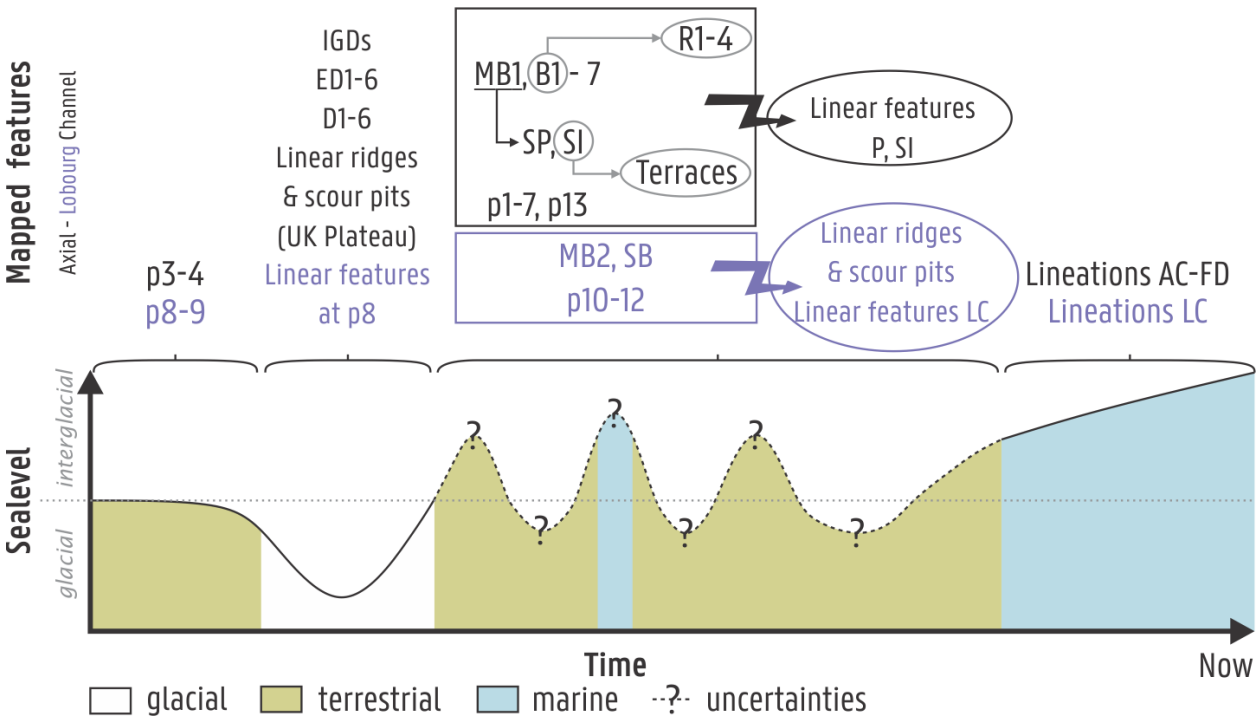


Figure 3-7. Schematic representation of the proposed evolution of the Axial (black) and Lobourg (purple) Channels, including relative chronology and simplified environmental interpretation. There are still many uncertainties due to the absence of absolute chronological constraints (question marks and dotted lined curve). AC: Axial Channel, B1-7: side branches of the Axial Channel, D1-6: depressions, ED1-6: elongated deeps, FD: Falls Deep, IGDs: Inner Gabbard Deeps, LC: Lobourg Channel, MB1: main branch Axial Channel, MB2: main branch Lobourg Channel, p1-13: channels connected to the Axial and Lobourg Channels, P: plateau, R1-4: transverse ridges, SB: side branch of the Lobourg Channel, SI: streamlined island; SP: streamlined plateau.

Linear features preserved on the plateau (P) and streamlined island (SI) may instead reflect a short-lived event. Depending on whether these features are depositional in nature or represent erosional remnants protruding the surrounding seabed, a different formational setting is inferred. In the latter case, they could be associated with a release of water from the north-northwest, potentially involving catastrophic flooding responsible for the preserved lineations. The timing of this short-lived phase relative to the prolonged terrestrial phase is uncertain, although it must postdate the formation of both the plateau (P) and streamlined island (SI).

The youngest geomorphological features are depositional, reflecting full marine conditions. These include sand waves and ridges, as well as furrows on the floors of the Axial Channel and Falls Deep, formed by tidal currents. The marine regime of the Outer Thames Estuary may also account for the linear features and terraces observed east of the Kentish Knock sandbank. The Lobourg Channel shows a parallel evolution, as the mapped features therein also reflect a glacio-fluvial imprint followed by a final marine phase (Figure 3-7).

Within the Pleistocene context of the southern North Sea, these phases predominantly reflect a non-inundated, terrestrial landscape. The interpreted glacial and fluvial phases are therefore more likely associated with glacial rather than interglacial periods. Nevertheless, as this study only shows the mapping of seabed expression of preserved geomorphological features, sub-bottom profiling and ground-truth data are required to fully resolve their extent, formative processes, and potential links to (inter)glacial periods.

CHAPTER 4. REASSESSMENT OF THE QUATERNARY SEISMIC STRATIGRAPHY OF THE WESTERN SECTOR OF THE SOUTHERN BIGHT (2°-3°E), NORTH SEA

ABSTRACT

Using newly acquired high-resolution sparker seismic data, the stratigraphic framework of the Southern Bight (52-53°N and 2-3°E) was re-evaluated. Nine seismic units have been identified, alongside six generations of incisions and three regional-scale erosional surfaces. These results allow a revision of the regional geological map and an updated seismic-stratigraphic framework, which is key in preparatory research for offshore wind-farm developments. Detailed examination of the seismic-stratigraphic units and geomorphological features provided new insights into the Quaternary evolution of the southern North Sea Basin. The Pliocene Red Crag Formation and Lower Pleistocene Southern North Sea Deltaic Group are described in unprecedented detail, with the former showing four incisional phases that reflect a dynamic, (inter-)tidal channel system. The top of the Yarmouth Roads Formation is marked by a regional-scale erosion surface, linked to the Elsterian (MIS12), that may include the southernmost buried tunnel-valley-type features in the Southern Bight. Three new units are identified and correlated with the Elsterian, the Holsteinian and/or early Saalian, and late Saalian and/or Eemian. The base and top of the stratigraphically younger and confidently identified Brown Bank Formation is marked by regional-scale erosional surfaces, indicative of two widespread erosional events. The basal surface could represent a preserved late Saalian landscape. The top surface, restricted to the Axial Channel system, reflects base-level fluctuations throughout the middle and late Weichselian. Our findings, some of which remaining inconclusive in places, highlight the need for future detailed investigations and the necessity of a continually regional stratigraphic framework for the Southern Bight.

This chapter has been submitted as: Vervoort, M., Plets, R., Kyriakoudi, D., Mestdagh, T., Busschers, F., van Heteren, S., De Clercq, M., Missiaen, T., & De Batist, M. (2026). Reassessment of the Quaternary seismic stratigraphy of the western sector of the Southern Bight (52-53°N and 2-3°E), North Sea. QUATERNARY SCIENCE REVIEWS.

Author contribution (CRediT): **Morgan Vervoort:** Conceptualisation, data curation, methodology, formal analysis, investigation, writing – original draft, writing – review & editing, visualisation. **Ruth Plets:** Conceptualisation, data curation, investigation, project administration, writing – original draft, writing – review & editing, supervision. **Despina Kyriakoudi:** Data curation, writing – review & editing. **Thomas Mestdagh:** Data curation, writing – review & editing. **Freek Busschers:** Conceptualisation, writing – review & editing. **Sytze van Heteren:** Conceptualisation, writing – review & editing. **Maikel De Clercq:** Data curation, writing – review & editing. **Tine Missiaen:** Conceptualisation, data curation, project administration, writing – review & editing. **Marc De Batist:** Conceptualisation, project administration, writing – review & editing, supervision.

4.1 Introduction

In the Southern Bight (the most southerly region of the southern North Sea) (Figure 4-1), extensive geological and geophysical datasets have been gathered since the 1960s, originally driven by oil and gas exploration, with the main aim to create offshore geological maps (BGS, 2000; Cameron et al., 1992; Long et al., 1988; Zagwijn and van Staalduinen, 1975). The Quaternary stratigraphic framework for the UK (Stoker et al., 2011) and Dutch (Rijsdijk et al 2005) sectors are based on these seismic and core data, and their derived products. The reference stratigraphies of Stoker et al. (2011) and Rijsdijk et al. (2005) are routinely applied by offshore developers and researchers when interpreting new seismic, acoustic and lithological data. However, many of the older seismic data on which these stratigraphic schemes are based, were acquired at lower frequencies than those that are commonly used today. As a result, while achieving deep penetration (up to several hundred metres below the seabed), they often lack the internal detail in the uppermost units that is critical for building robust Quaternary ground models. Furthermore, most of these early datasets were acquired in analogue format, excluding the possibility for dedicated post-processing.

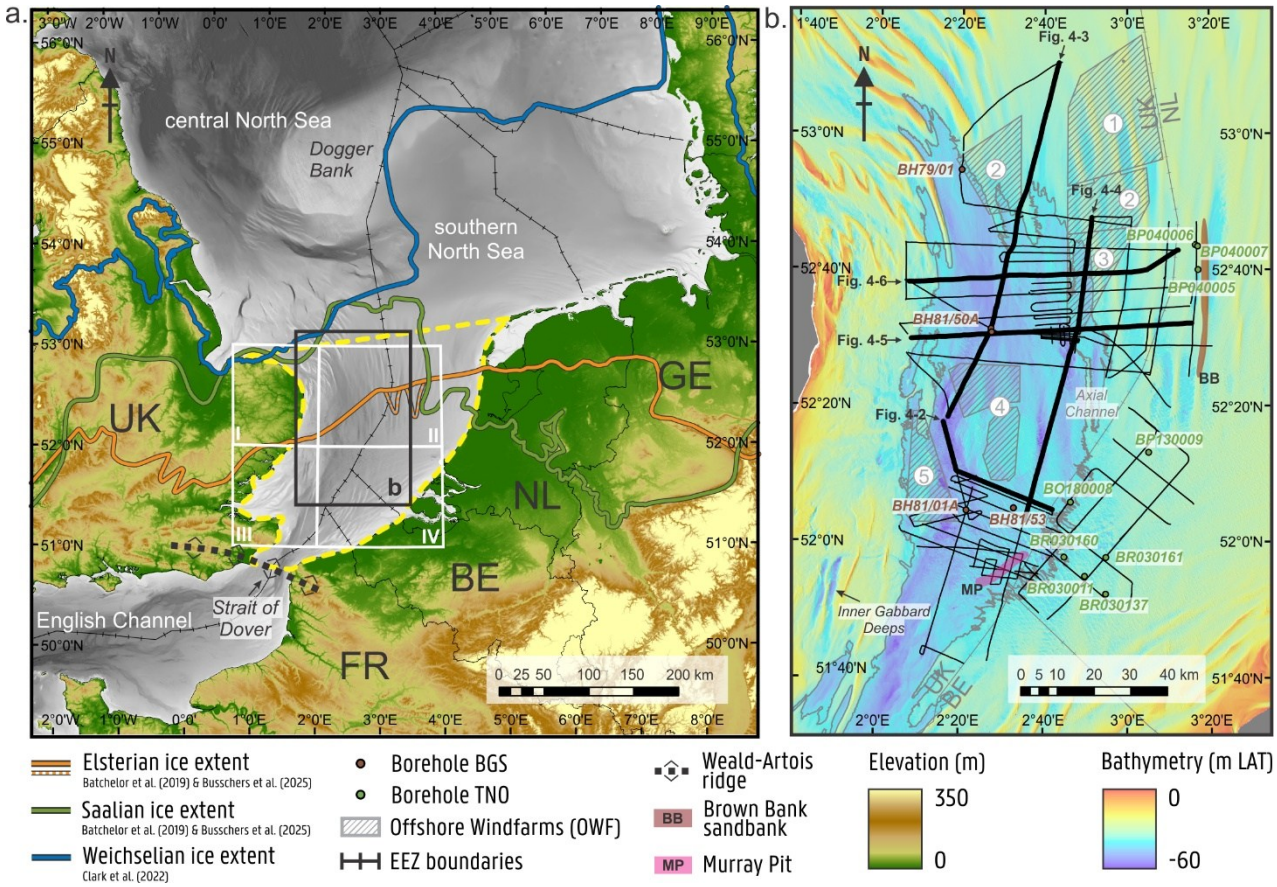


Figure 4-1. (a) Geographical setting of the Southern Bight (outlined by a yellow dotted line) and study area (black rectangle). Geological map sheets from the British Geological survey are outlined in white: I. East Anglia, II. Flemish Bight, III. Thames Estuary and IV. Ostend (Balson & D'Olier, 1990; Cameron et al., 1984; Harrison & Hopson, 1991; Laban et al., 1992). Southernmost ice margins of major glacial maxima after Batchelor et al. (2019), Busschers et al. (2025) and Clark et al. (2022). (b) Zoom of the study area, with seismic lines (black lines), borehole locations (brown and green dots) and offshore wind farms (OWF; grey shaded polygons: 1. Norfolk Boreas, 2. Norfolk Vanguard, 3. East Anglia THREE, 4. East Anglia ONE (North), 5. East Anglia TWO). The Brown Bank sandbank (BB), the Murray Pit (MP; after Cameron et al., 1992) and Axial Channel -40 m contour line (light grey; Chapter 3) are indicated for geographical reference. The bathymetric data (m to lowest astronomical tide, LAT) and elevation data (m above mean sea level) are derived from EMODnet (EMODnet Bathymetry Consortium, 2022) and the European Environmental Agency (European Environmental Agency (EEA), 2016), respectively.

The rapid development of offshore wind farms and other commercial projects, together with ever-increasing computing and processing power, has meant that large amounts of densely spaced, high-

resolution geophysical and ground-truth data have been acquired over the past few decades. Increasingly, these state-of-the-art data are also made available for geoscientific research (e.g. Cartelle et al., 2021; Cotterill et al., 2017; Eaton et al., 2020; Emery, 2020; McGuire et al., 2025; Mellett et al., 2020; Tizzard et al., 2014). Furthermore, a recent shallow (< 100 m below seabed) subsurface assessment was performed by the British Geological Survey (BGS) based on a compilation of information from UK offshore wind farms (OWFs) (Dakin et al., 2026), resulting in a new chronostratigraphic framework. Recently an updated stratigraphic framework of the Netherlands (on- and offshore) was published, with the main focus on the general depositional settings, sediment sources and processes throughout the Quaternary (Busschers et al., 2025). The BGS report highlights knowledge gaps and key uncertainties, outlining opportunities for future improvements and demonstrating the need for an updated and improved cross-boundary stratigraphic model for the southern North Sea. While the different OWF development reports and the newly proposed chronological frameworks are a great step forward, several limitations still persist: (i) the lack of data-supported interconnectivity to allow a regional-scale stratigraphic appraisal, (ii) the recent BGS report only incorporates UK OWFs, and (iii) OWF developers usually correlate seismic and lithological units with the established stratigraphic frameworks, rather than critically assessing or updating these.

Within the present study, we re-evaluate the current stratigraphic framework(s) of the Southern Bight area west of the Brown Bank sandbank (between 2°E and 3°E), using newly acquired, transnational high-resolution seismic (sparker) data. We examine seismic-stratigraphic units in unprecedented detail, correlate our results with findings from OWF sites in the study area, and describe and interpret geomorphological features in context of the Quaternary evolution of the southern North Sea Basin. The results can serve as a baseline for continual stratigraphic refinement and provide a link between development sites within and across national borders.

4.2 Geological background – current state of knowledge

This study focuses on the area between 2°-3°E and 52°-53° N in the Southern Bight (Figure 4-1), the southernmost region of the North Sea. The Southern Bight has water depths of (generally) less than 50 m and is located some 150 km to the south of Dogger Bank (south of an imaginary line joining the north of the coast of Norfolk (UK) and Terschelling (NL)) and to the north of the English Channel. The present-day seabed is characterised by several, kilometre-scale tidal sand ridges, which occur either as isolated features or clustered in fields (Balson et al., 1991; Balson and D'Olier, 1990; Johnson et al., 1982). In between these sand ridge fields, a prominent geomorphological feature known as the Axial Channel occurs. This c. 200 km long valley-like feature runs almost parallel to the present-day UK coastline, towards the English Channel in the south (Chapter 3; Figure 4-1b).

The Quaternary geology of the Southern Bight has been mapped and published as four different map sheets (Figure 4-1a; Balson & D'Olier, 1990; Cameron et al., 1984; Harrison & Hopson, 1991; Laban et al., 1992), compiled by the BGS (BGS, 2000). Deposition of these sediments occurred on the southern flank of the tectonically subsiding North Sea Basin (Arfai et al., 2018; Knox et al., 2010; Ottesen et al., 2018), with subsidence rates less than -0.25 m/kyr for the Southern Bight (Cohen et al., 2022; Hijma et al., 2025). The overall thickness of the Quaternary varies between 0 m in the south (51°-52°N) to 800-900 m in the north (c. 53°N) (Busschers et al., 2025; Lamb et al., 2018), following a regular pattern of south-to-north thickening. Between c. 10 and 1 Ma, deposition in the present-day southern North Sea was dominated by the Baltic or Eridanos River System, flowing westward along the present-day southern Baltic Sea Basin, and draining into a marine southern North Sea (e.g. Cohen et al., 2014; Gibbard and Lewin, 2016; Overeem et al., 2001). A massive increase in sediment supply led to significant infill of the basin and north(west) progradation of clinoforms during the first half of the Early

Table 4-1. Simplified stratigraphic classification for the shallow subsurface of the Southern Bight (modified from Busschers et al., 2025; Dakin et al., 2026; Rijsdijk et al., 2005; Stoker et al., 2011; TNO-GDN, 2026).

<table>
<tr><th colspan="2" rowspan="2">Stratigraphy UK sector</th><th colspan="2">Stratigraphical formations Dutch sector</th><th rowspan="2">Environment</th><th colspan="2" rowspan="2">Quaternary Stage (Europe/UK) and Epoch</th><th colspan="2" rowspan="2">MIS</th><th rowspan="2">Seismic units (this study)</th></tr>
<tr><th>Group</th><th>Formations</th></tr>
<tr><td rowspan="9">California Glacigenic Group</td><td>Southern Bight</td><td rowspan="9">Boven-Noordzee Group</td><td>Southern Bight</td><td>Open marine</td><td colspan="2" rowspan="3">Holocene</td><td colspan="2" rowspan="3">1</td><td rowspan="6">Unit 9</td></tr>
<tr><td rowspan="2">Elbow</td><td>Naaldwijk
(Wormer Bed)</td><td>Shallow marine, coastal, intertidal</td></tr>
<tr><td>Nieuwkoop
(Basal Peat Bed)</td><td>Coastal and terrestrial fluvial lowland</td></tr>
<tr><td>Botney Cut</td><td>Dogger Bight (Botney Cut Member)</td><td>(Post-)Glacial channel infill</td><td>Holocene to Weichselian/Devensian</td><td rowspan="5">Late Pleistocene</td><td colspan="2">2-1</td></tr>
<tr><td>Twente</td><td>Boxtel</td><td>Terrestrial aeolian and small-scale fluvial/lacustrine</td><td>Weichselian/Devensian</td><td>2</td><td>5d – 2</td></tr>
<tr><td>/</td><td>Kreftenheye</td><td>Fluvial (Rhine–Meuse)</td><td>Weichselian/Devensian to Saalian/Wolstonian</td><td colspan="2">6–2</td></tr>
<tr><td>Brown Bank</td><td>Brown Bank</td><td>Lagoonal, deltaic</td><td>Weichselian/Devensian–Eemian/Ipswichian transition</td><td colspan="2">5d–4</td><td>Unit 8</td></tr>
<tr><td>Eem</td><td>Eem</td><td>Estuarine, near coastal to open marine</td><td>Eemian/Ipswichian</td><td colspan="2">5e</td><td rowspan="2">Unit 7</td></tr>
<tr><td>Cleaver Bank</td><td>Drente</td><td>Glacigenic, including marine proglacial</td><td>Saalian/Wolstonian</td><td>Middle Pleisto</td><td>8 – 6</td><td>6</td></tr>
</table>

	Tea Kettle Hole		Drachten	Periglacial			10 – 6 / 8 –6	
	/		Urk	Fluvial	Holsteinian/Hoxnian		15–6	Unit 6
	Egmond Ground		Egmond Ground	Estuarine and shallow marine			11–7	
	Swarte Bank		Peelo	Subglacial	Elsterian/Anglian		12	Unit 6? Unit 5?
Dunwich Group	Yarmouth Roads		Appelscha, Sterksel, Urk (Uppermost parts Waalre, Peize)	Low-energy open-marine deltaic, delta (north) and coastal plain to fluvial (south) dominated by Rhine–Meuse sediments	Calabrian – Cromerian Stage		62–13	Unit 4
Southern North Sea Deltaic Group	Winterton Shoal		Waalre, Peize	Pro-delta, delta-front, delta-top, open marine and fluvial deposits associated with Eridanos, German, Rhine, Meuse and British Rivers	Eburonian	Early Pleistocene	62? –56	
	Smith's Knoll		IJmuiden Ground (Lowermost Waalre and Peize)		Mid-Tiglian		75? –63	Unit 3
	Westkapelle Ground		Maassluis		Praetiglian – Tiglian		103 –65	Unit 2
Crag Group	Red Crag		Oosterhout	Intertidal sand-flat deposits	Reuverian	Late-Pliocene	/	Unit 1

Pleistocene (Gibbard and Lewin, 2016; Ottesen et al., 2018; Overeem et al., 2001). The onset of major glaciations, particularly from the Middle Pleistocene onwards, led to the demise of the Eridanos, resulting in a provenance and depositional shift of the deltaic material toward more southerly sources and sinks (Bijlsma, 1981; Cohen et al., 2014; Gibbard et al., 1988; Ottesen et al., 2018).

Stratigraphically, the Lower Pleistocene sediments are grouped as the older, (pro-)deltaic and open marine sediments of the Southern North Sea Deltaic Group and the younger, deltaic, fluvial and low-energy marine deposits of the Dunwich Group (Table 4-1). The Southern North Sea Deltaic Group is dominated by sediments derived from the European mainland through a large delta system, but also from Britain through a smaller delta contiguous with present-day East Anglia (Cameron et al., 1992). It comprises thick, extensive sediments, deposited under relatively stable climatic conditions. This group has been subdivided into eight formations, of which only the Westkapelle Ground, Smith's Knoll (and its lateral equivalent IJmuiden Ground), and Winterton Shoal Formation are identified in the Southern Bight (Cameron et al., 1992, 1984a; Harrison and Hopson, 1991; Laban et al., 1992; Stoker et al., 2011) (Table 4-1). The Dunwich Group consists exclusively of the Yarmouth Roads Formation, correlated with a large depositional timeframe, from the Calabrian to the Middle Pleistocene Cromerian (Cameron et al., 1992; Stoker et al., 2011) (Table 4-1). The sediments of the Yarmouth Roads Formation reflect an intricate depositional environment controlled by local sea-level fluctuations, in which northward-flowing rivers filled the southern North Sea Basin with low-energy deltaic as well as fluvial sediments derived from the Proto-Thames and Rhine-Meuse systems (Cameron et al., 1992; Stoker et al., 2011). This sedimentary record is still poorly known and understood. Furthermore, the uppermost parts of the Yarmouth Roads Formation were either eroded and reworked (in case of the Proto-Thames) or significantly modified by overriding ice sheets, that deposited the California Glacigenic Group (Cameron et al., 1992; Stoker et al., 2011). Throughout the Early Pleistocene (up until the Elsterian glacial period), the Weald-Artois anticlinal chalk ridge (Figure 4-1a) and adjacent Palaeogene topography formed a structural and lithological barrier between the southern North Sea and the English Channel (Gibbard, 1995; Gibbard and Lewin, 2016; Hijma et al., 2012).

The increase in intensity of the Middle Pleistocene glacial-interglacial oscillations (known as the Mid Pleistocene Revolution, c. 1.2 Ma – 700 ka; Clark et al., 2006) generated larger variations in relative sea level (RSL) (Spratt and Lisiecki, 2016). This resulted in alternating periods during which the study area was fully terrestrial versus almost fully marine (e.g. Cohen et al., 2014; Hijma et al., 2012). With only fragmentary evidence for previous glacial phases (e.g. Bendixen et al., 2018), the first clear evidence for extensive British-Irish and Fennoscandian ice sheets (BIIS and FIS, respectively) over the present-day southern North Sea dates from the Elsterian (Anglian) glacial period (MIS12; c. 470-420 ka BP) (Böse et al., 2012; Cohen and Gibbard, 2019). When these ice sheets coalesced across the North Sea, a fluvial drainage route to the north was blocked (e.g. Cohen et al., 2014; Gibbard, 1995; Gibbard et al., 1988; Gibbard and Lewin, 2016; Hijma et al., 2012). This particular glacial configuration led to the accumulation of glacial deposits in the northern part of the study area (Swarte Bank Formation, Table 4-1), commonly found in deeply-scoured tunnel valleys (e.g. Cameron et al., 1992; Lonergan et al., 2006). A contested but broadly shared hypothesis supports the development of a large Elsterian proglacial lake dammed by the British-Fennoscandian ice sheet north of the Weald-Artois ridge (Gibbard, 1995; Gibbard and Lewin, 2016; Hijma et al., 2012). Thus far, evidence has only been found in terrestrial settings (Beets and Beets, 2003; Busschers et al., 2025, 2008; De Gans et al., 2000; Laban and van der Meer, 2011) while offshore sedimentological evidence is largely missing or at best strongly debated (e.g. Cohen et al., 2014). Geomorphological evidence from the English Channel (including scour pits, streamline islands, longitudinal lineations, ...) has been interpreted as overtopping of the Weald-Artois ridge at some point by large volumes of lake water, causing structural degeneration and initiating the opening of the Strait of Dover through catastrophic, high-magnitude flooding (Collier et al., 2015; García-Moreno et al., 2019; Gibbard, 1995; Gupta et al., 2017; 2007). This

initial breaching of the Weald-Artois ridge, although still debated, would have resulted in the formation of a south-westward-flowing drainage system that connected the southern North Sea Basin and English Channel (Collier et al., 2015). This may also have initiated the formation of the Axial Channel (e.g. Hijma et al., 2012; Mathys, 2009).

During the following interglacial, known as the Holsteinian or Hoxnian interglacial (MIS11; c.420 – 370 ka BP; Cohen and Gibbard, 2019) the North Sea Basin became a shallow sea again, with, to the north of our study area, marine sediments infilling and being deposited adjacent to Elsterian tunnel valleys (part of the Egmond Ground Formation, Table 4-1) (Cameron et al., 1992; Rijsdijk et al., 2005; Stoker et al., 2011). The southern North Sea and the English Channel appear to have remained separated during part of this interglacial (e.g. Hijma et al., 2012; White and Schreve, 2000). However, both basins were most-likely briefly connected during the Holsteinian maximum highstand, temporarily separating Britain from the European mainland (Gibbard, 1995; Meijer and Preece, 1995; White and Schreve, 2000). The onshore Urk Formation is the correlative equivalent of the marine Egmond Ground Formation (Busschers et al., 2025; Laban, 1995; Zagwijn, 1983) (Table 4-1). These sediments are typically found onshore in the Netherlands, consisting of fluvial deposits from the Rhine that ran a northward course, transitioning to estuarine and shallow marine deposits in offshore areas of the northern Netherlands (northeast of the study area) (Rijsdijk et al., 2005).

Subsequent glaciations are not believed to have advanced as far south into the present-day southern North Sea Basin as during the Elsterian glacial maximum, with the exception of the late Saalian glacial maximum in the Dutch offshore sector (Figure 4-1a). During this late Saalian glaciation (MIS6; c. 170-130 ka BP; Cohen and Gibbard, 2019), the presence of the British-Fennoscandian ice sheet in the North Sea Basin caused the northern fluvial route to be blocked once again (e.g. Cohen et al., 2014; Hijma et al., 2012). Two formations were identified to the north/northeast of the study area that record the periglacial and (marine) proglacial environment of the Saalian glaciation (Tea Kettle Hole and Cleaver Bank Formation (UK), Drachten and Drente Formation (NL); Table 4-1) (Cameron et al., 1992; Rijsdijk et al., 2005; Stoker et al., 2011). During the maximum extent of the ice (Drenthe substage; 160-150 ka BP; Cohen and Gibbard, 2019), a proglacial lake may have formed in front of the southern ice margin, which subsequently drained as the last vestiges of the land bridge between Britain and continental Europe eroded (Busschers et al., 2008; Gupta et al., 2017; Hijma et al., 2012; Toucanne et al., 2009a). In a more recent study, Cartelle et al. (2021) found no evidence of such an MIS6 proglacial lake in wind-farm data acquired just offshore the Dutch coastline. Irrespective of the presence of a proglacial lake, sedimentary and chronological evidence show that since MIS6 at least a part of the Rhine-Meuse system and the Thames occupied the Axial Channel (Hijma et al., 2012), flowing southward during lowstands through the Strait of Dover (Busschers et al., 2008; Mathys, 2009; Mellett et al., 2013; Toucanne et al., 2009b).

A shallow sea characterised the present-day Southern Bight during the ensuing Eemian or Ipswichian interglacial (MIS5e; 130-116 ka BP; Cohen and Gibbard, 2019), reaching a maximum level that was slightly higher than today (Cohen et al., 2022; Zagwijn, 1983). Eemian marine sands (Eem Formation, Table 4-1), where present, are partly overlain by the distinct fine-grained sands and clays of the Brown Bank Formation (Table 4-1) (Cameron et al., 1992; Rijsdijk et al., 2005; Stoker et al., 2011). These typically shallow-marine sediments were accumulated during the Weichselian Early Glacial (MIS5-4 transition; c. 70 ka) under cooler climatic conditions and a sea-level position that was lower than during the preceding Eemian period (Waajen-Labee et al., 2025).

When RSL continued to fall during the Weichselian Early Pleniglacial (MIS4), the fluvial systems extended their courses onto the former continental shelf, initiating a period of intensive fluvial erosion (Busschers et al., 2007; Hijma et al., 2012). The Rhine-Meuse and Scheldt rivers as well as the Thames joined to form the Axial Channel river system, discharging southwards via the Lobourg Channel and

through the Strait of Dover (De Clercq et al., 2018; Hijma et al., 2012; Mellett et al., 2013). At that time, however, the BIIS and FIS were not large enough to form a coalesced grounded ice barrier, meaning that North European river systems could still drain northwards, as indicated by the absence of sediments derived from the North European Plain in the Bay of Biscay (Toucanne et al., 2023). It was only during MIS2 that the ice sheets coalesced one final time, blocking a northern drainage route, forcing drainage through the Strait of Dover into the Englisch Channel river system (Mellett et al., 2013; Toucanne et al., 2010). In the terrestrial areas beyond the southernmost ice margin, aeolian (Twente Formation (UK); Boxtel Formation (NL)) and fluvial sands (Kreftenheye Formation) are widespread (Table 4-1), commonly with periglacial traces (Busschers et al., 2008; Rijsdijk et al., 2005; Törnqvist et al., 2000). North of our study area, Roberts et al. (2018) suggests a proglacial lake, referred to as Dogger Lake, formed in the wider area of Dogger Bank likely at the time when the ice sheets coalesced (MIS3-2). Subglacial, glaciofluvial and glacio-lacustrine Weichselian sediments dominate the Dogger Bank area (multiple formations; Cotterill et al., 2017; Stoker et al., 2011), alongside (post-)glacial channel infill on or in areas south of Dogger Bank (Botney Cut Formation (UK) and Dogger Bight Formation – Botney Cut Member (NL); Table 4-1) (Cameron et al., 1992; Rijsdijk et al., 2005; Stoker et al., 2011). Decoupling of the ice sheets during deglaciation (c. 21-18.5 ka BP) may have led to the northward drainage of the proglacial lake, followed by a marine inundation through the resulting gap (Hjelstuen et al., 2018; Roberts et al., 2018). In other recent studies, deposits reflecting smaller-scale, ice-marginal lakes have been identified on and south of Dogger Bank, revealing a complex (de-)glacial and depositional history (Cotterill et al., 2017; Emery et al., 2019; Kyriakoudi et al., 2026).

The start of the Holocene (11.7 ka BP; Cohen and Gibbard, 2019) signalled a dramatic change in landscape as a result of marine transgression, with an expanding embayment developing into today's Southern Bight (Cohen et al., 2014; Hijma et al., 2025). The glaciotectonised Dogger Bank high turned into a shrinking island and Britain became permanently separated from mainland Europe (c. 8-7.5 ka) (e.g. Cohen et al., 2017; Lambeck, 1995; Sturt et al., 2013). This transformation has been partially preserved in the sedimentary record, where intertidal to coastal deposits (Elbow Formation (UK); Wormer Bed - Naaldwijk Formation (NL)), locally overlie freshwater peats (Elbow Formation (UK); Basal Peat Bed - Nieuwkoop Formation (NL)) (Table 4-1) (Cameron et al., 1992; Rijsdijk et al., 2005; Stoker et al., 2011). In the Southern Bight, the Holocene sediments generally form a blanket deposit over Pleistocene or older formations (Cameron et al., 1992; Stoker et al., 2011), with open marine sands of the Southern Bight Formation (Table 4-1) forming the present-day seabed in most places.

4.3 Methodology

New data used for this study were collected during six scientific cruises, conducted in April 2018 (RV *Belgica* cruise 2018/09), May 2019 (RV *Belgica* cruise BE2019-13), October 2022 (RV *Belgica II* cruise BE2022-22), June 2023 (RV *Simon Stevin* cruise SS23-490), October 2023 (RV *Belgica II* cruise BE2023-19), and June 2025 (RV *Simon Stevin* cruise SS25-430). The geophysical surveys were designed to deliver data on the regional seismic-stratigraphic framework. The area covered by these surveys stretches from the western side of the Brown Bank sandbank to just offshore the coast of East Anglia (UK) (Figure 4-1b). In total c. 2170 km of lines were surveyed, reaching a line spacing of 200-600 m within certain areas.

In April 2018 and June 2023, seismic data were acquired using a multi-tip Centipede sparker source (centre frequency of 0.8-1.2 kHz) along with a SIG single-channel streamer. During the May 2019 and June 2025 surveys, a GSO high-resolution multi-tip sparker system (centre frequency of 350-800 Hz) was deployed alongside the SIG single-channel streamer. For the October 2022 and 2023 surveys, the GSO high-resolution multi-tip sparker system was combined with a multi-channel streamer (24 channels at 2 m spacing). Data were recorded using a Delph seismic acquisition unit, with a sampling frequency of 8 kHz (for multi-channel data) and 16 kHz (for single-channel data). A 1 s shot interval

was used during the earlier surveys (2018-2019) while a shot interval of 0.5 s was selected during the more recent surveys (2022 onwards). The sparker source and streamer were towed behind the vessel at respectively the port and starboard side of the aft-deck, with a layback of 20 to 30 m behind the stern. The signal penetrated up to 160 m below the seafloor, with the best image quality in the upper ~100 m, where a resolution of 0.5-1.5 m was achieved. Processing of the sparker data was performed in RadExPro 2022 (RadExPro Seismic Software LCC) and consisted of geometry assignment, amplitude corrections, filtering (bandpass filter, swell filter, burst noise removal, 2D spatial filter and FX filter) and tidal corrections (to lowest astronomical tide, LAT; EU Copernicus Marine Service, 2024). The multi-channel data required a few extra processing steps, including velocity analysis, stacking and post-stack migration.

All processed profiles were imported into the S&P Global Software Geoscience Package (Kingdom version 2019) for interpretation, visualisation and correlation with borehole data. Horizon and seismic unit characterisation was performed using the standard principles of seismic stratigraphy (Mitchum et al., 1977). A depth conversion from two-way travel time (TWT) to depth (m) was applied for gridding maps, using a sound velocity of 1550 m/s in water and 1650 m/s in sediments. Gridded thickness and depth structure maps were created using a flex gridding algorithm. A limiting distance between control point and input datapoint of 1500 m was set, as well as a grid cell size of 1500 m. The resulting grids were exported from the Kingdom software and incorporated in ArcGIS Pro (version 3.6) for further interpretation.

The seismic dataset was complemented with available information from four boreholes up to 77 m deep from the British Geological Survey (BGS; Geoindex Offshore), and nine boreholes (10 to 47 m deep) from the Netherlands Organisation for Applied Scientific Research (TNO; DINOloket) (for locations see Figure 4-1b). These boreholes were projected onto the seismic profiles if the radial distance was less than 5 km and used to assign lithologies and already interpreted formation names to the identified seismic units.

4.4 Results and interpretation

Nine main regional seismic units were identified, as well as a number of distinct geomorphological features at the base of or within these units. These are described below. Note that the generic unit names used have no regional connotation. Figure 4-2 to Figure 4-6 show five representative sparker profiles (two W-E oriented, two N-S and one roughly NW-SE; for location see Figure 4-1b). The units are described from bottom (older) to top (younger). Their interpretation is mostly based on the seismic-stratigraphic characteristics of the units (lower and upper unit boundaries and internal reflection configuration) and the stratigraphic order in which they appear, summarised in Figure 4-7. The available information from BGS and TNO boreholes (i.e. log sheets) have been incorporated to support the interpretation (see Supplementary Report S4). The thickness of the identified units, as well as the basal surfaces that could be traced regionally across the study area (i.e. surfaces that are not (fully) masked by the multiple) on the sparker data were calculated and gridded (Figure 4-8; Figure 4-9). A simplified geological map was reconstructed by plotting and extrapolating the units' basal surfaces along the seismic profiles, except for the youngest seismic-stratigraphic unit (Figure 4-10).

4.4.1 Seismic-stratigraphic units

Unit 1 (U1): The lowermost unit is imaged only on the sparker profiles in the southwest (Figure 4-2; Figure 4-3; Figure 4-8). It occurs as an infill of multiple, N-S-oriented, large (≥ 40 m deep) incisions (a-d; Figure 4-2; see also Figure 4-11b). The basal unconformity (S1) cuts into the underlying Pre-

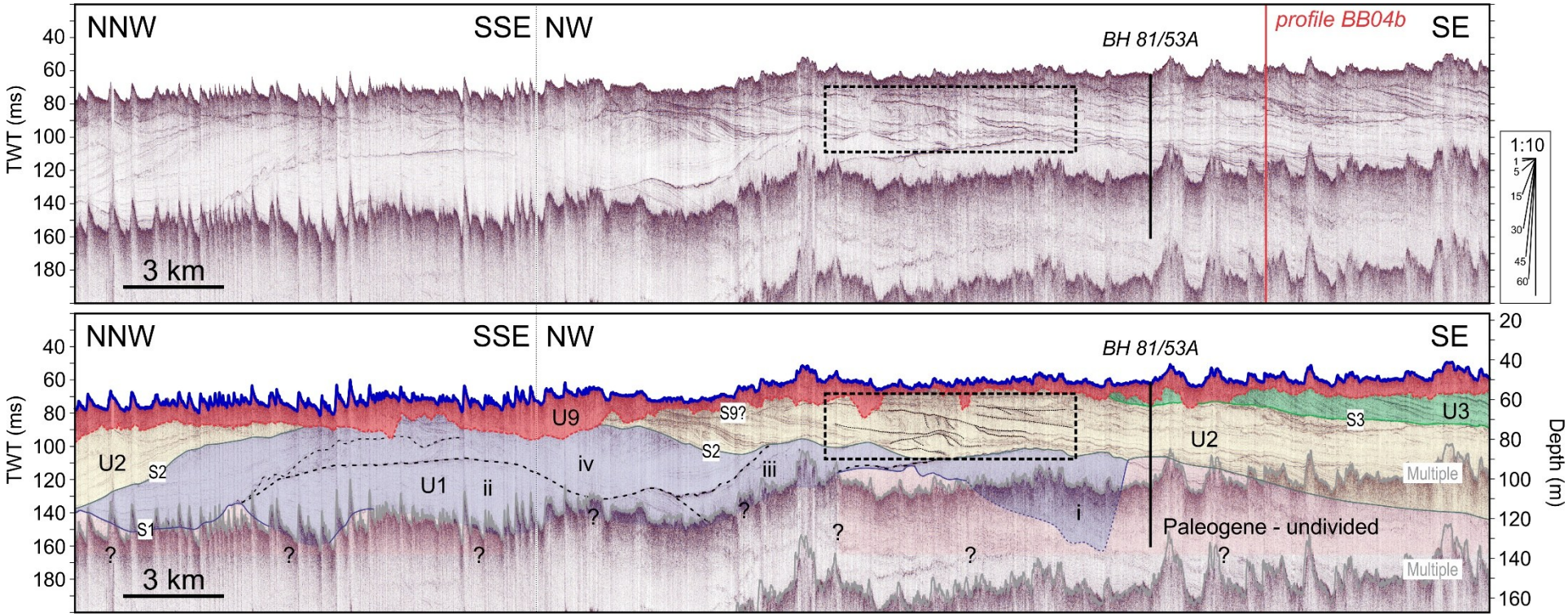


Figure 4-2. NNW-SSE to NW-SE oriented sparker line SB_ACW11-SB18 with projected BGS borehole BH 81/53A; for location see Figure 4-1. Incisions i-iv within U1 (generation A) are indicated. Black dotted box indicates subunits in U2 discussed in the main text.

Quaternary (Paleogene – undivided) strata and is marked by a medium-amplitude reflection. The unit is in turn unconformably overlain by U2, separated by a medium-amplitude reflection (S2) or, at shallower depths overlain by U9, separated by S9. In the southwest, U1 crops out at the seabed. The U1 infill shows deposition in multiple stages, characterised by recognisable seismic facies that range from a divergent fill to a transparent facies (Figure 4-7). As the unit consists of multiple incisions, the thickness is highly variable, reaching up to 57 m in the deepest parts (Figure 4-8; see also Section 4.4.3). Borehole logs (BH81/01A and BH81/53) describe this unit as glauconitic, green, muddy fine sands with abundant fine shells (BGS, 2026a; 2026b). Based on the borehole data and geographic occurrence, we interpret this unit as the Plio-Pleistocene Red Crag Formation. Almost 20 km to the southeast of BH81/53, a ~10 km long, < 4 km wide and 55 m deep incision is present, known as the Murray Pit (Figure 4-1b; Figure 4-11c; Balson et al., 1991). It is infilled by a prograding fill, with low-amplitude and low-frequency seismic reflections. Vibrocores in the topmost infill of the Murray Pit have recovered similar glauconitic muddy sands as described for the Red Crag Formation. However, microfossil species suggest an Early Pliocene age for these sediments, correlating it rather to the onshore Coralline Crag of eastern England (Cameron et al., 1992).

Unit 2 (U2): The second unit is characterised by continuous, medium-amplitude, medium-frequency, mostly sigmoidal to tangential oblique progradational reflections (Figure 4-2 to Figure 4-7). These reflections dip in a north-easterly direction in the western part (<0.2°), becoming more horizontal towards the east. The basal unconformity (S2) is a medium-amplitude reflection marked by downlapping of the basal reflections of U2. The upper boundary (S3) truncates the upper reflections of U2. The unit mostly comprises continuous reflections; however, at shallower depths (western part of the study area), multiple subunits with parallel dipping to tangential oblique facies are present (black dotted box in Figure 4-2). Here, the top of the unit is truncated by an irregular erosional surface (S9) and/or incised by S6 (Figure 4-3 to Figure 4-6). U2 is thin in the south (< 10 m), becoming thicker to the north and east (up to 75 m) (Figure 4-8). Available borehole data from the region (BH81/53 and 81/50A) suggest that this unit consists of Lower Pleistocene olive green sands, silts and muds overlying pre-Quaternary deposits (BGS, 2026c; 2026b). In the southeast (Dutch Continental Shelf), where the unit lies close to the seabed surface, the unit consists of more greyish brown, silty clay to fine sands with some gravel mixed in (BR030011 and BR03160) (TNO-GDN, 2026b). Based on its seismic expression and the existing borehole data, U2 is interpreted as the Lower Pleistocene prodeltaic Westkapelle Ground Formation.

Unit 3 (U3): Unit 3 is present in the central part of the study area (Figure 4-8). Seismically, it can be subdivided into several subunits with reflections displaying a parallel to sigmoidal geometry (black dotted box in Figure 4-3), prograding in a northeasterly direction (0.2° dip; with apparent easterly progradation on E-W profiles and northerly progradation on N-S profiles) (Figure 4-2 to Figure 4-7). The characteristics of the reflections vary spatially, ranging from low to high amplitude, low to high frequency, and from continuous to discontinuous. The reflections display downlap onto internal boundaries but become more parallel towards the centre of the area, where they appear conformable to the unit's basal unconformity S3, which is a high amplitude reflection. The top of the unit is truncated by an irregular, medium-amplitude reflection (S4) (Figure 4-7). Just as for U2, at shallower depths, U3 is truncated by the irregular surface S9 or incised by S6 (Figure 4-3 to Figure 4-6). The unit is up to 25 m thick in the east (NL), becoming thicker towards the centre (UK, up to 55 m) (Figure 4-8). This thickening may continue further towards the northeast, but cannot be confirmed as the top and bottom of the unit are masked by the seabed multiple. In boreholes BH81/50A and BR030161, the unit consists of olive green to greenish grey muddy sand, with some clay mixed in, and shell fragments (BGS, 2026c; TNO-GDN, 2026b). Compared to the lithological description of U2, the borehole data do not suggest a distinct sedimentary change between the units U2 and U3, implying that U3 also represents deltaic sediments. However, there is a clear change in the seismic architecture between these two units. The prograding reflections of U3 are steeper than

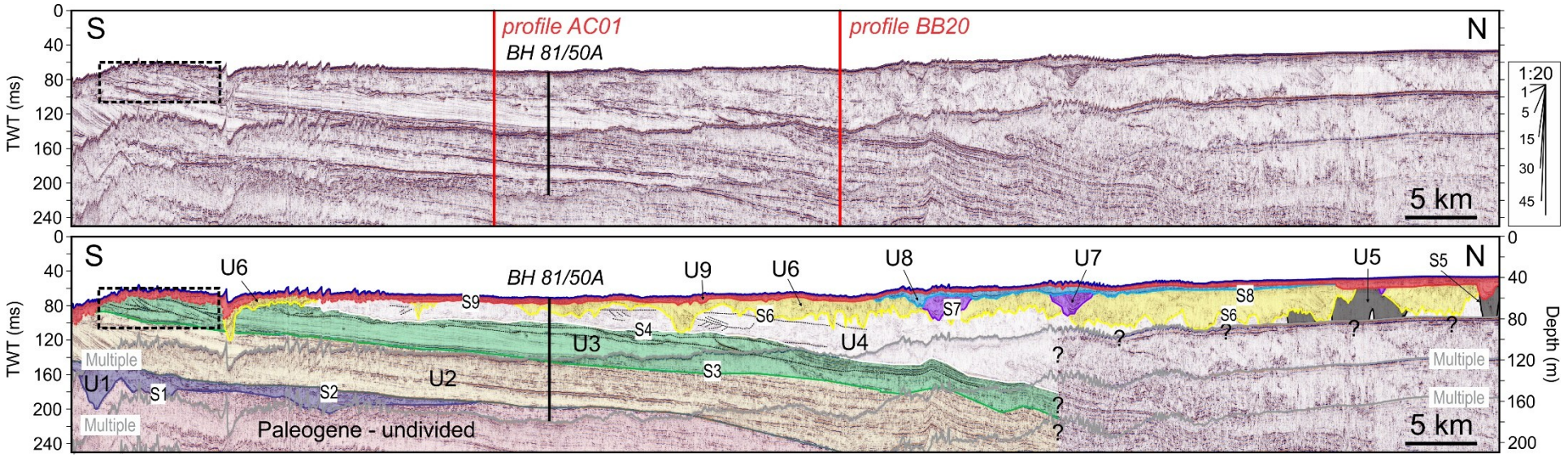


Figure 4-3. S-N oriented sparker line BB04b with projected BGS borehole BH 81/50A; for location see Figure 4-1. Black dotted box indicates subunits in U3 discussed in the main text.

those of U2, particularly on the western margin, where the unit is generally thicker (Figure 4-5; Figure 4-8). Based on both the seismic characteristics and lithology from the boreholes, U3 closely correlates with the open-marine prodeltaic deposits of the Lower Pleistocene Smith's Knoll Formation, representing sediment influx from onshore Britain (Cameron et al., 1992). Towards the (north)east, U3 is less clearly defined and upper and lower boundaries are undiscernible. Some internal reflections display a broad undulating appearance. Here, U3 has been interpreted as part of the IJmuiden Ground Formation. This formation represents open-marine and prodeltaic sediments originating from mainland Europe (Rhine, Meuse and North German rivers) and is contemporaneous with the sediments of the Smith's Knoll Formation (Rijsdijk et al., 2005; Cameron et al., 1992). The transition between the Smith's Knoll Formation in the west, and the IJmuiden Ground Formation in the east is not visible on our sparker data.

Unit 4 (U4): U4 represents a major change in seismic character, contrasting with the underlying prograding units U2 and U3 (Figure 4-3 to Figure 4-6). The lowermost part of U4 is characterised by a low-amplitude seismic facies that mostly lacks clear reflections. This facies is only imaged on two profiles in the central sector (including profile BB01; Figure 4-4) and is masked by the seabed multiple on other profiles. On this N-S profile, a few subhorizontal reflections onlap onto the basal unconformity (S4). For the largest part, U4 is characterised by mostly discontinuous, medium- to high-amplitude and low- to high-frequency reflections (Figure 4-7). Incisions, up to 15 km in width, are present throughout the entire unit, showing numerous cut-and-fill phases (Figure 4-11d). The reflections that delineate these incisions are all confined within the unit and do not cut into the underlying units. They occur mostly in the top c. 30 m of the unit. Interference of the multiple often makes it difficult to determine their base or maximum depth of the occurrence of the incisions. No internal boundary has been identified that clearly divides the more structureless lower part of U4 from the more complex upper part. The top of U4 is cut by an erosional surface (S6) that appears to be discontinuous throughout the study area, as reflected on its depth structure map (Figure 4-9). Where this boundary cannot be traced, the overlying Unit 6 (U6) is absent, and surfaces S5, S7 and S9 form the upper boundary. Even though the base of the unit in the north(east)ern sector is obscured by the multiple, it seems that U4 continues to increase in thickness towards the northeast, becoming ≥ 100 m thick (Figure 4-8).

In BGS boreholes BH81/50A and BH79/01, this unit is represented by mostly green-grey fine sand (commonly with clay laminations), interpreted as Lower to Middle Pleistocene deposits (BGS, 2026c; 2026d). In borehole BO180008, where the unit is close to the seabed, a different lithology is present, i.e. medium to coarse, grey-brown sand with some gravel mixed in (TNO-GDN, 2026b). In borehole BP130009, U4 corresponds to a 36 m thick unit consisting of two different lithologies. In the top 18 m the unit consists of (very) coarse, brown-grey sand, whereas the basal 18 m is represented by (light) grey, medium fine sands with some clay and silt at the base (TNO-GDN, 2026b). The numerous cut-and-fill phases marking the upper part of the unit on the seismic profiles, together with the different recorded lithologies from the borehole data, suggest that U4 represents the mainly fluvial sediments (albeit with possible marine incursions) of the Lower to Middle Pleistocene Yarmouth Roads Formation. The base of the Yarmouth Roads Formation is strongly diachronous (Cameron et al., 1992), which is also reflected in our dataset. In the (south)western to central part, U4 overlies the deltaic Lower Pleistocene U3, which we interpreted as Smith's Knoll Formation. In the centre and north, published stratigraphy and cross sections suggest that the Yarmouth Roads Formation overlies the Winterton Shoal Formation (Cameron et al., 1992), described mostly as structureless on seismic profiles, but with some gently dipping reflectors. This may correlate to the lowermost seismic facies of U4, but due to the interference of the multiple we cannot fully confirm that interpretation.

Unit 5 (U5): Located in the northernmost section of the study area only (Figure 4-3; Figure 4-8), this isolated and distinctive unit is characterised by a transparent seismic facies. U5 occurs as the infill of

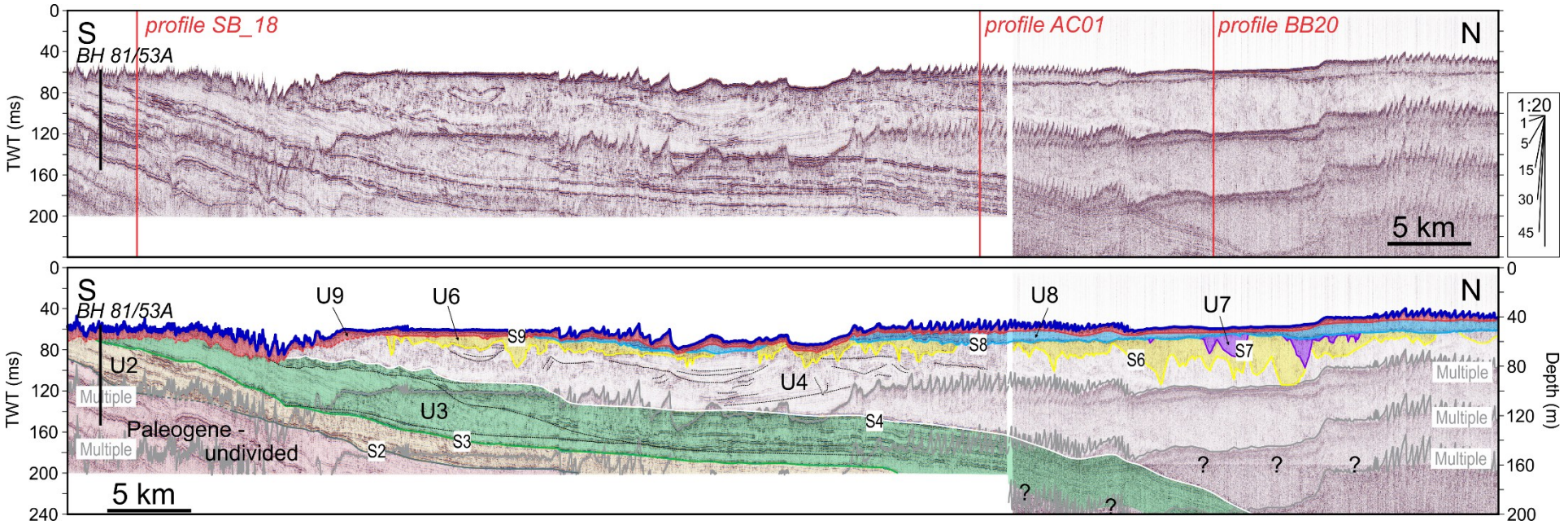


Figure 4-4. S-N oriented sparker line BB01-AC06 with projected BGS borehole BH 81/53A; for location see Figure 4-1.

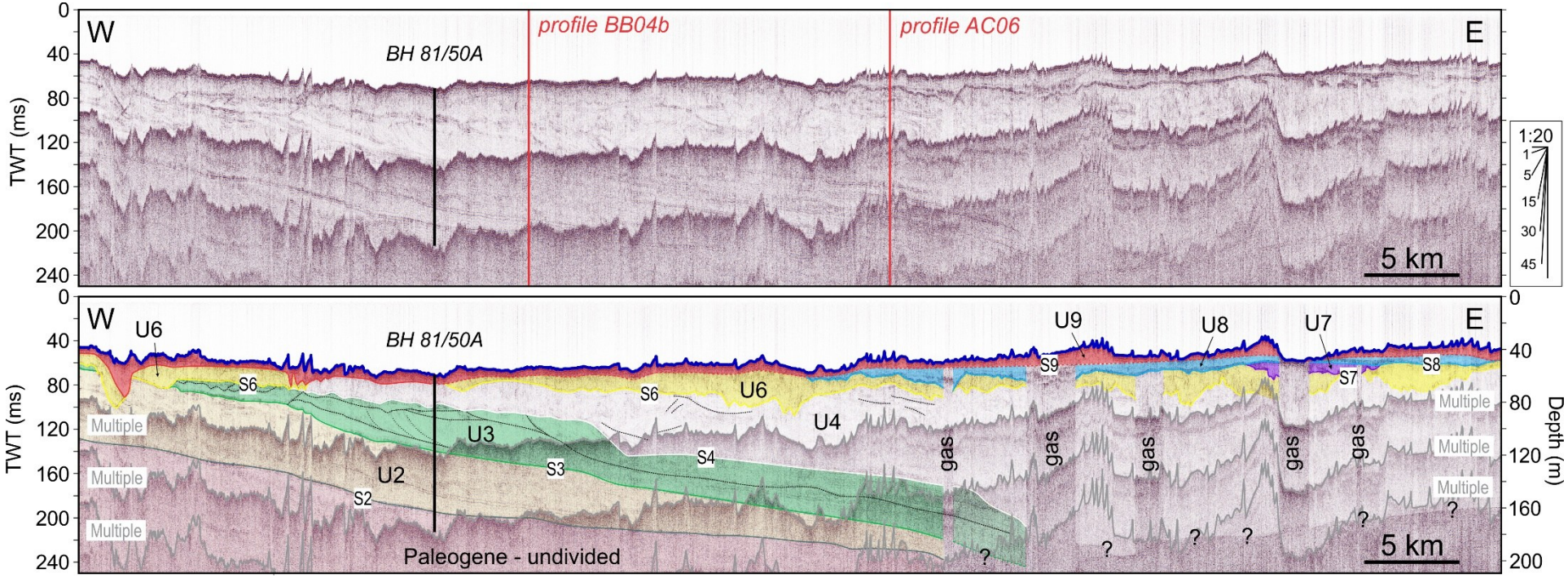


Figure 4-5. W-E oriented sparker line AC01 with projected BGS borehole BH 81/50A; for location see Figure 4-1.

an incision (1.5-2 km wide), with very steep flanks (c. 40°) that disappear under the seabed multiple, masking the unit's base (Figure 4-3; Figure 4-11e). The unit appears as an upstanding feature (Figure 4-3) but could represent the infill of an incision as well, as the base could not be identified. Nonetheless, the similarities between the structureless seismic facies have led us to correlate these as belonging to the same unit. Stratigraphically, the unit is placed between the older U4 (interpreted as the Yarmouth Roads Formation) and the younger U6. The unit has not been reached by any of the available boreholes, preventing us from proposing a stratigraphic interpretation.

Unit 6 (U6): In the eastern part of the study area, U6 is characterised by a predominantly transparent seismic facies, but locally displaying more chaotic configurations and some high-amplitude reflections (Figure 4-3 to Figure 4-7). The unit overlies S6, an erosional surface characterised by incisions of variable depth (tens of m) and width (hundreds of m) (e.g. Figure 4-3 to Figure 4-6; Figure 4-9). Towards the top of U6, a more complex, multi-phased cut-and-fill facies is present. This pattern is especially common in the north(east), where the unit becomes thicker (~40 m) (Figure 4-8, also visual on Figure 4-3). In the west, S6 is expressed as a medium-high amplitude reflection, eroding into U2, U3 (in the south) and U4 (towards the north) (e.g. Figure Figure 4-5; Figure 4-6). Here, U6 consists of multi-phase infill, with seismic facies that vary from subparallel to chaotic. Where S6 cuts through U2 and U3, these incisions are up to 25 m deep (see Section 4.4.3; Figure 4-11f). The top boundary is a clear, very-high-amplitude reflection (S8) in the east. In the centre, where U6 is directly overlain by Unit 9 (U9), S9 forms the top boundary. In the west, U6 is eroded by a very-high-amplitude reflection, interpreted as S9 as well. Where U7 is present, U6 is incised by surface S7.

In BGS borehole BH81/50A, the unit is described as Middle to Upper Pleistocene fining-upwards, grey-green, mica-rich, sandy silt to clay (BGS, 2026c). This description does not give a clear indication to which southern North Sea formation this unit belongs. However, judging from the erosional character of S6 and the seismic character of the unit, together with its geographical occurrence, we suggest that S6 and the deposits of U6 are of possible sub- and proglacial origin. Stratigraphically, this unit is younger than U4 and U5, as S6 erodes into U4 and U5, but older than the incisions of U7. The erosional surface S6 might have been formed subglacially during the Elsterian glaciation. However, as the sediments of U6 do not seem to be deformed but just display a complex facies, they were probably deposited after the Elsterian ice had receded northwards. The interglacial Holsteinian deposits (Egmond Ground Formation) and the Saalian pro- and periglacial sediments (Cleaver Bank and Tea Kettle Hole Formations) are likely candidates, although none of these formations have previously been described in the study area. They are, however, known to occur further north (Cameron et al., 1992).

Unit 7 (U7): Unit 7 is a highly discontinuous unit, present only in the central and eastern part of the study area. It consists of mostly dispersed incisions, reaching an infill thickness of up to ~40 m (Figure 4-3 to Figure 4-6; Figure 4-8; Figure 4-9). The infilling facies varies from divergent to multi-staged (see Section 4.4.3; Figure 4-7; Figure 4-11g). The reflections within U7 display mostly medium to high amplitudes and medium to high frequencies. The lower boundary S7 is discontinuous and can be marked by a clear reflection or by a distinctive horizon eroding the underlying sediments (U6, U5 or U4). The top boundary of U7 is marked by a very high-amplitude reflection (S8) that truncates the underlying infill structures. U7 is not reached by any boreholes. Judging from the geographical position (only in the central and eastern sector), and knowing that this unit postdates the deposits from U6, we tentatively relate these incisions to the late Saalian glacial period (Drenthe glacial; MIS6). As the incisions of U7 are located 30-50 km from the late Saalian maximum ice margin (Figure 4-9), they could be related to depositional systems in the associated periglacial outwash plain. The sediments infilling the incisions may relate to this glacial phase, therefore linking them to the Cleaver Bank and Tea Kettle Hole Formations. They could also relate to the ensuing interglacial Eemian phase, i.e. the Eem Formation, or a combination of both. This latter could explain the observed multiple infilling stages.

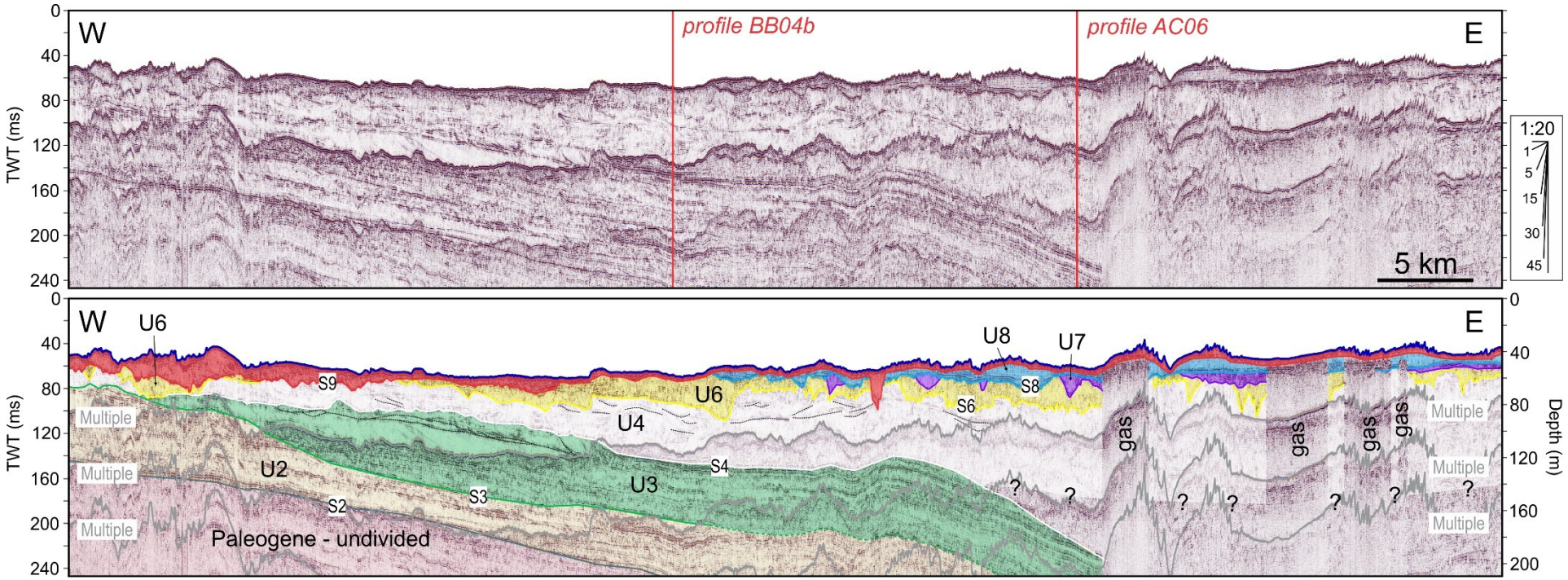


Figure 4-6. W-E oriented sparker line BB20; for location see Figure 4-1.

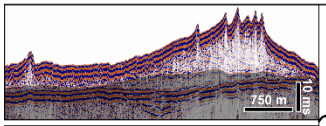
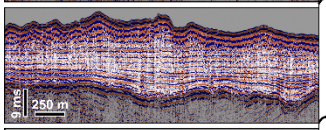
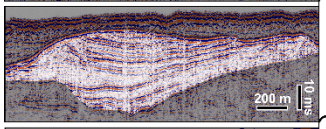
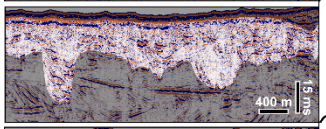
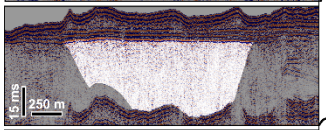
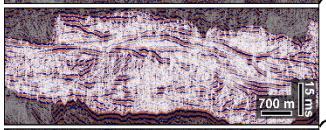
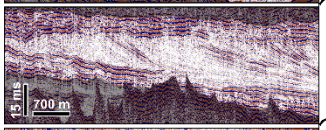
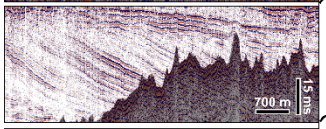
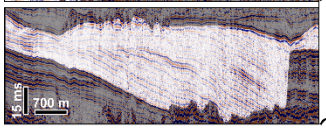
	Unit	Basal surface	Continuity / conformity	Amplitude	Frequency	Configuration	Lower reflection terminations	Upper reflection terminations	Interpretation
	U9		Discontinuous	Low	Low	Mostly transparent	Onlap / conformable ?	Seabed	Middle Weichselian to Holocene deposits
	?	? S9	Unconf.	Low					
	U8		Continuous	High	High	(sub-) Parallel	Conformable?	Conformable/ truncation?	Lower Weichselian deposits (Brown Bank Formation)
		S8	Unconf.	Very high					
	U7		Discontinuous	Medium to high	Medium to high	Divergent	Onlap	Truncation	Middle to Upper Pleistocene glacial (late Saalian) and/or interglacial (Eemian) deposits
		S7	Unconf.	Low to high					
	U6		Discontinuous	Low to high	Low to high	Mostly transparent to chaotic	Onlap	Truncation	Middle Pleistocene glacial (Elsterian/early Saalian) and/or interglacial (Holsteinian) deposits
		? S6	Unconf.	Low					
	U5		Discontinuous	Low	Low	Transparent	/	Truncation?	Middle Pleistocene glacial (Elsterian) deposits
		? S5	Unconf.	Low to High					
	U4		Discontinuous	Medium to high	Low to high	Complex (multiple facies)	Mostly onlap	Truncation	Lower to Middle Pleistocene (Yarmouth Roads Formation)
		S4	Unconf.	Medium					
	U3		Discontinuous/ continuous	Low to high	Low to high	Parallel to Sigmoidal	Proximal downlap, distal conformable	Truncation	Lower Pleistocene deposits (Smith's Knoll / IJmuiden Ground Formation)
		S3	Unconf.	High					
	U2		Continuous	Medium	Medium	Sigmoidal to tangential oblique	Downlap	Truncation	Lower Pleistocene deposits (Westkapelle Ground Formation)
		S2	Unconf.	Medium					
	U1		Continuous	Medium to high	Medium	Divergent to transparent	Onlap/ downlap	Truncation	Upper Pliocene to Lower Pleistocene deposits (Red Crag Formation)
		S1	Unconf.	Medium					

Figure 4-7. Overview of the seismic character of the seismic-stratigraphic classification derived from the sparker data.

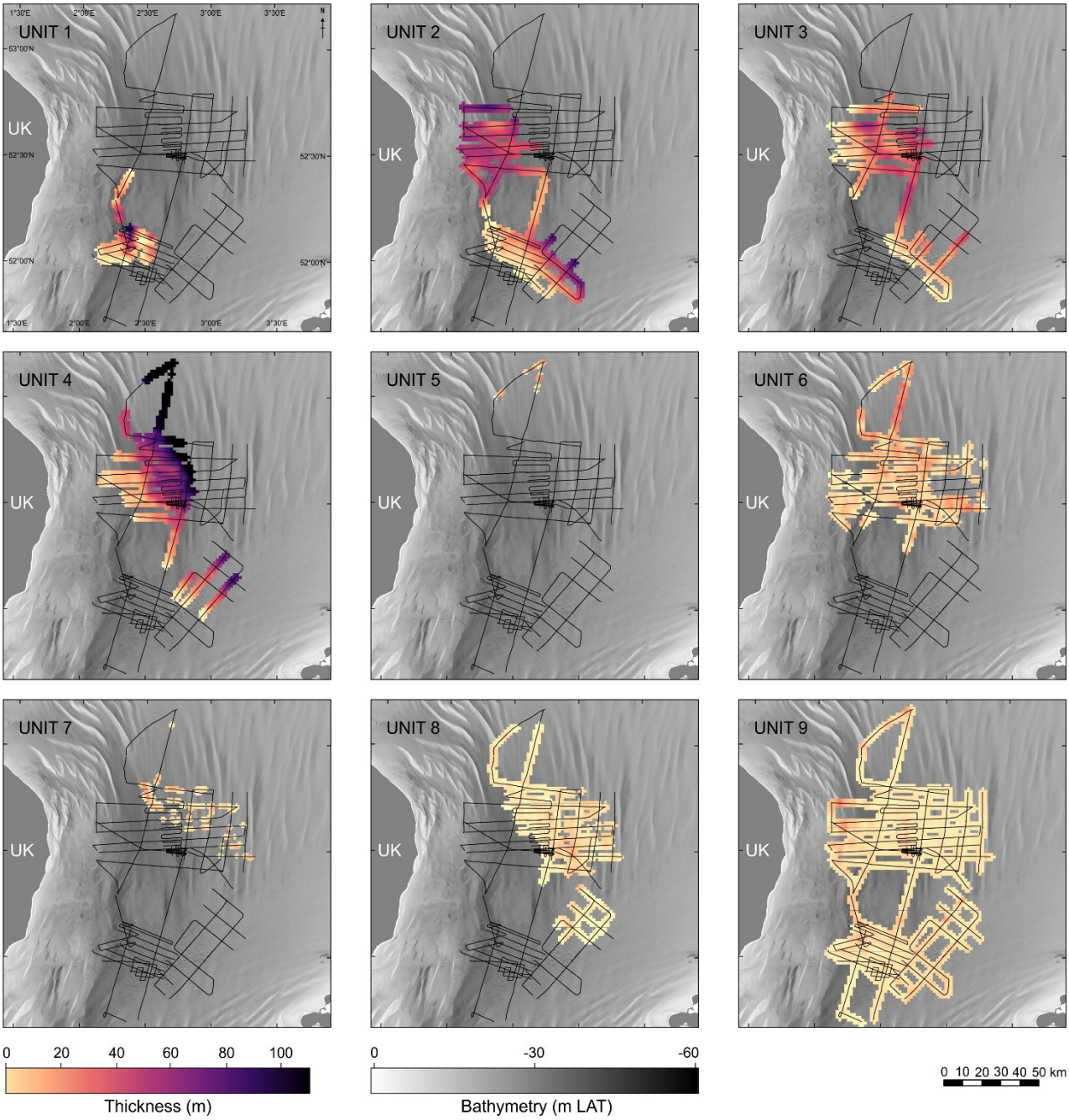


Figure 4-8. Maps showing distribution and thickness of all identified units (Unit 1-Unit 9) along the seismic profiles (black lines) in the study area.

Unit 8 (U8): In the sparker profiles, U8 is markedly thinner than the underlying units (Figure 4-3 to Figure 4-6). It is usually not much thicker than 5 m, but some lows in the typical irregular underlying topography (S8; Figure 4-9) are filled with up to ~20 m of U8 (Figure 4-8). The unit is widespread from the centre to the (north)east (Figure 4-8; Figure 4-9). The seismic facies varies from (sub)parallel, high-amplitude and high-frequency reflections to transparent intervals (Figure 4-7). The unit displays an overall increase in thickness towards the (north)east, however, in the latter area acoustic blanking is commonly observed (Figure 4-5; Figure 4-6). The base of U8 is defined by the very-high-amplitude reflection S8. This reflection sits c. 10 m deeper in the central part of the study area compared to the eastern part (Figure 4-9). The top of the unit is defined by the less distinct, medium- to low-amplitude reflection S9. Where the unit is thinner than 2 m, the sparker data cannot resolve the unit well. Here, S8 and S9 become a composite set of near-parallel, low- to medium-amplitude reflections.

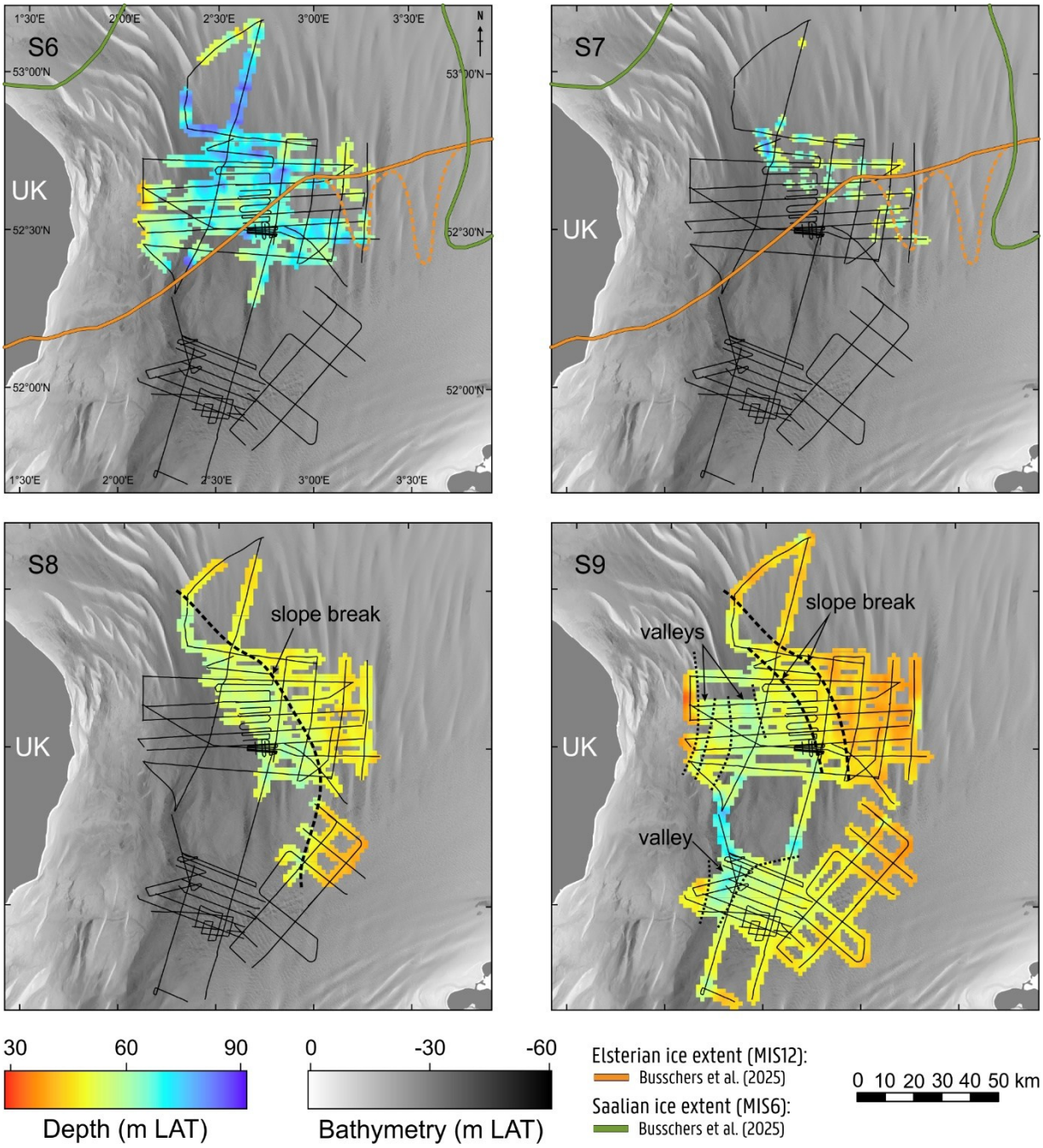


Figure 4-9. Depth structure maps of different identified Middle to Upper Pleistocene surfaces (S6-S9) in m LAT. The surfaces are plotted along the seismic profiles (black lines) and superimposed on the present-day bathymetry. Interpretations of valleys (black dotted lines) and slope breaks (black dashed lines) discussed in the main text are indicated. Southern ice margins of the Elsterian (MIS12) and Saalian (MIS6) maximal ice extent after Busschers et al. (2025).

In boreholes BP040005, BP040006, BP040007 and BP130009 this unit is described as grey clay, with some admixtures of fine sand (TNO-GDN, 2026b). In BP040006, peat is present in the basal 4 m of the borehole. Even though the lithological description is very generic, in combination with the geographical occurrence and seismic architecture, the unit is interpreted as the Brown Bank Formation. The basal surface S8 can be traced further east on the Dutch Continental Shelf and correlated with the continuous horizon H1 identified by Waajen-Labee et al. (2025). Where east of the present-day sandbank, known as the Brown Bank (Figure 4-1b), four different subunits were identified (Waajen-Labee et al., 2025), the overall lower resolution in the top 10-20 m of the sparker data used in our study does not allow us to make that distinction. The sediments of the Brown Bank Formation have been correlated with the MIS5-4 transition (Waajen et al., 2024; Waajen-Labee et al., 2025).

Unit 9 (U9): This uppermost unit lies just underneath the seabed and is present throughout the whole study area (Figure 4-2 to Figure 4-6; Figure 4-8). U9 is mostly acoustically transparent, locally showing continuous, sub-horizontal reflections (Figure 4-7). In the western sector, however, where S9 erodes the underlying units (U2, U3, U4, U6), U9 displays a complex infilling facies, with medium-amplitude and medium-frequency reflections. Where sand waves occur as part of U9, internal reflections are inclined (< 1°). The basal unconformity (S9) is not distinct in the sparker data, largely due to the limited vertical resolution of the source and the relatively thin nature of the unit (generally < 5 m). Only in the western and southern sector, where U9 is directly overlying the oldest units (U1, U2, U3, U4), S9 is recognised as an irregular, erosional, high-amplitude reflection. Here, the unit can become up to 25 m thick (Figure 4-2; Figure 4-8). In the central and northern areas, S9 incises the underlying unit U8 (and U6 and/or U4), with one incision that can be traced over multiple profiles (see Section 4.4.3; Figure 4-11h). The top of the unit is the present-day seafloor. In the west, it truncates the internal reflections of U9. U9 is described in almost all borehole data as yellow-brown, medium to coarse sand with shell fragments and locally some gravel mixed in. The seismic character and stratigraphic position of this unit, together with the generic lithological description, suggest a late Weichselian (post MIS4) to Holocene age for these deposits.

4.4.2 Revised geological map

Based on the updated seismic stratigraphy and on the occurrence of the different units, their thicknesses (Figure 4-8) and bounding surfaces (Figure 4-9), the regional geological map was revised (Figure 4-10b). In the southernmost part of the study area, we identified the pre-Quaternary (Palaeogene – undivided) unit. The pre-Quaternary strata are overlain by U1 in the west. Towards the east, they are directly overlain by U2. From the centre towards the north(east), units become progressively younger (U1-U8). Both U5 and U7 are more localised units, found in the north and northeast, respectively. The latter is identified in areas where it is covered by U8 and does therefore not appear on the map. In the west, unit U6 covers older units (U2-U4). Due to the wide spacing of the seismic lines, there remains an uncertainty on the exact position of the units' boundaries. Especially for the central area, where data are lacking, the uncertainty of the mapped units U2, U3, U4 and U6 is high and will need to be improved by the acquisition of additional data.

4.4.3 Incisions and channel features

The presence of large, regionally traceable channels, incisions and valley-like structures is apparent in several of the identified units (Figure 4-11a, see also Section 4.4.1). Here, we describe these features in more detail in stratigraphical order and group them into different generations. Actual feature depths are reported relative to the upper bounding surface of the unit in which they occur and in metres below LAT (m LAT).

Generation A: The basal unit (U1) consists of a complex of large (≥ 40 m deep) infilled incisions. On our data, four different cut-and-fill phases could be identified (labelled i to iv Figure 4-2; Figure 4-11b) and mapped (Figure 4-11a), displaying a north(west)-south(east) orientation. Both incision (i) and (ii) are cut by incision (iii), which in turn is cut by incision (iv) (Figure 4-2; Figure 4-11a, b). Their length and width vary: c. 21.5 km by 12.5 (iv), c. 16.2 km by 11.0 km (iii), c. 28.9 km by 17.7 km (ii) and c. 13.9 km by 6.2 km (i). On the profiles, incision (iii), (ii) and (i) are characterised by a steeper eastern flank (0.4°) and a more gradual western flank (<0.2°) (Figure 4-11b). All incisions deepen in a north-northwestern direction (arrows Figure 4-11a). Incision (iii) is the deepest, measuring up to 52 m deep (c. 119 m LAT); while (iv) is up to 40 m (c. 115 m LAT), (ii) 45 m (c. 153 m LAT) and (i) 47 m (c. 106 m LAT) deep. Incision (iv) is characterised by a complex fill facies (Figure 4-2), while the other incisions display a prograding facies (Figure 4-2; Figure 4-11b). The frequency and amplitude of the reflections differ between incision (iii), (ii) and (i). Incision (iii) has the highest-amplitude reflections but a lower frequency

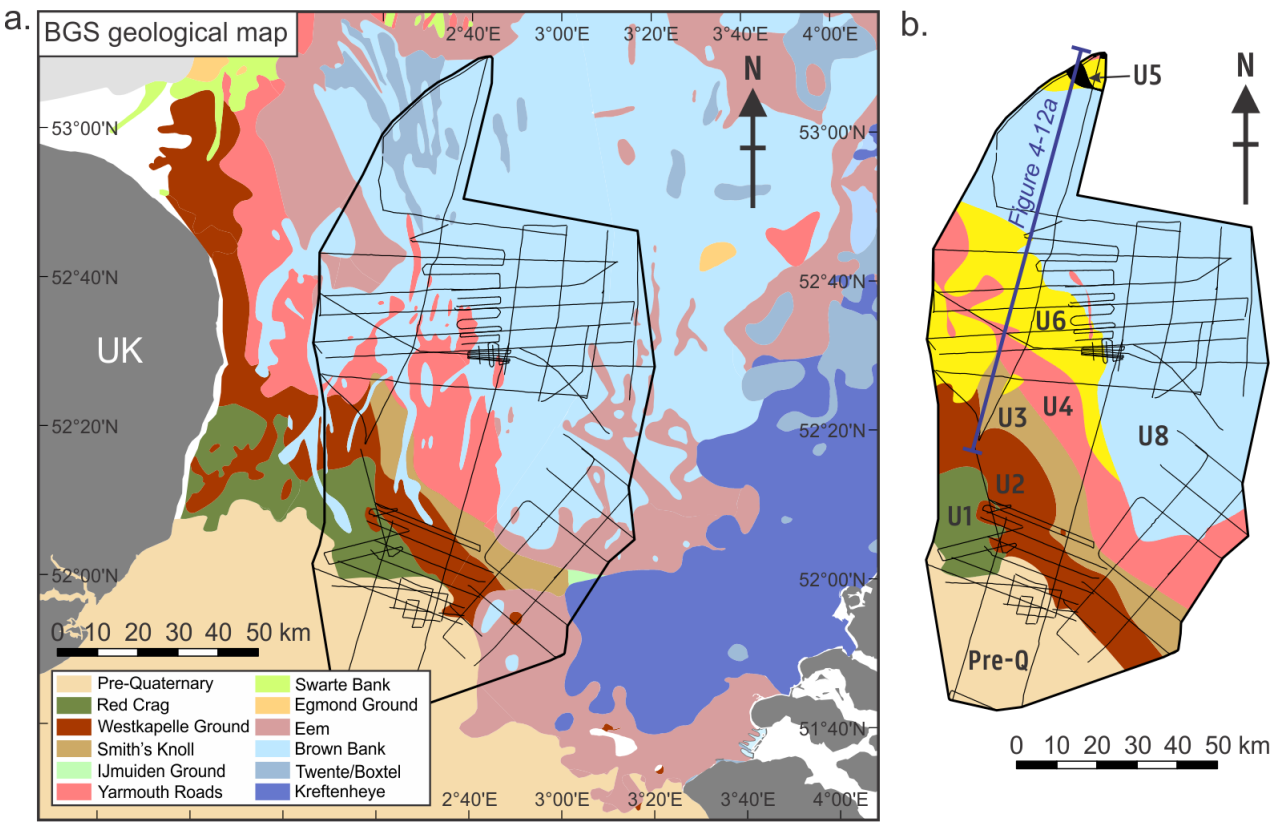


Figure 4-10. Geological map of the study area (a) compiled from Balson & D'Olier (1990); Cameron et al. (1984); Harrison & Hopson (1991) and Laban et al. (1992) and published by the British Geological Survey (BGS, 2000), Holocene sediments not included; (b) based on our data, U9 not included. Black lines represent the location of seismic data from this study. Profile for the synthetic cross-section (Figure 4-12a) is indicated.

compared to (ii) and (i). The reflections of incision (i) have a lower amplitude compared to (ii). The differences in seismic facies point to a dynamic progradational system, indicating a changing sediment input and/or sea level. U1 has been correlated with the Red Crag Formation (see Section 4.4.1), therefore assigning these incisions a Late Pliocene to Early Pleistocene age. The location, similar prograding facies and geomorphology of the Murray Pit (Figure 4-11a, c; see Section 4.4.1), alongside the fact that it erodes the underlying Paleogene strata similar as incisions (i) to (iv), could indicate that this feature is part of the same generation of incisions.

Generation B: The second generation comprises the valley structures identified within U4. In the centre of the study area, a channel belt with different infill phases can be traced over c. 50 km (light grey; Figure 4-11a), displaying a northwest to southeast orientation. Owing to the limited seismic grid, the channel belt cannot be traced further north- or southwards. This c. 15 km wide and up to c. 40 m (c. 85 m LAT) deep channel belt shows at least nine phases of incision and infill at the location of its mapped southern end (Figure 4-11d). The seismic facies for the different infill sequences range from prograding or divergent to complex or even structureless. Towards the north it becomes harder to distinguish the different phases, and only the eighth phase can be confidently traced northwards. A drainage direction cannot be inferred as there are no clear longitudinal changes in the depth of the incisions. This channel belt likely represents a large, dynamic fluvial system, in line with the interpretation of U4 as the Yarmouth Roads Formation (see Section 4.4.1).

Generation C: Two separate incisions are identified as part of U5 (dark grey; Figure 4-11a). Both incisions have a transparent seismic facies and steep slopes (> 10°) that disappear underneath the multiple (Figure 4-11e). Figure 4-11a shows the occurrence of these incisions in the northernmost sector of our dataset. Owing to the limited seismic data in this part of the study area, no further characteristics (length, orientation) can be determined. One of these incisions may be linked to

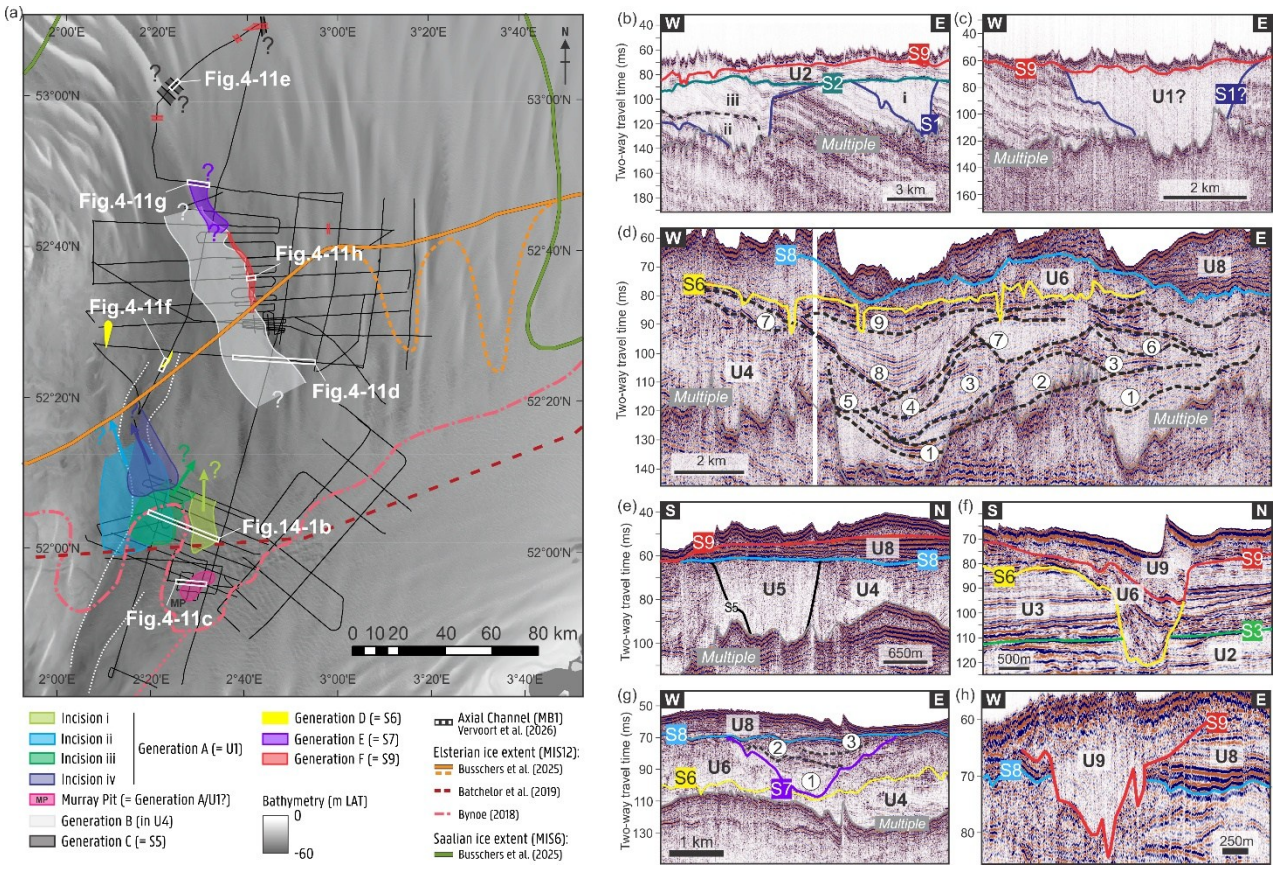


Figure 4-11. (a) Mapped extent of different generations of incisions discussed in the main text superimposed on the present-day bathymetry. Interpretation of the Axial Channel main branch (white dotted lines; Chapter 3). Maximum extent the Elsterian (MIS12) and Saalian (MIS6) ice margin after Batchelor et al. (2019); Busschers et al. (2025) and Bynoe (2018). Examples of the different incisional generations (location indicated in a): (b) Generation A (U1), incisions i, ii and iii; (c) Murray Pit (possibly part of generation A); (d) Generation B (complex channel belt in U4), showing nine different phases of cut and infill; (e) Generation C (S5); (f) Generation D (S6), deep incisions eroding U2 and U3. (g) Generation E (S7); (h) Generation F (S9).

similar features that were identified in the area by Eaton et al. (2020), which were correlated with the Elsterian (MIS12) (see also discussion Section 4.5.2).

Generation D: In the western sector deep incisions at the base of U6 (S6) are identified that erode U2 and U3, where these units lie close to the seabed, and U4 (most southerly section of Figure 4-3 and most westerly section of Figure 4-5; yellow; Figure 4-11a). They have a north(east)-south(west) orientation and are situated in the branches of the present-day Axial Channel (Chapter 3; Figure 4-11a). The westernmost incision is up to 1.8 km wide and c. 20 m deep (c. 80 m LAT) U-shaped feature cutting through U2 (Figure 4-5). Its infill shows a chaotic seismic facies, in which some high-amplitude reflections can be discerned. The second incision, located further to the southeast, has a similar morphology. It is just over 1 km wide and c. 25 m deep (c. 97 m LAT). It erodes the underlying units U2 and U3 (Figure 4-3; Figure 4-11f). Here two infilling facies can be identified, a basal chaotic facies and a more parallel facies in the top part of the infill. They are separated by a high-amplitude reflection. As hypothesised in Section 4.4.1, S6 could be related to the Elsterian glacial phase (MIS12). The U-shape geometry and the location of the incisions in relation to the maximum ice extent (Figure 4-11a) would further support an Elsterian (sub)glacial origin.

Generation E: The fifth generation of incisions, occurring as dispersed incisional remnants, is present at the base of U7 (S7). In the north, one incision can be traced over multiple seismic profiles in a northwest-southeast orientation, that is seen cutting through U4, U5 and U6 (purple; Figure 4-11a). This c. 13 km long feature is up to 37 m deep (c. 95 m LAT) and c. 5 km wide. Three different infilling

phases are identified (Figure 4-11g). The basal infill consists of parallel draped, medium- to low-amplitude reflections onlapping onto the basal reflector (S7). The second infill is more chaotic, while the third is a prograding to divergent infill, truncated by S8. As described in Section 4.4.1, based on both the stratigraphic position and geographical spread, the generation E incisions could be of late Saalian age (Drenthe glacial; MIS6).

Generation F: The final generation of incisions is identified at the base of U9 (S9). In the centre, a c. 22 km long incision can be traced over multiple profiles (red; Figure 4-11a). This incision is 1.5 km wide and reaches depths of up to 18 m (c. 70 m LAT) in the centre. Towards both the northern and southern end, this incision becomes shallower and narrower, to the point where it can no longer be identified in the seismic profiles. It has a general V-shape with a highly irregular base (Figure 4-11h). The infill is either acoustically transparent (Figure 4-11h) or displays a subparallel onlapping pattern with low-amplitude reflections. Apart from this traceable incision, multiple dispersed incisions (widths of c. 0.3-2 km and depths of c.10-20 m), mainly in the northern and one in the eastern sector, are identified at the base of U9 (Figure 4-11a). The northernmost incision (Figure 4-11a) displays a general U-shape, with prograding infilling reflections, whereas other incisions display a chaotic to complex facies. The incisions of generation F are stratigraphically the youngest system, cutting through units U8, U6 and/or U4. As the incisions cut through U8, which we interpreted as Brown Bank Formation (see Section 4.4.1), their infill must post-date these deposits, placing them within late MIS4 and/or subsequent times.

4.5 Discussion

The seismic data presented in this study enabled a detailed description and analysis of the stratigraphic units composing the subsurface of the Southern Bight. By revealing one Upper Pliocene and eight Quaternary depositional units, partially constrained by extant borehole data, the new set of sparker data supports and allows for a refining of the regional-scale depositional environment. These units comprise: Late Pliocene open marine, and near coastal tidal deposits (U1); Lower Pleistocene marine deltaic sediments (Southern North Sea Deltaic Group; U2 and U3); Lower Pleistocene deltaic to fluvial deposits of the Yarmouth Roads Formation (Dunwich Group – U4); Elsterian and/or lower Saalian sub-, pro- and periglacial sediments with possible interglacial late-infilling stages (U6); (upper) Saalian infilled incisional remnants with possible interglacial late-infilling marine sediments (U7); middle Weichselian shallow-marine sediments of the Brown Bank Formation (U8); and upper Weichselian and Holocene fluvial and sediments (U9). A detailed discussion on the relevance and implications of our updated interpretations of the nine units and associated basal unconformities is presented in the following sections. It highlights matches and mismatches with the current stratigraphic frameworks of the southern North Sea (Busschers et al., 2025; Dakin et al., 2026; Rijsdijk et al., 2005; Stoker et al., 2011).

4.5.1 New light on the Upper Pliocene to Middle Pleistocene stratigraphy (U1-U4)

Both the Upper Pliocene sediments of U1 and Lower Pleistocene sediments of the Southern North Sea Deltaic Group (U2, U3) are described in unprecedented detail. While their lithofacies, fossil content and correlation with onshore deposits have been the subject of multiple studies (Cameron et al., 1992, and references therein), their seismic configurations have only been described previously by Cameron et al. (1989) through lower resolution systems, and updated for the NL sector by Hijma et al. (2012). The higher resolution sparker data presented here provide new insights into the seismic facies and geometry of U1, interpreted as the Red Crag Formation (Table 4-1). This seismic unit was originally described as dominated by low-amplitude reflections, inclined towards the NE and resting in a single broad trough (Cameron et al., 1992, 1989). We identified four different incisions (assigned to generation A; i-iv), with different (locally multiple) seismic facies. Existing lithological descriptions of

the deposits of U1 (BGS, 2026b; 2026a) demonstrated that the infill represents a period during which a marine environment dominated. Cameron et al. (1992) interpreted these deposits as intertidal sand-flat deposits. Our data, however, rather suggest a broad, dynamic system with multiple (inter-)tidal channels, that deepen in a northwards direction. These channels would have formed a connection to an open marine shelf located further north (Gibbard and Cohen, 2015; Gibbard and Lewin, 2016). As suggested in Section 4.4.3, the Murray Pit may also be attributed to the generation A incisions. The previously reported Early Pliocene age of these sediments is based on microfossils (Cameron et al., 1992), which may reflect sediment reworking and could cast doubt on this inferred age. Unlike the other incisions of generation A, the Murray Pit is an enclosed feature. In an earlier study, one of the proposed formational processes was tidal scouring (Liu et al., 1993), which is in-line with the tidal environment interpreted for the incisions of generation A.

The sparker data further show the seismic character of U2 and U3. The observed seismic patterns linked to delta-top and, in a broader sense, progradational environments are in line with previous interpretations about the depositional environment of the Westkapelle Ground (U2) and Smith's Knoll/IJmuiden Ground (U3) Formations (Table 4-1). These reflect the progressive northward migration of the coastline during the Late Pliocene to Early Pleistocene. Though interrupted undoubtedly by some phases of stability or slight southward migration, this long-term process was characterised by the development of large deltas with sediment supply from Great Britain (Thames) and the Netherlands (Rhine-Meuse) (Busschers et al., 2025; Cameron et al., 1992; Gibbard and Cohen, 2015; Gibbard and Lewin, 2016; Hijma et al., 2012). In our dataset, especially in the west, the prograding reflectors of U3 appear steeper than those of U2. We tentatively interpret this difference in configuration as an indication for an alteration in sediment supply from the British sector into the southern North Sea at the transition between U2 and U3. This change was either caused by a change in sediment source, speed of sediment flux or sea-level position. Nevertheless, the correlation of U3 to the Smith's Knoll Formation matches with previous interpretations. This formation represents a sediment flux from mainly onshore Great Britain (Thames) that changes laterally to the Ijmuiden Ground Formation, representing a main sediment flux from the Netherlands (Rhine-Meuse) (e.g. Cameron et al., 1992). Our mapping of the pre-Quaternary and U1-U3 compares relatively well with the compiled map from BGS (Figure 4-10; BGS, 2000).

U4, identified in the study area above the deltaic deposits of U2 and U3, is interpreted as the Lower to Middle Pleistocene Yarmouth Roads Formation (Table 4-1). The clear difference in seismic character between U2/U3 and U4, from NE-dipping prograding reflections to sub-horizontal discontinuous reflections and evidence of numerous channels (generation B), can now be placed in the broader depositional context. The deposits of the Yarmouth Roads Formation span a long period of time; from the Early Pleistocene Calabrian to the Middle Pleistocene Cromerian (Busschers et al., 2025; Stoker et al., 2011). The formation captures a temporally and spatially variable response to alternating sedimentation and erosion. It includes evidence of increasing glacial-interglacial climate oscillations and resulting sea-level variations (Gibbard and Cohen, 2015; Gibbard and Lewin, 2016; Hijma et al., 2012). Overall, shorelines had shifted further north/northwestward as the deltaic complexes prograded (including U2, U3) and infilled the southern North Sea Basin (Gibbard and Cohen, 2015; Gibbard and Lewin, 2016), turning the study area into a low lying terrestrial landscape where fluvial systems prevailed. This is also reflected in our dataset. The lowermost part of U4 may represent an extension of the delta system (and may include the Winterton Shoal Formation), progressively infilling the underlying topography towards the (early) Cromerian (visible on Figure 4-4, otherwise masked by the seabed multiple). These developments created a relatively flat, low-lying landscape. The preserved channel belt (generation B) at the top of U4 is considered evidence of a long-lived braided channel system, confirming the long-term overall change to a fluvially dominated environment at the end of the Cromerian. No drainage direction of the channel belt could be established from our data as no gradient was identified. However, with the Weald-Artois still forming a barrier separating the study

area from the English Channel and the Atlantic Ocean in the south at that time, the main drainage direction would have been northward, towards a North Sea located relatively far (and more northwards) at that time (Gibbard and Cohen, 2015; Gibbard and Lewin, 2016; Hijma et al., 2012). Our mapping of U4 compares well with the compiled map from BGS in the eastern and central area. In the western area we have identified U6 covering the Lower Pleistocene deposits of U2 and U3, implying a remarkable absence of U4 (Figure 4-10; BGS, 2000) (see Section 4.5.2). U4 may have been subsequently eroded, which can be explained by limited vertical accommodation space, which restricted the development of deposits of sufficient thickness to ensure their long-term preservation.

4.5.2 Deposits of the Middle to Upper Pleistocene (U5-U7)

Previously identified and mapped formations in our study area suggested a depositional hiatus between the final Cromerian (MIS13) and the Eemian (MIS5e). Stratigraphically, this means that the Yarmouth Roads Formation would be directly overlain by the Eem and Brown Bank Formations (Figure 4-10a; Cameron et al., 1984; Laban et al., 1992). In this study, however, we identified three different units that postdate the deposits of the Yarmouth Roads Formation (U4) and predate the Brown Bank Formation (U8), i.e. U5, U6 and U7. This ultimately changes the idea of a long-term depositional hiatus between MIS13 and MIS5e. Their mapped extent therefore marks a major difference compared to the existing geological map (Figure 4-10b; . These units were previously most likely interpreted as part of the Yarmouth Roads Formation, which explains the difference in thickness described in literature (160-180 m; Cameron et al., 1992) compared to the thickness we derived in this study (c. 100 m) for the Yarmouth Roads Formation. New (albeit saturated) OSL ages of >268 ka for deposits directly overlain by the Brown Bank Formation were published by Waajen-Labee et al. (2025) that further highlight the depositional hiatus. However, it is not clear from said publication which of our identified units (U6 or U7) this age correlates to.

U5 is a structureless unit occurring in the northernmost sector of our study area. Only in the Norfolk Vanguard OWF (polygon 2; Figure 4-1b), a unit with similar structureless facies is described. It was reported to be confined to large linear features and interpreted as the infill of tunnel valleys, attributed to the Swarte Bank Formation (Eaton et al., 2020; Wessex Archaeology, 2017). Owing to the limited seismic lines in this part of our study area, it was not possible to determine whether the two incisions (generation C) are part of larger, linear valley systems. One of the tunnel valleys identified by Eaton et al. (2020) can be extrapolated further north, where it connects to one of the identified incisions of generation C. This would indicate that these features are indeed linear subglacial tunnel valleys, justifying the attribution of this unit to the Swarte Bank Formation (MIS12).

All OWFs in the study area (polygons 1-5; Figure 4-1b) have identified the Yarmouth Roads Formation (Wessex Archaeology, 2018a; 2018b; 2018c; 2017; 2014), but some have identified younger phases at the top of and eroding into the Yarmouth Roads Formation (Wessex Archaeology, 2014; 2018a). These features, however, are not differentiated as a separate unit/formation due to insufficient penetration of seismic systems, lack of ground-truthing and/or chronological constraints. In the East Anglia THREE site (polygon 3; Figure 4-1b), these channel features were given a broad age range, i.e. sometime between the Late Elsterian and the Eemian (Wessex Archaeology, 2014). We suggest they could be linked to U6 or U7 identified in our study area.

Within our study we clearly see an erosional surface (S6) cutting into U4 (Yarmouth Roads Formation). Following the Cromerian Stage, major climatic changes occurred during the Middle to Early Pleistocene, with the British and Fennoscandian ice sheets expanding and merging into the North Sea during multiple glacial phases (MIS12-10-8-6). The exact maximum extents of the Elsterian (MIS12) and Saalian (MIS10-6) ice sheets are, however, still largely speculative. Over the past decades, this has resulted in the publication of a number of different reconstructions of these maximum extents

(e.g. Batchelor et al., 2019; Bynoe, 2018; Cartelle et al., 2021; Eaton et al., 2020; Graham et al., 2011). Within our study area, the Elsterian ice margin is thought to have been located across the northern and northwestern sector (Figure 4-1a). Based on the stratigraphic position as well as the geographic occurrence of S6, we suggest that the erosional surface S6 is related to the Elsterian (MIS12) glacial phase (Figure 4-9).

A further indication of an Elsterian age is the presence of deep incisions of S6 (generation D, yellow; Figure 4-11a, f) that erode into U2 and U3 in the western part of the study area, which we interpret as having a (sub)glacial origin. Their U-shape geometry and (basal) infill, showing a chaotic facies, are two typical characteristics of subglacial tunnel valleys (e.g. Huuse and Lykke-Andersen, 2000; Kristensen et al., 2007; Praeg, 2003). The location of these generation D incisions matches well with the position of the maximum Elsterian ice sheet extent (Figure 4-11a; Batchelor et al., 2019; Busschers et al., 2025). It also matches well with the redrawn limit from Bynoe (2018) (Figure 4-11a), which is based on the position of the Inner Gabbard Deeps (located west of our study area; Figure 4-1b). The Inner Gabbard Deeps are located c. 60 km south/southwest of the generation D incisions from this study and were previously interpreted as shallow subglacial tunnel valleys related to the Elsterian glacial phase (Chapter 3; Bynoe, 2018; Dix and Sturt, 2011). The orientation and depths of the Inner Gabbard Deeps (21-24 m deep and NNE-SSW- oriented; Chapter 3) are very similar to the generation D incisions (c. 20-25 m deep and N-S orientation), strengthening their interpretation as subglacial features. If the incisions of generation D are indeed tunnel valleys, they would be the southernmost buried tunnel-valley-type features in the southern North Sea. However, as the incisions of generation D have much smaller dimensions than the tunnel valleys identified further north (e.g. Eaton et al., 2020; Praeg, 2003), it is also possible that they formed in a proglacial environment as meltwater drainage systems fed by the ice front. The parallel infilling facies identified in the eastern incision could in this scenario represent a post-glacial depositional system on an outwash plain. If S6 is indeed related to the Elsterian glacial phase, the deposits of U6 could then be correlated with the Swarte Bank Formation (Table 4-1). This means that, aside from extensive subglacial valley systems north of the study area (e.g. Eaton et al., 2020; Praeg, 2003) and in our northernmost sector (U5, generation C), other (albeit smaller) valley systems further south are included. This suggest that the Swarte Bank Formation is a geographically more extensive and complex formation than previously thought. Interglacial sediments related to the Holsteinian phase (Egmond Ground Formation; Table 4-1) could also be part of U6, especially in the northeastern sector, where the unit becomes thicker and multi-phased infills are observed. We note that deposits related to the early Saalian (MIS10 or even MIS8) could also be part of U6. However, as there are large uncertainties on the ice-sheet reconstructions and limits in the southern North Sea during MIS10 or 8 (e.g. Batchelor et al., 2019), significant doubt remains regarding the depositional environment at that time.

U7 has been classified as a separate unit because the incisions (S7; generation E) and associated infill that outline and make up this unit show a distinctly different seismic character compared to the incisions and cut-and-fills from both U4 and U6. U7 generally has a clear reflection at the base, shows higher-amplitude internal reflections and is always truncated at the top by S8. As the base of the incisions is observed to have eroded into U6, which is tentatively interpreted as having an Elsterian age, we suggest that U7 could be attributed to the late Saalian (Drenthe glacial) and/or subsequent interglacial phase (i.e. Eemian). The numerous dispersed channel remnants and their proximity to the Saalian (MIS6) maximum extent (Figure 4-9) are a further indication that S7 is most likely related to incisions from a late Saalian glaciofluvial outwash plain. Following this reasoning, the infilling deposits of U7 could then be correlated with Cleaver Bank and Tea Kettle Hole Formations, and/or to the Eem Formation from the ensuing Eemian interglacial (Table 4-1).

In the Norfolk Vanguard and East Anglia THREE OWFs (polygons 2-3; Figure 4-1b) similar channel features truncating the top of the Yarmouth Roads Formation were identified (Wessex Archaeology,

2018a; 2014). In these reports, it was noted how they differ in character from those observed within the Yarmouth Roads Formation. In the East Anglia THREE OWF, the channel features were found to be widespread but could not be traced between survey lines. Their seismic character was described as comprising "numerous internal subparallel reflectors" (Wessex Archaeology, 2014). One of the channels shown in this OWF report can be correlated with an incision attributed to U7 identified in our sparker data. We therefore attribute these channel features identified in the East Anglia THREE but also the Norfolk Vanguard OWF to U7. The traceable incision of S7 (Figure 4-11a, g) can furthermore be correlated with one of the incisions identified by Eaton et al. (2020) (i.e. valley V1) in the Norfolk Vanguard OWF dataset. This valley structure was interpreted as part of the Yarmouth Roads Formation (Eaton et al., 2020), but our data suggest that it could be significantly younger and be part of U7, with a potential late Saalian age.

Noteworthy is the current standing hypothesis that during the Elsterian and Saalian glacial maximum, proglacial lakes formed south of the inferred ice margins (e.g. Busschers et al., 2008; Cohen et al., 2017; Gibbard, 2007, 1995; Gibbard and Cohen, 2015; Moreau et al., 2012). In our seismic data, direct depositional evidence of such proglacial lakes is not observed, corroborating earlier observations by Cartelle et al. (2021) for the Saalian proglacial lake hypothesis. Nonetheless, the identification of U6 and U7 shows the importance of creating an updated stratigraphic framework and targeted ground-truthing in the area, as these units may contain important information to better understand those glacial phases (MIS12, 10, 8, 6) in the southern North Sea Basin.

4.5.3 New light on the Upper Pleistocene stratigraphy (U8 and U9)

On the BGS geological map, the Eem Formation is mapped in the southeastern and northwestern sector of the study area (Figure 4-10a; BGS, 2000). Based on our data, the Eem Formation is not conclusively identified in the study area but possibly present as late-infilling stages of U7 (see Section 4.4.1 and 4.5.2). Instead, where the Eem Formation is mapped on the BGS geological map, other units (mostly U4 and U6) appear in our reconstructed map (Figure 4-10b). None of the OWF reports in the study area definitively identify the Eem Formation (Wessex Archaeology, 2018a; 2018b, 2018c; 2017; 2014). Only in East Anglia THREE, an acoustically transparent unit was identified that possibly correlates to the Eem Formation (Wessex Archaeology, 2014).

The high-amplitude reflection S8 marks the base of U8, which we interpret as the Brown Bank Formation (Table 4-1). The identification of S8 and its correlation to H1 of Waajen-Labee et al. (2025) (see Section 4.4.1) allow us to trace this regional-scale erosional surface across a wider area of the southern North Sea (Figure 4-9). It is likely that S8 was formed by a large-scale erosional event that truncated the underlying Middle Pleistocene sediments. When comparing this surface to the present-day seafloor, we can see that the deepest part of S8 coincides with a similar topographic low in the bathymetry. The drop of 5-10 m (black dashed line in Figure 4-9) overlaps with the eastern limit of the present-day Axial Channel, showing the same crescent-shaped curvature (Chapter 3). This suggests that prior to deposition of the Brown Bank Formation, there was already a topographic low present in the landscape. As U7 is attributed to the late Saalian (MIS6) and U8 to the Brown Bank Formation (MIS5-4), the erosional surface S8 can be related to either that same glacial phase (MIS6), the Eemian transgression (MIS5e) or the onset of the Weichselian (MIS5d or c). Surprisingly, U8 deposits are much thinner in this deeper area compared to the area further east. We hypothesise that the sediments of U8 were originally deposited in this deeper area but have been subsequently eroded by S9. Judging from the depth structure map of S9 (Figure 4-9), this erosion was mostly restricted to the western and central sector of the study area. Here, the deeper areas appear as delineated valleys that also compare well with the present-day bathymetry (black dotted lines in Figure 4-9).

The lower resolution of our sparker data in the top 10-20 m did not allow us to make an exact correlation of U8 to either one or multiple subunits of the Brown Bank Formation identified by Waajen-Labee et al. (2025). A possible scenario that could explain why we only observe one facies of the Brown Bank Formation is that our study area is located further offshore and deeper (50 to 60 m LAT) compared to the study area of Waajen-Labee et al. (2025) (30 m LAT). This latter study suggested that the variety in seismic facies, and thus identification of multiple subunits, can be related to a more marginal depositional environment. The mapped extent of the Brown Bank Formation in this study (U8) differs from that on the BGS geological map (Figure 4-10; BGS, 2000). While an overall match is observed in the east, our data indicate that U8 is limited to the centre of the study area and is absent in the west (Figure 4-10b). Although the Brown Bank Formation was mapped in the western sector by Cameron et al. (1992), the sedimentary facies described by these authors (i.e. sandy and lacking bioturbation) differs clearly from the sedimentary facies of the Brown Bank Formation in the central and eastern sector (i.e. clay-rich facies with abundant bioturbation; Cameron et al., 1992). In our sparker data, the seismic facies identified in the western sector covering the older units (U2, U3, U4 and U6) shows a complex facies infilling an irregular basal surface, which differs from the typical (sub)parallel facies of the Brown Bank Formation and is therefore attributed to U9. As discussed in the previous paragraph, we identified valleys in the depth structure map of S9 in this western sector (black dotted lines in Figure 4-9) that could correspond to the north-south channels mapped for the Brown Bank Formation by Cameron et al. (1992; 1984b) (Figure 4-10a). OWF reports in the southwestern sector (i.e. East Anglia ONE North and East Anglia TWO; polygons 4-5; Figure 4-1b) identified NNW-SSE oriented channel features cutting into the Lower Pleistocene deposits (i.e. Red Crag, Westkapelle Ground and/or Yarmouth Roads Formation) and were interpreted to have formed during periods of low sea level when that area was exposed as a terrestrial landscape. Even though the OWF reports highlight their uncertainty in age for these features, as the reports use the framework of Cameron et al. (1992), they were interpreted as and correlated with the Brown Bank Formation (Wessex Archaeology, 2018b; 2018c). Importantly, another report assigned the infilling deposits of these channel features a younger age corresponding to MIS3 (Limpenny et al., 2011). This is in contrast to the currently accepted depositional timeframe of the Brown Bank Formation, i.e. MIS5-4 transition (Waajen et al., 2024; Waajen-Labee et al., 2025). We therefore hypothesise that the sediments identified in the western sector of the study area by Cameron et al. (1992) and the East Anglia TWO and ONE North wind farms are younger and therefore incorrectly correlated with the Brown Bank Formation. In the recent BGS assessment report, these NNW-SSE oriented channel features were correlated with the Botney Cut Formation rather than the Brown Bank Formation. In this report, it is assumed that late Weichselian channel-like fills resulting from a range of sedimentary processes are generally incorporated in this formation (Dakin et al., 2026). We follow this reasoning and therefore suggest that the valleys and infilling deposits most likely belong to an undifferentiated subfacies of the stratigraphically younger U9. This explains why our new map (Figure 4-10b) looks simpler and does not include valley-features related to the Brown Bank Formation as shown in the original map sheets (Figure 4-10a).

Knowing that the youngest published ages for the Brown Bank Formation are c. 60 ka BP (Waajen et al., 2024; Waajen-Labee et al., 2025), U9 comprises sediments deposited from the middle Weichselian (MIS4-3) to the Holocene (MIS1). Based on this relatively large depositional timeframe, combined with the geographical distribution (Figure 4-8) and the multiple subfacies (Figure 4-2; Figure 4-6; Figure 4-7), we infer that U9 likely comprises multiple formations, including the Kreftenheye, Twente/Boxtel, Botney Cut/Dogger Bight, Elbow/Nieuwkoop/Naaldwijk and Southern Bight Formations (Table 4-1). One prominent incision and multiple incision-related remnants were identified at the base of U9 (S9 – generation F; Figure 4-11a). Following a similar reasoning that U9 incorporates multiple formations, the incisions and channel remnants attributed to generation F likely reflect multiple, succeeding incisional phases throughout the middle Weichselian to Holocene. These may therefore have multiple formational mechanisms, ranging from marine (tidal) to terrestrial (fluvial

and/or peri- or proglacial). All OWFs in the study area report the presence of small, shallow channel fills that post-date the deposition of the Brown Bank Formation and were attributed to a Holocene pre-transgression unit (Wessex Archaeology, 2018a; 2018b; 2018c; 2017; 2014). Some of those can be correlated with our generation F incisional remnants. Following the earlier reasoning on the age of the underlying deposits from the Brown Bank Formation, we can infer a depositional age of anywhere between the middle Weichselian to Holocene for these channel remnants as opposed to the OWFs reported Holocene pre-transgression age. Apart from the channel remnants, the OWF reports describe other pre- and post-transgression Holocene units (Wessex Archaeology, 2018a; 2018b; 2018c; 2017; 2014). The limited resolution of the sparker data in the top 10-20 m precludes any further correlations, apart from the last post-transgression unit that incorporates sand waves and larger sandbanks, that we also identified as part of U9.

U9's basal surface (S9) is recognised as a final, regional-scale erosional surface. As previously mentioned, the topography of this erosional surface displays similarities to the present-day bathymetry (Figure 4-9). Its deepest area overlaps with where the present-day Axial Channel can be seen on the bathymetry (Chapter 3). On the depth structure map of S9, this deepening is characterised on the eastern side by two drops of c. 5 m (black dashed lines in Figure 4-9), and on the western side and towards the south by delineated deeper valleys (black dotted lines in Figure 4-9). Knowing that S9 post-dates the Brown Bank Formation, the final erosional phase could therefore be related to the MIS4-3 transition and/or even be younger, related to MIS2 drainage (see Section 4.5.4). Even though we cannot constrain the formational age, this final erosional phase seems to be restricted to the central to western and southern sector of our study area, i.e. the Axial Channel system.

4.5.4 Regional-scale environmental reconstruction throughout the Pleistocene

Following the previous discussion, the identification of distinct units, incisional phases and major erosional surfaces allows for an interpretation of the depositional environment and correlation to the Pleistocene chronostratigraphic framework (Figure 4-12). For now, assigning the identified units to specific time intervals remains tentative. Each of the identified basal surfaces, together with their associated (infilling) deposits, requires ground-truthing and direct dating to achieve a robust framework. Only then can it be determined which parts of the Pleistocene record are preserved and which parts are missing (either removed or never deposited in the study area). However, by identifying large erosional surfaces and geomorphological characteristics of the different units and generations of incisions, a chronological and stratigraphic framework could be reconstructed (Figure 4-12c).

As described in Section 4.5.1, the Lower Pleistocene deltaic sediments of the Southern North Sea Deltaic Group were deposited over an extended time period. These reflect relatively stable environmental and depositional conditions, where accommodation space increased towards the northeast as a consequence of compaction and load-induced subsidence in the central North Sea Basin (Arfai et al., 2018; Knox et al., 2010; Ottesen et al., 2018). The thickening of U2 and U3 in a north/northeastward direction, as well as the northern position of U3 compared to U2 (Figure 4-8) are indicative of a northward prograding depositional system. Our findings are therefore consistent with the deltaic systems prograding towards a northwards located basin as proposed by Cohen et al. (2014) and Gibbard and Lewin (2016). The Lower to Middle Pleistocene deposits of the Yarmouth Roads Formation (U4), however, reflect the onset of a changing depositional environment caused by the increasing amplitude and duration of the glacial-interglacial cycles and coupled sea-level fluctuations linked to the Mid Pleistocene Revolution (Clark et al., 2006). As discussed in Section 4.5.1, the largest part of the Yarmouth Roads Formation is masked in our data by the seabed multiple but is assumed to fill the pre-existing basin throughout most of the Calabrian and Cromerian. Filling of the accommodation space during deposition of the Yarmouth Roads Formation marks a significant shift in depositional setting. This is clearly shown in our sparker data, where the uppermost part of the

Yarmouth Roads Formation reflects the change from a deltaic to a fluvial dominated environment (generation B; Figure 4-12a). The multiple incisional and infilling stages of generation B, interpreted as a remnant of a long-lived, braided fluvial system, can be linked to fluctuating sea levels at the end of the Cromerian (Figure 4-12b). The absence of a gradient for this preserved braided river system is an indication that the southern North Sea Basin geometry changed and became a relatively flat, low-lying area. A northward drainage direction is inferred, consistent with the reconstructed courses of the major West European river systems during the Cromerian (Busschers et al., 2025; Gibbard and Lewin, 2016; Hijma et al., 2012). Based on the recent reconstructions of Busschers et al. (2025), a connection between the channel belt and Paleo-Scheldt cannot be excluded. The Rhine-Meuse System was likely located too far north to allow a correlation (Busschers et al., 2025), but also the NE-SW orientation of the Proto-Thames (Gibbard and Lewin, 2016) is inconsistent with the NW-SE orientation of the generation B channel belt.

The younger units (U5-U9) can be placed in the context of the major Pleistocene glaciations, with regional erosional surfaces and incisional phases linked to accompanying sea-level changes (Figure 4-12b). Erosional unconformity S6 (including generation D) and, to a lesser extent, also S7 (generation E), indicate a major drop in base level and are correlated with the Elsterian (MIS12) and late Saalian glacial phases (MIS6) (Figure 4-12b). Previous regional stratigraphic studies have documented the erosion of the uppermost part of the Yarmouth Roads Formation (Cameron et al., 1992; Stoker et al., 2011). The identification of the major erosional surface S6, and its correlation with the Elsterian glacial phase, confirms that the erosion of U4/Yarmouth Roads Formation is linked to that glacial period. The presence of an extensive Elsterian ice sheet in the study area is further inferred from the incisions in the north (S5; generation C) and west of the study area (generation D) and their interpretation as buried tunnel valleys. The identification of S6, however, cannot yet give further clues regarding the exact (maximum) extent of the Elsterian ice sheet or on fluctuations in the ice margin. Many uncertainties also remain on the glacial phases associated with MIS10 or MIS8 (e.g. Batchelor et al., 2019; Hughes et al., 2020). We can only infer that after the deposition of U6, subsequent ice advances did not cover the study area again as the deposits of U6 do not seem to be deformed by glaciotectonic processes. That said, deposits of U6 most likely span multiple climatic cycles. They could incorporate (pro-)glacial and glaciofluvial deposits related to a sub- and proglacial landscape as well as marine deposits related to the inundation of the southern North Sea during subsequent interglacial periods (Figure 4-12b). Similarly, if the erosional surface S7 is related to the late Saalian glacial phase (MIS6), its associated deposits (U7) could span one glacial-interglacial cycle (late Saalian MIS6 to Eemian MIS5e; Figure 4-12b), and thus include glacial, fluvial and marine sediments.

Onshore and offshore sedimentary and chronological evidence from previous studies indicate that drainage directions of major West European river systems (Thames, Scheldt, Rhine and Meuse) shifted for the first time towards the south after the onset of the Elsterian glacial phase (e.g. Busschers et al., 2025 and references therein; Hijma et al., 2012; Toucanne et al., 2009b; 2009a). Our dataset does not provide new information regarding these southward deflected systems, nor does it support the existence of a southward flowing, confluent river system following the Elsterian glacial phase or subsequent glacial phases (MIS10, MIS8 or MI6). We can infer a southern drainage from the generation D and E incisions, i.e. drainage away from the ice front that blocks a northern route. The only evidence that might indicate major southward draining systems, including the (re-) activation of the Axial Channel system, is the erosion of the Lower Pleistocene formations (U1, U2, U3) in the southern(most) part of the study area. Here, even though the overlying deposits are attributed to U9, the erosional surface (attributed to S9) can be linked to one or multiple phases of base-level lowering throughout the Middle or Late Pleistocene, as the only chronological constraint is its stratigraphic position, i.e. being younger than the underlying Lower Pleistocene deposits.

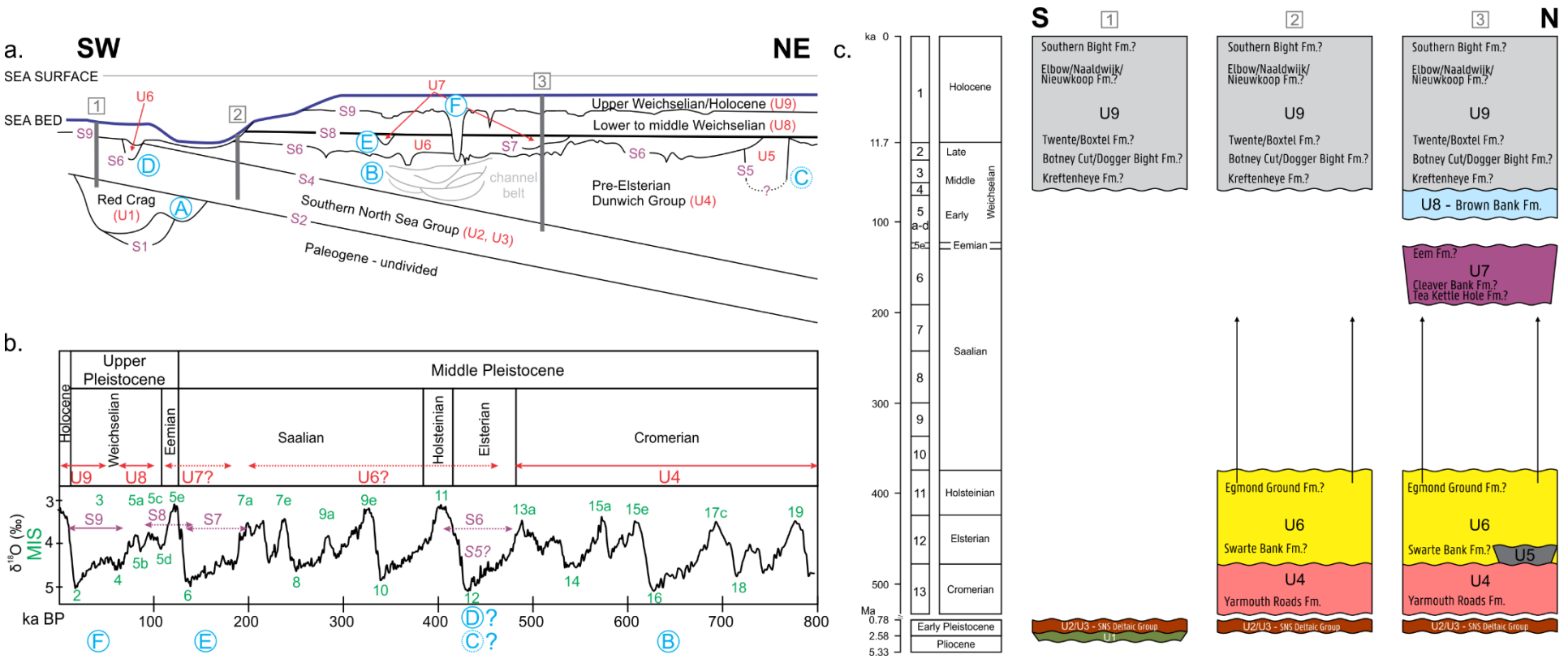


Figure 4-12. (a) Synthetic cross-section with summary of the interpreted units (red), basal surfaces (purple) and incisional generations (light blue) derived from our data. For location of cross-section profile see Figure 4-10b. (b) An interpreted chronology for the different units and generation of incisions along the $\delta^{18}O$ curve (including MIS correlation) adapted from Lisiecki & Raymo (2005). (c) Reconstructed stratigraphic framework for the study area following the framework of Dakin et al. (2026), locations 1-2-3 indicated on (a).

Surface S8 can be seen as a second major erosional event, truncating the Middle Pleistocene deposits of U6 and U7. It is, however, uncertain if S8 is linked to the MIS5e transgression (Eemian) or to changes in base-level at the onset of the Weichselian (MIS5d or c; Figure 4-12b). An alternative interpretation is that the topographic low in the central sector of the study area reflects an earlier major drainage system, related to deglaciation at the end of the Saalian (Drenthe) period. Large-scale drainage through the Axial Channel system at the end of the Saalian (MIS6) would explain the correlation between the break in slope identified in S8 and the eastern limit of the Axial Channel (see also Section 4.5.3).

More certainty surrounding the depositional environment of the overlying deposits from U8 was achieved through the correlation of S8 with the regional-scale erosional surface already identified by Waajen-Labee et al. (2025). This allowed U8 to be linked to the shallow-marine sediments of the Brown Bank Formation, deposited during the MIS5-4 transition (Figure 4-12b). The lower resolution of our sparker data in the top 10-20 m, acoustic blanking (due to shallow gas) in the eastern sector, and the erosion of U8/Brown Bank Formation marked by S9 in the central, western and southern sector, hamper further interpretations regarding the depositional environment or palaeogeographic setting compared to Waajen-Labee et al. (2025). This includes, for example, that we were not able to address the position of the palaeocoastline in the western sector or the influence of the Rhine in the eastern sector.

A significant drop in base level, associated with the cooling climatic conditions at the onset of the Early Pleniglacial (MIS4) and/or subsequent sea-level fluctuations throughout the late Weichselian could explain the final, large-scale erosional event of S9 and the incisions of generation F (Figure 4-12b). In Section 4.5.3, we have indicated that generation F most-likely represents different incisional phases that relate to marine (tidal) and/or terrestrial (fluvial and/or peri- or proglacial) processes, and U9 therefore deposits related to these different processes. Regardless of the nature of the generation F incisions, the similarities of S9 to the present-day bathymetry (see Section 4.5.3) are a first, direct indication of the re-activation of the Axial Channel system after deposition of the Brown Bank Formation. Drainage towards the south was inferred for both the Pleniglacial (MIS4-3) and LGM (MIS2), as a connection was present between the southern North Sea and the Atlantic through the Strait of Dover (e.g. Hijma et al., 2012; Toucanne et al., 2023; Waajen-Labee et al., 2025). NNW-SSE oriented channel fills in the western sector, mapped originally as Brown Bank Formation but now interpreted to be part of U9, were linked to MIS3 (Limpenny et al., 2011), therefore confirming activity through and deposition in the Axial Channel during that same period (Figure 4-12b). With the BIIS and FIS coalescing and forming a grounded ice sheet one final time during MIS2, large-scale glaciofluvial drainage from the ice front, accompanied by drainage from the West European river systems, to the south occurred. Erosion of U9 in the western sector is therefore correlated with this large-scale glaciofluvial drainage event. This further confirms activity within the Axial Channel system, and most likely shaped the present-day Axial Channel morphology.

4.6 Conclusions

The geophysical data presented in this study demonstrate the transition from a deltaic and fluvial North Sea environment in the Late Pliocene to Middle Pleistocene to a glacially influenced landscape during three consecutive Middle to Late Pleistocene major glacial phases. Plio-Pleistocene (Red Crag Formation) and Lower Pleistocene (Westkapelle Ground, Smiths Knoll and IJmuiden Ground Formation) deposits, imaged in unprecedented detail, support previous palaeogeographic reconstructions of northward progressing deltaic systems associated with a northward migrating North Sea. A clear change in basin configuration is recorded in the Yarmouth Roads Formation. This complex unit shows the shift from pre-existing basin infill to braided river systems that prevailed in a relatively flat southern North Sea landscape. We were able to link the presence of a large-scale

erosional surface that marks the top of the Yarmouth Roads Formation to the Elsterian glacial advance (MIS12). Whereas many uncertainties remain on the depositional environment and timeframe of the overlying unit (tentatively linked to the Swarte Bank and Egmond Ground Formations). Dispersed younger incisions with a multi-staged infill were further identified and correlated with the late Saalian (Drenthe; MIS6). The identification of a major erosional surface, incisions and multiple preserved deposits in between the Yarmouth Roads Formation and Brown Bank Formation is an important step in improving our understanding of the Middle Pleistocene glacial configuration in the present-day Southern Bight. In addition, two Late Pleistocene large-scale erosional surfaces, marking both the base and the top of the Brown Bank Formation, are indicative of two widespread erosional events. Uncertainties remain about their exact age, but they most likely reflect a preserved, late Saalian deglacial landscape and base-level fluctuations throughout the middle and late Weichselian (including base level drops at MIS4 and MIS2), respectively. Alongside new insights into the configuration of these Pleistocene formations, six different incisional phases (generations) were identified that could be placed in the stratigraphical timescale. We have discussed our interpretations together with findings from different OWF reports in the study area, which allowed us to corroborate their results and place everything in an updated regional (seismic) stratigraphic framework for the southern North Sea. Given the relatively wide line spacing (c. 5 km) and lack of deep ground-truthing some interpretations remain uncertain in places. Nonetheless, our data clearly indicates the need to continue refining the regional stratigraphic framework using higher resolution and more closely spaced seismic data, as well as new ground-truth information.

CHAPTER 5. NEW CHRONOSTRATIGRAPHIC INSIGHTS INTO THE EVOLUTION OF THE AXIAL CHANNEL (SOUTHERN NORTH SEA) FROM PRESERVED UPPER PLEISTOCENE DEPOSITS

ABSTRACT

The Axial Channel is a prominent geomorphological feature in the southern North Sea, however, little is known about its origin and evolution due to limited and poorly constrained stratigraphic and lithological information. In this study, newly acquired sub-bottom profiler and core data, combined with palaeoenvironmental (pollen, molluscs and foraminifera) and chronological (OSL) results, allowed for a detailed investigation of preserved Upper Pleistocene deposits in the present-day Axial Channel system. Deposits reflecting a marine environment were dated to MIS5 and include (i) the first *in-situ* identified open marine sediments of the Eem Formation (MIS5e) in the study area and (ii) the shallow-marine sediments of the Brown Bank Formation (MIS5a-MIS4). Sediments infilling an incision tentatively interpreted as a tidal channel were dated to early MIS3. In addition to deposits linked to a marine regime, two erosional surfaces confined to the western Axial Channel were identified evidencing (glacio-)fluvial activity correlated with MIS4 and late MIS3. The late MIS3 correlation was inferred from overlying deposits dated to c. 29 ka, where sedimentological and pollen data indicate a proglacial lacustrine environment. Erosion at the top of these deposits confirms previously established large-scale glaciofluvial drainage during the Last Glacial Maximum (LGM; MIS2). These new findings demonstrate rapid climate and sea-level fluctuations throughout the Late Pleistocene and enable the reconstruction of the palaeogeographic evolution of the Axial Channel and wider southern North Sea region from the late Saalian to the Holocene.

This chapter will be submitted as: Vervoort, M., Plets, R., Kyriakoudi, D., Mestdagh, T., Demey, A., Waajen-Labee, I., Wesselingh, F., Grant, M., Kinnaird, T., Missiaen, T., De Batist, M. New chronostratigraphic insights into the evolution of the Axial Channel (southern North Sea) from preserved Upper Pleistocene deposits. JOURNAL OF QUATERNARY SCIENCE.

Author contribution (CRediT): **Morgan Vervoort:** Conceptualisation, data curation, methodology, formal analysis, investigation, writing – original draft, writing – review & editing, visualisation. **Ruth Plets:** Conceptualisation, data curation, project administration, writing – original draft, writing – review & editing, supervision. **Despina Kyriakoudi:** Data curation, methodology, writing – review & editing. **Thomas Mestdagh:** Data curation, methodology, writing – review & editing. **Anke Demey:** Data curation, methodology, writing – review & editing.**Irene Waajen-Labee:** Data curation, methodology, writing – review & editing. **Frank Wesselingh:** Data curation, methodology, writing – review & editing. **Michael Grant:** Data curation, methodology, writing – review & editing. **Tim Kinnaerd:** Data curation, methodology, writing – review & editing. **Tine Missiaen:** Data curation, project administration, writing – review & editing. **Marc De Batist:** Project administration, writing – review & editing, supervision.

5.1 Introduction

During the Middle to Late Pleistocene, rapid climatic changes influenced the landscapes and ecosystems of the southern North Sea throughout multiple glacial-interglacial cycles (e.g. Busschers et al., 2007; Cohen et al., 2014; Eaton et al., 2020; Gibbard & Cohen, 2015; Hijma et al., 2012; Spratt & Lisiecki, 2016). At least three times, the British-Irish and Fennoscandian Ice Sheets (BIIS and FIS, respectively) merged and extended into the southern North Sea basin; i.e. during the Elsterian/Anglian (Marine Isotope Stage or MIS12), Saalian/Wolstonian (MIS10-6) and Weichselian/Devensian (MIS5d-2) glacial periods (e.g. Batchelor et al., 2019; Böse et al., 2012; Graham et al., 2011). The development of these large ice sheets and accompanying sea-level fluctuations led to coastline changes, rerouting of large West European river systems, as well as the creation of new (glacio-)fluvial drainage pathways in the southern North Sea basin during sea-level lowstands, when the area was a dry, terrestrial landscape (e.g. Busschers et al., 2008; Cohen et al., 2014; Gibbard & Lewin, 2016; Hijma et al., 2012). The subsurface of the southern North Sea therefore holds a complex (and mostly discontinuous) geological record of marine, fluvial and/or glacial depositional as well as erosional phases.

The Axial Channel is a large palaeovalley system and prominent feature in the present-day bathymetry of the southern North Sea (Figure 5-1a, b). It is believed to be a remnant of a large-scale drainage system (Chapter 3; Hijma et al., 2012). However, many uncertainties regarding its formation, evolution and role as a (glacio-)fluvial drainage pathway still exist (e.g. Chapter 3; Bridgland and D'Olier, 1995; De Clercq et al., 2018; Hijma et al., 2012). The earliest indirect evidence of the Axial Channel system acting as a confluent river system draining the southern North Sea basin is linked to the inferred two-staged opening of the Strait of Dover (Pas de Calais; Figure 5-1a) during the Elsterian (MIS12; c. 450 ka) and Saalian (MIS6; c. 160 ka) (Collier et al., 2015; Gupta et al., 2017). There is a long-standing hypothesis that proglacial lakes existed in front of the Elsterian and Saalian ice sheets, fed by major European rivers (Rhine-Meuse, Thames) and glacial meltwater (e.g. Cohen et al., 2017; Gibbard, 1995; Gupta et al., 2017; Murton and Murton, 2012). Overspilling of this lake and catastrophic flooding at the end of these glacial periods led to the breaching of the Weald-Artois land bridge that connected mainland Europe to Britain, and thus to the opening of the Strait of Dover (Collier et al., 2015; Gibbard and Cohen, 2015; Gupta et al., 2017, 2007). Even though the exact extent (or even the existence) of these large proglacial lakes during the Elsterian and Saalian is still debated (e.g. Cartelle et al., 2021; Cohen et al., 2014), evidence from the Bay of Biscay confirms increased discharges and thus a southern drainage route through the Strait of Dover at MIS12, 10, 8 and 6 (Toucanne et al., 2009a, 2009b). Onshore evidence from the Netherlands further indicates that the Rhine and Meuse river systems deflected southwards when the Elsterian and Saalian ice sheets blocked their northerly drainage route (e.g. Busschers et al., 2025, 2008, 2007; Hijma et al., 2012). Even though the river courses of the Rhine and Meuse are well established for the Middle Pleistocene in the terrestrial and adjacent coastal areas (e.g. Busschers et al., 2025, 2008, 2007; Hijma et al., 2012), large uncertainties remain on their extended offshore course into the southern North Sea Basin. It is generally believed that the major river systems (i.e. Rhine, Meuse, Thames), but also smaller rivers (e.g. Scheldt (BE) and Stour (UK)) and glacial drainage systems linked to the ice front, converged towards the south into a central valley system, the Axial Channel (e.g. Busschers et al., 2025; Cohen et al., 2014; De Clercq et al., 2018; Hijma et al., 2012).

During the Weichselian glacial period (MIS5d-2; c. 120-11.7 ka) similar southern drainage routes are considered to have followed previously established valleys towards the Strait of Dover (e.g. Hijma et al., 2012). New insights into the depositional systems of the southern North Sea basin have revealed that Weichselian climate fluctuations strongly influenced landscape and ecosystem changes in the region (e.g. Waajen-Labee et al., 2025). However, uncertainties about the extent of the BIIS and FIS and whether or not they coalesced across the North Sea (e.g. Batchelor et al., 2019; Clark et al., 2022; Roberts et al., 2018; Sejrup et al., 2016), alongside the overall lack of dated deposits, suggest that

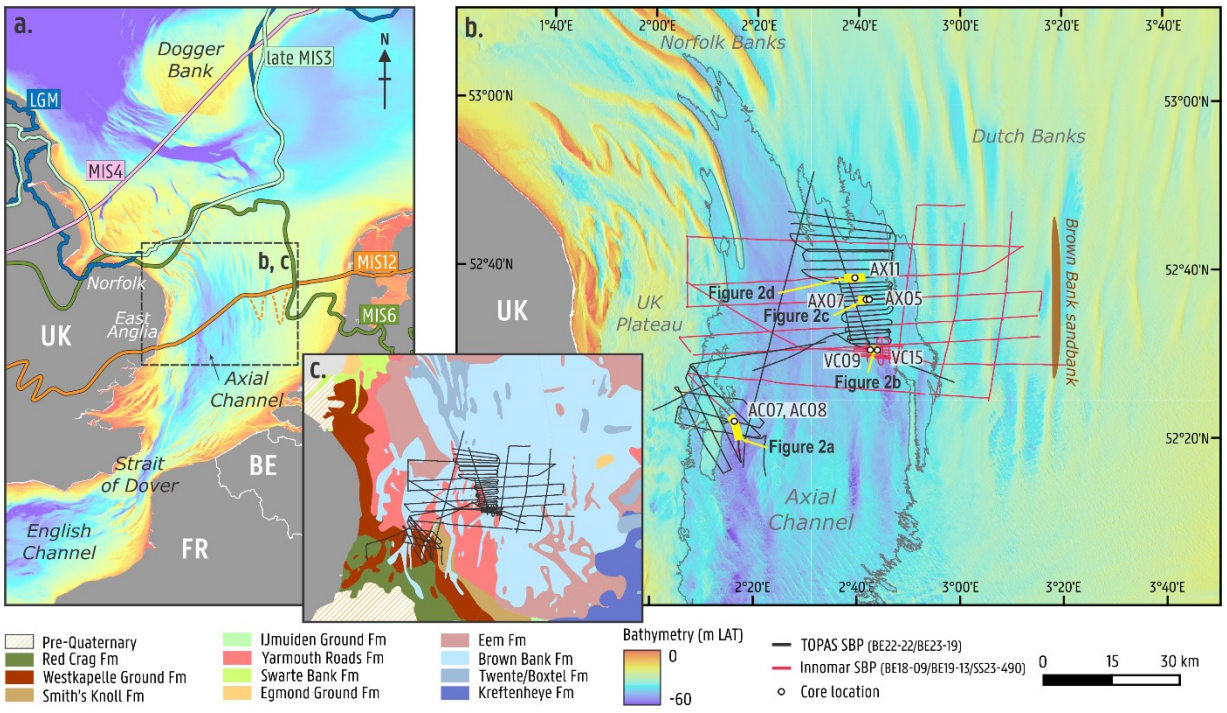


Figure 5-1. (a) Bathymetric map of the southern North Sea with depth in m below lowest astronomical tide (LAT). The maximum ice extent reconstructions are shown for MIS12 (Elsterian glaciation; Batchelor et al., 2019; Busschers et al., 2025), MIS6 (late Saalian, Drenthe glaciation; Batchelor et al. (2019); Busschers et al. (2025), MIS4 (Batchelor et al., 2019), late MIS3 (30 ka; Clark et al., 2022) and Last Glacial Maximum (LGM; Clark et al., 2022). (b) Bathymetric map (in m LAT) of the study area. Sub-bottom profiles (black: TOPAS, pink: Innomar) and core locations (white dots) are indicated. The Axial Channel (delineated by the -40 m contour line), UK Plateau, Norfolk Banks and Dutch Banks sandbank areas, and Brown Bank sandbank are indicated for geographical reference. (c) Geological map with different Pleistocene formations (Fm) in the study area, as compiled and published by BGS (2000). Bathymetric data are available through EMODnet (EMODnet Bathymetry Consortium, 2022).

coastline positions and drainage directions throughout the pre-LGM (MIS2) Weichselian period are still largely unresolved. The exact drainage pathways and (re-)occupation of the Axial Channel system as a large, confluent river system throughout the Late Pleistocene remain therefore largely unknown (e.g. Hijma et al., 2012). Furthermore, as sea levels rose at the end of each glacial period, marine inundation from the north and the south would have influenced the antecedent landscape. As such, not only (glacio-)fluvial processes but also marine processes would have played a significant role in shaping the Axial Channel and wider southern North Sea region during interglacial periods, i.e. during the Holsteinian (MIS11), Eemian (MIS5e) and the Holocene (MIS1).

A recent study that examined the bathymetry and geomorphology of the southern North Sea showed that the Axial Channel reflects an extended period (multiple glacial-interglacial cycles) of fluvial activity (Chapter 3). Whilst that study focussed on the currently exposed seafloor geomorphology, subsurface investigations are needed to fully understand and time-constrain the evolution of the Axial Channel system through different glacial and interglacial periods. As such, in this study, extensive new, high-resolution sub-bottom profiles and core data in the northern and central Axial Channel area are analysed with the aim of reconstructing the evolution of the Axial Channel system. In a first step, sub-bottom profiler (SBP) data interpretations combined with lithological and palaeoenvironmental (pollen, molluscs, foraminifera) characterisation, as well as geochronological constraints derived by optically stimulated luminescence (OSL) dating, enabled a detailed investigation into the Middle to Late Pleistocene (MIS6 onwards) stratigraphy of the area. The resulting chronostratigraphic framework, in turn, provides new insights into the (late) Saalian to the Holocene palaeogeography and evolution of the Axial Channel system, a period characterised by rapid climate and accompanying sea-level fluctuations. Our findings are further discussed within the framework of published

reconstructions of (major) NW-European river systems (e.g. Busschers et al., 2025; Gibbard et al., 1988; Gibbard and Lewin, 2016; Hijma et al., 2012; Waajen-Labee et al., 2025).

5.2 Regional setting

The Axial Channel is a c. 200 km long, crescent-shaped, depressional feature in the present-day bathymetry of the southern North Sea, that runs parallel to the East Anglia coast (Figure 5-1a, b). The study area focuses on the central to northern Axial Channel region (52°10'N-52°50'N), from c. 30 km east of the East Anglia coast (2°E) to the Brown Bank sandbank (3°20'E) (Figure 5-1a, b). It is situated in between large tidal sandbank fields that dominate the region towards the northwest (Norfolk Banks) and (north)east (Dutch Banks). In the west a relatively flat, elevated area is present (UK Plateau; Chapter 3) that forms the western edge of the Axial Channel (Figure 5-1b). The Axial Channel can be traced further southwards to the Lobourg Channel and Strait of Dover (Figure 5-1a). Within the study area, the present-day bathymetry is highly variable ranging from 20 m below lowest astronomical tide (LAT) in the areas of the sandbanks, down to 60 m LAT in the deeper parts of the Axial Channel.

The succession of Quaternary sediments in the study area unconformably overlies Palaeogene strata. It is at least 50 m thick, becoming successively younger and thicker from south to north (Figure 5-1c; Cameron et al., 1992; Rijsdijk et al., 2005; Stoker et al., 2011). More specifically, Lower Pleistocene deltaic deposits of the Southern North Sea Deltaic Group and Lower to Middle Pleistocene deposits of the Yarmouth Roads Formation (Fm) in the southwest are unconformably overlain by Upper Pleistocene deposits in the northeast (for individual formations see Figure 5-1c; Cameron et al., 1984; Stoker et al., 2011). After the late Saalian glacial period (MIS6), sea level started to rise and inundated the southern North Sea region reaching a mean sea level that was as high as or even higher than today (e.g. Busschers et al., 2007; Hijma et al., 2012; Medina-Elizalde, 2013; Spratt & Lisiecki, 2016; Zagwijn, 1983). The only deposits that date back to this last interglacial period are the marine, shelly sands of the Eem Fm (Cameron et al., 1992; Rijsdijk et al., 2005; Stoker et al., 2011). The Eem Fm has been described as isolated and discontinuous patches in the study area (Cameron et al., 1984a; Limpenny et al., 2011). Until now, however, no *in-situ* Eemian deposits have been conclusively identified in the study area by recent offshore wind-farm (OWF) datasets from the UK or in the region east of the Brown Bank sandbank (Dakin et al., 2026; Waajen-Labee, 2025). Climate cooling at the onset of the Weichselian Early Glacial (MIS5d-a) and associated sea-level fall caused the southern North Sea Region to become a shallow and cool embayment with limited connection to the English Channel, as indicated by the fine-grained, shallow-marine sediments and cold marine faunas from the Brown Bank Fm (Waajen et al., 2024; Waajen-Labee et al., 2025). An erosional surface at the top of that formation was linked to further sea-level lowering during MIS4 (Chapter 4; Waajen-Labee et al., 2025). A depositional hiatus has been inferred for the study area for the remainder of the Weichselian Pleniglacial (MIS4-3) and Late Glacial (MIS2) period (Figure 5-1c; Cameron et al., 1992; Rijsdijk et al., 2005; Stoker et al., 2011). However, deposits within the valleys of the western Axial Channel, previously mapped and correlated with the Brown Bank Fm (Figure 5-1c), have recently been reinterpreted as postdating that formation (Chapter 4; Dakin et al., 2026). In the updated UK stratigraphic framework by Dakin et al. (2026), this infill has been tentatively attributed to the Botney Cut Fm. In the wider southern North Sea, Weichselian deposits include the fluvial Rhine-Meuse deposits of the Kreftenheye Fm (southeast of the study area; Figure 5-1c), aeolian/lacustrine/fluvial deposits of the Twente (UK)/Boxtel (NL) Fm and glaciolacustrine/fluvial deposits of the Botney Cut (UK)/Dogger Bight (NL) Fm (both north of the study area; Figure 5-1c; Cameron et al., 1992; Rijsdijk et al., 2005; Stoker et al., 2011).

5.3 Methods

5.3.1 High-resolution acoustic data

The data used for this study were collected during five scientific cruises: RV *Belgica* BE2018-09 (April 2018), *RV Belgica* BE2019-13 (May 2019), *RV Belgica II* BE2022-22 (October 2022), *RV Simon Stevin* SS23-490 (June 2023) and *RV Belgica II* BE2023-19 (October 2023). During the RV *Belgica II* surveys, high-resolution acoustic data were acquired using a hull-mounted TOPAS PS18 (Kongsberg) sub-bottom profiler (SBP) while during the RV *Belgica* and *Simon Stevin* cruises, a pole-mounted Innomar SBP was used.

The TOPAS PS18 operates at 2-4 kHz central frequencies with a 0.2 s ping interval, recording full waveform signals at a sampling frequency of 64 kHz. With these acquisition settings, the top c. 50 m of the subsurface could be imaged with a vertical resolution of a few decimetres. The Innomar SBP data were collected using a multi-transducer SES-2000 Quattro system mounted on the starboard side of the vessel. The four transducers were arranged in a square configuration and operated in single-beam mode. Secondary low frequencies of 6-8 kHz were used depending on the required penetration. The pulse repetition rate was auto-optimised and ranged between 10 and 15 pings per second (0.1 – 0.075 s interval). The received signal was recorded in full-waveform format at a sampling frequency of 96 kHz. On average, a penetration depth up to 15 m below the seafloor was achieved, with a vertical resolution of 5-15 cm.

Additional processing for both types of datasets was performed in RadExPro 2022 (RADEXPRO Seismic Software LLC) and consisted of amplitude balancing, filtering (burst noise removal and 2D spatial filtering) and tidal corrections (in LAT; EU Copernicus Marine Service, 2024). All processed SBP profiles were imported into the S&P Global Software Geoscience Package (Kingdom version 2019) for interpretation, visualisation and correlation with the core data. Horizon and acoustic unit characterisation was performed using the standard principles of seismic stratigraphy (Mitchum et al., 1977). Conversion from two-way travel time (TWT) to depth (m) was done using an average sound velocity of 1550 m/s in water and 1650 m/s in sediments.

5.3.2 Sediment cores

Core locations (Figure 5-1b) were selected based on acoustic facies interpretation. In total seven vibrocores were analysed in this study, of which three were taken during the BE2022-22 survey (AX05, AX07 and AX11), two during the BE2023-19 survey (AC07 and AC08) and two during the SS23-490 survey (VC09 and VC15) (Table 5-1). A 3 m OSIL vibrocorer was used for core collection. For the BE2023-19 survey, an extension was added to the frame and core barrel, allowing 4.5 m core penetration. All cores were split in two halves under red light conditions and stored at the Marine Station Ostend (MSO) of Flanders Marine Institute (VLIZ). One half was retained for archival purposes and OSL dating (archive half), while the other half was used for sedimentological and geochemical analyses (work half). Each core was described and logged, focusing on grain size, colour, bioturbation, fossil content and sedimentary structures. Distinct sedimentary units were subsequently defined, and each unit was assigned a lithofacies (Lf1-8). True-colour line-scans were acquired of the complete core surface at high resolution with either the GEOTEK Multi-Sensor Core Logger (MSCL) of Ghent University (50 x 50 µm) or the AvaaTech core scanner ('CORA') of the Royal Netherlands Institute for Sea Research (70 x 70 µm). For one core (AC07) a histogram equalization filter was applied on the line-scan images to enhance colour contrasts (e.g. Gonzalez and Woods, 2002).

Table 5-1. Details of vibrocores acquired during the different surveys and used in this study, including the type of analysis performed on the different cores. [a]Geodetic system: WGS84; [b]Depths in m relative to LAT from EMODnet bathymetry (EMODnet Bathymetry Consortium, 2022).

Core name	Survey	Coring date	Latitude (N)[a]	Longitude (E)[a]	Core length (m)	Core depth (m LAT[b])	Type of analysis
AX05	BE22-22	21/09/2022	52.609925	2.703618	1.87	41.86	OSL
AX07	BE22-22	21/09/2022	52.609706	2.693813	1.08	43.18	OSL
AX11	BE22-22	21/09/2022	52.652676	2.657141	2.44	46.00	OSL, pollen, forams
VC09	SS23-490	14/06/2023	52.510132	2.707879	0.94	43.90	OSL, pollen, molluscs
VC15	SS23-490	14/06/2023	52.509854	2.730797	1.76	49.05	OSL, molluscs
AC07	BE23-19	05/10/2023	52.366893	2.268013	3.08	54.34	OSL, pollen, grainsize, XRF, CT
AC08	BE23-19	05/10/2023	52.365819	2.268935	3.42	52.44	/

5.3.3 Sedimentological analysis

Detailed sedimentological analyses were performed on the AC07 sediment core to investigate the changes in sediment composition observed in preliminary core descriptions, including X-ray computed tomography (CT), X-ray fluorescence (XRF) and grain-size analysis. In addition, subsamples were taken from a specific interval identified during core logging to identify sedimentary components under a stereo microscope.

CT-analysis

Core AC07 (108-308 cm) was scanned with a medical CT-scanner (SOMATOM Definition Flash, Siemens AG) at Ghent University Hospital (operational settings: 120 kV, effective mAs of 400) with a x-y resolution of c. 0.2 mm and a downcore vertical resolution of 0.3 mm. The VGStudio software (Volume Graphics, Hexagon) was used for visualization and analysis. This non-destructive method allows identification of sedimentary structures based on radiodensity contrasts. Furthermore, as different material is characterised by a specific range of Hounsfield Units (HU), modification of the intensity threshold allows for visualization of the different sediment types. Higher HU values indicate material/sediment with a higher (radio-)density, whereas lower HU values represent lower radiodensity.

XRF-analysis

XRF measurements were performed on AC07 (108-308 cm) using the AvaaTech core scanner ('DEX') of the Royal Netherlands Institute for Sea Research (NIOZ). XRF scanning is a non-destructive method to assess the elemental composition of sediments, which can be used as a proxy for climate reconstructions and as a tool to determine sedimentation patterns and sediment sources (e.g. Croudace and Rothwell, 2015; Martin-Puertas et al., 2017). The scanning resolution was set to 1 mm

and scanning was performed in three different runs; 5 s at 10 kV, 5 s at 30 kV and 10 s at 50 kV. Replicate measurements were performed to test the robustness and reproducibility of the repeated measurements. These replicate measurements were used to calculate the Pearson correlation coefficient (r). Only the elements where this coefficient was ≥ 0.75 were included for further analysis (e.g. Verweirder et al., 2026). Centre log-ratios (clr) were calculated to eliminate the effects from changes in physical properties of the sediment (e.g. organic and water content), measurement times or non-linear matrix effects (Bertrand et al., 2024). The clr-values of the different selected elements (Mg, Al, Si, S, K, Ca, Ti, Mn, Fe, Zn, Rb, Sr, Zr, Ba) were subjected to hierarchical clustering analysis (HCA) in the RStudio software (methodology after Martin-Puertas et al., 2017; McGuire, 2020) to identify covarying elemental groups. The Ward's HCA was applied following the Euclidian method, using the 'ward.D2' option from the 'hclust' R package 'stats'. Ward's analysis is applied to obtain a minimum number of clusters whereas the Euclidian methodology is applied to find the appropriate number of clusters that best explain the variability of the dataset with the aim of still obtaining a satisfactory description of the studied sediments (e.g. Martin-Puertas et al., 2017; McGuire, 2020; Waajen-Labee et al., 2025).

Grain-size analysis

A sample set spanning a specific interval of the AC07 core (269-289 cm), with a 2-3 mm sampling interval, was taken for grain-size analysis. Measurements were performed with the Malvern Mastersizer 3000 laser diffraction analyser at the Department of Geology, Ghent University. Samples were chemically pretreated before measuring to remove the organic matter (30% H_2O_2), carbonate (10% HCl) and biogenic silica content (2N NaOH), following the procedure outlined in Van Daele et al. (2016). The results were processed and statistics were calculated in GRADISTAT version 8.0 (Blott and Pye, 2001). Statistical results were plotted in Grapher (Golden software, version 23.1) and used to classify the sediments based on the Udden-Wentworth scale (Udden, 1914; Wentworth, 1922).

5.3.4 Palaeoenvironmental analysis

Pollen

Palynological assessment of cores AC07 and VC09 was conducted at Coastal and Offshore Archaeological Research Services (COARS), University of Southampton and of core AX11 at the Faculty of Geoscience, Utrecht University (see Chapter 2 - Section 2.2.3 for chemical pretreatment procedures). In total 18 pollen samples from core AC07 (15) and VC09 (3) were processed following the standard preparation procedure after Moore et al. (1991), each sample containing 2-4 cm^3 of sediment. Determinable pollen and spore types were identified to the lowest possible taxonomic level with the aid of a reference collection kept at COARS, University of Southampton. A total land pollen (TLP; not including aquatics and *pteridophytes*) sum of 100 grains was sought for all samples for assessment purposes. In the samples that failed to reach the 100 TLP sum, a minimum of two full mounted slides were assessed with all encountered pollen recorded. In total three pollen samples were taken from core AX11 following the procedure described in Waajen et al. (2024), where each sample contained 1 cm^3 of sediment. Here, a sum of 200 pollen grains (not including aquatics and *pteridophytes*) was sought for each sample.

Foraminifera

A rapid foraminiferal assessment was carried out on three samples from core AX11 at the MSO facility of VLIZ. Samples were processed by wet sieving using distilled water through a stacked sieve column with mesh sizes of 500, 63 and 45 µm. The 500–63 µm and 63–45 µm fractions were collected for micropalaeontological analysis. Following sieving, residues were transferred to labelled containers and examined under a stereomicroscope. Foraminiferal specimens were hand-picked from each size fraction, counted, and mounted on standard micropalaeontological slides. Picked specimens were

subsequently examined at higher magnification for taxonomic identification based on external morphology and preservation characteristics.

Molluscs

A malacological analysis was conducted on six samples from core VC09 (3) and VC15 (3) at the Naturalis Biodiversity Centre (Leiden, The Netherlands). The samples were soaked in warm water for 4 to 8 hours after which they were wet sieved at multiple grain sizes, concentrating on the samples with fractions over 500 µm for analysis. Afterwards, the samples were dried in an oven at 40 °C. The washed and dried residues were qualitatively characterised by looking at abundance of shells and fragments, preservation characteristics, dominant species, interpreted palaeoenvironment (salinity, depth, energy levels, general sea temperature regimes) and potential *in-situ* species. This latter is identified by a combination of preservation of fine surface details, lack of abrasion structures, occurrence of paired bivalves (rare) and ecological consistency of the species. Species ecology data were mostly derived from the OBIS dataset (OBIS, 2026). Within Quaternary units in the southern North Sea Basin, reworking by currents and waves, fluvial transport, or through bioturbation are common phenomena resulting in samples often dominated by *ex-situ* shells. Determination of the potential *in-situ* faunal components was then used to establish palaeoenvironmental reconstructions.

5.3.5 OSL dating

OSL dating is an absolute dating technique that is used to quantify the radiation dose absorbed in sand-sized quartz minerals since the last exposure to light and thus retrieve the time of deposition and burial. To optimise sample selection for absolute dating, OSL profiling measurements were performed at VLIZ under safe light conditions using a SUERC portable OSL reader (Sanderson and Murphy, 2010). Based on these profiling results 23 sediment samples were taken at different depths throughout six cores (AX05, AX07, AX11, AC07, VC09 and VC15; Table 5-1, Table 5-3). Quartz OSL dating was performed at the School of Earth and Environmental Sciences (SEES), University of St Andrews, on all cores except AC07. For this core, polymineral fine fraction OSL was applied as the sediment did not contain sufficient grains for conventional small aliquot OSL dating (i.e. > 90 µm fractions). A detailed description of the OSL dating methods and measurement protocols is provided in Supplementary Report S9.

A limiting factor in luminescence dating is the saturation of the quartz signal, also highlighted by Waajen et al. (2024) and Waajen-Labee et al. (2025). In case of OSL signals approaching saturation, accurate dating is no longer possible. The threshold of 2D0 (twice the characteristic saturation dose) is often used to quantify the onset of saturation and assess the validity of the protocol (Wintle and Murray, 2006). Equivalent doses above the saturation limit, but within the confines of the dose response curve, were included in the palaeodose estimation using the central dose estimate of Galbraith et al. (1999). For samples where more than 35% of single aliquot data was above 2D0 the results are less reliable and reflect a best estimate of the palaeodose (and thus presented as ‘best-estimate’ age). If more than 35% of single aliquot data is above 2D0 and few aliquots were accepted results are presented as minimum estimate of the palaeodose (and thus presented as ‘minimum-estimate’ age).

5.4 Results and interpretations

5.4.1 Acoustic record

The acoustic stratigraphy in the study area is characterised by multiple major erosional surfaces and incisions (horizons H1-H6), and six preserved infilling and/or depositional units (Units A-F) (Figure 5-2, Table 5-2). Gridding of the basal or top surfaces of the different units resulted in depth structure maps (Figure 5-3).

Unit A: Unit A is the basal, undifferentiated unit identified in all acoustic profiles. Where the unit occurs at greater depth, it is characterised by a mostly transparent acoustic facies with some low-amplitude, discontinuous reflections (due to limitations in penetration depth; Figure 5-2). Where the unit is less deeply buried by overlying units, different facies with higher-amplitude and higher-frequency reflections are observed (e.g. Figure 5-2a). The upper boundary of Unit A is diachronous. In the centre and east, the upper boundary is formed by the high-amplitude reflector H1, overlain by Unit B (Figure 5-2b, c, d). Where this unit is incised by H3 (in the centre) or H4 (in the west), the unit is overlain by Unit D and Unit C, respectively (Figure 5-2a, c, d). In other areas, the unit is truncated by the high-amplitude reflector H5 or the seafloor.

Unit B: Unit B is an extensive unit present in the centre and east of the study area. It is divided into three subunits: B1, B2 and B3 (from oldest to youngest). The basal surface, H1, is an undulating, high-amplitude reflection that truncates the underlying strata (Unit A). Only where subunit B1 is identified, H1 is a low-amplitude reflection. H1 generally shallows towards the (north)east (Figure 5-3a). In the deeper, central area, two S-shaped N-S to NW-SE depressions are present in H1 (Figure 5-3a). These depressions are c. 10 m deeper (c. 60 m LAT) compared to the surrounding areas of H1 (c. 50 m LAT) but their depth does not consistently change in a northern or southern direction (Figure 5-3a). Both subunits B1 and B2 are discontinuous (Figure 5-3b, c) and display a chaotic-transparent acoustic facies (Figure 5-2d). Subunit B1 is restricted to depressions created by the highly variable relief of H1 (thus occurring as “pockets”; Figure 5-2d). Its top bounding surface is a high-amplitude reflection, H1.1, that separates B1 from either subunit B2 or B3. Subunit B2 appears as a blanket deposit, covering the basal surface H1 or subunit B1 (and thus H1.1; Figure 5-2d). Its top bounding surface is the medium-amplitude reflection H1.2, that separates B2 from B3. The acoustic facies of subunit B3 is characterised by mostly parallel continuous reflections, onlapping the basal horizon H1 or subunits B1 and/or B2 where present (Figure 5-2b, c, d). Within subunit B3, towards the north and east, there are subfacies with a more transparent or more chaotic appearance that interrupt the otherwise continuous reflections, suggesting the presence of small-scale deformation structures (inset Figure 5-2d). In the east, acoustic blanking is visible and likely related to the presence of gas in this unit, which sometimes hampers the identification of surfaces H1, H1.1 and H1.2 (white hatched areas in Figure 5-3a-c). Reflections at the top of the unit are truncated by H5 (Figure 5-2b, c, d). At various locations in the north of the study area, narrow (few tens of m) incisions with steep flanks (> 20°) cut through the top of Unit B (Figure 5-2d). In the centre, Unit B is incised by H3 (Figure 5-2c, d).

Unit C: Unit C is geographically restricted to the centre and west (Figure 5-3d). It is composed of a discontinuous infill with several subunits that all display a transparent to chaotic acoustic facies and are bounded by minor erosional horizons (Figure 5-2a). Its basal surface is the high-amplitude reflection H2. Two parallel north-south valleys become visible in the southwest when gridding this surface, separated by a topographic high (island) inferred from the absence of surface H2 and Unit C deposits (white dotted shape in Figure 5-3d). A second island can be discerned in the eastern valley (white dotted shape in Figure 5-3d). In the south, the eastern valley is deeper (up to c. 76 m LAT) and wider (c. 7 km) compared to the western valley (up to c. 68 m LAT deep and c. 3 km wide) (Figure 5-3d). The western valley cannot be traced further north due to the limited penetration of the Innomar SBP

data (white hatched area in Figure 5-3d). The eastern valley can be traced northwards, where it becomes wider (c. 15 km) and shallower (up to c. 61 m LAT) (Figure 5-3d). Unit C is incised by the high-amplitude reflection H4 (Figure 5-2a). Where this horizon is not present, the surface H5 or the seafloor forms the upper boundary (Figure 5-2a).

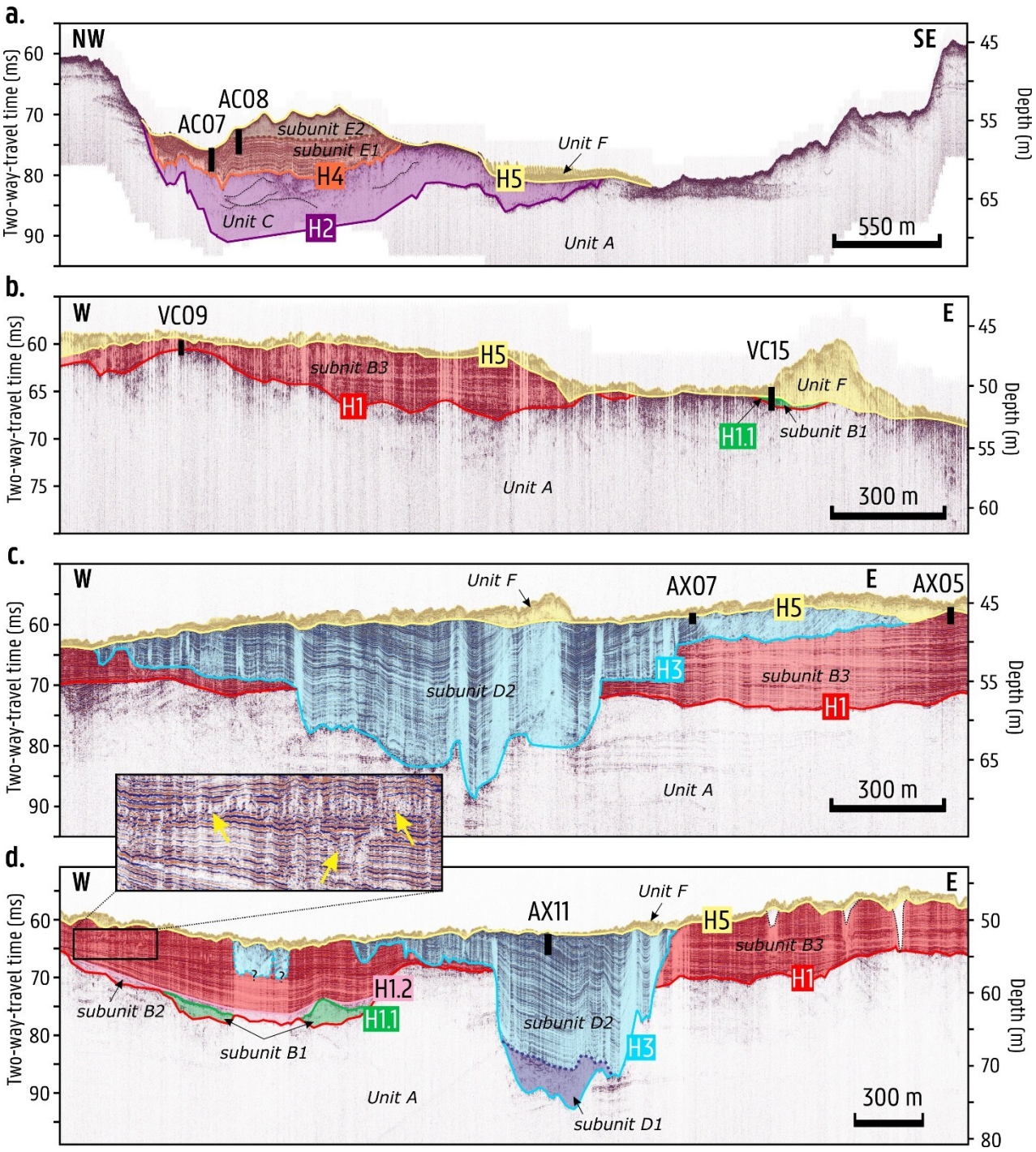


Figure 5-2. High resolution 2D sub-bottom profiles (a-b: Innomar SBP, c-d: TOPAS SBP) and core locations, with interpretations of the different identified horizons (H1-6) and acoustic (sub-) units (Unit A-F). Inset (d): detailed zoom of the small-scale deformation structures present in subunit B3. See Figure 5-1 for the location of the profile and cores. For uninterpreted profiles see Supplementary Figure S5.

Unit D: Unit D comprises the infill of a c. 35 km long and up to 2.5 km wide incision (H3; Figure 5-2c, d; Figure 5-3e). It consists of two subunits (D1 and D2), although the basal subunit D1, characterised by a transparent to chaotic acoustic facies (Figure 5-2d), is not always present. The main infill, subunit

D2, consists of a divergent infilling acoustic facies (Figure 5-2c, d). The incision (H3) is c. 30 m deep (c. 67 m LAT) in the centre and shallows both at its northern and southern end (Figure 5-3e). Where it cuts into Unit A (Figure 5-2c, d), H3 is an easily identifiable, high-amplitude reflection. However, where it erodes Unit B, H3 is harder to distinguish from the parallel acoustic facies of Unit B. The top is defined by a high-amplitude reflection (H5) that truncates the infilling reflections of Unit D (Figure 5-2c, d).

Unit E: Unit E also occurs as the infill unit of an incision (H4) that cuts into the underlying Unit C (Figure 5-2a). The unit is divided in two subunits that have different acoustic facies. The basal subunit E1 consists of a divergent acoustic facies with sub-parallel, high-amplitude and high-frequency reflectors (Figure 5-2a). The upper subunit E2 has either a transparent (as visible on the Innomar SBP data; Figure 5-2a) or a prograding acoustic facies, with high-amplitude and high-frequency reflections (visible on the TOPAS SBP data). The top of Unit E is defined by horizon H5 or by the seafloor (Figure 5-2a). Its basal surface H4 displays two north-south valleys that are spatially aligned with those of H2 and are similarly divided by a topographic high or island (white dotted shape in Figure 5-3f). The eastern valley reaches depths of c. 67 m LAT and is c. 5-6 km wide in the south, becoming wider northwards (up to c. 12 km) (Figure 5-3f). Similar as for H2, a second island is visible in this eastern valley (white dotted shape in Figure 5-3f). The western valley is shallower (up to c. 64 m LAT) and slightly narrower (c. 4-5 km wide) (Figure 5-3f). Similar as observed for H2, the western valley cannot be traced further north due to the limited penetration of the Innomar SBP data (white hatched area in Figure 5-3f).

Unit F: Unit F is the youngest unit identified in the study area. It is discontinuous and displays a mostly transparent acoustic facies with some low-amplitude reflections (Figure 5-2). Where present, the unit either occurs as a blanket deposit overlying units A-E or as sand waves. The basal surface H5 is a widespread erosional surface that for a large part reflects the present-day bathymetry and thus the Axial Channel system (Figure 5-3g).

5.4.2 Sedimentary record

The lithofacies description, palaeoenvironmental proxies, OSL ages and/or other analyses (CT, XRF, grain size) are described and matched to the acoustic record (see Section 5.4.1, Table 5-2). Only Unit C and subunits B2 and D1 were not reached by any of the cores. The pollen analysis is quantitative (percentage diagrams can be found in Supplementary Figure S6 to Supplementary Figure S8), whereas for the mollusc and foraminifera analysis a qualitative characterisation is presented. OSL dating produced mostly reliable and robust burial dates (Table 5-3; see also Supplementary Report S9). Environmental dose rates vary across the samples as they are controlled by the geochemistry of the different lithologies (Table 5-3; Figure 5-4). For some samples, however, the reliability of the dates is low due to the dose limits imposed through saturation of the quartz OSL signal, which results in best-estimate and minimum-estimate ages (Table 5-3). Best-estimate ages are the two basal samples of AX05 (134 and 174 cm) and the top sample of VC09 (51 cm) (Table 5-3). A minimum-estimate age is obtained for the basal sample of VC09 (72 cm) (as indicated by the high palaeodose; Table 5-3). The reliability of the age from the sample at 174 cm of AX05 is too low as it shows signs of complete saturation and is therefore excluded from further interpretations (Table 5-3; see also Supplementary Report S9). Additionally, the depositional ages in AX05 at 97 cm depth and of AX11 at 192 cm depth are out of stratigraphic sequence (reversal). It is likely that these samples did not experience sufficient daylight prior to deposition to reset the luminescence signal, hence these ages are likely an overestimation and are excluded from further age interpretation (Table 5-3). For acoustic units where multiple samples were taken, a mean age was calculated (Table 5-3).

Table 5-2. Acoustic units identified within the study area with acoustic facies description, correlation to vibrocores, lithofacies description, depositional environment, correlation to marine isotope stages (MIS; Lisiecki and Raymo, 2005) and correlation with regional southern North Sea Formations (Busschers et al., 2025; Dakin et al., 2026; Stoker et al., 2011). See Figure 5-2 for examples of acoustic units.

Unit	Basal surface	Acoustic facies/characteristics	Reached by core	Lithofacies	Depositional environment	MIS	Stratigraphic formation (UK)
F		Various (mostly transparent)	AC07, AX05, AX07, VC15	Lf8: yellow-brown, medium-coarse sand; shell fragments	Marine	Holocene	Southern Bight Fm
	H5						
E		E2: Transparent (Innomar SBP)/ progradational (TOPAS SBP)	AC09	Lf7(iv): light brown, very fine silt-clay	Proglacial lacustrine	Late MIS3	Botney Cut Fm?
		E1: Divergent infill	AC07, AC09	Lf7: brown-red, silt-clay; rhythmic laminae (i-v)			
	H4						
D		D2: Divergent infill	AX07, AX11	Lf5 (AX07): brown-grey, fine sand; mica's; clay laminae; organics Lf6 (AX11): brown-grey, clay; thick fine sand laminae; mica's; organics	Tidal?	Early MIS3	/
		D1: Transparent-chaotic	/	/			
	H3						
C		Transparent-chaotic	/	/	Glaciofluvial?	MIS4?	/
	H2						
B		B3: Parallel	AX05, VC09	Lf4: dark grey, mottled clay-silt, organics	Shallow marine	MIS5a	Brown Bank Fm

	H1.2						
		B2: Transparent-chaotic	/	/	Shallow marine	MIS5b-a?	Brown Bank Fm
	H1.1 & H1*		VC09	Lf2: shell/gravel lag, medium sand matrix	Shallow marine (coastal)	MIS5b-c	
		B1: Transparent-chaotic	VC15	Lf3: dark grey, medium sand; silt stringers; shell fragments	Marine	MIS5e	Eem Fm
	H1		VC09, VC15	Lf2: shell lag, medium sand matrix	Shallow marine (coastal)	MIS6-5e	
A		Various	VC09, VC15	Lf1: dark grey, fine-medium sand; organics	Various	Pre-MIS6	Unspecified

Unit A

Lithofacies: Unit A was reached by VC09 and VC15 (Figure 5-4). Its lithofacies (Lf1) is a dark grey, well sorted, fine to medium sand facies with some black, organic-rich layers (with wood fragments). It is characterised by a high mica content and some thin clay stringers. This facies is indicative of a moderate-low energy environment with periods of slow-flowing or stagnant water (organic intervals).

Pollen: Both samples (at 80 and 86 cm in VC09) yielded sufficient pollen to meet the 100 TLP assessment count. The assemblage is dominated by *Pinus*, Cyperaceae and Poaceae. In the upper sample (80 cm) *Quercus*, *Corylus avellana*-type, Chenopodiaceae and *Pteropsida* (monolete) indet. are also prominent, whereas in the lower sample (86 cm) *Betula* is prominent. Also present in both samples are *Picea*, *Ulmus Empetrum nigrum*, *Calluna vulgaris*, *Cichorium intybus*-type and *Ophioglossum*. Bryophyta are also present in both samples along with *Tilletia sphagni*, representing *Sphagnum* communities. This pollen assemblage may represent the transition from local *Betula* and *Pinus* woodland to early temperate woodland within an area supporting heath communities, probably in proximity to the coast or an estuary. The assemblage is similar to the early Pastonian assemblage from Happisburgh II (West, 1980), pre-dating the Happisburgh III site dated to >0.78 Ma (Parfitt et al., 2010).

Molluscs: The sample in VC09 (65-95 cm) is barren in shells, and only wood and plant material was identified.

OSL: Only one OSL sample was taken from Unit A (VC09; Table 5-3). The dose rate to the quartz fraction is relatively low but the palaeodose is very high. The equivalent doses exceed the 2D0 threshold; however, the normalised OSL signals lie within the range of the regenerative dose curve. The age of 271.3 ka ± 23.1 is therefore a minimum estimate and the true depositional age is likely older (> 270 ka).

H1(*) and H1.1

Lithofacies: Horizons H1 and H1.1 are identified as high-amplitude reflectors in the acoustic data (see Section 5.4.1), but in the cores these surfaces correspond to a distinct sedimentary unit. Both units consist of the same lithofacies Lf2, which is identified as a shell lag. In VC15, H1 corresponds to a 5 cm thick unit characterised by numerous shells and shell fragments in a brown-grey fine sand matrix with some organic plant fragments. In that same core, H1.1 is a 17 cm thick unit consisting of a poorly sorted brown-grey medium sand matrix with numerous shells and shell fragments, as well as gravel of various sizes (< 5 cm) (Figure 5-4). In VC09, H1 is a c. 10 cm thick unit also consisting of shells, shell fragments and gravel of various sizes (< 5 cm) in a brown-grey medium sand matrix (Figure 5-4). A shell lag such as Lf2 is indicative of a high-energy, coastal marine depositional setting (e.g. active seafloor).

Molluscs: The samples for H1 (46-56/65 cm in VC09) and H1.1 (77-94 cm in VC15) show a very similar marine fauna with a mixed preservation of shells and shell fragments, including worn shells to shells with fine details and a preserved periostracum. The only distinct difference is that the shells and fragments from H1.1 (VC15) show a common reddish stain. In H1 (VC09), *in-situ* species identified are *Mya truncata, Spisula elliptica, Boreotrophon barvicensis, Astarte montagui* and *Modiolus modiolus* (Figure 5-5) whereas reworked species include *Ocenebra erinaceum*, *Lucinella divaricata,* common *Mimachlamys varia*. *In-situ* species for the sample of H1.1 (VC15) include *Mya truncata* and *Spisula elliptica* while worn species include *Diodora apertura*. The *in-situ* fauna for both H1 and H1.1 reflect a cool, marine, mixed soft and hard/firmground environment. The mixed *in-situ* and allochthonous species indicate a reworked sea floor, confirming the lithofacies interpretation. Notably in the sample from VC09 is the fragmentation of the *in-situ Mya truncata* (Figure 5-5). *Mya truncata* is a major food

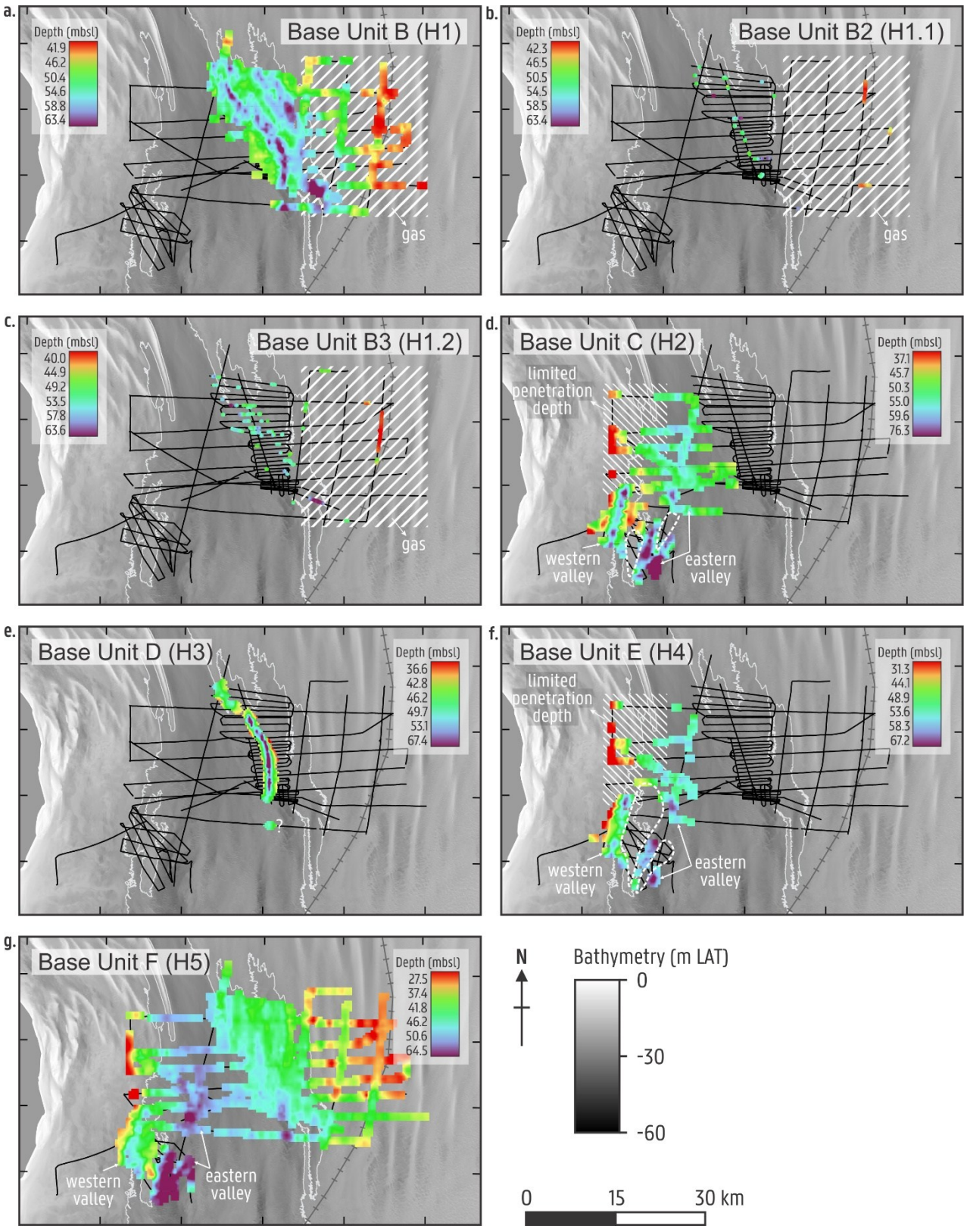


Figure 5-3. Distribution of the acoustic units' basal or top surfaces (depth structure maps) identified in the study area. The Axial Channel is delineated by the -40 m contour line (white line; Chapter 3). Topographic highs (islands) inferred from the absence of unit deposits and basal surface are indicated by white dotted shapes. White hatched lines mark areas where shallow gas occurs or where there is a limited penetration depth of the Innomar SBP data.

Table 5-3. Optically stimulated luminescence (OSL) results per acoustic unit and per core with indication of validity. Ages retrieved from polymineral fine fraction OSL indicated by (*). Ages used for calculating the mean age are indicated in blue. For additional information on OSL methodology and age interpretation see main text and Supplementary Report S9.

Unit	Core	Depth (cm)	Lab code	Palaeodose (Gy)	Dose rate (mGy/a)	Age ± 1 sigma error (ka)	Mean age ± 1 sigma error (ka)	Validity
F	AX05	97	cersa1206/12	7.2 ± 1.0	1.5 ± 0.11	4.8 ± 0.8	2.4 ± 0.3 *(n=2)*	outlier (reversal)
		101	cersa1206/13	4.7 ± 0.4	1.91 ± 0.14	2.5 ± 0.3		reliable
		105	cersa1206/14	4.7 ± 0.3	2.02 ± 0.19	2.3 ± 0.3		reliable
E	AC07	76*	cersa1768A*	87.2 ± 2.0*	2.77 ± 0.16*	29.5 ± 1.9*	29.2 ± 1.8 *(n=3)*	reliable*
		143*	cersa1768E*	66.9 ± 1.4*	2.00 ± 0.11*	31.5 ± 2.0*		reliable*
		269*	cersa1768G*	61.7 ± 0.9*	2.13 ± 0.11*	26.5 ± 1.6*		reliable*
D2	AX07	72	cersa1208/9	78.4 ± 4.0	1.45 ± 0.05	54.0 ± 3.4	56.1 ± 3.7 *(n=7)*	reliable
		82	cersa1208/10	81.0 ± 1.3	1.45 ± 0.05	55.7 ± 2.2		reliable
		90	cersa1208/11	82.7 ± 2.3	1.54 ± 0.10	53.5 ± 3.8		reliable
		97	cersa1208/12	70.9 ± 2.4	1.30 ± 0.09	54.6 ± 4.0		reliable
	AX11	175	cersa1210/18	58.6 ± 2.1	0.96 ± 0.05	61.0 ± 3.9		reliable
		192	cersa1210/20	88.0 ± 8.8	1.00 ± 0.07	87.9 ± 10.7		outlier (reversal)
		202	cersa1210/22	62.1 ± 2.2	1.07 ± 0.08	58.3 ± 4.6		reliable
		207	cersa1210/23	61.0 ± 1.7	1.10 ± 0.07	55.6 ± 4.0		reliable
B3	AX05	134	cersa1206/17	109 ± 15.5	1.47 ± 0.12	74.1 ± 12.2	72.2 ± 8.6 *(n=2)*	best-estimate
		174	cersa1206/19	175 ± 22.8	1.47 ± 0.12	119.1 ± 18.3		outlier (saturation)
	VC09	44	cersa1770A	138.7 ± 7.1	1.97 ± 0.10	70.2 ± 5.1		best-estimate
H1*	VC09	51	cersa1770D	104.3 ± 5.3	0.94 ± 0.05	94.5 ± 8.4	94.5 ± 8.4	reliable
B1	VC15	113	cersa1772A	116.7 ± 5.6	0.95 ± 0.07	122.2 ± 10.3	122.2 ± 10.3	reliable
H1	VC15	134	cersa1772D	162.3 ± 10.6	0.97 ± 0.07	144.8 ± 16.6	144.8 ± 16.6	reliable
A	VC09	72	cersa1770G	300.5 ± 15.7	1.11 ± 0.07	271.3 ± 23.1	> 270	minimum estimate

source for walrus, and its fragmentation is a typical sign of walrus predation. If these are indeed predation marks, it would mean that the North Sea likely had winter sea ice at that time.

OSL: Two distinct ages are retrieved from the OSL dating of the samples from the sedimentary unit corresponding to H1. The quartz dose rate and palaeodose for both OSL samples of H1 are low and did not approach saturation. The palaeodoses and corresponding ages are therefore considered reliable. An older OSL age of 144.8 ± 16.6 ka is retrieved from the sample at 134 cm in core VC15 (Figure 5-4), where this surface is directly overlain by subunit B1 (dated to 122.2 ± 10.3 ka; see Section Subunit B1). A younger OSL age of 94.5 ± 8.4 ka is retrieved from the sample at 51 cm in VC09 (Figure 5-4), where the surface is directly overlain by subunit B3 (dated to 72.2 ka ± 8.6; see Section Subunit B3). This stratigraphy suggests that the obtained age of H1 in VC09 does not represent the true depositional age but rather a reworking event, hereby indicated as H1*. The oldest age for H1 (134 cm in VC15, 144.8 ± 16.6 ka) therefore most likely reflects the initial depositional age. The age retrieved from the sample at 51 cm in VC09 (94.5 ± 8.4 ka), where H1* directly underlies subunit B3, represents the age of an event that caused partial bleaching of the OSL signal. Seeing the nature of the lithofacies of H1 (i.e. a shell lag), this event most likely represents a period of seafloor reworking (e.g. during transgression/regression). H1 is therefore interpreted as a heterochronic and/or composite surface.

Subunit B1

Lithofacies: Subunit B1 consists of lithofacies Lf3 and has been identified in core VC15 (Figure 5-4). It is a dark grey, medium sand facies with small shell fragments and finer grained silt stringers. Increasing shell fragments occur towards the top of the unit. The depositional environment for Lf3 reflects relatively stable conditions (moderate-low energy environment), whereas the presence of marine shells (see further) indicates a marine or brackish environment.

Molluscs: The lower sample (112-130 cm in VC15) in this unit is characterised by a few mixed marine species and shell fragments with mixed preservation; from worn and discoloured fragments to shells with preserved fine surface structures and some corrosion. Only two *in-situ* species could be determined: *Nucula nucleus* and *Hiatella arctica*. These are euhaline species that occur in deeper water, below storm wave base. In the upper sample (94-112 cm in VC15), a higher concentration of shells and shell fragments occur, alongside some rare bryozoans, echinoids and barnacles. This sample is again characterised by mixed marine species with a mixed preservation; both worn and corroded fragments as well as shells with fine details and sometimes a periostracum preserved. *In-situ* species are *Mya truncata* (with fine details and periostracum)*, Propebela nobilis, Lacuna pallida, Parvicardium* cf. *pinnulatum, Spisula elliptica, Boreotrophon, Gibbula tumida and cineraria, Modiolus modiolus, Heteranomia squamula* and *Astarte montagui*, alongside some *Hiatella* species (e.g. *Hiatella Propebela*) and worn *Mimachlamys* and *Nucula nucleus*. These are cool, marine species with a mix of both soft and hard/firmground species. The presence of *Lacuna* signifies the presence of brown algae, which in turn indicates a fauna in the deeper photic zone (≤ 60 m water depth). Worn species include *Solen margiantus*, *Anomia ephippium*, *Flexopecten flexuosus*, *Parvicardium exiguum*, *Diodora apertura, Digitaria digitaria* (however, reasonably well preserved) and one ashgrey *Cerastoderma edule* cf spp. *Major*. The identified *in-situ Mya truncata* displays fragmentation similar as identified in the underlying sedimentary unit of H1.1 (Figure 5-4; see Section H1(*) and H1.1), which could indicate walrus predation and thus similar cold climatic conditions. The distinct change between the lower and upper samples from subunit B1 therefore suggests a climate cooling accompanied by a transition to a shallower marine environment.

OSL: The depositional age for subunit B1 is provided from a single OSL sample in core VC15 at 113 cm (Table 5-3). This sample had no issues with OSL signal saturation and therefore the palaeodose and corresponding age are considered reliable. The depositional age of subunit B1 is 122.2 ± 10.3 ka.

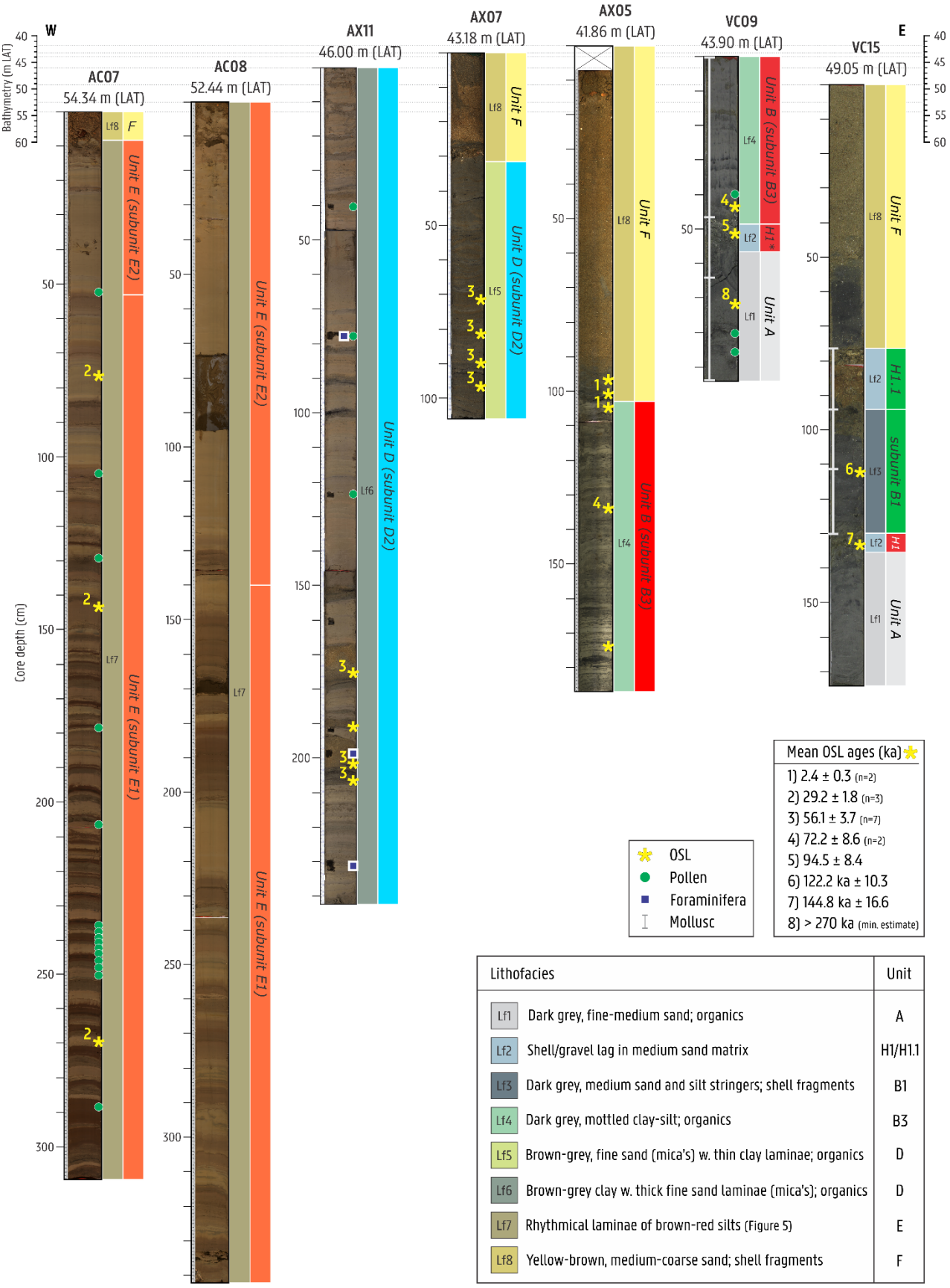


Figure 5-4. High-resolution line-scan images of the sediment cores with lithofacies description, correlation to the acoustic units and (mean) OSL ages (see Table 5-3). For geographic location of the cores see Figure 5-1, for location on the acoustic profiles see Figure 5-2.

Subunit B3

Lithofacies: Subunit B3 consists of lithofacies Lf4 and has been identified in cores VC09 and AX05 (Figure 5-4). It is a dark grey, mottled clay-silt facies with black, organic and mica rich very fine sand. Bioturbation is visible in the top 20 cm of both cores. Lf4 in VC09 contains a stiffer grey clay facies towards the top of the core. Facies Lf4 reflects a low-energy setting, possibly with relatively low sedimentation rates and oxic bottom conditions, typical for shallow-marine environments (e.g. Waajen-Labee et al., 2025).

Pollen: The sample (40 cm in VC09; Figure 5-4) yielded sufficient pollen to meet the 100 TLP assessment count. It contains an assemblage dominated by *Alnus* and monolete spores, with *Quercus*, *Betula*, *Vaccinium*-type and *Osmunda regalis*. Cyperaceae and Poaceae are further present. *Pinus* contributes less than 7% TLP, with *Ulmus* and *Corylus avellana*-type only present in low amount. The strong presence of *Alnus* would suggest a local damp woodland environment, with ferns forming the understorey.

Molluscs: In the sample from this unit (0-64 cm in VC09; Figure 5-4) very few shell fragments were present and only one *in-situ* species occurs, i.e. *Macoma balthica*. This species is indicative of low-energy, meso- to euhaline, shallow-marine (upper shoreface-intertidal) conditions.

OSL: The depositional age for subunit B3 is constrained by two OSL samples derived from VC09 (44 cm) and AX05 (134 cm) (Table 5-3). As subunit B3 comprises of heterogenous sediments (Lf4; Figure 5-4), the quartz dose rates and especially the palaeodoses for this unit are relatively high, showing signs of saturation (best-estimate ages) (Table 5-3). The average mean age (and standard deviation) for subunit B3 is 72.2 ka ± 8.6 (*n=2*), but these results may underestimate the true depositional age as fewer aliquots were accepted (see Supplementary Report S9).

Subunit D2

Lithofacies: Unit D consists of two subunits (D1 and D2) of which only subunit D2 was sampled by cores AX07 and AX11 (Figure 5-4). It comprises two different lithofacies: Lf5 present in AX05 and Lf6 present in AX11. Lf5 consists of interbedded grey (turned brown after splitting), mica-rich, fine sand and clay, with some black, organic-rich stringers (AX05; Figure 5-4). Lf6 is a grey (turned brown after splitting) laminated silty clay facies with a few thick (up to 10 cm) layers of mica rich, fine sand (AX11; Figure 5-4). Some black, organic-rich stringers are also present in Lf6 and occur mostly in the sand layers. The two lithofacies may reflect different energy conditions and/or a change in sedimentation rate throughout the subunit, but overall, they are indicative of a relatively low-energy depositional environment with relatively high sedimentation rates. The interbedded facies Lf5 may reflect heterolithic bedding, often associated with tidal environments (e.g. Nichols, 2010; Rieu et al., 2005).

Pollen: All three samples (40, 78 and 125 cm in AX11) show mostly boreal taxa (*Pinus*, *Betula*, *Picea*) with little temperate taxa (*Alnus*, *Corylus*, *Quercus*). In total between 50-70% of all pollen grains have been identified as tree pollen. Poaceae and Cyperaceae are also abundant. Badly preserved pollen and spore grains (characterised by torn or partially missing walls) were also counted and constituted c.13% of the total. The assemblage is consistent with those from other NW European Early Weichselian interstadials (e.g. Behre and Lade, 1986; Kasse et al., 2022; Zagwijn, 1983, 1961) and with the recently published record from the Brown Bank Fm (Waajen et al., 2024; Waajen-Labee et al., 2025). However, the badly preserved grains might indicate sediment reworking.

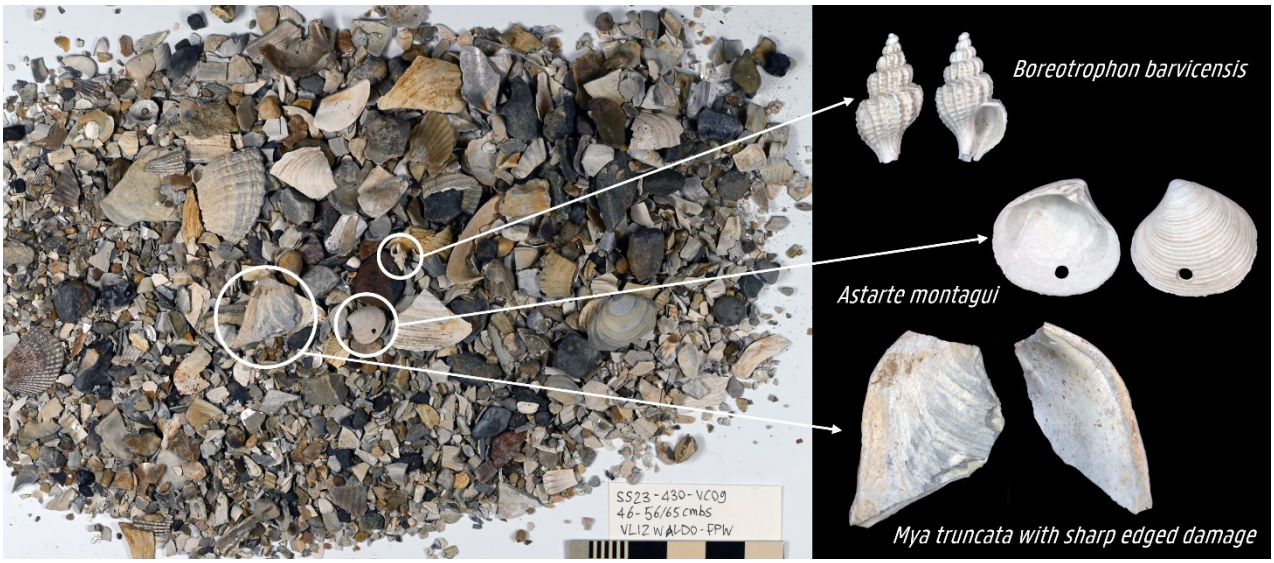


Figure 5-5. Mollusc assemblage of H1 (basal surface Unit B3) from core VC09 (46-56/65 cm; see Figure 5-4), with identified in-situ species Boreotrophon barvicensis, Astarte montagui and Mya truncata with sharp edged damage.*

Foraminifera: Foraminiferal assemblages are extremely sparse, with only a few specimens recovered from the analysed samples (78, 198 and 230 cm in AX11). Overall preservation is very poor, preventing reliable identification to genus or species level in most cases. Specimen abundance is low throughout the core and foraminifera are nearly absent within organic-rich deposits. Most recovered tests are highly abraded and fragmented, commonly exhibiting broken chambers, together with pervasive discolouration and brownish iron staining, which further hampers taxonomic identification. Therefore, only four taxa could be identified, all benthic in lifeform: *Ammonia* sp., *Quinqueloculina* sp., *Haynesina germanica* and *Aubignyna perlucida*. These taxa are generally associated with shallow-marine to brackish environments and may occur across estuarine, lagoonal, intertidal and shallow subtidal settings (Francescangeli et al., 2021, 2017; Frontalini et al., 2018; Issa, 2024; Murray et al., 2000; Selvam et al., 2025). The fragmented and abraded nature of the assemblage likely suggests reworking and transport of specimens. Given the restricted assemblages no further robust environmental interpretation can be derived.

OSL: Similar as for subunit B3, subunit D2 also comprises heterogeneous deposits (Lf5 and Lf6, Figure 5-4). However, all samples selected for dating were taken from the sandy intervals within this unit (cores AX07 and AX11; Table 5-3, Figure 5-4). The palaeodoses and corresponding ages for all samples are considered reliable as there were no issues with OSL signal saturation (except sample at 192 cm in AX11, which indicated an age reversal). Based on the unweighted combination of seven samples across cores AX07 and AX11, the deposition of Unit D most likely occurred at 56.1 ± 3.7 ka (Table 5-3).

Unit E

Lithofacies: Unit E, which consists of lithofacies Lf7, was recovered in AC07 (subunit E2) and AC08 (subunit E1, E2) (Figure 5-4). Lf7 consists of rhythmic bedding characterised by an alternation of four different layers or beds (< 5 cm thick) consisting of silty clay to very fine sand. The rhythmic beds are: (1) Lf7(i): mica-rich, mostly dark brown to grey coarse silt; (2) Lf7(ii): red-brown stiff, very fine silt-clay; (3) Lf7(iii): light brown, mica-rich, medium to coarse silt; and (4) Lf7(iv): light brown very fine silt to clay (Figure 5-6a). In the top 55 cm of AC07 only Lf7(iv) is present. AC08 mostly consists of Lf7(iv) that displays some colour variations, whereas some intervals of Lf7(iii) occur. Boundaries between the different beds are sharp, except between Lf7(iii) and Lf7(iv), where the transition can be gradual. In the coarser beds Lf7(i) and Lf7(iii), sedimentary structures like cross-lamination (Figure 5-6b close-up 1, 3) and flaser bedding (close-up 2; Figure 5-6b) occur. Additionally, on the CT-images cracks can be

observed that occur in specific beds (Lf7(i); arrows in Figure 5-6). The cracks are interpreted as primary sedimentary structures rather than (post-)coring artefacts. Not only because of their restricted occurrence at the top of Lf7(i) and the fact that they exhibit a downward-tapering V-shape (Figure 5-6c; e.g. Nichols, 2010), but also because of the lack of any infilling sediment. In some cases, high-density granules can be observed within these cracks (Figure 5-6c). These granules are composed of cemented very fine sand and silt grains (Figure 5-6c). It is, however, uncertain if the observed cracks are formed subaqueous (below or at the sediment interface) or through subaerial exposure (desiccation cracks). The T-shaped junctions as opposed to polygonal shapes could be in favour of a subaqueous interpretation (Figure 5-6c). However, a single-drying out event (immature desiccation cracks) could lead to a similar T-shaped appearance (S. Silver, personal communication; e.g. Haque et al., 2023). In this latter case, the fact that these cracks are not entirely infilled and only contain isolated cemented granules could be indicative of a fast-flooding event and immediate burial (S. Silver, personal communication). Regardless of their origin, Lf7 comprises a complex but overall low-energy depositional environment, with occasional periods of stagnant water as well as periods of flowing water (cross-lamination).

Pollen: In total fifteen pollen samples were taken from core AC07 where only two samples reached the desired 100 TLP count (at 108 cm and 242 cm). Other samples reached 45 (at 252.5 cm), 44 (at 252.5 cm) or less than 30 TLP. Most of the samples are dominated by pre-Quaternary spores. For the samples exceeding 40 TLP, the assemblage is dominated by *Pinus* and Poaceae, with *Betula* and monolete spores present in lower amounts. Within all four samples *Picea* was present, along with *Quercus*, *Alnus*, *Corylus avellana*-type, *Ranunculus acris*-type and Cyperaceae. *Ostrya carpinifolia*-type were only present in their trizonoporate form, making them likely to be *Ostrya carpinifolia*. Within the sample from 108 cm, Chenopodiaceae, *Empetrum nigrum* and *Saxifraga granulata*-type were present. It has been noted that in North Sea pollen assemblages, the presence of pre-Quaternary palynomorphs and only a small number of thermophiles are indicative of sedimentation in a cold or glacial climate (e.g. Ekman, 1998), with the former also used as a measure of reworked material. The presence of *Linum catharticum* is consistent with the British and Irish record where pollen and seeds were widespread in British glacial sites (Bell and Dickinson, 1971; Godwin, 1975; Reid, 1949; Watts, 1977; West, 2000). Also present in some samples were aquatic species, including *Potamogeton natans*-type, *Sparganium emersum*-type and *Typha latifolia*, all commonly found in freshwater environments (lakes, ponds, shallow wetlands). The dominance of pre-Quaternary spores within all samples suggests a high input of allochthonous material, which may also be the source of some of the pollen, including taxa such *Ostrya carpinifolia*-type which are usually associated with Early Pleistocene assemblages (e.g. the Yarmouth Roads Fm). Pollen concentrations are inversely proportional to the abundance of pre-Quaternary spores, possibly suggesting a dilution of contemporary Pleistocene pollen by high sedimentation rates. This relationship is also observed with the presence of *Pediastrum* and *Botryococcus*. These are both genus of green algae, the former widely found to inhabit freshwater environments (ponds and wetlands) (Jankovská and Komárek, 2000; Nielsen and Sørensen, 1992). The abundance of *Pediastrum* can be linked to climatic conditions with low productivity, such as reported during cold climate periods (e.g. Björck et al., 1994; Rundgren, 1995; Sarmaja-Korjonen et al., 2006). Fluctuations in the concentration of *Pediastrum* may reflect the dynamics of the wetland environment, including nutrient status, salinity or temperature (Gosling et al., 2008; Huang et al., 2021; Jankovská and Komárek, 2000; Nielsen and Sørensen, 1992; Turner et al., 2014; Van Geel, 2002). Sarmaja-Korjonen et al. (2006) have also noted that *Pediastrum* and other aquatic organisms may have been affected by turbidity, with periods of high input of allochthonous matter leading to both reduced productivity and dilution within the record. The pollen record therefore provides a taphonomically complex assemblage incorporating allochthonous reworked material along with some possible contemporary pollen floras.

OSL: The sediments of Unit E consist of clayey silts and very fine sands, which necessitated a quartz-enriched polymineral 4-11µm SAR OSL protocol. As no issues were reported for the OSL signal saturation, the palaeodose and corresponding age are considered reliable. The depositional age of Unit E is therefore estimated at 29.2 ± 1.8 ka based on the unweighted combination of three ages from AC07 (Table 5-3).

XRF HCA: The HCA and Euclidian distances suggested to subdivide the dataset into six different clusters with a similar geochemical composition. By plotting the clusters against depth, this subdivision provided the best correspondence with the different beds, keeping a good level of detail (Figure 5-6). The six clusters reflect compositional changes by identifying concurrent variations across all elements measured via the XRF core scanning. The geochemical data on which the clustering is based can be found in Supplementary Figure S10 and Supplementary Figure S11. Visual observation already led to the identification of four different beds that reflect four different clusters. However, the clustering analysis showed that both beds (i) and (iv) can be subdivided in two distinct (geochemical) signatures that reflect differences in grain size but also correspond to density changes, as observed in the CT images for these specific beds (Figure 5-6). In summary, cluster 2 and 3 (higher Si, Zr content) correspond to Lf7(i), cluster 4 (higher Al, S, Fe and Ti content) to Lf7(ii), cluster 6 (higher Ca, Sr and Ba content) to Lf7(iii) and cluster 1 and 5 (higher Mn and Ca content) correspond to Lf7(iv) (Figure 5-6; see also Supplementary Figure S10; Supplementary Figure S11).

Unit F

Lithofacies: Unit F was present in all cores, except AC08, AX11, VC09 (Figure 5-4). Its lithofacies Lf8 consists of yellow-brown, medium-coarse sand. In AX05, a coarsening-upwards trend is observed. Lf8 has abundant shells and shell fragments and sometimes contains gravel (≤ 1 cm). It represents a medium- to high-energy, marine setting (e.g. active seafloor).

OSL: Three OSL samples were taken close to the subunit B3 – Unit F boundary in core AX05 (Figure 5-4). Whereas the age from the sample at 97 cm is an outlier (age reversal), the ages from samples at 101 and 105 cm had no issues with OSL signal saturation and are therefore considered reliable. These ages are very similar and can both be correlated with Unit F (Table 5-3). The combination of the ages for Unit F therefore suggest deposition at 2.4 ± 0.3 ka.

5.5 Discussion

5.5.1 Pre-MIS6 deposits

The mostly transparent seismic facies of Unit A is not diagnostic for an unequivocal formation-level correlation (Table 5-2) given the marked variability of the southern North Sea Quaternary formations (e.g. Cameron et al., 1992; Rijsdijk et al., 2005). The OSL age of 144.8 ± 16.6 ka from sedimentary unit H1 in VC15 (Table 5-3) constrains the underlying Unit A to MIS6 or older, whereas the >270 ka age from Unit A in VC09 (minimum estimate; Table 5-3) and the retrieved pollen assemblage indicate deposition predating MIS8. These deposits could therefore comprise a long and/or multiple depositional timeframes. In contrast, the same lithofacies (Lf1; organic-rich, fine-medium sand) of VC09 and VC15 and the proximity of these cores to each other indicates a similar depositional environment, most-likely fluvial or deltaic given the lithofacies description and absence of shells, suggesting correlation to a single Early to Middle Pleistocene formation. The ages retrieved from the overlying younger units in the study area (Table 5-3) indicate the presence of a hiatus following deposition of Unit A.

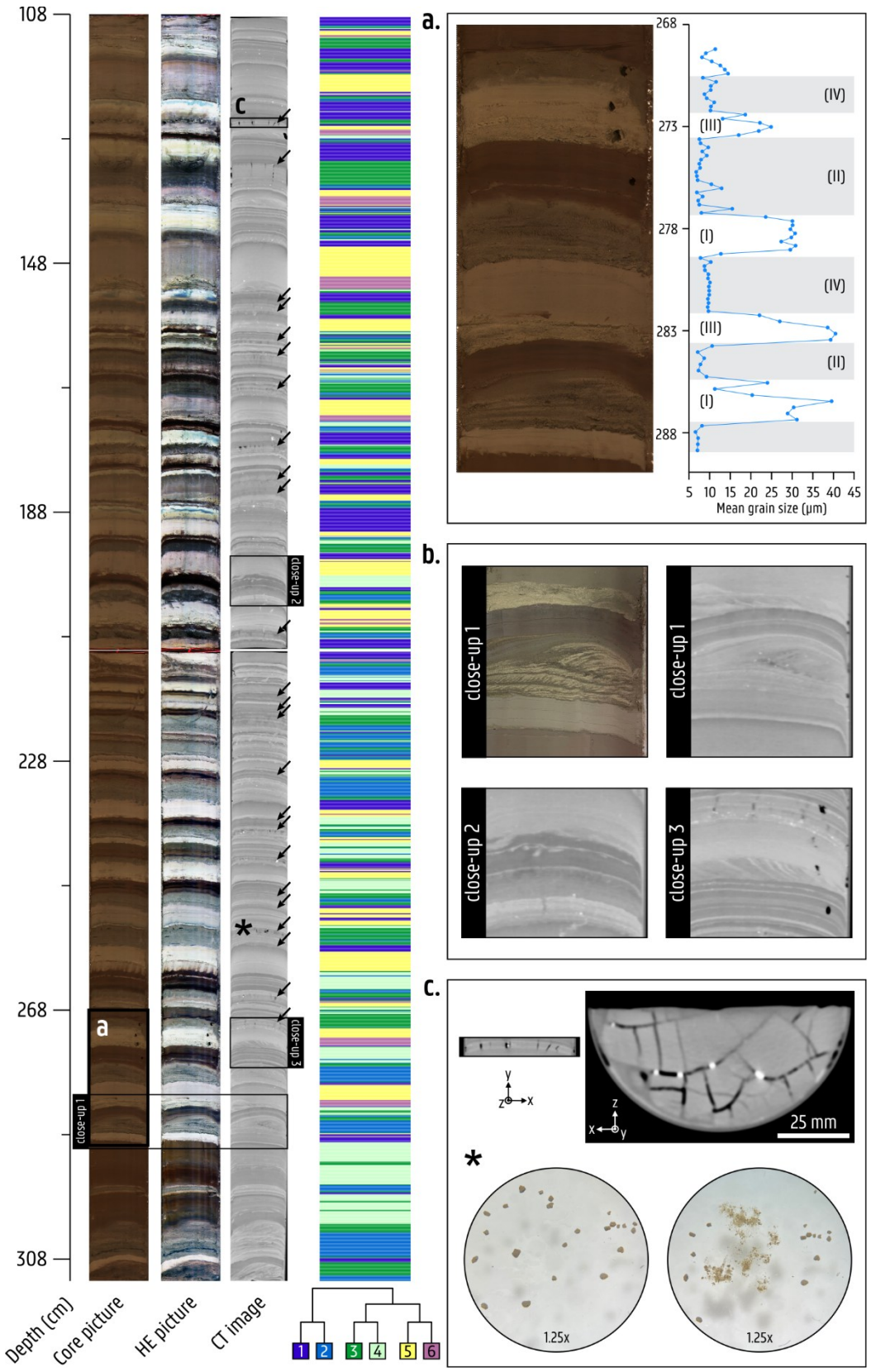


Figure 5-6. Compilation of sedimentological results, including a high-resolution line-scan, histogram equalised and CT scan image of sediment core AC07 (108 – 308 cm) next to the results of the hierarchical cluster analysis (HCA) based on the XRF data. (a) Grain-size distribution for a section of sediment core AC07 (c. 268-288 cm) plotted alongside the respective section of the core image. (b) Close-up (1, 2, 3) of sedimentary structures identified on the line-scan image and CT images. (c) Cross-view CT-image displaying the mud cracks (with arrows on CT-image for their occurrence throughout the core sections) and stereo microscope image of cemented granules.

5.5.2 Marine deposits of MIS5

In the southern North Sea region, the Eemian interglacial (MIS5e) and the Early Glacial period (MIS5d-a) are represented by two regional-scale formations: the Eem and the Brown Bank Fm, respectively (Cameron et al., 1992; Rijsdijk et al., 2005; Stoker et al., 2011). The Eem Fm has initially been mapped as an extensive formation across the region (Figure 5-1c; Cameron et al., 1984). However, some of its occurrence was subsequently re-interpreted and re-assigned to the older Egmond Ground Fm (MIS11-7; Cameron et al., 1992), leaving the Eem Fm preserved only in discontinuous patches that are acoustically difficult to distinguish from the Egmond Ground Fm (e.g. Cameron et al., 1992; Eaton et al., 2020; Limpenny et al., 2011). Thus far, the Eem Fm has not been conclusively identified in the study area (Dakin et al., 2026; Eaton et al., 2020; Waajen-Labee et al., 2025).

In this study, one unit (**Unit B**) can be assigned to MIS5 based on retrieved OSL ages. Based on its sandy lithofacies (Lf3) and the occurrence of a mixed marine mollusc assemblage, subunit B1 reflects a marine depositional setting. With an OSL age of 122.2 ± 10.3 ka (Table 5-3), centred on MIS5e, this indicates deposition during the Eemian interglacial, when eustatic sea level was comparable to or higher than today's sea level (Figure 5-7). The *in-situ* Eemian mollusc assemblage at the base of subunit B1 together with its sandy lithofacies further corroborates a positive correlation to the Eem Fm (Table 5-2; Cameron et al., 1992; TNO-GDN, 2026). The mollusc assemblage towards the top of this subunit indicates a transition to colder environmental conditions. Subunit B1 may therefore record both the warm interglacial conditions during the MIS5e highstand as well as the onset of climatic cooling associated with the MIS5e-d transition (Figure 5-7). Subunit B1 thus represents the first dated and described *in-situ* preserved Eemian deposits in the study area. Its spatial distribution (Figure 5-3b) supports the discontinuous occurrence of the Eem Fm across the wider southern North Sea region.

Subunit B3 is correlated with the Early Weichselian shallow-marine deposits of the Brown Bank Fm based on its acoustic facies, its grey mottled clay-silt lithofacies (Lf4) and a mean OSL age of 72.2 ± 8.6 (Table 5-2, Table 5-3). This age, however, may underestimate the true depositional age (see Section Subunit B3). The pollen assemblage indicates more temperate conditions compared to the boreal environment typically associated with the Brown Bank Fm (Waajen et al., 2024; Waajen-Labee et al., 2025). This discrepancy could be related to the fact that a single pollen sample was examined, which may not be representative of the whole unit. Waajen et al. (2024) interpreted the clay-rich sediments of the Brown Bank Fm as having been deposited in a shallow-marine environment during late MIS5a, when global eustatic sea level was 25-35 m below present mean sea level (bmsl) (Figure 5-7; Spratt and Lisiecki, 2016). The top of subunit B3 currently occurs at 42 m LAT (Figure 5-3g). Even without accounting for subsidence (less than -0.085 m/kyr; Cohen et al., 2022; Hijma et al., 2025) or glacio-isostatic adjustments, this depth is below the eustatic sea level suggested for MIS5a (Figure 5-7), supporting a shallow-marine depositional environment. Whilst subunit B2 was not sampled by any of the cores, it is tentatively correlated with the lower part of the Brown Bank Fm based on its transparent-chaotic acoustic facies resembling the basal unit BB1 described by Waajen-Labee et al. (2025) in the Dutch offshore sector. Following this reasoning, it is likely that subunit B3 corresponds to units BB2-BB4 of the Brown Bank Fm (Waajen-Labee et al., 2025). The lack of stacked subunits and/or multiple facies in subunit B3 can be explained by the relatively deeper offshore setting (42-63 m LAT; Figure 5-3g) compared to the study area of Waajen-Labee et al. (2025) (situated further east, at 34-59 m LAT). The more uniform acoustic character of subunit B3 may reflect a more stable or consistent depositional setting (also suggested by Waajen-Labee et al., 2025).

The **basal surface** (and corresponding sedimentary unit) of Unit B, **H1 or H1***, reflects a heterochronic and/or composite surface. An OSL age of 144.8 ± 16.6 ka was obtained for H1 (i.e. where it is overlain by subunit B1; Table 5-3), suggesting that the associated sedimentary unit was deposited during the

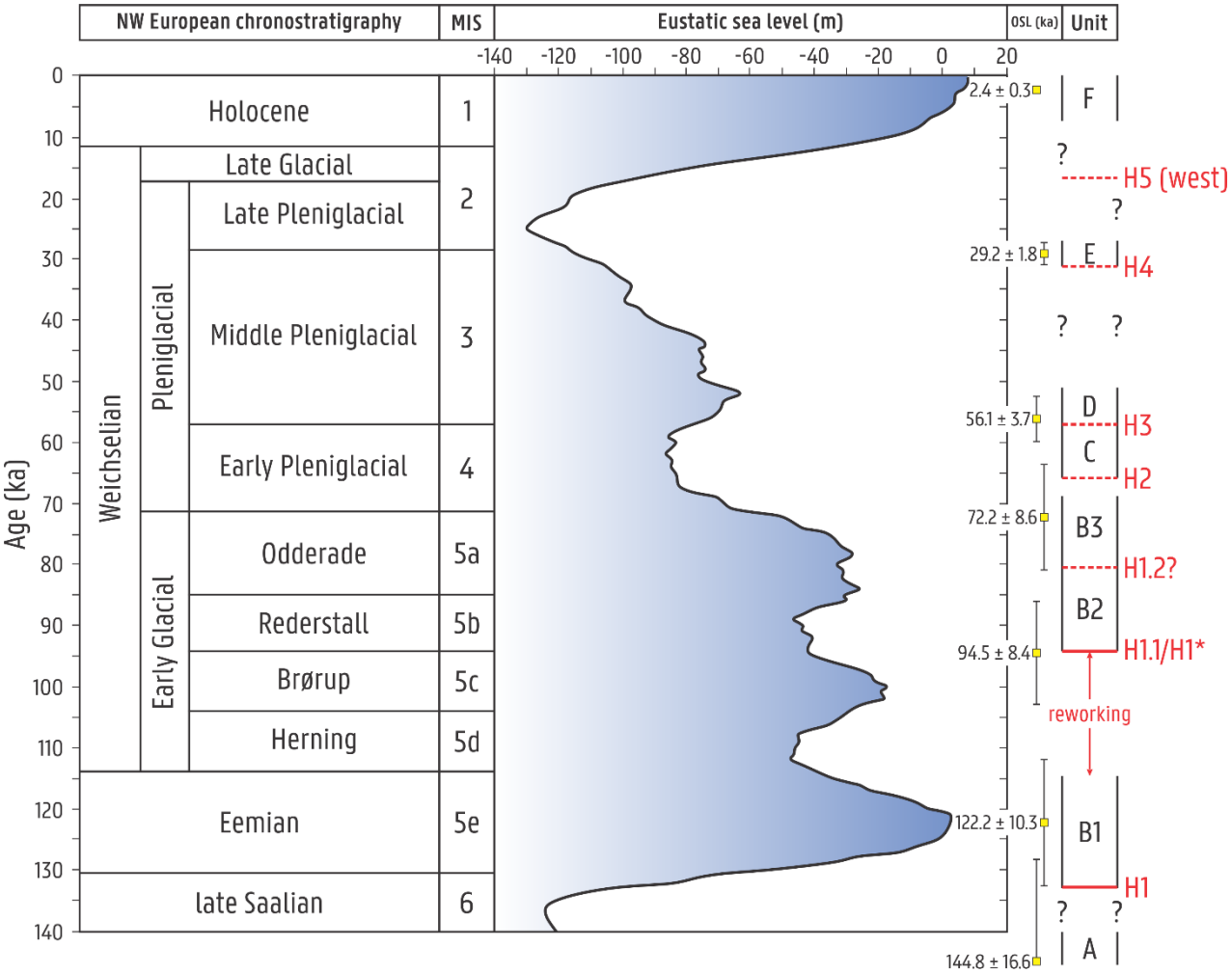


Figure 5-7. Late Pleistocene NW European chronostratigraphic stages, Marine Isotope Stages (MIS) (Lisiecki and Raymo, 2005) and eustatic sea-level curve (Spratt and Lisiecki, 2016) with (mean) OSL ages (± 1 sigma error bar) in ka and corresponding acoustic (sub-) units identified in this study. Figure adapted from Waajen et al. (2024).

latest phase of MIS6 (Figure 5-7). Considering the Eemian age correlation of the overlying deposits and the error range on the retrieved OSL age for H1, this surface most likely formed during the transgression at the onset of the Eemian (Figure 5-7). For H1* (directly overlain by subunit B2 and/or B3, with subunit B1 missing), a depositional age of 94.5 ± 8.4 ka was obtained (Table 5-3), corresponding to the MIS5c-b transition (Figure 5-7). The associated reworked mollusc assemblage is indicative of a marine environment with conditions cold enough to allow the development of winter sea ice. This surface is therefore attributed to the Rederstall stadial (MIS5b; Figure 5-7). These interpretations for H1 and H1* and correlations to the eustatic sea-level curve are consistent with the lithofacies interpretations for an active or reworked seafloor (see Section H1(*) and H1.1). The OSL chronology supports a two-phased development: an initial depositional phase associated with H1 (and subunit B1) followed by a reworking phase, represented by H1* and subsequently overlain by subunit B2 and/or B3 (Figure 5-8). The nearly identical mollusc assemblages observed for H1* (in VC09) and H1.1 (in VC15) further suggests a correlation of these two surfaces to the same reworking event (Figure 5-8). The increasing shell abundance at the top of subunit B1 and gradual transition from subunit B1 to surface H1.1 (in VC15) indicates a rapid onset of reworking. The fragmentation of *Mya truncata* in both H1* (VC09) and the top of subunit B1 (VC15) indicates a similar cold environment, whereas the retrieved OSL ages suggest an extended period of these climatic conditions. This suggests that the onset of reworking of H1.1/H*started during MIS5d and persisted until MIS5b, potentially with limited or no reworking during the higher sea levels of MIS5c (Figure 5-7; Figure 5-8).

5.5.3 Filling the gap: deposits correlated with MIS4-3

The current understanding of the depositional environment in the Axial Channel region during MIS4-3 remains limited because of a presumed stratigraphic hiatus between MIS5a (Brown Bank Fm) and MIS1/Holocene (multiple formations; Cameron et al., 1992; Rijsdijk et al., 2005; Stoker et al., 2011). Further east, on the Dutch continental shelf, fluvial deposits of the Kreftenheye Fm span the MIS6-1 interval (Figure 5-1c; Busschers et al., 2025; Cameron et al., 1984). Additionally, in areas towards the Dogger Bank (Figure 5-1a), glacial, periglacial and aeolian deposits of a (late) Weichselian age have been identified. These include the Dogger Bank Fm, Bolders Bank Fm and Botney Cut Fm (UK) (or Dogger Bight Fm (NL)) and Twente Fm (UK) (or Boxtel Fm (NL)) (Figure 5-1c; Cameron et al., 1984; Rijsdijk et al., 2005; Stoker et al., 2011).

In this study, three units (C, D and E) are identified above subunit B3 (Brown Bank Fm) and below the Holocene sediments of Unit F, partly filling the stratigraphic hiatus. Due to the absence of ground-truth data and chronological control, uncertainties remain surrounding the depositional environment for **Unit C** and the nature of the incision at its base (H2). Nevertheless, the unit's transparent-chaotic acoustic facies as well as the erosional nature of H2 suggests high-energy conditions (e.g. Nanda, 2021) following the MIS5a shallow-marine interval in the study area. During early MIS4, global sea levels dropped to 80-90 m bmsl (Figure 5-7; Spratt and Lisiecki, 2016). This considerable sea-level fall would have exposed the southern North Sea as a terrestrial landscape (e.g. Hijma et al., 2012). Under these conditions, H2 likely resulted from a fluvial incision restricted to the western Axial Channel (Figure 5-3d) during the Early Pleniglacial (MIS4; Figure 5-7). This incision therefore provides the first direct evidence of activity in the Axial Channel system (see also Section 5.5.4), whilst this erosional event may account for the (partial) removal and absence of preserved deposits of Unit B (including subunit B3/Brown Bank Fm) in the western sector (Figure 5-3a-c).

Horizon H3, which erodes all underlying units and boundaries, and the overlying **Unit D** correspond to an infilled c. 35 km long incision in the central part of the study area (Figure 5-3e). Unit D has a mean OSL age of 56.1 ± 3.7 ka, corresponding to early MIS3 (Middle Pleniglacial; Figure 5-7). However, its pollen assemblage resembles assemblages reported from NW European MIS5a records and records from the Brown Bank Fm (see Section Subunit B3; Waajen et al., 2024; Waajen-Labee et al., 2025). The poor preservation of pollen and foraminifera suggest sediment reworking. This reworked microfossil assemblage together with the lithofacies similarities to subunit B3 (Lf3 compared to Lf5/6) suggests

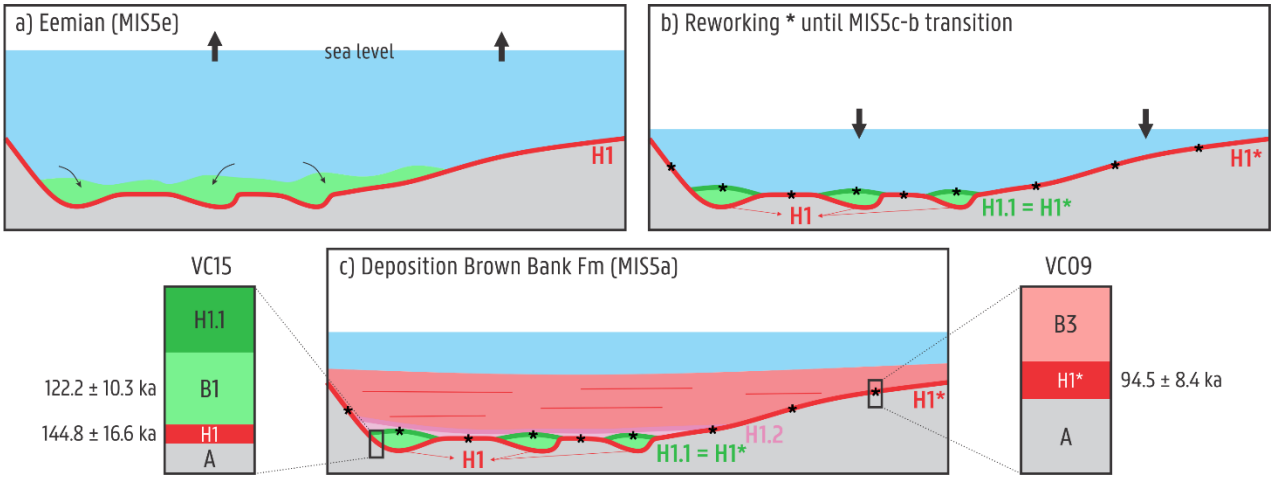


Figure 5-8. Schematic representation of (a) deposition of the Eem Formation during the Eemian interglacial (MIS5e); (b) reworking of surface H1 (= H1) and H1.1 throughout MIS5d and MIS5c (until MIS5c-b transition); and (c) deposition of the Brown Bank Formation during MIS5a and schematic visualisation of cores VC09 and VC15 (see main text for additional information).*

that Unit D largely comprises reworked deposits of the Brown Bank Fm. The internally stratified acoustic facies of subunit D2, the heterolithic bedding of this subunit's lithofacies (Lf5) and the channel morphology of H3 (i.e. deepening in the centre and shallowing towards its northern and southern end) are characteristic of (inter-)tidal channels (e.g. Rieu et al., 2005; Ronchi et al., 2018). The eustatic sea level during early MIS3 rose from c. 80 m to 60 m bmsl (Figure 5-7; Spratt and Lisiecki, 2016). Without applying subsidence and glacio-isostatic corrections, the base of the incision (up to 67 m LAT) is broadly comparable to the eustatic sea level during this interval. H3 is therefore tentatively attributed to a tidal channel that formed during early MIS3, where the initial incision under high-energy conditions is evidenced by the chaotic basal infill (subunit D1).

Unit E, occurring isolated along the western margin of the Axial Channel, has a depositional age of 29.2 ± 1.8 ka, corresponding to the MIS3-2 transition (Middle to Late Pleniglacial; Figure 5-7). Eustatic sea level at that time reached 115-120 m bmsl (Figure 5-7; Spratt and Lisiecki, 2016), linked to the expansion of the BIIS and FIS (e.g. Clark et al., 2022). After a brief marine interval during early MIS3, the southern North Sea became once more an emerged, terrestrial environment (e.g. Hijma et al., 2012). This unit's basal surface (H4; Figure 5-3f) shows strong similarities to H2 (Figure 5-3d) and is similarly interpreted as a fluvial incision, indicating renewed occupation of the western Axial Channel system (see also Section 5.5.4). Based on the correlation of the infilling deposits (Unit E) with the MIS3-2 transition, this occupation phase is assigned to the late MIS3 period, when sea level was falling (Figure 5-7; Spratt and Lisiecki, 2016). Unit E is therefore interpreted as having been deposited after the incision under low-energy conditions, as evidenced by the internally stratified acoustic facies and the characteristic rhythmically laminated lithofacies (Lf7). Its pollen assemblage reflects a cold environment and is consistent with the glacial conditions of the MIS3-2 transition (Clark et al., 2022; Lisiecki and Raymo, 2005). The relatively thick rhythmic bedding of Lf7, together with the similar OSL ages (all overlapping within the error margins; Table 5-3) and the strongly reworked pollen component suggest high sediment input and rapid deposition. The cold, freshwater conditions inferred from the pollen data, combined with the rhythmic geochemical alternations identified from the XRF clustering, may indicate seasonal varves, typical of peri- or proglacial lacustrine environments (e.g. Smith and Ashley, 1985; Zolitschka et al., 2015). Overall, Unit E is interpreted to represent a low-energy, likely proglacial lacustrine environment within the pre-existing Axial Channel system following the high-energy fluvial incision (H4). Based on the regional stratigraphic frameworks, the parallel acoustic facies and glaciolacustrine character of Unit E are compatible with the Botney Cut Fm, commonly associated with infill of glacial valleys and basins (Busschers et al., 2025; Cameron et al., 1992; Rijsdijk et al., 2005; Stoker et al., 2011). However, a range of late Weichselian channel and basin fills generated by different sedimentary processes have been correlated with this formation, and its internal stratigraphic subdivision and depositional interpretation remain variable (Dakin et al., 2026). Consequently, a correlation of Unit E with the Botney Cut Fm remains tentative.

The occurrence of an internally stratified acoustic facies in the southern North Sea has often been used as a diagnostic characteristic of the Brown Bank Fm. For example, a sediment core located c. 2 km northeast of AC07 contains deposits that correspond in location and lithology to our identified Unit E. An OSL age of c. 30 ka has been obtained from these sediments (Limpenny et al., 2011), consistent with our dating of Unit E. Nevertheless, Limpenny et al. (2011) assigned these deposits to the shallow-marine Brown Bank Fm based largely on their similar internally stratified acoustic signature. In another example, deposits 10 km northwest of the northern extent of incision H3 were correlated with the Brown Bank Fm in an archaeological study (Wessex Archaeology, 2015). However, the retrieved OSL age of c. 50 ka (Wessex Archaeology, 2015) instead more likely correlates these deposits with our Unit D, which is stratigraphically younger. Units D and E therefore demonstrate that internally stratified acoustic facies are not exclusive to the Brown Bank Fm and may represent different depositional conditions (e.g. Unit E) or indicate a similar depositional setting at a different time (e.g. Unit D).

The identification of Units C, D and E in the study area challenges the concept of a depositional hiatus between MIS5a and MIS1 in the Axial Channel region. Instead, these units preserve a detailed record of the MIS4-3 interval, a period characterised by rapid sea-level and climatic fluctuations (Figure 5-7). Although relative sea level in the southern North Sea may have deviated from the global eustatic record, particularly during MIS4 and MIS2 when glacio-isostatic adjustments associated with ice-sheet growth likely influenced local sea levels (e.g. Gibbard et al., 2022), our data suggest that there is an overall agreement between local and eustatic sea-level trends (Figure 5-7).

5.5.4 Evolution of the Axial Channel system

The identification of the different units together with new chronological constraints and palaeoenvironmental data (pollen, molluscs and foraminifera) provides new insights into the evolution and occupation history of the central and northern Axial Channel system. Integrated with existing reconstructions of NW European rivers (Rhine, Meuse, Scheldt and Thames), these data allow a palaeogeographic reconstruction of the wider study area throughout the (Late) Pleistocene (Figure 5-9).

Early to Middle Pleistocene (pre-MIS6)

The present dataset offers limited insights into the Early and Middle Pleistocene and existing interpretations remain largely unchanged. As previous research has indicated, the southern North Sea formed a shallow-marine, near-shore environment dominated by large, northward-prograding deltaic systems throughout most of the Pleistocene (c. 2.6 – 0.45 Ma; e.g. Cameron et al., 1992; Gibbard and Lewin, 2016; Ottesen et al., 2018). During the Elsterian glaciation (MIS12), major river systems, including the Thames and Scheldt, were diverted southward for the first time (Gibbard et al., 1988; Hijma et al., 2012). The Rhine and Meuse likely underwent a similar southward diversion, merging with proglacial drainage systems south of the ice margin, although direct evidence for this reorganisation remains lacking (Busschers et al., 2025; Hijma et al., 2012). The newly collected data cannot provide a conclusive answer whether these rivers converged into a precursor Axial Channel system south of our study area (with our study area largely covered by the Elsterian ice sheet; Figure 5-1a). Thus far, evidence for such a major glaciofluvial system remains limited to indirect indications in the Strait of Dover and the English Channel (e.g. Collier et al., 2015; Gupta et al., 2007).

The earliest evidence for southward diversion of the Rhine-Meuse system dates to the late Saalian glaciation (MIS6; Busschers et al., 2008; Hijma et al., 2012). Existing reconstructions indicate that the confluence of the Rhine-Meuse and Thames systems, and subsequent concentration of flow into the Axial Channel system was located south of our study area (Figure 5-9a; Busschers et al., 2025, 2008; Hijma et al., 2012). The depth structure map of H1 (base of Unit B; see also Section 5.5.2) reveals a broad central depression and two NNW-SSE oriented valleys (Figure 5-3a). In Chapter 4 it was proposed that the basal surface of the Brown Bank Fm may represent an older, late Saalian glaciofluvial drainage system. Consistent with this interpretation, surface H1 may therefore preserve a late Saalian palaeotopography. Two hypotheses can be proposed for the central depression and associated valleys in H1: (i) southward drainage from the Saalian ice margin that merged with the diverted Rhine-Meuse system, similar to the reconstruction of Busschers et al. (2025) (Figure 5-9a); or (ii) postglacial re-organisation of the (Rhine-) Meuse, involving a northward shift in drainage direction. This latter interpretation is less likely, as previous studies suggest a northward diversion of the Rhine (Busschers et al., 2008; Peeters et al., 2016), significantly further to the north to be directly connected to H1 in our study area.

Marine regime during the Eemian and Early Glacial (MIS5)

A marine setting in the Axial Channel region is evidenced by deposits of subunit B1, which is correlated with the Eem Fm and indicates open-marine conditions during the Eemian interglacial (MIS5e; inset on Figure 5-9b). Following deposition of these Eemian sediments, relative sea level fell and the Axial Channel region evolved into a shallow-marine (to coastal) environment, represented by surface H1.1/H1* (MIS5c-b; Figure 5-7). Relative sea levels rose again during late MIS5b and MIS5a, although not as high as Eemian highstand levels, allowing deposition of the Brown Bank Fm (subunit B2 and B3) (Waajen et al., 2024; Waajen-Labee et al., 2025). The gradual transition from subunit B1 to surface H1.1 observed in VC15 together with the preservation of MIS5c-b deposits in this surface, suggests that the study area remained submerged throughout MIS5. The Axial Channel region thus experienced a succession of open marine to coastal and subsequently shallow(er) marine conditions during this period.

The cooler fauna recorded at the top of the Eem Fm (across the gradual transition from subunit B1 to surface H1.1 in VC15; Figure 5-4) is substantially different from that of the Brown Bank Fm. Whereas the latter is characterised by predominantly high boreal to arctic species (Waajen-Labee et al., 2025), the assemblage identified at the top of the Eem Fm in this study is indicative of cool, boreal conditions (see Section Subunit B1). This contrast may reflect a changing palaeogeography during MIS5. During MIS5e, the southern North Sea likely maintained an open connection with the Atlantic Ocean through the English Channel and the Strait of Dover, whereas this connection may have been restricted or absent following MIS5e, particularly during late MIS5a (Figure 5-9b). Such a disconnection could explain the strong cooling of marine habitats in the southern North Sea, resulting in the dominance of boreal and arctic species during MIS5a and the development of a cold embayment, as proposed by Waajen-Labee et al. (2025).

Early Pleniglacial (MIS4)

Following deposition of the Brown Bank Fm, a large-scale erosional event (resulting in surface H2) occurred in the western Axial Channel region, which is correlated with the early MIS4 sea-level fall (Section 5.5.3; Figure 5-7). H2 records a broad (c. 30 km wide) meandering channel containing two preserved streamlined islands (Figure 5-3d), indicating a fluvial origin (Figure 5-9c). The tapered southern tip of these islands suggests a southward drainage (Figure 5-9c). The identification of this drainage route provides new insights into the MIS4 glacial period, for which direct sedimentary evidence has thus far been lacking in the present-day southern North Sea (Gibbard et al., 2022; Graham et al., 2011). Recent studies have linked MIS4 to extensive ice-sheet advance in the North Sea region (Batchelor et al., 2019; Gibbard et al., 2022; Gowan et al., 2021). During this period, drainage through the Strait of Dover is inferred from sedimentary records in the Bay of Biscay, which indicate a watershed comprising northern French, Belgian and southern British river systems (Toucanne et al., 2023). These likely included the Scheldt and Meuse systems (Figure 5-9c; Busschers et al., 2025; Hijma et al., 2012; Toucanne et al., 2023; Waajen-Labee et al., 2025). However, the absence of a Baltic derived signal in these sedimentary records suggests that meltwater from the FIS and northern European river systems did not drain southward through the English Channel but instead flowed northward (Toucanne et al., 2023). This implies that (1) the BIIS and the FIS did not coalesce into a continuous grounded ice sheet, therefore allowing subglacial drainage or (2) (more likely) a terrestrial corridor remained between opposing ice lobes (see discussion in Toucanne et al., 2023). The morphology of H2, characterised by a curving shape and southward deepening (Figure 5-3d), is consistent with drainage from a northern ice margin. This ice margin would have been located north of the Norfolk Coast of East Anglia (Figure 5-1a, inset on Figure 5-9c), as suggested by the maximum MIS4 reconstructions from Batchelor et al. (2019). South of our study area, this drainage likely followed pre-existing topographic lows, interpreted as remnants of MIS6 Rhine-Meuse pathways, before connecting to the English Channel via the Strait of Dover (Figure 5-9c). As no sedimentological

data are available for the infilling Unit C, linking the deposition of these sediments to this MIS4 drainage event remains tentative.

The sea-level fall at the start of MIS4 is associated with widespread fluvial incision across NW Europe (Hijma et al., 2012 and references therein). During this period, the Rhine and Meuse extended their courses into the southern North Sea (Hijma et al., 2012; Waajen-Labee et al., 2025). The Rhine developed into an extensive braid plain that eroded the deposits of the Brown Bank Fm northeast of our study area (Figure 5-9c; Periplus Archeomare, 2023; Waajen-Labee et al., 2025). In our dataset, the top of subunit B3 forms an erosional surface (indicated as H5; e.g. Figure 5-2b, d). Given the absence of depositional units between subunit B3 and Unit F in the eastern part of the study area, erosion of subunit B3/Brown Bank Fm in this area could also be related to the early MIS4 sea-level fall and Rhine braid plain. This reasoning suggests that H5 represents a heterochronic surface.

Marine incursion during early MIS3

Following MIS4, deglaciation of the BIIS and FIS led to a relative sea-level rise (Figure 5-7; e.g. Gowan et al., 2021; Spratt and Lisiecki, 2016). The deposits of Unit D, correlated with this early MIS3 transgression (Figure 5-7), are interpreted as evidence for renewed marine inundation in the southern North Sea (Figure 5-9d). The extent of this inundation, however, remains uncertain. Likewise, the interpretation of H3 as a tidal channel remains tentative, primarily due to the absence of *in-situ* microfossils. It further remains unclear why a tidal channel would have developed c. 10 km east of the previously established MIS4 western Axial Channel (Figure 5-3d, e; Figure 5-9c, d). In addition, the complete infill of this incision by reworked deposits from the Brown Bank Fm (Unit D) is not observed in the western Axial Channel. It is however possible that the infill comprising Unit C in the western Axial Channel is also related to the early MIS3 marine inundation, with the pre-existing western Axial Channel acting as a marine and tidally active conduit rather than having a glaciofluvial depositional origin (see previous section). The similar transparent-chaotic facies observed in Unit C and subunit D1 may support this interpretation. With the absence of sedimentological data, however, the depositional environments of both Unit C and subunit D1 remain uncertain. Consequently, the relationship between the western Axial Channel (H2 – Unit C) and the H3 tidal channel (Unit D) remains unresolved.

As proposed by Waajen-Labee et al. (2025), sea-level fluctuations during MIS4 and early MIS3 likely displaced the Rhine braided river plain northeastward, enabling further erosion of the top of subunit B3/Brown Bank Fm (see previous section; Figure 5-9d). A marine incursion during early MIS3 has also been suggested by Waajen-Labee et al. (2025), who identified a clay interval overlying the Brown Bank Fm east of our study area that may represent a fresh-brackish to shallow-marine depositional environment (core BP050087).

Middle to Late Pleniglacial (MIS3-2)

The remainder of the Middle Pleniglacial was characterised by a substantial drop in sea level and progressive climatic cooling (Clark et al., 2022; Lisiecki and Raymo, 2005; Spratt and Lisiecki, 2016). Horizon H4 is linked to the development of a (glacio-)fluvial system that formed during the late MIS3 sea-level fall (Figure 5-7). Erosion is again confined to the western Axial Channel, where reoccupation of channels established as part of a MIS4 drainage system further shaped the streamlined islands (Figure 5-3f; Figure 5-9e). The morphology of both the channel and the streamlined islands indicate southward drainage (Figure 5-3f; Figure 5-9e). Fluvial incision likely persisted until the maximum glacial extent was reached at c. 30 ka, where reconstructions indicate the presence of an ice lobe of the BIIS along the Norfolk Coast of East Anglia (Figure 5-1a; Figure 5-9e; Clark et al., 2022). During this maximum

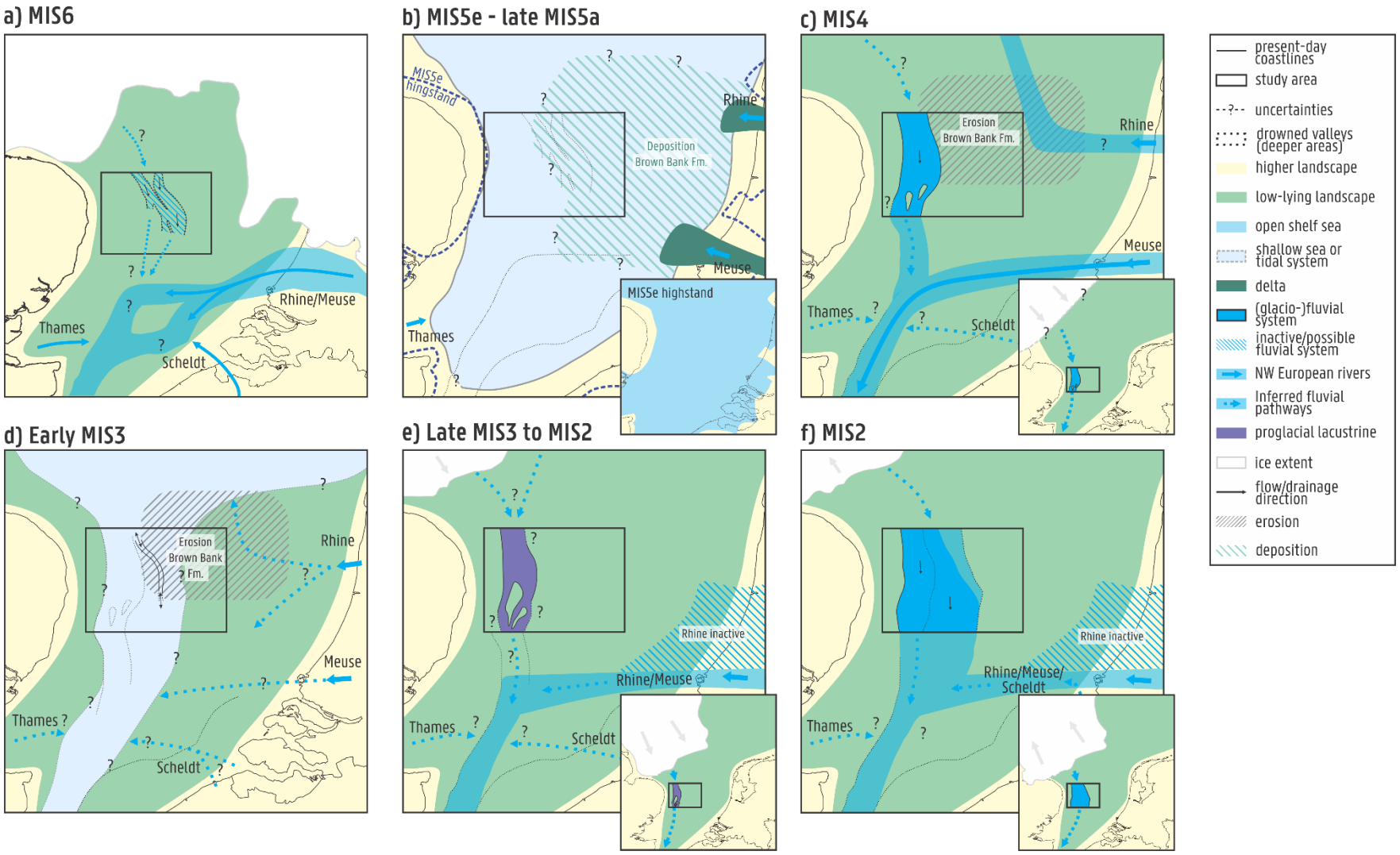


Figure 5-9. Palaeogeographic evolution of the southern North Sea, focussing on the Axial Channel system with snapshots at: (a) MIS6; (b) MIS5e and late MIS5a; (c) MIS4; (d) early MIS3; (e) late MIS3 to MIS2 transition; and (f) MIS2. Courses of the Thames, Scheldt, Rhine and Meuse are adapted from Busschers et al.(2025); Hijma et al. (2012); Slupik et al. (2013). Coastline positions during (b) MIS5e and MIS5a are adapted from Hijma et al. (2012) and Waajen-Labee et al. (2025), respectively. Glacial limits during (a) MIS6 after Batchelor et al. (2019) and Busschers et al. (2025); (c) MIS4 after the maximum limit reconstructions from Batchelor et al. (2019); and (e) late MIS3 to MIS2 transition and (f) MIS2 after the maximum limit reconstructions from Clark et al. (2022). The present-day coastline (black lines) and study area (rectangle) are indicated for geographical reference. Dashed lines and question marks indicate uncertainties in exact location and/or extent.

advance, colder and drier climate conditions persisted. These glacial conditions are reflected in the deposits of Unit E, which are rhythmically bedded sediments deposited in a proglacial lake environment (see Section 5.5.3). These sediments imply deposition in an enclosed lacustrine environment characterised by continuous sediment accumulation under low-energy conditions. Owing to subsequent erosion of Unit E by H5, the original extent and morphology of this sheltered lacustrine setting cannot be reconstructed. The rhythmically bedded lithofacies of Unit E together with the absence of ice-rafted debris (e.g. dropstones) indicate deposition in a distal proglacial lacustrine environment (e.g. Carrivick and Tweed, 2013). Only the maximum 29-31 ka ice-margin reconstructions of Clark et al. (2022) locate an ice margin in proximity to our study area, with an ice lobe along the Norfolk Coast of East Anglia (Figure 5-1, inset Figure 5-9e).

Further evidence supporting the maximum ice limit reconstructions of Clark et al. (2022), but also proglacial lake development during the MIS3-2 interval has recently been reported south of the Dogger Bank, north of our study area (Figure 5-1a). In this area, more ice-marginal conditions resulted in the accumulation of massive fine-grained deposits containing dropstones, associated with the c. 31 ka maximum ice extent (Kyriakoudi et al., 2026). The identification of Unit E therefore suggests that in addition to the network of smaller ice-proximal proglacial basins recognised in the Dogger Bank region during the MIS3-2 transition (Emery et al., 2019; Kyriakoudi et al., 2026), a more-extensive distal proglacial system may have existed further south within the southern North Sea Basin.

Late Glacial (MIS2) and Holocene

The heterochronic nature of surface H5 is evident from its erosion of the Brown Bank Fm (subunit B3) in the eastern part of the study area, which likely records prolonged erosion during MIS4 and MIS3. In the centre and to the west, H5 reflects an up to 30 km wide depressional feature that may represent the erosional expression of a major drainage event. This event can be linked to the climate warming after the Last Glacial Maximum (LGM, MIS2), which triggered ice-sheet retreat and large-scale glaciofluvial drainage towards the Strait of Dover (Toucanne et al., 2010, 2009a). This broad drainage system reoccupied topographic lows associated with earlier (glacio-) fluvial pathways within the study area and extended further south, where it connected with the Rhine-Meuse system (Busschers et al., 2025; Hijma et al., 2012), ultimately routing this discharge towards the Strait of Dover (Figure 5-9f). Compared to the MIS4 and late MIS3 drainage phases, this system was considerably more extensive, occupying the central part of the study area (Figure 5-9f). It likely shaped the Axial Channel system to its present-day expression. This interpretation is consistent with the findings of Toucanne et al. (2010, 2009a), who documented enhanced meltwater discharge through the Strait of Dover between c. 30 and 20 ka, with a marked increase in sediment flux at c. 20 ka corresponding to the onset of deglaciation.

During the subsequent Holocene period, rapid sea-level rise transformed the southern North Sea into a marine environment (Figure 5-7; e.g. Hijma et al., 2025; Spratt and Lisiecki, 2016). Marine conditions are supported by the lithofacies of Unit F (comprising yellow-brown sands with shell fragments) and its mean OSL age of 2.4 ± 0.3 ka, indicating deposition during the late Holocene (Southern Bight Fm.; Table 5-2, Table 5-3). The uniform lithofacies observed across all cores, together with the uniform acoustic character of Unit F, suggests that an early- or middle-Holocene sedimentary record may be absent in our study area. This absence could reflect either non-deposition during this interval or subsequent erosion by high-energy marine processes such as tidal currents. This contrasts with areas further north and east in the southern North Sea, where early- to middle-Holocene landscapes have been preserved and reconstructed from peat deposits and fluvial systems (e.g. Eaton et al., 2024; Missiaen et al., 2021).

5.6 Conclusions

An integrated analysis of sub-bottom profiler and lithological data from the central and northern Axial Channel region has revealed the complex stratigraphic record of climate and sea-level driven environmental changes throughout the Late Pleistocene. The identification and characterisation of depositional units and erosional surfaces using sedimentological, palaeoenvironmental (pollen, foraminifera and molluscs) and chronological (OSL) evidence enabled a correlation with the global eustatic sea-level record and a detailed palaeogeographic reconstruction of the Axial Channel system.

Marine deposits of both the Eem and Brown Bank Formations were identified that reflect (shallow) marine conditions in the study area. The occurrence of *in-situ* Eemian shell species confirms the first documented *in-situ* preservation of the Eem Formation within the study area. Following deposition of the Eem Fm, a prolonged phase of shallow marine reworking under colder conditions from MIS5d to MIS5b is evidenced by a distinct erosional surface. Renewed higher sea levels during MIS5a resulted in the deposition of the Brown Bank Fm above this surface. Relative sea-level fall during MIS4 subsequently transformed the area into a terrestrial environment. A newly identified incision in the western Axial Channel provides the first direct evidence for the activation of the Axial Channel system related to glaciofluvial drainage from a northern ice-margin during MIS4 (maximum reconstructions from Batchelor et al., 2019). A second incision east of the established western Axial Channel records a subsequent phase of environmental change during MIS3. This incision has tentatively been interpreted as a tidal channel. Its infill comprises reworked deposits of the Brown Bank Fm, evidenced by a reworked MIS5a microfossil content and the retrieved depositional age of c. 56 ka. Continued cooling and sea-level lowering during late MIS3 resulted once more in terrestrial conditions in the study area, and the establishment of a renewed incision within the western Axial Channel. Its infill consists of sediments with characteristic rhythmic bedding dated to c. 29 ka, interpreted as distal proglacial lacustrine sediments deposited within an enclosed environment. Their age suggests a link with the ice lobe along the Norfolk Coast during the MIS3-2 transition (maximum reconstructions of c. 29-31 ka; Clark et al., 2022). A final phase of large-scale glaciofluvial drainage was identified and linked to the retreat of the BIIS and FIS during MIS2, which most likely established the present-day morphology of the Axial Channel system.

This study provides valuable new insights into the (late) Pleistocene evolution of the southern North Sea by identifying previously unrecognised MIS4-MIS3 deposits and reconstructing, for the first time, a detailed palaeogeographic evolution of the Axial Channel system. The results demonstrate that the Axial Channel functioned as a major glaciofluvial drainage route throughout the Weichselian and highlight its importance within the broader network of NW European drainage systems.



Picture taken at sunset onboard the RV *Belgica II* during the August 2022 DynaMOD II survey (BE2022-18).

CHAPTER 6. SYNTHESIS AND OUTLOOK

6.1 Stratigraphy of the Axial Channel 52°-53°N

An integration of the datasets presented throughout this dissertation enabled the reconstruction of a (sub-)regional stratigraphic framework for the central-northern Axial Channel (52°10'N-52°50'N and 2°E-3°20'E). Table 6-1 summarises the stratigraphic units and associated basal surfaces identified in Chapter 4 and Chapter 5, together with their regional correlations. Figure 6-1 presents the resulting stratigraphy in context of the most recent frameworks of Busschers et al. (2025) and Dakin et al. (2026).

Table 6-1. Overview table of the stratigraphic units identified in Chapter 4 and Chapter 5 and regional correlations (where possible).

Unit / basal surface Chapter 4	Unit / basal surface Chapter 5	Regional southern North Sea Formation (UK)
Unit 9 *S9*	Unit F *H5*	Southern Bight
	Unit E *H4*	/
	Unit D *H3*	/
	Unit C *H2*	/
Unit 8 *S8*	Unit B2-3 *H1*	Brown Bank
/	Unit B1 *H1*	Eem
Unit 7 *S7*	Unit A	Cleaver Bank (+ Eem?)
Unit 6 *S6*		Swarte Bank (+ Egmond Ground?)
Unit 5 *S5*		Swarte Bank
Unit 4 *S4*		Yarmouth Roads (+ Winterton Shoal?)
Unit 3 *S3*		Smith's Knoll
Unit 2 *S2*		Westkapelle Ground
Unit 1 *S1*		Red Crag

The resulting framework is predominantly based on seismic stratigraphy for the older units (**Objective 3**), whereas the Upper Pleistocene units are constrained within a chronostratigraphic framework (**Objective 5**). In total, thirteen stratigraphic units were identified, of which ten could be correlated with established regional formations in the southern North Sea (**Objective 4**) (Table 6-1; Figure 6-1). As the study area is largely situated within the British sector, the nomenclature of the UK stratigraphic framework proposed by Dakin et al. (2026) was adopted throughout this dissertation. The remaining three units (Unit C, D and E) could not be correlated with an existing regional formation and are

therefore referred to by their informal unit names introduced in Chapter 5. The following sections summarise the seismic and acoustic characteristics, lithology (where available), depositional environment and palaeogeographic context of each of the thirteen units, presented from old to young.

Red Crag Formation: The oldest unit identified in the sparker seismic data was correlated with the Plio-Pleistocene Red Crag Formation (Unit 1; Chapter 4). This unit was identified as the infill of four large incisions that erode the underlying Paleogene deposits. These incisions are 40-52 m deep, 16-29 km long and 6-18 km wide, and their prograding infilling facies indicates deposition within a dynamic progradational system. Available borehole data describe the deposits as glauconitic muddy, fine sands with shells and fine shell fragments, consistent with a shallow-marine depositional environment (BGS, 2026a, 2026b). In the wider palaeogeographic context, these incisions were interpreted as (inter-)tidal channel systems connected to a northerly positioned North Sea (e.g. Gibbard and Lewin, 2016). Previous interpretations described the Red Crag Formation as shallow-marine deposits resting unconformably on Palaeogene formations within a single broad through (Cameron et al., 1992; Stoker et al., 2011). Our results allowed to refine this interpretation by demonstrating that the formation is not infilling a single trough, but rather four distinct incisions. While we confirmed the shallow-marine depositional environment and the presence of an unconformable basal surface, our data indicate deposition under more dynamic, higher-energy conditions than previously envisaged.

Westkapelle Ground & Smith's Knoll Formation: Two Lower Pleistocene formations were identified in our sparker seismic dataset (Unit 2-3; Chapter 4), confirming previous regional observations and interpretations for the Westkapelle Ground and Smith's Knoll Formations (Cameron et al., 1992; Stoker et al., 2011). Both formations reach thicknesses of up to 55 m thick, display a mostly sigmoidal seismic facies and are described in borehole data as glauconitic muddy sands (BGS, 2026c, 2026b; TNO-GDN, 2026b). The deposits represent deltaic systems, with sediment supply from major NW European rivers (e.g. Gibbard and Lewin, 2016). Within the Smith's Knoll Formation, steeper dipping reflectors identified in our seismic data may indicate a change in sediment provenance, with increased sediment input from the British sector into the southern North Sea during the transition from the Westkapelle Ground to the Smith's Knoll Formation. The northward thickening of both formations, combined with the more northerly distribution of the Smith's Knoll Formation, supports a progressive northwards progradation of the deltaic systems related to the northward migration of the North Sea during the Early Pleistocene (Cohen et al., 2014; Gibbard and Lewin, 2016).

Yarmouth Roads Formation (& Winterton Shoal Formation?): The Yarmouth Roads Formation represents a ≥ 100 m thick succession, deposited between the Early Pleistocene Calabrian and the Middle Pleistocene Cromerian. Much of this formation is obscured by the seabed multiple in the sparker seismic data (Unit 4; Chapter 4), however, its basal part compared to its upper part provides important insights into a changing depositional environment. The basal part was interpreted as the final stage of the preceding deltaic depositional system, with some reflections potentially corresponding to the Winterton Shoal Formation, although this correlation remains uncertain. The upper part of the Yarmouth Roads Formation was interpreted as an extensive fluvial braid plain, based on the occurrence of preserved channel remnants and a traceable channel belt of c. 15 km wide and 50 km long. Borehole data indicate a highly variable lithological composition (BGS, 2026c, 2026d; TNO-GDN, 2026b). The transition from a (pro-)deltaic to terrestrial depositional setting reflects broader climatic and environmental changes during the Cromerian, with the lower succession representing a relatively stable, marine setting and the upper succession recording the shift to a low-lying, terrestrial landscape. The multiple incisional and infilling phases reflect glacial-interglacial variability and associated sea-level fluctuations. Previous studies generally described the Yarmouth Roads Formation as a complex delta-top succession, reflecting diverse depositional environments (Cameron et al., 1992; Stoker et al., 2011). Our results provided a more detailed interpretation,

distinguishing two distinct depositional phases: an initial deltaic marine phase, similar as the underlying Lower Pleistocene deposits, followed by a fluvial phase that reflects the climatic changes throughout the Cromerian.

Swarte Bank & Egmond Ground Formation: In the Axial Channel area, the sparker data enabled the identification of a unit tentatively correlated with the Swarte Bank Formation (Unit 6; Chapter 4). This unit is characterised by a predominantly transparent to chaotic seismic facies and an erosional basal surface comprising variable incisions with depths of tens of metres and widths of hundreds of metres. This basal surface represents a regionally extensive erosional unconformity that was linked to the Elsterian ice advance based on (1) its geographical distribution relative to the reconstructed Elsterian ice limit (Batchelor et al., 2019; Busschers et al., 2025) and (2) the identification of two deep incisions (20-25 m) that, based on their geometry and infilling facies, were interpreted as Elsterian tunnel valleys. Previous interpretations placed the southernmost limit of the Swarte Brank Formation at tunnel valleys identified by Eaton et al. (2020), situated near the northern boundary of our study area (52°50'N). The in this study identified two tunnel valleys, located within the present-day branches of the Axial Channel at c. 52°27'N, are therefore the southernmost buried tunnel valleys currently identified in the southern North Sea Basin. Our sparker data suggest that the infill of the incisions and tunnel valleys may not be restricted to glacial deposits of the Swarte Bank Formation but may also incorporate deposits attributed to the Holsteinian and early Saalian Egmond Ground Formation. Especially in the eastern part of our study area, where Unit 6 reaches thicknesses of up to 40 m and is characterised by multi-phase, cut-and-fill geometries. Although this interpretation requires confirmation through ground-truth data, the seismic architecture suggests that the unit incorporates glacial, fluvial and marine deposits associated with at least one glacial and interglacial phase. Previous stratigraphic frameworks correlated the Egmond Ground Formation exclusively with the Holsteinian interglacial (MIS11; Cameron et al., 1992; Rijsdijk et al., 2005; Stoker et al., 2011). However, the more recent stratigraphic scheme of Busschers et al. (2025) extends the correlation of the Egmond Ground Formation to the MIS11-7 interval, aligning with our interpretation that Unit 6 encompasses deposits spanning the Elsterian, Holsteinian and early Saalian.

Cleaver Bank Formation: This formation was identified in the sparker dataset as the infill of multiple incisional remnants, interpreted to have formed in a periglacial outwash plain during the late Saalian glacial period (MIS6) (Unit 7; Chapter 4*)*. This correlation is based on the spatial distribution of the unit in relation to the reconstructed late Saalian (Drenthe) ice limit (Batchelor et al., 2019; Busschers et al., 2025). The unit reaches a thickness of up to 40 m and displays a predominantly divergent to complex (multiple phases) seismic facies. In the existing stratigraphic framework of the UK sector, the Cleaver Bank Formation is generally considered to be restricted to areas north of our study area (Cameron et al., 1992; Stoker et al., 2011). Similarly, its regional equivalent, the Drente Formation, is mainly documented onshore the northern Netherlands and its adjacent offshore sector (Busschers et al., 2025). Albeit tentative, our correlation of these infilling deposits with the Cleaver Bank suggests that its distribution extends further south than previously recognised, rendering them the southernmost interpreted late Saalian deposits. Beyond the inferred glaciofluvial depositional environment, further interpretations regarding the lithological characteristics of this formation remain limited due to the absence of ground-truth data.

Eem Formation: The Eem Formation is the first unit that can be characterised using both SBP and lithological data (Unit B1, Chapter 5). On the SBP data, this unit occurs as discontinuous pockets with a mostly transparent to chaotic facies. Lithologically, it consists of grey, medium-grained sand with small shell fragments and occasional finer-grained silty stringers. An OSL age of c. 122 ka, together with the presence of the *in-situ* mollusc species *Nucula nucleus* and *Hiatella arctica*, confirms correlation with the Eemian interglacial. Both the lithofacies and the mollusc assemblage indicate deposition in an open-marine environment. The base of this unit is marked by a c. 10 cm thick shell

lag that yields an OSL age of c. 128-161 ka (MIS6-MIS5e). Based on this depositional age range, the shell lag was interpreted as a marine transgressive surface associated with the Eemian transgression. Earlier studies described the Eem Formation as a widespread unit (e.g. Cameron et al., 1989), although much of these deposits have been subsequently reinterpreted as belonging to the Egmond Ground Formation (Cameron et al., 1992). In areas east of our study area, sandy marine deposits of the Eem Formation have been reworked and redeposited during the Early Glacial (MIS5b-a; Waajen-Labee, 2025). Consequently, we document the first known, directly dated, *in situ* occurrence of the Eem Formation in the study area.

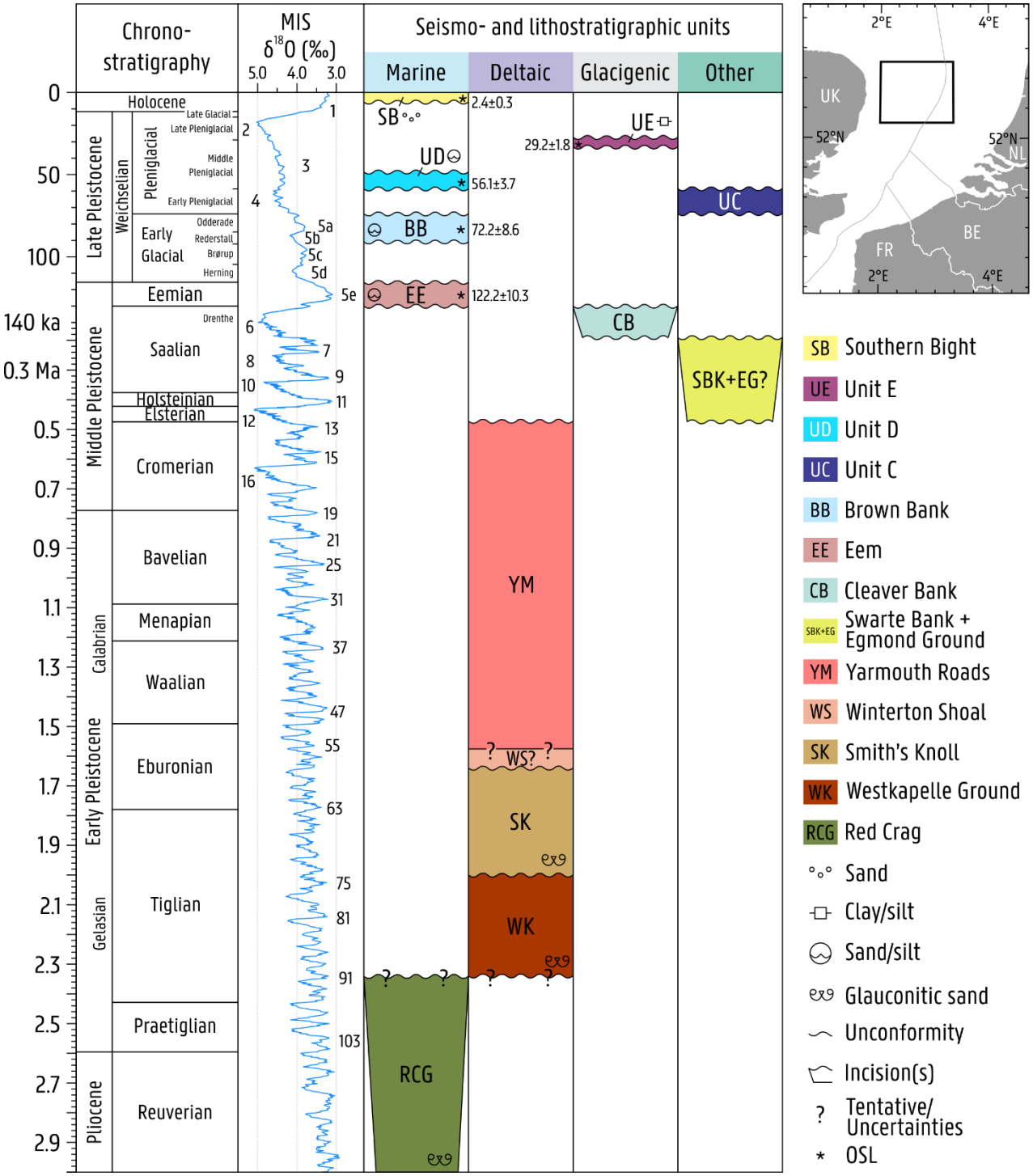


Figure 6-1. Compiled stratigraphic framework of the central and northern Axial Channel area (location indicated on inset map), following the frameworks of Busschers et al. (2025) and Dakin et al. (2026). Chronostratigraphic subseries and stages after Cohen and Gibbard (2019) and deep-ocean oxygen isotope sequence (including Marine Isotope Stages; MIS) after Lisiecki and Raymo (2005).

Brown Bank Formation: In the study area, the Eem Formation is unconformably overlain by deposits of the Brown Bank Formation. This unit is widespread and comprises two different seismic facies: a basal transparent to chaotic facies and an overlying (sub-)parallel laminated facies (Unit B2 and B3, respectively, Chapter 5). Unit B2 and B3 were correlated to seismic units BB1 and BB2-4, respectively, that have been recognised in the Dutch sector of the southern North Sea (Waajen-Labee et al., 2025). The lithofacies of the upper part of the formation consists of grey, mottled, silty to stiff clays containing mica and organic matter. Only a limited mollusc assemblage was recovered, including the *in-situ* species *Macoma balthica*. Together, the lithofacies and mollusc assemblage indicate deposition in a cold, shallow-marine environment. The acoustic and lithological descriptions, as well as the recovered mean OSL age of c. 72 ka are consistent with previous descriptions and age determinations for the Brown Bank Formation (Waajen-Labee et al., 2025). The basal boundary is marked by a c. 5-20 cm thick shell lag that yields an OSL age of c. 95 ka (MIS5c-b). This shell lag was interpreted as the reworked Eemian transgressive surface. Compared to the geological map of Cameron et al. (1984b), our findings highlight a markedly different distribution of the Brown Bank Formation: (1) the formation is restricted to the central and eastern parts rather than being present throughout the study area and (2) the western channels previously assigned to the Brown Bank Formation by Cameron et al. (1984b) were reinterpreted and correlated with Unit E.

Unit C: Unit C is a newly identified unit in the study area (Unit C, Chapter 5). The deposits are interpreted as the sedimentary infill of an incision confined to the western side branch and main branch of the present-day Axial Channel system (as defined in Chapter 3). In the SBP data, the unit is characterised by a transparent to chaotic facies. The basal incision (H2, Chapter 5) was correlated with the Early Pleniglacial (MIS4) based on its stratigraphic position, i.e. overlying the deposits of the Brown Bank Formation (MIS5a) and predating Unit D (early MIS3). This incision was interpreted as the preserved remnant of a (glacio-)fluvial drainage system that developed during the MIS4 glacial phase (see discussion Chapter 5). In the absence of direct sedimentological data, however, the age and depositional environment of the infilling Unit C remain uncertain. The unit may represent sediments deposited during the same glaciofluvial phase that formed the incision. Alternatively, Unit C may may have been deposited during the subsequent marine inundation, in which case it would comprise marine or tidal sediments comparable to those of Unit D.

Unit D: This unit is restricted to a N-S oriented incision of 2.5 km wide, 35 km long, and c. 67 m (LAT) deep in its centre (Unit D, Chapter 5). It is characterised by a divergent infilling facies on the SBP data. Lithologically, it consists of brown-grey laminated silty clay and very fine sand. Unit D was tentatively interpreted as representing (inter-)tidal channel deposits based on its lithology in combination with the morphology of the basal incision (particularly the progressive northwards and southwards shallowing of H3; Chapter 5). The lithofacies, together with reworked microfossil assemblages (pollen, foraminifera), indicate that the sediments are largely derived from erosion and redeposition of the underlying Brown Bank Formation. A mean OSL age of c. 56 ka correlates Unit D with the Middle Pleniglacial (early MIS3). This age is supported by the SBP data, which show the incision clearly cutting into the Brown Bank Formation. Marine deposits of an early MIS3 age have previously been identified in the southern North Sea, either overlying the Brown Bank Formation (Periplus Archeomare, 2023; Waajen-Labee et al., 2025) or previously interpreted incorrectly as part of the Brown Bank Formation (e.g. Wessex Archaeology, 2015). The deposits described here provide the first evidence for a relatively extensive marine incursion into the southern North Sea during early MIS3.

Unit E: Unit E is described as the infill of an incision confined to the western and main branch of the Axial Channel system (H4; Chapter 5). The unit is easily distinguished by its laminated, divergent infilling seismic facies. Lithological data show that the unit consists of rhythmic bedding of reddish-brown silts, clays and very fine sands. The coarser beds exhibit sedimentary structures such as cross-lamination, reflecting the presence of flowing water during deposition. Pollen analyses indicate

deposition in a cold, freshwater environment but also reveal a significant reworked component. A mean OSL age of c. 29 ka places the unit at the transition of the Middle to Late Pleniglacial (MIS3-2). Together, the geochronological, sedimentological and palynological evidence indicates rapid deposition in a proglacial lacustrine environment, with the rhythmic lamination potentially representing seasonal varves. This interpretation links Unit E to the maximum ice advance reconstructed for c. 29-31 ka from Clark et al. (2022). Proglacial lacustrine deposits with a similar age have been identified closer to the ice margin, e.g. in the Dogger Bank area (e.g. Kyriakoudi et al., 2026; Roberts et al., 2018), but never this far south within the southern North Sea Basin. Similar deposits were also recognised by Limpenny et al. (2011), although they were incorrectly assigned to the Brown Bank Formation based on their laminated acoustic facies. Furthermore, we reinterpreted and correlated the valleys mapped as Brown Bank Formation by Cameron et al. (1984b) in the western part of the study area with Unit E.

Southern Bight Formation: The youngest stratigraphic unit is correlated with the Southern Bight Formation (Unit F, Chapter 5). It occurs either as a blanket deposit or as part of (large) sandbanks. Lithologically, this formation consists of yellow-brown, medium- to coarse-grained sand containing abundant shell fragments. A mean OSL age of c. 2.4 ka from the Axial Channel area confirms a late Holocene age.

6.2 Role of the Axial Channel throughout the Middle to Late Pleistocene

The three main research chapters of this dissertation focussed on preserved geomorphological features on the present-day seafloor (**Objective 1**), as well as (large-scale) subsurface geomorphological features and sedimentary deposits. In the following sections, the relative chronology established in Chapter 3 (**Objective 2**) is integrated with the seismostratigraphic framework presented in Chapter 4 (**Objective 3**) and the absolute chronological framework and palaeogeographic reconstructions developed in Chapter 5 (**Objective 5 and 6**). Together, Chapters 3 and 5 demonstrate that the Axial Channel has a multi-phased origin, shaped by repeated drainage activity during periods when the southern North Sea floor was exposed as a terrestrial landscape, therefore corresponding to (glacial) sea-level lowstands. However, direct lithological evidence for these fluvial phases remains scarce. Most of the Upper Pleistocene deposits that were ground-truthed in the central and northern Axial Channel system instead record marine conditions associated with sea-level highstands, including the Eem Formation (subunit B1), Brown Bank Formation (subunit B3/Unit 8) and Southern Bight Formation (Unit F) (Chapter 4, Chapter 5). Although Unit E correlates with a glacial sea-level lowstand, it represents deposition in a proglacial lake rather than a fluvial environment. Unit C is the only unit that may record glaciofluvial deposition, but this interpretation needs to be confirmed through ground-truthing. In the southern Axial Channel, deposits up to c. 20 m thick (Unit 9; Chapter 4) overlie the Paleogene and Lower Pleistocene strata. However, the lack of chronological constraints and lithological data prevents determination of both their age and depositional environment. The evolution of the southern Axial Channel could therefore not yet be constrained.

6.2.1 (Pre-) Elsterian glaciation

The identification and interpretation of the Inner Gabbard Deeps (IGD; Figure 6-2b) as preserved subglacial tunnel valleys related to the Elsterian glaciation provides the first anchor point in the relative chronology of geomorphological features associated with the Axial Channel (Chapter 3; Sturt et al., 2009). The erosional relationship of the IGDs with the two large E-W channels visible on the UK Plateau (p3, 4) indicate that these channels predate the Elsterian glaciation (pre-MIS12; Figure 6-2a). Sturt et al. (2009) already suggested that these two palaeochannels functioned as tributaries of the Thames-Medway System during the Cromerian Stage. Their presence indicates that the study area

transitioned from an Early Pleistocene marine-deltaic setting to an emergent terrestrial landscape during the Cromerian. This transition is supported by the braided river plain identified in our seismic data at the top of the Yarmouth Roads Formation (Chapter 4). The palaeochannels preserved on the western plateau of the Lobourg Channel (p8, 9) are also likely associated with this pre-Elsterian sea-level lowstand phase (Figure 6-2a).

Other geomorphological features mapped from the bathymetric data and tentatively assigned to the Elsterian glacial phase (analogous to the IGDs) include the Falls Deep (FD), elongated deeps ED1-6, depressions D1-6 and linear ridges, scour pits and associated linear features on the UK Plateau (Figure 6-2b). In Chapter 3, these features were interpreted as having a (sub-)glacial origin. Given their proximity to the reconstructed Elsterian ice limit of Bynoe (2018) (Figure 6-2b), we link these to that same glacial phase. The bathymetric data further indicate that palaeochannels p5 and p7 are connected to the IGDs and EDs. These channels are therefore interpreted as drainage systems that developed during the retreat of the Elsterian ice sheet (Figure 6-2b).

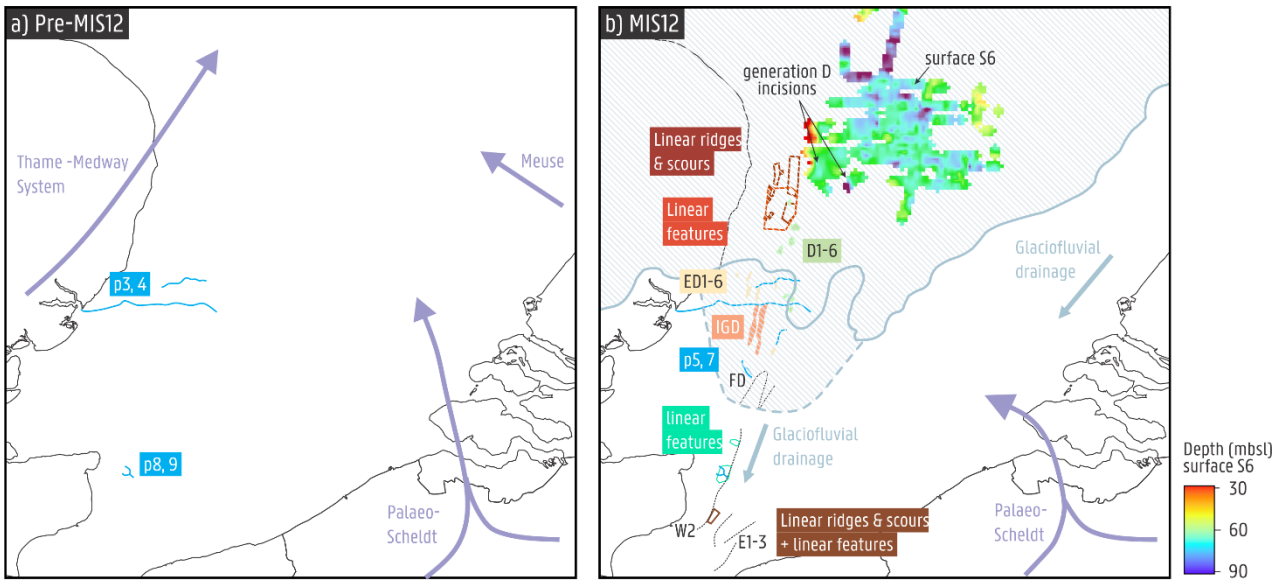


Figure 6-2. Reconstruction of geomorphological features related to the Axial Channel for (a) pre-MIS12 and (b) MIS12. Reconstruction of NW European river systems after Busschers et al. (2025); Gibbard and Lewin (2016) (drainage direction indicated by purple arrows). Light grey dashed area in (b) represent the Elsterian ice sheet, based on the reconstructed ice limit from Bynoe (2018). The generation D incisions and depth structure map of surface S6 identified in the sparker data are indicated in (b). ED: Elongated deeps; IGD; Inner Gabbard Deeps; D1-6; depressions; p: palaeochannel; FD: Falls Deep; W2; western escarpment Lobourg Channel; E1-3; eastern escarpments Lobourg Channel (see Chapter 3).

The linear features at the base of the Lobourg Channel and on the western plateau (at p8, 9) closely resemble the morphology of the linear ridge-and-grooves sets mapped c. 10 km further south in the Strait of Dover (Table 6-2; La and Lb; García-Moreno et al., 2021). García-Moreno et al. (2021) interpreted these ridges as the product of glaciofluvial erosion during the Elsterian deglaciation. This large-scale glaciofluvial erosion has, in turn, been associated with the breaching of the Strait of Dover (e.g. Collier et al., 2015; Gupta et al., 2007). The initial incision of the Lobourg Channel may therefore have been contemporaneous with the opening of the Strait of Dover, particularly the development of the western (W2) and eastern escarpments (E1, E2, E3), as previously suggested by García-Moreno et al. (2021) (Figure 6-2b). The opening of the Strait of Dover has commonly been attributed to catastrophic drainage of a proglacial lake impounded during the Elsterian glaciation (megaflood hypothesis; García-Moreno et al., 2019; Gupta et al., 2017). However, the seismic stratigraphic analysis presented in Chapter 4 did not reveal any direct depositional evidence for such a proglacial lake in the southern North Sea. Furthermore, in a recent publication, the parallel ridges and grooves in the Strait of Dover have been reinterpreted as mega-scale glacial lineations (MSGLs) and attributed to subglacial erosion (Murton et al., 2026). This not only reopens the discussion on the formation of

the linear features, but also on the presence of an ice stream into the Strait of Dover and the exact timing of its presence (most-likely MIS12, as suggested by Murton et al., 2026). Additionally, it raises the question whether the presence of an ice lobe caused the opening of the Strait of Dover or modified it after a megaflood event related to the Elsterian glaciation (Murton et al., 2026). Regardless of the exact formational mechanism, we tentatively assign the linear features at the base of and on the shoulders of the Lobourg Channel, and those in the Strait of Dover, to the same Elsterian (de-)glaciation phase based on their similar morphology (Table 6-2).

Table 6-2. Comparison table on the metrics between the linear features and ridges (and scour pits) of the Lobourg Channel (LC) identified in Chapter 3 and the linear grooves and ridges in the Strait of Dover by (García-Moreno et al., 2021).

Landform	Min-max length (m)	Min-max width (m)	Amplitude (m)	Orientation
Linear features LC (Chapter 3)	34-800	15-65	< 2	212°
Linear grooves Strait of Dover (García-Moreno et al., 2021)	30-1000	5-43	0.1-2	216°
Linear ridges (and scour pits) LC (Chapter 3)	106-774	10-20	/	210°
Linear ridges Strait of Dover (García-Moreno et al., 2021)	30-1000	3-20	/	216°

The in Chapter 4 identified large-scale erosional surface S6, which largely coincides with the present-day Axial Channel system, together with a series of deep incisions (generation D; interpreted as buried tunnel valleys) located in the branches of the Axial Channel, were correlated with the Elsterian glacial phase (Figure 6-2b). Both S6 and the associated deep incisions truncate the Lower Pleistocene deltaic deposits of the Westkapelle Ground, Smiths's Knoll and Yarmouth Roads Formations. These pre-existing erosional features likely facilitated subsequent erosion and may therefore have exerted an important control on the location of the main branch and western side branch of the Axial Channel. A similar relationship is observed further south, where the main branch of the Axial Channel coincides with four large incisions (generation A; Red Crag Formation) identified and eroding the Paleogene strata (Chapter 4; Figure 4-11), suggesting that these four older erosional features likewise influenced the position of the present-day Axial Channel system.

6.2.2 Holsteinian interglacial and early Saalian glacial

No deposits related to the Holsteinian interglacial had been identified in the study area prior to our study (e.g. Cameron et al., 1984b; Dakin et al., 2026). The stratigraphic framework presented in Chapter 4 suggests that deposits of the Egmond Ground Formation, which overlie the regional surface S6, may represent the Holsteinian interglacial and early Saalian (MIS11-7). In contrast, the bathymetric mapping provides no direct evidence to correlate any of the mapped geomorphological features to the Holsteinian interglacial or early Saalian glacial period.

6.2.3 Late Saalian (Drenthe) glaciation

On the sparker seismic and SBP data, a slope break and associated topographic low (surface S8 in Chapter 4; Figure 4-9), together with two NNW-SSE-oriented valleys (H1 in Chapter 5; Figure 5-3), were identified at the base of the Eem and Brown Bank Formation. These coincide with the northeastern

slope and part of the present-day Axial Channel depression (Figure 6-3). The overlying shell lag of surface H1 yields an OSL age of c. 128-161 ka (Chapter 5), linking this surface to the transgression at the onset of the Eemian interglacial. The underlying topography, however, was linked to the late Saalian glacial period (Drenthe; MIS6), where the valleys were interpreted as remnants of a (glacio-)fluvial drainage system (Chapter 4, 5). This surface therefore provides the first direct evidence for a late Saalian precursor to the present-day Axial Channel system.

In areas further south, late Saalian activation of the Axial Channel has previously been linked to the Rhine-Meuse river system (Busschers et al., 2008; De Clercq et al., 2016; Hijma et al., 2012). During this glacial phase, the courses of the Rhine and Meuse were strongly influenced by the lobate ice front covering the northern and central Netherlands (Figure 6-3; Busschers et al., 2008; Peeters et al., 2016). The ice front created a series of glaciotectonic ridges, which forced the Rhine-Meuse river system to adopt a southwestward-directed proglacial course (Figure 6-3; Busschers et al., 2008; Hijma et al., 2012). In the most recent reconstruction by Busschers et al. (2025), the offshore continuation of this system can be extrapolated towards the eastern slopes of the Axial Channel (s2, 3), its side branches (B5-7), the southernmost part of the main branch (MB1) and the western escarpment (W1) identified in the bathymetry in Chapter 3 (Figure 6-3). These geomorphological features are therefore interpreted as the product of fluvial erosion by the southwestward-deflected Rhine-Meuse river system during MIS6 (Figure 6-3). This interpretation is further supported by the fact that the easternmost slope (s3) forms the present-day seabed expression of the Offshore Scarp on the Belgian sector of the North Sea, previously interpreted as a MIS6 Rhine-Meuse System river terrace (Busschers et al., 2008; De Clercq et al., 2018, 2016; Hijma et al., 2012).

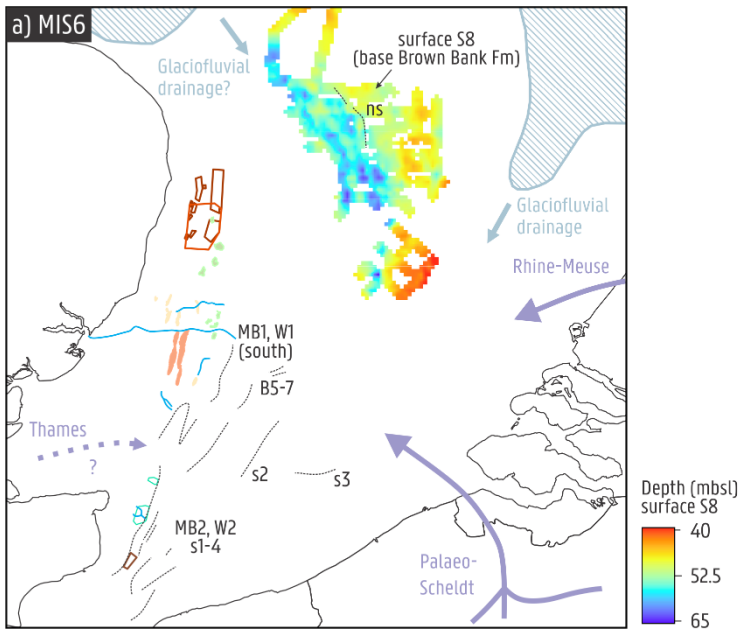


Figure 6-3. Reconstruction of geomorphological features related to the Axial Channel for MIS6. Reconstruction of NW European river systems after Busschers et al. (2025); Gibbard and Lewin (2016) (drainage direction indicated by purple arrows). Light grey dashed area represents the Saalian ice sheet, based on the reconstructed ice limit from Busschers et al. (2025). The depth structure map of surface S8 identified in the sparker data is further indicated. MB1: main branch Axial Channel; W1: western escarpment Axial Channel; B5-7: branches Axial Channel; ns; northern slope Axial Channel; s1-4: eastern slopes Axial Channel and Lobourg Channel; MB2: main branch Lobourg Channel; W2: western escarpment Lobourg Channel (see Chapter 3).

As drainage during MIS6 is inferred to have been directed southwards through the Strait of Dover (e.g. Mellett et al., 2013; Toucanne et al., 2009b, 2009a), incision of the main branch (MB2) and side branch (SB) of the Lobourg Channel is similarly linked to the late Saalian period (Figure 6-3). This erosional drainage event may also have modified and further deepened the pre-existing Elsterian escarpments and slopes (W2, E1-3, s1-4).

6.2.4 Eemian interglacial

During the Eemian interglacial, the Axial Channel area and wider southern North Sea were inundated by the marine transgression associated with this period. Discontinuous pockets of the Eem Formation were identified, infilling the highly variable relief of the late Saalian erosional surface (surface S8 in Chapter 4 and H1 in Chapter 5). In contrast, the bathymetry provides no evidence for geomorphological features attributed to the Eemian interglacial.

6.2.5 Weichselian glaciation

Whereas the southern part of the Axial Channel was likely already established during the Saalian period (Figure 6-3), Chapter 5 provides the first evidence for the occupation of its central and northern sectors during the Weichselian period. The initial incision of the main branch (MB1), together with the western side branch (B1), plateau (P) and streamlined island (SI), was linked to an erosional surface identified in the SBP data (H2; base Unit C; Chapter 5). Based on its stratigraphic position, i.e. post-dating the deposits of the Brown Bank Formation (MIS5a) and predating Unit D (early MIS3; Chapter 5), this erosional phase is tentatively correlated with drainage during MIS4 (Figure 6-4a). Toucanne et al. (2023) inferred enhanced drainage activity of the Channel River system (with a watershed consisting of northern French, Belgian and the southern British Isles river systems) through the Strait of Dover during the MIS4 glacial period. We link this drainage of the Channel River system for the first time to enhanced meltwater drainage within the Axial Channel system during MIS4, although uncertainties remain on the presence and exact extent of an MIS4 ice sheet (Batchelor et al., 2019; Carr et al., 2006; Stewart and Lonergan, 2011; see also discussion in Toucanne et al., 2023). This MIS4 drainage event likely also further modified the pre-existing Saalian morphology of both the southern Axial Channel (MB1, W1, s1) and the Lobourg Channel (MB2, W2, s1-4) (Figure 6-4a). During MIS4, the southern Axial Channel is inferred to have merged with the Meuse, Scheldt and Thames river (Figure 6-4a; Busschers et al., 2025; Hijma et al., 2012), while the Rhine still followed a more northerly course across the exposed southern North Sea floor (Figure 6-4a; Peeters et al., 2016; Waajen-Labee et al., 2025).

A renewed marine incursion during early MIS3 is evidenced by an infilled tidal channel in the Axial Channel region (Chapter 5). The incision, infilled by deposits of Unit D dated to c. 56 ka, is located c. 10 km east of the previously established western Axial Channel during MIS4 (MB1, B1; Figure 6-4a). However, the relationship between this tidal channel and the western Axial Channel could not be resolved (see discussion in Chapter 5). Following this marine phase, significant sea-level fall during middle and late MIS3 triggered a second phase of incision within the western Axial Channel system (H4; base Unit E; Chapter 5), resulting in further development of the main branch (MB1), western side branch (B1), plateau (P) and streamlined island (SI) (Figure 6-4b). Based on the age of the overlying deposits of Unit E (c. 29 ka), this erosional phase is correlated with meltwater drainage during the expansion of the BIIS and FIS (Figure 6-4b; Clark et al., 2022). Similar as during MIS4, the Axial Channel most likely functioned as a glaciofluvial drainage system connected to the major NW European river systems further south (Figure 6-4b; Hijma et al., 2012; Peeters et al., 2016). These include the Meuse and Thames, as well as the Rhine, which progressively shifted to a more southerly course prior to becoming confluent with the Meuse during the Middle Pleniglacial (MIS3; Busschers et al., 2007; Peeters et al., 2016). Also the Scheldt adopted a new, more northerly course during late MIS3 (Slupik et al., 2013), merging with the newly established Rhine-Meuse system near the present-day Port of Rotterdam (Busschers et al., 2025).

Further shaping of the southern Axial Channel (MB1, W1, s1) and the Lobourg Channel (MB2, W2, s1-4) likely also occurred during late MIS3 (Figure 6-4b). The erosional relationship between palaeochannels p10-12 and the eastern slopes of the Lobourg Channel (s1-4) demonstrates that the

channels postdate the formation of these slopes. As the latter are interpreted to have developed during MIS6 and further modified during MIS4, palaeochannels p10-12 must relate to a subsequent terrestrial phase, most likely during late MIS3, MIS2 or MIS1 (Figure 6-4b, c).

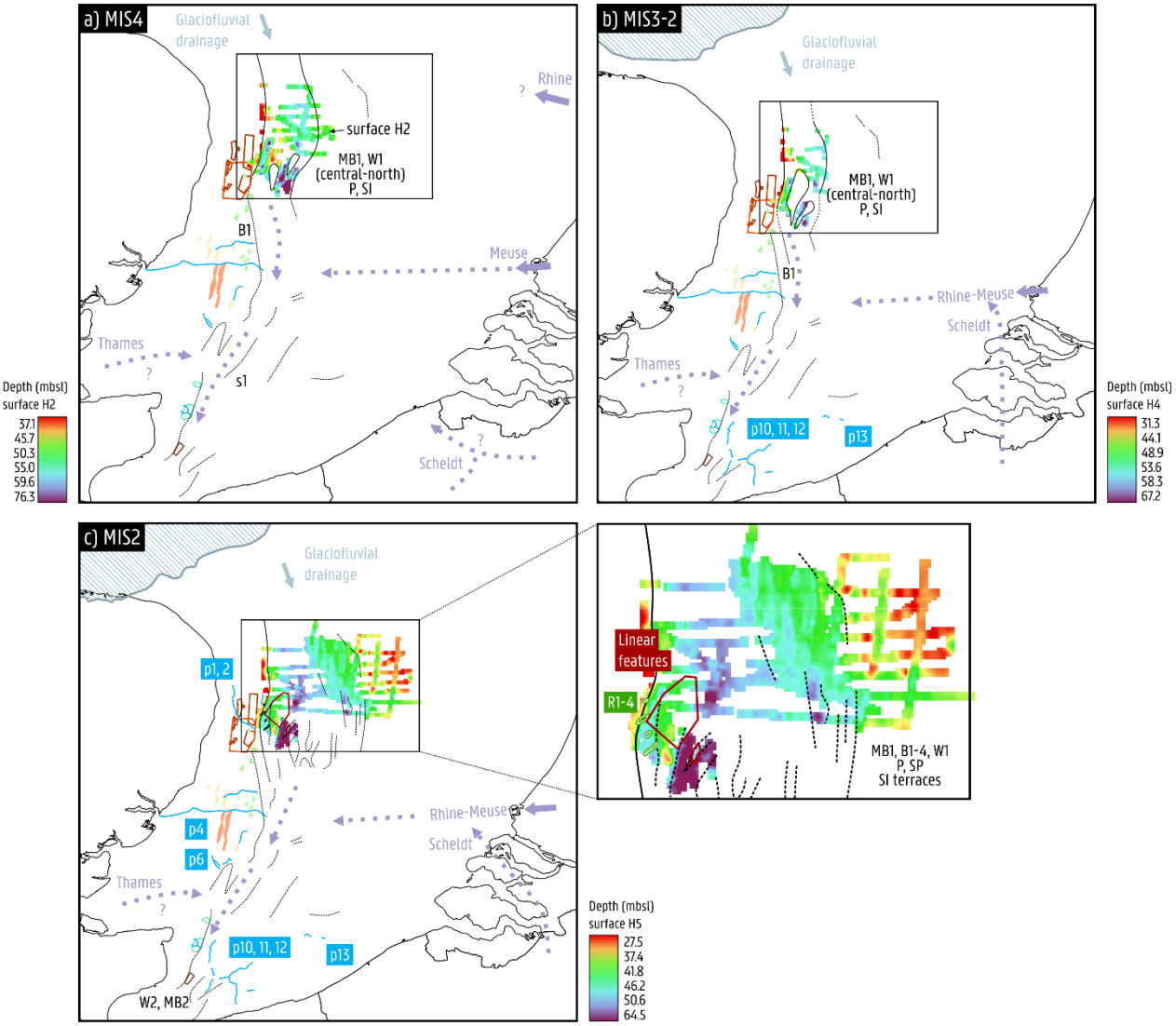


Figure 6-4. Reconstruction of geomorphological features related to the Axial Channel for (a) MIS4, (b) the MIS3-2 transition and (c) MIS2. Reconstruction of NW European river systems after Busschers et al. (2025); Gibbard and Lewin (2016); Slupik et al. (2013) (drainage direction indicated by purple arrows). MB1: main branch Axial Channel; W1: western escarpment Axial Channel; B1-4: branches Axial Channel; MB2: main branch Lobourg Channel; W2: western escarpment Lobourg Channel; p: palaeochannel; P: plateau; SI: streamlined island; SP: streamlined plateau (see Chapter 3).

Unit E was deposited within the western Axial Channel following the late MIS3 glaciofluvial incision (H4; Chapter 5). This unit was interpreted as representing proglacial lacustrine sediments dated to c. 29 ka and linked to the extensive ice lobe along the Norfolk Coast of East Anglia as reconstructed by Clark et al. (2022) (Figure 6-4b; Chapter 5). The final erosional surface identified in the SBP data (western and central part of H5; Chapter 5) most likely resulted in the present-day morphology of the Axial Channel system. Based on the age of the underlying Unit E, this erosional phase is correlated with extensive meltwater drainage that followed the Last Glacial Maximum (LGM; MIS2) (Chapter 5; Toucanne et al., 2010). During this final phase, the whole Axial Channel functioned as a major glaciofluvial system connected to the Rhine-Meuse, Scheldt and Thames river systems (Figure 6-4c) (Busschers et al., 2007; Hijma et al., 2012). Unlike the preceding drainage phases during MIS4 or late MIS3, which were largely confined to the western Axial Channel, this episode occupied the full width of the Axial Channel system, likely forming the streamlined plateau (SP) and eastern branches (B2, 3, 4) (Figure 6-4c). This drainage event also provides the most plausible explanation for the linear

features on the streamlined island (SI) and plateau (P), which were interpreted in Chapter 3 as resulting from a high-energy erosional event. The Lobourg Channel likely attained its present-day morphology at a similar timing (Figure 6-4c).

New constraints can also be given on the formational age of the ridges (R1-4) identified within the western side branch (B1), as these overlie the Unit E deposits dated to c. 29 ka (Chapter 5). Opposed to the Eemian age proposed by Limpenny et al. (2011), these ridges can now be assigned to either MIS2 or MIS1 (Figure 6-4c). The tentative interpretation of R1-4 as river dunes remains consistent with this revised chronology, as they must have formed after the abandonment of the western side branch (Chapter 3).

6.2.6 Holocene

With the southern North Sea exposed as a terrestrial landscape from late MIS3 until the early Holocene (MIS1), several pre-existing palaeochannels were likely reactivated. This prolonged period of subaerial exposure would explain their well-preserved expression on the present-day seabed. Channel p1 identified in the bathymetric mapping, was previously described and interpreted as an early Holocene channel by Limpenny et al. (2011) and Tizzard et al. (2014). Its infill comprises a basal fluvial succession overlain by estuarine deposits, therefore recording the Holocene marine transgression (Limpenny et al., 2011). Similarly, channel p4 was reactivated during the Late Glacial (MIS2) and Holocene (MIS1) as demonstrated by preserved deposits dated to these periods (Dix and Sturt, 2011).

Fully marine conditions in the southern North Sea during the Holocene led to the formation of furrows on the floors of the Axial Channel, Lobourg Channel and Falls Deep, as well as sand waves (areas 1-6) and extensive linear sand banks (Chapter 3; Figure 3-6). The linear features and terraces identified in the outer Thames Estuary are also tentatively attributed to the modern marine regime of this estuary system (Chapter 3).

6.3 Final thoughts, wider implications and future perspectives

While the overall seismic stratigraphy of the Lower Pleistocene succession described in this dissertation is generally consistent with previous studies, our data provide the first detailed images of the internal seismic architecture of these formations. These observations form a valuable basis for future palaeogeographic reconstructions of the Early Pleistocene. For example, detailed analysis of the Westkapelle Ground and Smith's Knoll/IJmuiden Ground Formations could provide new insights into the evolution of the Thames and other river systems in response to Early Pleistocene sea-level fluctuations, as well as the progressive northward migration of the North Sea coastline. On a wider scale, a regional correlation to time-equivalent onshore deposits/formations could also be established. Further investigation of the (inter-)tidal channel deposits of the Red Crag Formation (generation A; Chapter 4) may also improve reconstructions of the Plio-Pleistocene coastline, particularly as the tidal depositional environment identified in this study contrasts with previous interpretations (see Section 6.1). High-resolution sparker datasets acquired for offshore wind-farm developments may offer the spatial resolution required for such investigations. New regional datasets linking individual wind farm areas on the other hand could improve our understanding of the lateral continuity and variability of the Lower Pleistocene deltaic succession.

The Yarmouth Roads Formation, previously interpreted as a complex delta-top succession (Cameron et al., 1992), is here shown to record a major change in basin evolution, with its depositional architecture reflecting a significant change in accommodation space. The transition from (pro-)deltaic basin infill to the development of a large braid plain is a key new finding of this dissertation. This

change may reflect the increasing pronounced glacial-interglacial oscillations that characterised the Cromerian Stage. The braided river system was tentatively attributed to the Palaeo-Scheldt, as the recent reconstructions of this river's course indicate a similar orientation, while the mapped braided channel belt aligns with its inferred northern trajectory (Chapter 4; Busschers et al., 2025). Additional seismic data from the Dutch sector of the North Sea could provide answers to support this interpretation. However, it is also likely that part of the original depositional record was removed by subsequent erosion associated with the late Saalian and Weichselian Rhine-Meuse system (Kreftenheye Formation; Busschers et al., 2025; Rijsdijk et al., 2005).

The identification of erosional surfaces and deposits associated with the Elsterian glaciation not only demonstrates that the current stratigraphic framework of the southern North Sea requires revision but also has important implications for reconstructions of the Elsterian ice limit. Existing reconstructions are mainly based on geomorphological evidence such as tunnel valleys and till deposits. The regional erosional surface S6 and the buried tunnel valleys of generation D identified in Chapter 4 therefore provide additional constraints on the maximum extent of the ice sheet. Although some of these interpretations remain tentative, our results support several refinements to the currently accepted Elsterian ice limit (red dotted line; Figure 6-5). These include: (1) a more southerly ice limit in the central Southern Bight, based on the distribution of erosional surface S6; and (2) a more extensive ice lobe along the UK coastline, based on the location of the Inner Gabbard Deeps and consistent with the reconstructions of Bynoe (2018).

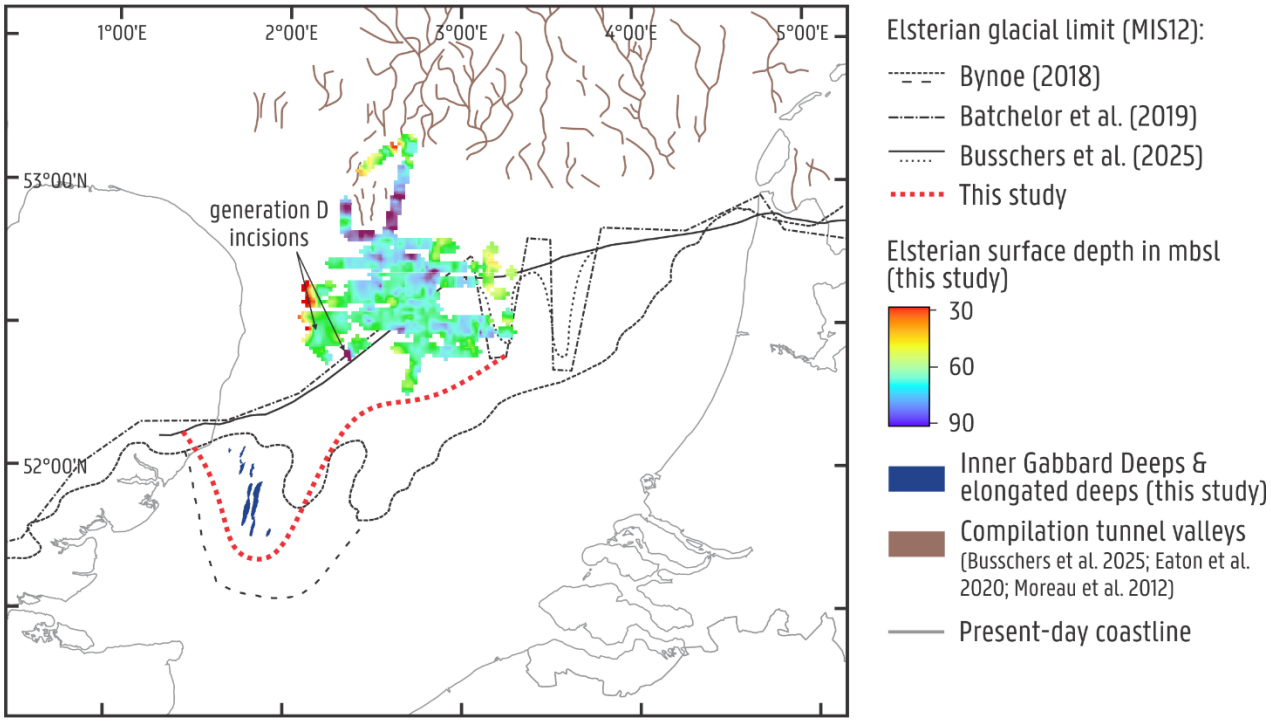


Figure 6-5. Proposed adaptations to the Elsterian (MIS12) glacial limit in the southern North Sea Basin, compiled from data presented in this research and in relation to previous reconstructions from Batchelor et al. (2019; Busschers et al. (2025) and Bynoe (2018).

Deposits (tentatively) assigned to the Elsterian, Holsteinian (and early Saalian) and late Saalian were correlated with the Swarte Bank, Egmond Ground and Cleaver Bank Formations, respectively. However, our interpretation on the depositional environments remains limited by the available lithological information, which is restricted to a single borehole description. Importantly, the seismic data provide no depositional evidence for extensive proglacial lakes that have previously been hypothesised to occur in the southern North Sea Basin during the Elsterian and Saalian glaciations. This could be due to data limitations such as the spatial resolution of the sparker seismic dataset. However, our observations in Chapter 5 could also suggest that smaller-scale, dynamic proglacial

lake systems developed in response to ice-margin fluctuations as opposed to large proglacial lakes (Carrivick and Tweed, 2013; Cohen et al., 2014; Murton and Murton, 2012). This interpretation is supported by recent evidence from the Dogger Bank area, where a network of proglacial lakes developed during the Weichselian (c. 30 ka) rather than a single extensive lake (Kyriakoudi et al., 2026). Combined with our identification of a contemporaneous proglacial lake environment in the Axial Channel (c. 29 ka; Unit E; Chapter 5), these findings indicate that smaller-scale proglacial lake networks may have been the dominant configuration in front of the Weichselian ice margin. A similar scenario may therefore also have characterised the Elsterian and Saalian glaciations.

The SBP and core data presented in this dissertation indicate that the central and northern Axial Channel are relatively young geomorphological features, formed after deposition of the Brown Bank Formation, which was correlated with MIS5a (Chapter 5). A precursor of the Axial Channel may already have developed during the late Saalian (MIS6; Chapter 5), indicating that the Axial Channel evolved through multiple phases. This interpretation is consistent with the proposed multi-phase evolution of the Lobourg Channel, Strait of Dover and English Channel (e.g. Arosio et al., 2021; García-Moreno et al., 2021; Mellett et al., 2013). Furthermore, as drainage through the central and northern Axial Channel is inferred to have been consistently directed southwards (Chapter 5), surface waters must have followed a pathway through the Lobourg Channel and the Strait of Dover into the English Channel, establishing a direct geomorphological and hydrological connection between these systems. The palaeogeographic reconstruction of the Axial Channel presented in this dissertation provides a valuable framework for future comparative studies of their evolution. However, as suggested by Mellett et al. (2013), repeated erosion during successive glacial-interglacial and sea-level cycles likely resulted in preferential preservation of landforms associated with the most recent erosional episode, i.e. the high-energy glaciofluvial drainage following the LGM (MIS2). Consequently, reconstructing drainage configurations predating MIS2 will remain challenging.

The research results in this dissertation are not only of importance for future scientific research (including palaeolandscape reconstructions, climate science and archaeology) but also for the Offshore Renewable Energy (ORE) sector. The identification of (new) geological units and their heterogeneity within the subsurface (Unit 5, 6 and 7 in Chapter 4 and Unit C, D and E in Chapter 5), as well as the identification of buried erosional surfaces (S6-8 in Chapter 4 and H1-4 in Chapter 5) are important for geotechnical and geoengineering considerations and thus ultimately for sustainable offshore developments (e.g. Dakin et al., 2026).

6.3.1 Data specific perspectives

During the WALDO-project, extensive sparker seismic, SBP and lithological datasets were acquired (Supplementary Figure S1, Supplementary Table S2). However, many of these datasets were beyond the scope of this dissertation. These include TOPAS SBP data collected north of the Belgian sector of the North Sea (i.e. in the UK sector) and across the Dutch sector of the North Sea (Supplementary Figure S1). The dataset in the Dutch sector offers considerable potential for refining reconstructions of the Weichselian courses of the Rhine and Meuse rivers and their connection to the Axial Channel system. The geology observed in the dataset north of the Belgian sector consists predominantly of pre-Quaternary deposits, although several isolated depositional pockets overlying the Paleogene strata are preserved. Detailed mapping of these deposits, combined with targeted ground-truthing, could provide valuable insights into their depositional environments and their relationship to the (southern) Axial Channel.

Additional vibrocores and survey lines had been planned for the final WALDO survey in August 2024, but the campaign was ultimately cancelled. This proposed planning was mostly aimed to ground-truth (1) Unit E in the western side branch of the Axial Channel; (2) ridges R1-4, to better constrain their age

and depositional origin; (3) Unit D, to determine its depositional environment and chronology; and (4) the depositional pockets overlying the Paleogene strata, to similarly establish their depositional environment and chronology. Sediment core AC07 could also be subjected to additional analyses to further constrain the depositional environment of Unit E, here identified as a proglacial lake environment. In addition to further exploring the XRF data, x-ray diffraction (XRD) analysis could be used to determine the provenance of the source material for the observed rhythmic bedding.

6.4 Conclusional remarks

Despite its generally assumed importance as a major NW European (glacio-)fluvial drainage route, investigations into the genesis, evolution and role of the Axial Channel within the Quaternary landscape have been limited. This dissertation presents the first detailed reconstruction of the evolution of the Axial Channel system. We demonstrated that the Axial Channel has a multi-phased origin and played a key role in regional (glacio-)fluvial drainage during the late Saalian (MIS6) and the middle and late Weichselian (MIS4 and MIS2). This was established by combining detailed bathymetric mapping, which provided an initial relative chronology for its evolution, with high-resolution sparker seismic, SBP and ground-truth data that enabled the reconstruction of an absolute chronological framework. Our results demonstrate the value of integrating complementary geophysical and geological datasets to unravel the evolution of large geomorphological features such as the Axial Channel system. Beyond improving our understanding of the Axial Channel itself, the identification of new stratigraphic units and reinterpretation of established formations demonstrate that the Quaternary geology of the southern North Sea is more complex than previously recognised, highlighting the need for an updated, transnational stratigraphic framework. Such a framework will be essential for both future scientific investigations as well as the growing offshore industry.

LIST OF ABBREVIATIONS

AC	Axial Channel
BELSPO	Belgian Science Policy Office
BGS	British Geological Survey
BIIS	British-Irish Ice Sheet
BP	Before Present
CDP	Common depth point
clr	Centre-log ratio
COARS	Coastal and Offshore Archaeological Research Services
CT	Computed tomography
DINOloket	Data and Information of the Dutch Subsurface
DTM	Digital terrain model
ED	Elongated deeps
EEA	European Environmental Agency
EEZ	Exclusive Economic Zone
EMODnet	European Marine Observation and Data Network
FD	Falls Deep
FIS	Fennoscandian Ice Sheet
GIS	Geographical Information System
GLOF	Glacial lake outburst flood
HCA	Hierarchical clustering analysis
HU	Hounsfield Units
ICP-MS	Inductively coupled plasma mass spectrometry
ICP-OES	Inductively coupled plasma optical emission spectrometry
IGD	Inner Gabbard Deeps
IRSL	Infrared stimulated luminescence
LAT	Lowest atronomical tide
LC	Lobourg Channel
LGM	Last Glacial Maximum
MIS	Marine Isotope Stage
MPR	Mid Pleistocene Revolution
MS	Magnetic susceptibility
MSCL	Multi-sensor core logger
MSGL	Mega-scale glacial lineations
NIOZ	Royal Netherlands Institute for Sea Research
NMO	Normal move-out
OBIS	Ocean Biodiversity Information System
OSL	Optically stimulated luminescence
OWF	Offshore wind farm
RCMG	Renard Centre of Marine Geology

RSL	Relative sea level
SAR	Single aliquot regenerative dose
SBP	Sub-bottom profiler
SEES	School of Earth and Environmental Sciences
SSH	Sea surface height
TLP	Total land pollen
TNO	Netherlands Organisation for Applied Scientific Research
TWT	Two-way travel time
UKHO	United Kingdom Hydrographic Office
VLIZ	Flanders Marine Institute
WALDO	Where are all the (proglacial) lake sediments in the North Sea Basin?
XRD	X-ray diffraction
XRF	X-ray fluorescence

LIST OF FIGURES

Figure 1-1. (a) Overview bathymetric map (in m to lowest astronomical tide; LAT) of the North Sea with Southern Bight area (black dotted line) and Quaternary depocenters (Central Graben and Southern Bight Basin; purple line) indicated. The Dogger Bank, Strait of Dover and English Channel are indicated for geographical reference. (b) Bathymetric map (in m LAT) of the Southern Bight, with linear sandbank fields, North-South Falls sandbank (red; NSF), Axial Channel, Lobourg Channel indicated for geographical reference.

Figure 1-2. Oxygen isotope sequence for the last 1800 ka, with Marine Isotope Stages (MIS; red – interglacial stages; blue – glacial stages) and sea-level stack for the last 800 ka (superimposed on oxygen isotope sequence) adapted from Lisiecki and Raymo (2005) and Spratt and Lisiecki (2016). Average depth of southern North Sea (-50 m LAT) indicated by green line. Subdivision of the Early Pleistocene (EP) to Holocene after Cohen and Gibbard (2019).

Figure 1-3. Palaeogeographic setting during the Early Pleistocene (Calabrian) adapted from Busschers et al. (2025) and Hijma et al. (2012).

Figure 1-4. Middle to Late Pleistocene ice limit reconstructions after Batchelor et al. (2019); Busschers et al. (2025); Clark et al. (2022). Reconstructions of the courses of major NW European river systems (Thames, Rhine, Meuse, Scheldt) at MIS12 (orange arrows), MIS6 (green arrows) and MIS2 (blue arrows) are adapted from Busschers et al. (2025); De Clercq et al. (2018); Hijma et al. (2012); Rose (2009).

Figure 1-5. Schematic representation of the research aim, objectives and dissertation outline. It further includes the four main datasets: bathymetric, seismic sparker, sub-bottom profiler (SBP) and vibrocore data.

Figure 2-1. Overview of seismic and sub-bottom profiler (SBP) data used in this study.

(a) Bathymetric map of the Southern Bight, southern North Sea. The mapped area is indicated, as well as the bathymetry blocks obtained from the UK Hydrographic Office (UKHO; ©The Crown). Geomorphological features (the Axial Channel and Lobourg Channel), geographic features (boundaries of the Exclusive Economic Zone (EEZ), Inner Silver Pit, English Channel, Oyster Ground) and tidal sandbanks (Dutch Banks, Zeeland Banks, Flemish Banks, Hinder Banks, Thames Banks and Norfolk Banks) are also indicated; (b) Pre-Holocene Geological map of the Southern Bight, compiled by the BGS (2000). The Pleistocene ice extents by Clark et al. (2022), Eaton et al. (2020) and Hijma et al. (2012) are also shown.

Figure 3-2. (a) Bathymetric map of the Axial Channel (map location indicated on Figure 3-1a) indicating the northern, central and southern sectors of the Axial Channel (white boxes). UKHO bathymetry data are indicated by the more shaded blocks. Breaks in slope are indicated by white dotted lines, escarpments by a white line with triangles. Tidal sandbanks are shown in brown and the main branch of the Axial Channel is overlain by red shading; (b) Zoom of the central Axial Channel sector; (c) Zoom of the southern Axial Channel sector. (d) Vertical profile over the central Axial Channel, location of the profile is shown by a dark blue line in (a). B1-7: side branches, D5-6: depressions, FD: Falls Deep, LC: Lobourg Channel, MB1: main branch, P: plateau, s1-3: slope-breaks, SI: streamlined island, SP: streamlined plateau, W1: western escarpment.

Figure 3-3. (a) Bathymetric map of the Lobourg Channel, map location indicated on Figure 3-1a. UKHO bathymetry data are indicated by the more shaded blocks. Breaks in slope are indicated by white

dotted lines, escarpment by a white line with triangles. Tidal sandbanks are shown in brown; (b) Zoom of the northern Lobourg Channel valley; (c) Zoom of the southern Lobourg Channel valley. MB2: main branch, SB: side branch, W2: western escarpment, E1-3: eastern escarpments, SP: streamlined plateau, SI: streamlined island, s1-4: slope-breaks.

Figure 3-4. (a) Palaeochannels connected to the Axial Channel and Lobourg Channel (indicated in light blue lines). (b) Zoom of palaeochannels p1 and p2; (c) Zoom of palaeochannels p4-7, as well as Inner Gabbard Deeps, elongated deeps and depressions on the UK Plateau; (d) Zoom of palaeochannels p8 and p9; (e) Zoom of palaeochannels p10-12; (f) Zoom of palaeochannel p13; (g) Vertical profile over the eastern Inner Gabbard Deep, location of the profile is shown by a dark blue line in (c), arrows indicate overdeepend areas. UKHO bathymetry data are indicated by the more shaded blocks. B1: western side branch of Axial Channel, D1-4: depressions, ED1-6: Elongated deeps, IGD: Inner Gabbard Deeps, MB1: main branch of Axial Channel, MB2: main branch of Lobourg Channel, PB: point bar, SI: streamlined island.

Figure 3-5. (a) Linear feature areas in the Southern Bight (indicated by different coloured polygons), with the orientation of the linear features indicated by arrows. UKHO bathymetry data are indicated by the more shaded blocks; (b) Linear ridges and scour pits on the UK Plateau (a: purple polygons), superimposed by linear features (a: orange polygon); (c) Linear features upstanding from the seabed on the plateau and streamlined island in the central Axial Channel (a: dark red polygons); (d) Linear features in a step-like terraced landscape in the Falls Deep (a: blue polygon); (e) Linear features upstanding from the seabed at the dendritic palaeochannel p8 (a: light green polygons); (f) Linear ridges and scour pits, superimposed by linear features, in a step like terraced landscape, at the base of the main branch of the Lobourg Channel (a: brown polygon); (g, h) Linear features at the base of the Axial Channel valley and Falls Deep (a: white polygons). B1: western side branch of Axial Channel, FD: Falls Deep, MB1: main branch of Axial Channel, MB2: main branch of Lobourg Channel, p1, 3, 4, 8, 12: smaller channels connecting to the Axial and Lobourg Channels, P: plateau, SI: streamlined island.

Figure 3-6. Depositional bedforms in the Southern Bight: (a) Sand wave field areas indicated by encircled numbers 1-6; (b) Rose plot with the mean orientation and mean length of the different sand waves. Area 1: yellow, light orange and dark orange, Area 2: dark and light pink, Area 3: green, Area 4: light blue, Area 5: dark blue, Area 6: red; (c) Transverse ridges (R1-4), west of plateau (P) and crossing the western side branch (B1) of the Axial Channel; (d) Vertical profile over the transverse ridges, location of the profile is shown by a dark blue line in (c).

Figure 3-7. Schematic representation of the proposed evolution of the Axial (black) and Lobourg (purple) Channels, including relative chronology and simplified environmental interpretation. There are still many uncertainties due to the absence of absolute chronological constraints (question marks and dotted lined curve). AC: Axial Channel, B1-7: side branches of the Axial Channel, D1-6: depressions, ED1-6: elongated deeps, FD: Falls Deep, IGDs: Inner Gabbard Deeps, LC: Lobourg Channel, MB1: main branch Axial Channel, MB2: main branch Lobourg Channel, p1-13: channels connected to the Axial and Lobourg Channels, P: plateau, R1-4: transverse ridges, SB: side branch of the Lobourg Channel, SI: streamlined island; SP: streamlined plateau.

Figure 4-1. (a) Geographical setting of the Southern Bight (outlined by a yellow dotted line) and study area (black rectangle). Geological map sheets from the British Geological survey are outlined in white: I. East Anglia, II. Flemish Bight, III. Thames Estuary and IV. Ostend (Balson & D'Olier, 1990; Cameron et al., 1984; Harrison & Hopson, 1991; Laban et al., 1992). Southernmost ice margins of major glacial maxima after Batchelor et al. (2019), Busschers et al. (2025) and Clark et al. (2022). (b) Zoom of the study area, with seismic lines (black lines), borehole locations (brown and green dots) and offshore wind farms (OWF; grey shaded polygons: 1. Norfolk Boreas, 2. Norfolk Vanguard, 3. East Anglia THREE,

4. East Anglia ONE (North), 5. East Anglia TWO). The Brown Bank sandbank (BB), the Murray Pit (MP; after Cameron et al., 1992) and Axial Channel -40 m contour line (light grey; Chapter 3) are indicated for geographical reference. The bathymetric data (m to lowest astronomical tide, LAT) and elevation data (m above mean sea level) are derived from EMODnet (EMODnet Bathymetry Consortium, 2022) and the European Environmental Agency (European Environmental Agency (EEA), 2016), respectively.

Figure 4-2. NNW-SSE to NW-SE oriented sparker line SB_ACW11-SB18 with projected BGS borehole BH 81/53A; for location see Figure 4-1. Incisions i-iv within U1 (generation A) are indicated. Black dotted box indicates subunits in U2 discussed in the main text.

Figure 4-3. S-N oriented sparker line BB04b with projected BGS borehole BH 81/50A; for location see Figure 4-1. Black dotted box indicates subunits in U3 discussed in the main text.

Figure 4-4. S-N oriented sparker line BB01-AC06 with projected BGS borehole BH 81/53A; for location see Figure 4-1.

Figure 4-5. W-E oriented sparker line AC01 with projected BGS borehole BH 81/50A; for location see Figure 4-1.

Figure 4-6. W-E oriented sparker line BB20; for location see Figure 4-1.

Figure 4-7. Overview of the seismic character of the seismic-stratigraphic classification derived from the sparker data.

Figure 4-8. Maps showing distribution and thickness of all identified units (Unit 1-Unit 9) along the seismic profiles (black lines) in the study area.

Figure 4-9. Depth structure maps of different identified Middle to Upper Pleistocene surfaces (S6-S9) in m LAT. The surfaces are plotted along the seismic profiles (black lines) and superimposed on the present-day bathymetry. Interpretations of valleys (black dotted lines) and slope breaks (black dashed lines) discussed in the main text are indicated. Southern ice margins of the Elsterian (MIS12) and Saalian (MIS6) maximal ice extent after Busschers et al. (2025).

Figure 4-10. Geological map of the study area (a) compiled from Balson & D'Olier (1990); Cameron et al. (1984); Harrison & Hopson (1991) and Laban et al. (1992) and published by the British Geological Survey (BGS, 2000), Holocene sediments not included; (b) based on our data, U9 not included. Black lines represent the location of seismic data from this study. Profile for the synthetic cross-section (Figure 4-12a) is indicated.

Figure 4-11. (a) Mapped extent of different generations of incisions discussed in the main text superimposed on the present-day bathymetry. Interpretation of the Axial Channel main branch (white dotted lines; Chapter 3). Maximum extent the Elsterian (MIS12) and Saalian (MIS6) ice margin after Batchelor et al. (2019); Busschers et al. (2025) and Bynoe (2018). Examples of the different incisional generations (location indicated in a): (b) Generation A (U1), incisions i, ii and iii; (c) Murray Pit (possibly part of generation A); (d) Generation B (complex channel belt in U4), showing nine different phases of cut and infill; (e) Generation C (S5); (f) Generation D (S6), deep incisions eroding U2 and U3. (g) Generation E (S7); (h) Generation F (S9).

Figure 4-12. (a) Synthetic cross-section with summary of the interpreted units (red), basal surfaces (purple) and incisional generations (light blue) derived from our data. For location of cross-section profile see Figure 4-10b. (b) An interpreted chronology for the different units and generation of incisions along the $\delta^{18}O$ curve (including MIS correlation) adapted from Lisiecki & Raymo (2005). (c)

Reconstructed stratigraphic framework for the study area following the framework of Dakin et al. (2026), locations 1-2-3 indicated on (a).

Figure 5-1. (a) Bathymetric map of the southern North Sea with depth in m below lowest astronomical tide (LAT). The maximum ice extent reconstructions are shown for MIS12 (Elsterian glaciation; Batchelor et al., 2019; Busschers et al., 2025), MIS6 (late Saalian, Drenthe glaciation; Batchelor et al. (2019); Busschers et al. (2025), MIS4 (Batchelor et al., 2019), late MIS3 (30 ka; Clark et al., 2022) and Last Glacial Maximum (LGM; Clark et al., 2022). (b) Bathymetric map (in m LAT) of the study area. Sub-bottom profiles (black: TOPAS, pink: Innomar) and core locations (white dots) are indicated. The Axial Channel (delineated by the -40 m contour line), UK Plateau, Norfolk Banks and Dutch Banks sandbank areas, and Brown Bank sandbank are indicated for geographical reference. (c) Geological map with different Pleistocene formations (Fm) in the study area, as compiled and published by BGS (2000). Bathymetric data are available through EMODnet (EMODnet Bathymetry Consortium, 2022).

Figure 5-2. High resolution 2D sub-bottom profiles (a-b: Innomar SBP, c-d: TOPAS SBP) and core locations, with interpretations of the different identified horizons (H1-6) and acoustic (sub-) units (Unit A-F). Inset (d): detailed zoom of the small-scale deformation structures present in subunit B3. See Figure 5-1 for the location of the profile and cores. For uninterpreted profiles see Supplementary Figure S5.

Figure 5-3. Distribution of the acoustic units' basal or top surfaces (depth structure maps) identified in the study area. The Axial Channel is delineated by the -40 m contour line (white line; Chapter 3). Topographic highs (islands) inferred from the absence of unit deposits and basal surface are indicated by white dotted shapes. White hatched lines mark areas where shallow gas occurs or where there is a limited penetration depth of the Innomar SBP data

Figure 5-4. High-resolution line-scan images of the sediment cores with lithofacies description, correlation to the acoustic units and (mean) OSL ages (see Table 5-3). For geographic location of the cores see Figure 5-1, for location on the acoustic profiles see Figure 5-2.

Figure 5-5. Mollusc assemblage of H1* (basal surface Unit B3) from core VC09 (46-56/65 cm; see Figure 5-4), with identified in-situ species *Boreotrophon barvicensis*, *Astarte montagui* and *Mya truncata* with sharp edged damage.

Figure 5-6. Compilation of sedimentological results, including a high-resolution line-scan, histogram equalised and CT scan image of sediment core AC07 (108 – 308 cm) next to the results of the hierarchical cluster analysis (HCA) based on the XRF data. (a) Grain-size distribution for a section of sediment core AC07 (c. 268-288 cm) plotted alongside the respective section of the core image. (b) Close-up (1, 2, 3) of sedimentary structures identified on the line-scan image and CT images. (c) Cross-view CT-image displaying the mud cracks (with arrows on CT-image for their occurrence throughout the core sections) and stereo microscope image of cemented granules.

Figure 5-7. Late Pleistocene NW European chronostratigraphic stages, Marine Isotope Stages (MIS) (Lisiecki and Raymo, 2005) and eustatic sea-level curve (Spratt and Lisiecki, 2016) with (mean) OSL ages (± 1 sigma error bar) in ka and corresponding acoustic (sub-) units identified in this study. Figure adapted from Waajen et al. (2024).

Figure 5-8. Schematic representation of (a) deposition of the Eem Formation during the Eemian interglacial (MIS5e); (b) reworking of surface H1 (= H1*) and H1.1 throughout MIS5d and MIS5c (until MIS5c-b transition); and (c) deposition of the Brown Bank Formation during MIS5a and schematic visualisation of cores VC09 and VC15 (see main text for additional information).

Figure 5-9. Palaeogeographic evolution of the southern North Sea, focussing on the Axial Channel system with snapshots at: (a) MIS6; (b) MIS5e and late MIS5a; (c) MIS4; (d) early MIS3; (e) late MIS3 to MIS2 transition; and (f) MIS2. Courses of the Thames, Scheldt, Rhine and Meuse are adapted from Busschers et al.(2025); Hijma et al. (2012); Slupik et al. (2013). Coastline positions during (b) MIS5e and MIS5a are adapted from Hijma et al. (2012) and Waajen-Labee et al. (2025), respectively. Glacial limits during (a) MIS6 after Batchelor et al. (2019) and Busschers et al. (2025); (c) MIS4 after the maximum limit reconstructions from Batchelor et al. (2019); and (e) late MIS3 to MIS2 transition and (f) MIS2 after the maximum limit reconstructions from Clark et al. (2022). The present-day coastline (black lines) and study area (rectangle) are indicated for geographical reference. Dashed lines and question marks indicate uncertainties in exact location and/or extent.

Figure 6-1. Compiled stratigraphic framework of the central and northern Axial Channel area (location indicated on inset map), following the frameworks of Busschers et al. (2025) and Dakin et al. (2026). Chronostratigraphic subseries and stages after Cohen and Gibbard (2019) and deep-ocean oxygen isotope sequence (including Marine Isotope Stages; MIS) after Lisiecki and Raymo (2005).

Figure 6-2. Reconstruction of geomorphological features related to the Axial Channel for (a) pre-MIS12 and (b) MIS12. Reconstruction of NW European river systems after Busschers et al. (2025); Gibbard and Lewin (2016) (drainage direction indicated by purple arrows). Light grey dashed area in (b) represent the Elsterian ice sheet, based on the reconstructed ice limit from Bynoe (2018). The generation D incisions and depth structure map of surface S6 identified in the sparker data are indicated in (b). ED: Elongated deeps; IGD; Inner Gabbard Deeps; D1-6; depressions; p: palaeochannel; FD: Falls Deep; W2; western escarpment Lobourg Channel; E1-3; eastern escarpments Lobourg Channel (see Chapter 3).

Figure 6-3. Reconstruction of geomorphological features related to the Axial Channel for MIS6. Reconstruction of NW European river systems after Busschers et al. (2025); Gibbard and Lewin (2016) (drainage direction indicated by purple arrows). Light grey dashed area represents the Saalian ice sheet, based on the reconstructed ice limit from Busschers et al. (2025). The depth structure map of surface S8 identified in the sparker data is further indicated. MB1: main branch Axial Channel; W1: western escarpment Axial Channel; B5-7: branches Axial Channel; ns; northern slope Axial Channel; s1-4: eastern slopes Axial Channel and Lobourg Channel; MB2: main branch Lobourg Channel; W2: western escarpment Lobourg Channel (see Chapter 3).

Figure 6-4. Reconstruction of geomorphological features related to the Axial Channel for (a) MIS4, (b) the MIS3-2 transition and (c) MIS2. Reconstruction of NW European river systems after Busschers et al. (2025); Gibbard and Lewin (2016); Slupik et al. (2013) (drainage direction indicated by purple arrows). MB1: main branch Axial Channel; W1: western escarpment Axial Channel; B1-4: branches Axial Channel; MB2: main branch Lobourg Channel; W2: western escarpment Lobourg Channel; p: palaeochannel; P: plateau; SI: streamlined island; SP: streamlined plateau (see Chapter 3).

Figure 6-5. Proposed adaptations to the Elsterian (MIS12) glacial limit in the southern North Sea Basin, compiled from data presented in this research and in relation to previous reconstructions from Batchelor et al. (2019; Busschers et al. (2025) and Bynoe (2018).

LIST OF TABLES

Table 2-1. Overview of settings for the different sparker seismic and SBP datasets used for this dissertation.

Table 2-2. Overview of processing steps for the multi-channel sparker data in the RadExPro software.

Table 2-3. Settings of the Avaatech XRF Core Scanner "DEX" at the Royal Netherlands Institute for Sea Research (NIOZ).

Table 4-1. Simplified stratigraphic classification for the shallow subsurface of the Southern Bight (modified from Busschers et al., 2025; Dakin et al., 2026; Rijsdijk et al., 2005; Stoker et al., 2011; TNO-GDN, 2026).

Table 5-1. Details of vibrocores acquired during the different surveys and used in this study, including the type of analysis performed on the different cores. [a]Geodetic system: WGS84; [b]Depths in m relative to LAT from EMODnet bathymetry

Table 5-2. Acoustic units identified within the study area with acoustic facies description, correlation to vibrocores, lithofacies description, depositional environment, correlation to marine isotope stages (MIS; Lisiecki and Raymo, 2005) and correlation with regional southern North Sea Formations (Busschers et al., 2025; Dakin et al., 2026; Stoker et al., 2011). See Figure 5-2 for examples of acoustic units.

Table 5-3. Optically stimulated luminescence (OSL) results per acoustic unit and per core with indication of validity. Ages retrieved from polymineral fine fraction OSL indicated by (*). Ages used for calculating the mean age are indicated in blue.

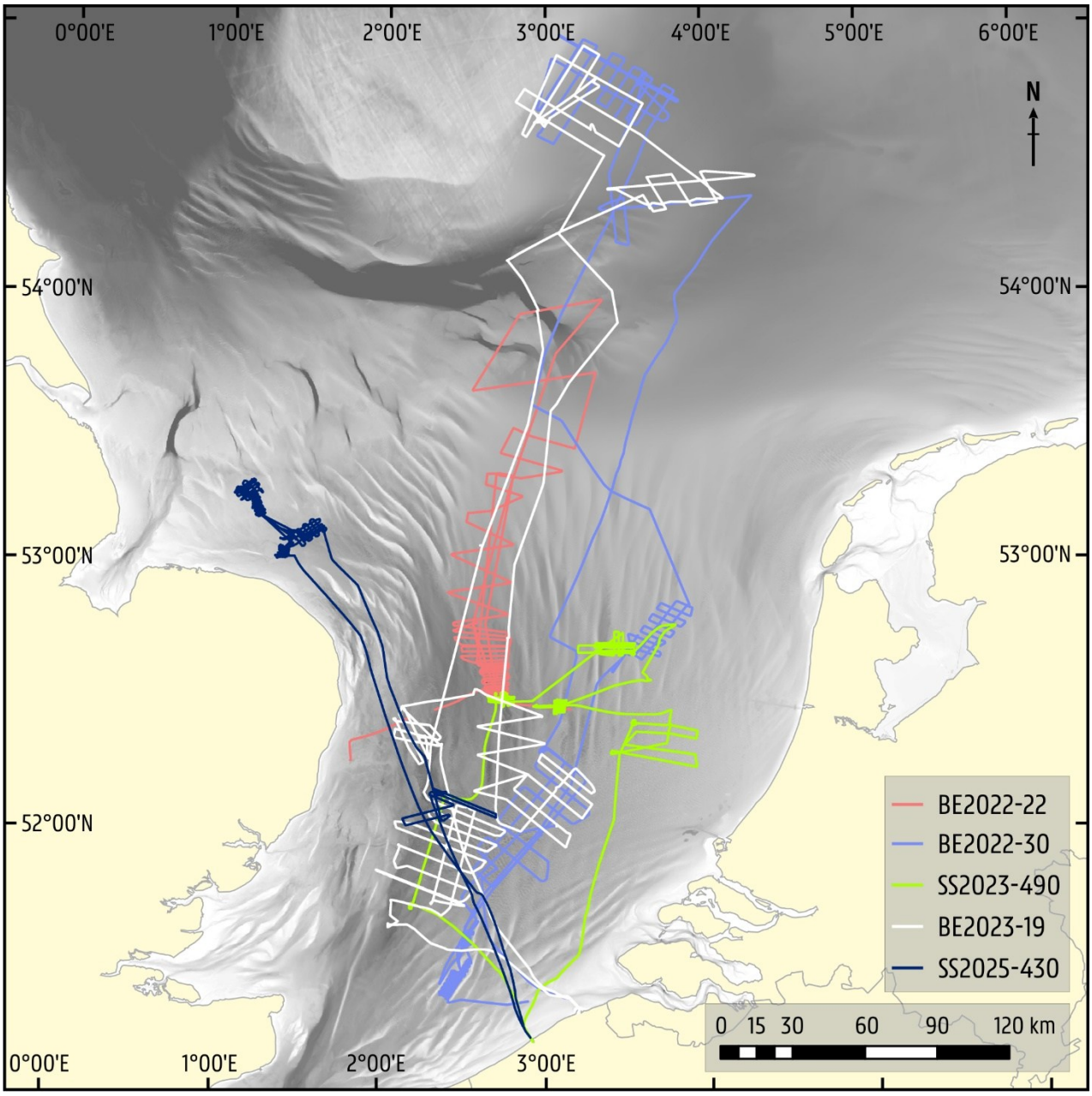
Table 6-1. Overview table of the stratigraphic units identified in Chapter 4 and Chapter 5 and regional correlations (where possible).

Table 6-2. Comparison table on the metrics between the linear features and ridges (and scour pits) of the Lobourg Channel (LC) identified in Chapter 3 and the linear grooves and ridges in the Strait of Dover by (García-Moreno et al., 2021).

SUPPLEMENTARY MATERIAL

Supplementary Figure S1

Overview map of all survey lines (trackplot) from surveys related to the WALDO-project.



Supplementary Table S2

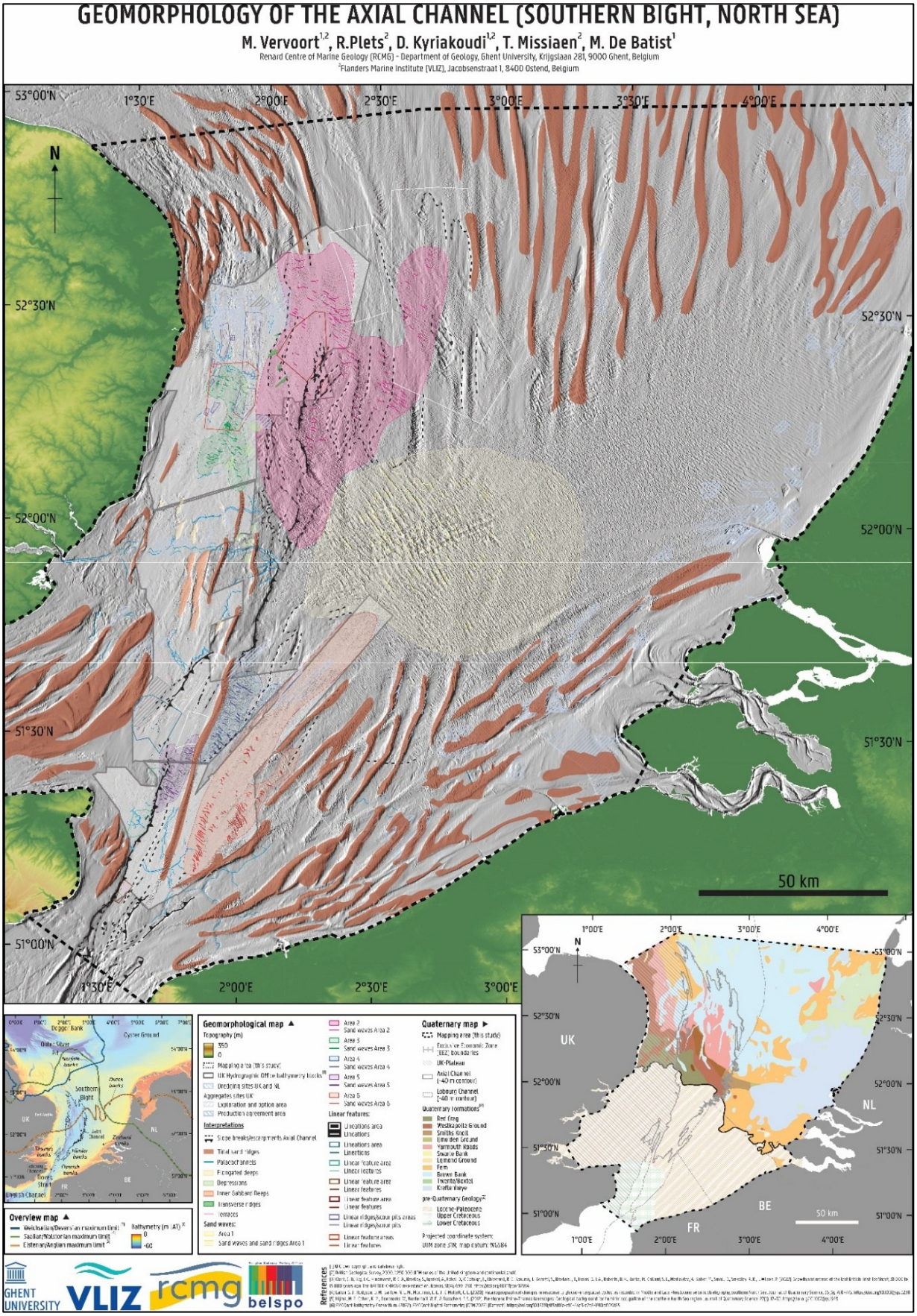
Overview table of acquired vibrocores during surveys from the WALDO-project, and types of analysis conducted.

Core name	Survey	Coring date	Latitude (N)	Longitude (E)	Core length (m)	Core depth (m LAT)	Type of analysis
AX01	BE2022-22	21/09/2022	52.557028	2.695045	2.00	45.86	-
AX02	BE2022-22	21/09/2022	52.557064	2.695903	2.65	41.94	-
AX04	BE2022-22	21/09/2022	52.610059	2.708410	2.53	44.08	-
AX05	BE2022-22	21/09/2022	52.609925	2.703618	1.87	41.86	MSCL, OSL, XRF
AX06	BE2022-22	21/09/2022	52.609773	2.698831	2.00	41.43	-
AX07	BE2022-22	21/09/2022	52.609706	2.693813	1.08	43.18	MSCL, OSL
AX08	BE2022-22	21/09/2022	52.652668	2.668010	1.54	44.62	-
AX09	BE2022-22	21/09/2022	52.652673	2.666074	2.10	44.78	-
AX11	BE2022-22	21/09/2022	52.652676	2.657141	2.44	46.00	MSCL, OSL, pollen, forams, XRF
AX12	BE2022-22	21/09/2022	52.652656	2.638610	2.02	47.07	-
AX13	BE2022-22	22/09/2022	52.789174	2.556460	2.47	41.00	-
AX14	BE2022-22	22/09/2022	52.789994	2.556630	1.60	41.00	-
AX15	BE2022-22	22/09/2022	52.790786	2.556773	1.71	41.56	-
AX16	BE2022-22	22/09/2022	52.791707	2.556964	1.74	41.57	-
VC04	SS23-490	14/06/2023	52.509620	2.742675	2.17	51.85	-
VC05	SS23-490	14/06/2023	52.509460	2.746910	2.67	51.70	-
VC06	SS23-490	14/06/2023	52.509326	2.767234	2.37	48.06	-
VC08	SS23-490	14/06/2023	52.510230	2.697461	1.00	44.72	-
VC09	SS23-490	14/06/2023	52.510132	2.707879	0.94	43.90	OSL, pollen, molluscs
VC10	SS23-490	14/06/2023	52.511690	2.712291	1.72	43.45	-

VC12	SS23-490	14/06/2023	52.510970	2.719284	2.87	45.65	-
VC13	SS23-490	14/06/2023	52.509770	2.723555	1.00	46.76	-
VC14	SS23-490	14/06/2023	52.506510	2.731742	2.32	49.51	OSl, CT
VC15	SS23-490	14/06/2023	52.509854	2.730797	1.76	49.05	OSL, molluscs
AC07	BE2023-19	05/10/2023	52.366893	2.268013	3.08	54.34	MSCL, OSL, pollen, grainsize, XRF, CT
AC08	BE2023-19	05/10/2023	52.365819	2.268935	3.42	52.44	MSCL, XRF, CT
AC09	BE2023-19	05/10/2023	52.364278	2.269756	0.7	50.67	MSCL, CT
AC12	BE2023-19	05/10/2023	52.343507	2.280291	1.73	56.66	OSL, CT, molluscs

Supplementary Dataset S3

Main Map Geomorphology of the Axial Channel (Southern Bight, North Sea). We refer to the online version for high-resolution image: https://doi.org/10.1080/17445647.2026.2620910.



Supplementary Report S4

Example borehole-seismic correlation:

The location of the borehole was projected onto the seismic profile in Kingdom (S&P Global Software Geoscience Package) where the radial distance to the profile was less than 5 km. In that location, the depth (in m) of the unit boundaries was calculated using the time-depth conversion formula:

$$depth\ (m) = \frac{TWT\ (s) * velocity\ (m\ s^{-1})}{2}$$

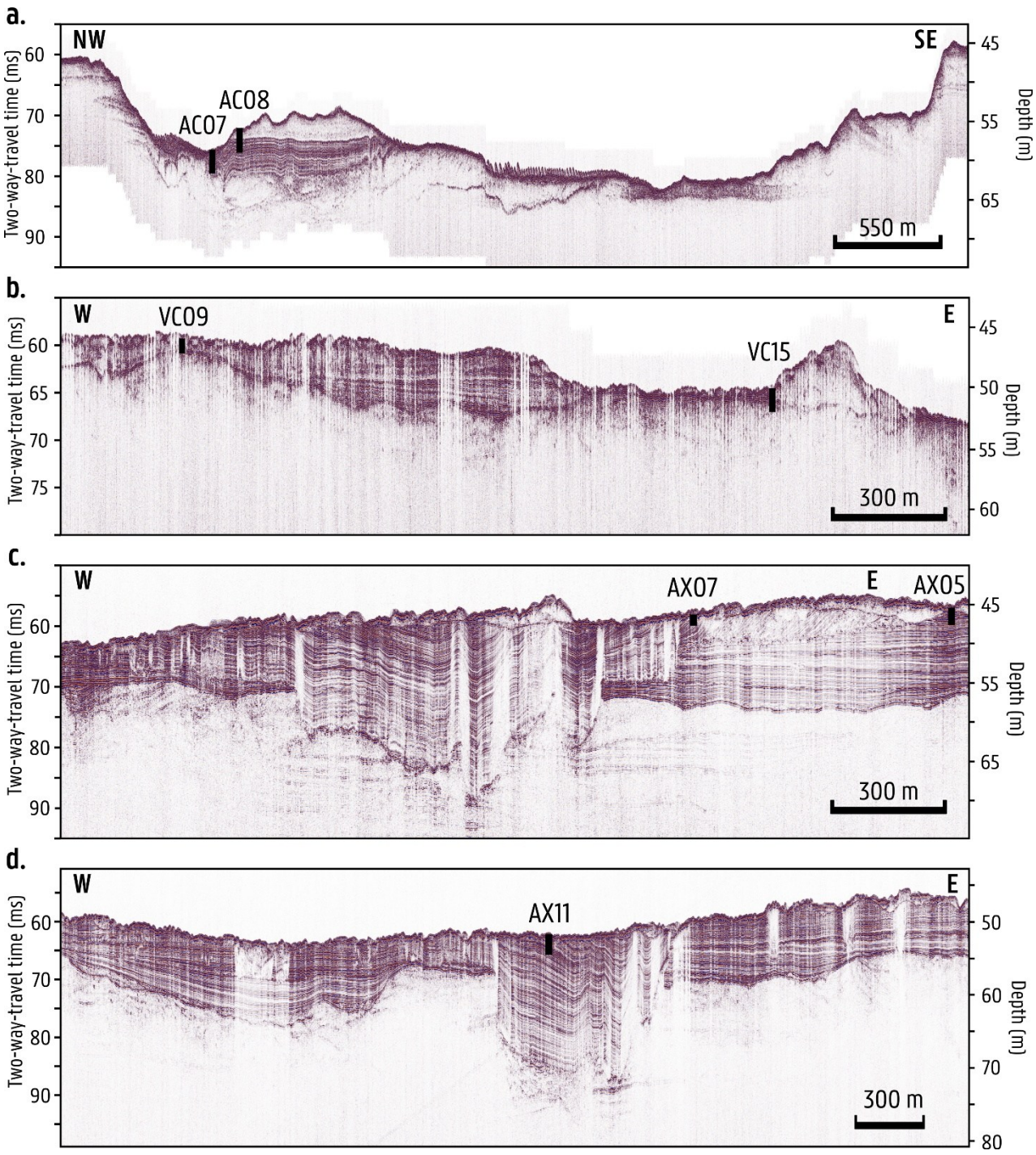
TWT is the two-way-travel time in s, and Velocity is the assumed average sound velocity in sediment (i.e. 1650 m/s).

For each of the boreholes a table as followed was made, that allowed the correlation between the borehole lithologies and seismic data.

Description sheets BGS for BH81/53(A) (BGS, 2026b)			**This study**	
Borehole depth interval (m)	*Lithological description*	*Tentative BH interpretation*	*Seismic depth interval (m)*	*Unit correlation*
0-20	Yellow brown-greenish grey, medium sand, shells and gravel	Holocene	0-19	U9?
20-35	Sand-clay interlaminated; clay: olive-grey, stiff; sand: very fine, greenish-grey	Lower Pleistocene	19-33	U2
35-70	Greenish-grey, fine, muddy sand, abundant glauconite, scattered shells	Middle-Upper Eocene	33-65/70	U1
70-77	Green grey, muddy silt, glauconite/mica	Middle Eocene	65/70 -77	Paleogene undivided

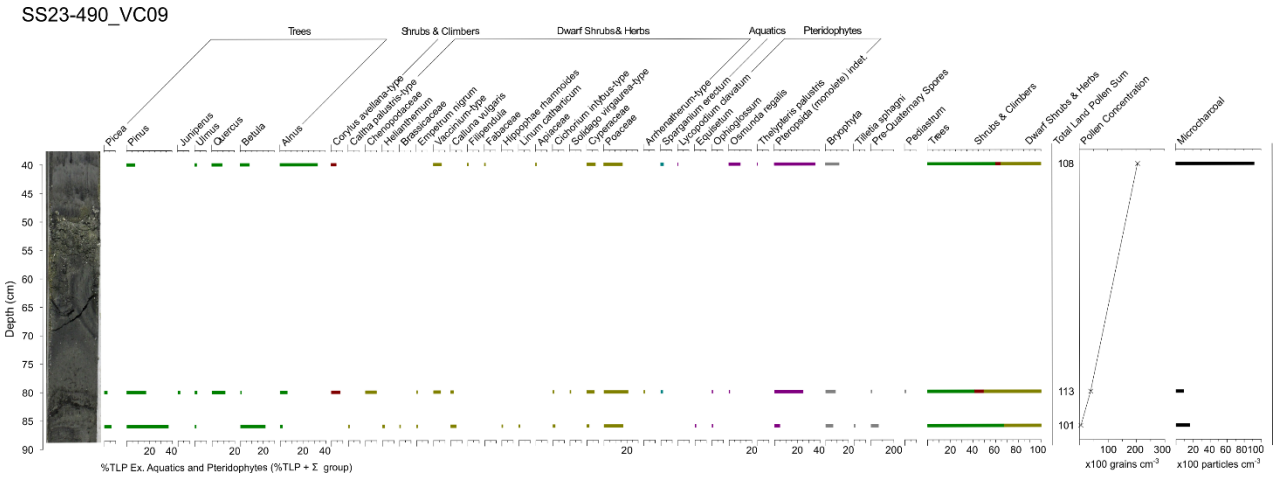
Supplementary Figure S5

High resolution 2D acoustic profiles (a-b: PES, c-d: TOPAS) along the core locations, without interpretations. For location of the seismic profiles, see Chapter 5 Figure 5-1.



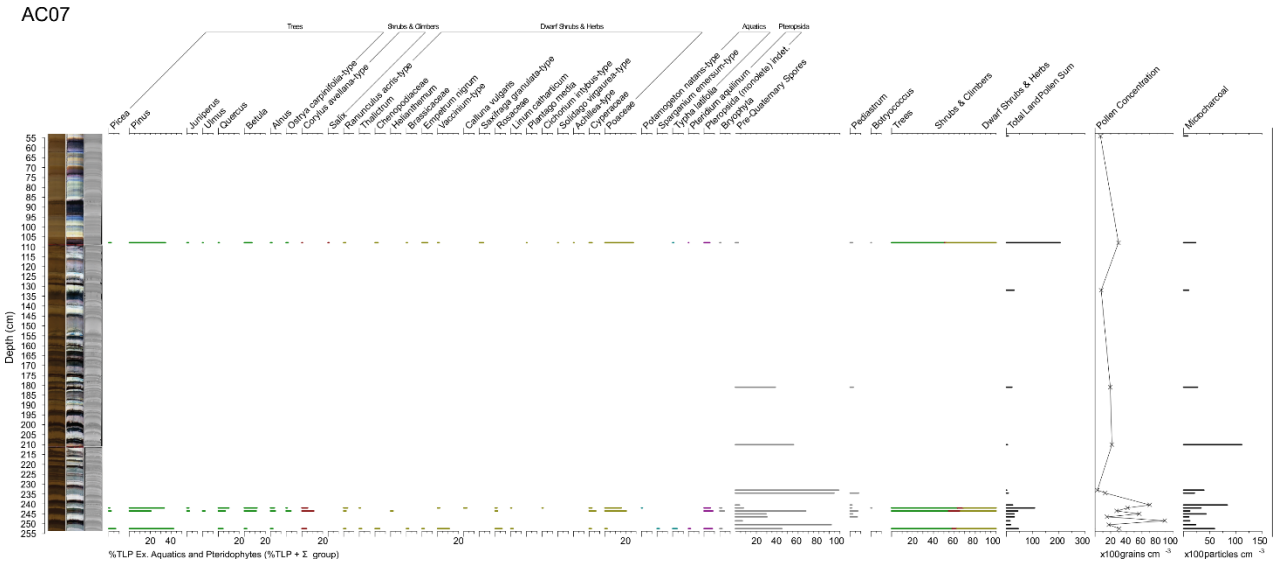
Supplementary Figure S6

Percentage pollen diagram of core VC09 (Chapter 5).



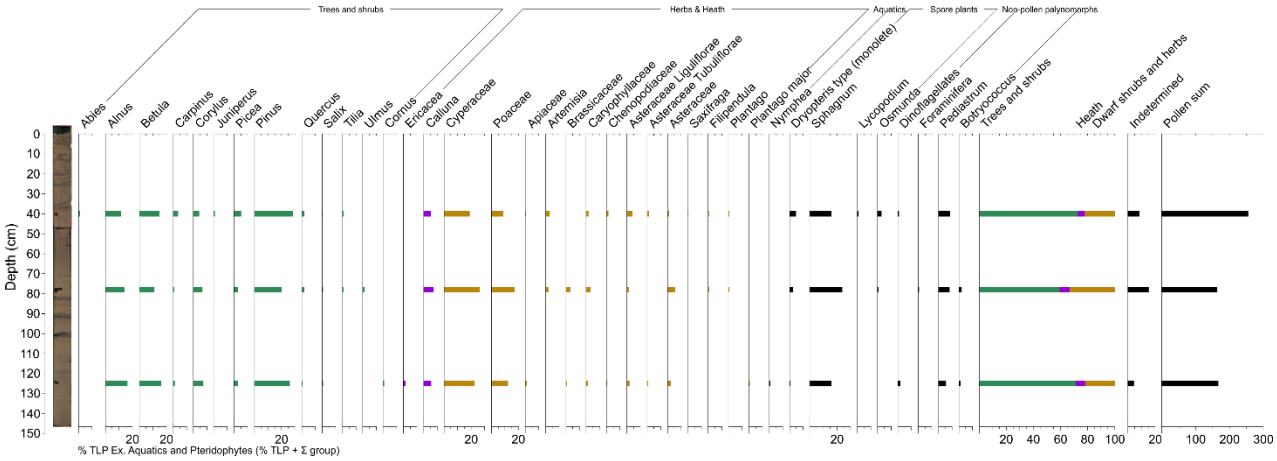
Supplementary Figure S7

Percentage pollen diagram of core AC07 (Chapter 5).



Supplementary Figure S8

Percentage pollen diagram of core AX11. Taxa with <2% occurrences in two or three of the samples have been excluded (Chapter 5).



Supplementary Report S9

Luminescence dating report

This supplementary data file concerns optically stimulated luminescence (OSL) investigations of sedimentary cores (vibrocores) from the southern North Sea, Axial Channel region.

1. Sampling and OSL screening

Tim Kinnaird visited VLIZ between the 26th and 28th of January 2023 to sample cores AX05, AX07 and AX11 for OSL P-D. Cores AC07, VC09, VC15 were sampled in October 2024 by Morgan Vervoort, Ruth Plets and Soetkin Vervust. The cores had been split under subdued light conditions at VLIZ, with one half retained for sedimentological analyses, and the other stored in dark conditions at VLIZ awaiting luminescence profiling and sampling. A dark room was set-up at VLIZ, and it was here that the cores were sub-sampled for luminescence screening, and profiled using portable OSL equipment (Munyikwa et al., 2021). Bulk sediment samples were collected during profiling: 20 from AX05, 13 from AX07, 27 from AX11, 8 from AC07, 3 from VC09, 2 from VC15. The portable OSL reader was programmed with an interleaved measurement sequence of system dark count (background, 15 s), infra-red stimulated luminescence (IRSL) (60 or 30 s) and OSL (60 or 30 s). This allowed for the calculation of net IRSL and OSL signal intensities, IRSL and OSL depletion indices and the IRSL : OSL ratio (Munyikwa et al., 2021). Table 1 lists the sample details provided on submission for luminescence dating. Each sample was sealed in a ziploc bag and additionally in black opaque bags and transferred to the luminescence laboratories at the School of Earth and Environmental Sciences at the University of St. Andrews for analysis.

Table 1. Sample details submitted for OSL dating.

Full core name	Short core name	CERSA#	Depth / cm
BE2022-22_AX05	AX05	cersa1206/12	97
		cersa1206/13	101
		cersa1206/14	105
		cersa1206/16	124
		cersa1206/17	134
		cersa1206/18	154
		cersa1206/19	174
BE2022-22_AX07	AX07	cersa1208/9	72
		cersa1208/10	82
		cersa1208/11	90
		cersa1208/12	97
BE2022-22_AX11	AX11	cersa1210/18	175
		cersa1210/20	192
		cersa1210/22	202
		cersa1210/23	207
SS23-490_VC09	VC09	cersa1770A	44
		cersa1770D	51
		cersa1770G	72
SS23-490_VC15	VC15	cersa1772A	113
		cersa1772D	134
BE2023-19_AC07	AC07	cersa1768A	76
		cersa1768E	143
		cersa1768G	269

AX05, AX07, AX11: OSL signal intensities ranged from 130 to 2.5 x 10^4 counts Gy^{-1}. Luminescence behaviour varies with lithology and stratigraphy: the medium to coarse grained sands, representing the earlier Holocene environments, are characterised by higher recuperation values, 15.3 ± 10.5 and 28.7 ± 20.1 %, units AX05-1 and AX07-1, respectively; whereas, the underlying units, AX05-2, AX07-2 and AX07-3, return lower recuperation values, 1.2 ± 0.6 and 1.9 ± 1.1 %, respectively. Units AX05-1 and AX07-1 are characterised by recycling ratios, marginally less than unity, 0.98 ± 0.06 and 0.95 ± 0.06; whereas, for AX05-1, AX07-2 and AX07-3, the recycling ratios are closer to unity, 1.00 ± 0.03 and 1.00 ± 0.05. The dose recovery was good to moderate, with values close to unity across both AX05 and AX07, irrespective of lithology, 1.01 ± 0.05 and 1.07 ± 0.10, respectively.

AC07, VC09 and VC15: OSL sensitivities ranged from 1.9 to 4.2 × 10^4 counts Gy^{-1}. Recuperation was low with a mean value of 1.3 ± 0.3 % (error expressed here, as elsewhere, as standard deviation). Recycling ratios were similar with a mean of 1.00 ± 0.01. The mean value for pseudo-dose recovery was 1.00 ± 0.02.

2. Quartz SAR OSL dating

A luminescence age is the quotient of the burial dose (in Gy) over the effective environmental dose rate (in mGy a-1). It requires that the sediment was fully bleached prior to burial. Equivalent dose (De) determinations were made on sets of 24 aliquots using the single aliquot regenerative dose (SAR) OSL protocol. Different permutations of the assimilation of equivalent doses to obtain the burial dose were considered, including weighted combinations and statistical dose models (see Guérin et al., 2017). Dose rates to these sediments were determined from quantification of radionuclide concentrations of U, Th and K by mass spectrometry.

Equivalent dose determinations. Equivalent dose determinations were made using a single-aliquot regenerative dose (SAR) method (Murray and Wintle, 2000). The SAR technique involves making a series of paired measurements of OSL intensity - the Ln and Lx outlined above, and the response to a fixed test dose, Tn and Tx. Each measurement is standardised to the test dose response determined immediately after its readout, to compensate for observed changes in sensitivity during the laboratory measurement sequence. De values are then estimated using the corrected OSL intensities Ln/Tn and Lx/Tx and the interpolated dose-response curve (Table 2).

Table 2. Measurement procedure used in quartz OSL SAR dating

Step	Action	Measured
1	Natural dose (or regenerative beta dose)	
2	preheat discs to 220 °C at rate of 5 °C/s, held for 10 s	
3	60s blue stimulation at 125 °C, 230 channels, 10 channels background either side of stimulation	Ln, Li
4	Beta test dose	
5	preheat discs to 220 °C at rate of 5 °C/s, held for 10 s	
6	60s blue stimulation at 125 °C, 230 channels, 10 channels background either side of stimulation	Tn, Ti
7	Repeat step 1-7 for a range of doses (incl. zero, repeat, and IRSL dose)	

Waajen et al. (2024) highlighted a challenge in luminescence dating of the sediments recovered from the Brown Bank – the saturation of the quartz OSL signal. As OSL signals approach saturation, accurate dating is no longer possible. Wintle and Murray (2006) recommend the threshold of 2D0 to assess the validity of the results, where the D0 parameter quantifies the onset of saturation. Equivalent doses above 2D0 are considered less reliable. The regenerative dose response curves for

the samples continues to grow to doses in excess of ~ 480 Gy. Equivalent doses above the saturation limit were included in the palaeodose estimation, using the central dose estimate of Galbraith et al. (1999). For samples where more than 35% of single aliquot data was above 2D0, results are less reliable and presented as 'best-estimate doses'; if more than 35% of single aliquot data is above 2D0 and few aliquots were accepted, results are presented as 'minimum-doses' (Waajen-Labee, 2025). A comment on the reliability of the results is provided in Table 8. The central dose estimate of Galbraith et al. (1999) was used to assimilate equivalent doses to obtain palaeodose.

Radionuclide concentrations and Environmental dose rates. Radionuclide concentrations of ^{232}Th, ^{238}U and ^{40}K were determined from inductively coupled plasma mass spectrometry (ICP-MS; U, Th) and inductively coupled plasma optical emission spectrometry (ICP-OES; K) at X-Ray Mineral Services, Welshpool (Table 3). Infinite matrix dose rates were calculated from these using the conversion factors of Cresswell et al. (2018) and adjusted for attenuation by grain size and chemical etching using the datasets of Mejdahl (1979) and Bell and Zimmerman (1978), respectively (Table 4).

Water content. Water contents as received were measured for all samples in the laboratory: fractional water content values of 11.0-26.8% were adopted to determine effective environmental dose rates (Ḋ). The dry infinite matrix dose rates measurements were used in combination with the assumed burial water contents to determine the total effective dose rates for age estimation (Table 5).

Cosmic dose contributions. Contributions from the cosmic dose were modelled after Sanderson and Kinnaird (2019), by combining latitude and altitude specific dose rates (0.19 ± 0.07 mGy a^{-1}), with time-dependent corrections for water depth and overburden (Table 5). Two possible scenarios (extreme end members) are considered; (i) assuming unknown amount of erosion and/or immediate flooding or sediment burial, receiving no contribution of cosmic dose and (ii) assuming little to no erosion therefore receiving a contribution from cosmic dose until burial/flooding.

Table 3. ICP-MS and ICP-OES determinations of K (%), U (ppm) and Th (ppm) concentrations.

Core	Lab code	Depth in core / cm	K / %	U / ppm	Th / ppm
AX05	1207B	98-101	0.97 ± 0.05	0.76 ± 0.04	2.45 ± 0.12
AX05	1207C	103-105	1.26 ± 0.06	1.63 ± 0.08	5.16 ± 0.26
AX05	1207D	107-109	1.57 ± 0.08	2.68 ± 0.13	8.80 ± 0.44
AX05	1207E	111-113	1.79 ± 0.09	2.67 ± 0.13	9.04 ± 0.45
AX05	1207F	125-127	-	-	-
AX05	1207G	129-132	-	-	-
AX07	1209B	82.5-85.5	1.43 ± 0.07	1.68 ± 0.08	5.76 ± 0.29
AX07	1209C	85.5-89.5	1.55 ± 0.08	1.89 ± 0.09	6.44 ± 0.32
AX07	1209D	89.5-93.5	1.51 ± 0.08	1.69 ± 0.08	5.70 ± 0.29
AX07	1209E	93.5-97.5	1.57 ± 0.08	1.37 ± 0.07	4.70 ± 0.24
AX07	1209F	98.5-100.5	-	-	-
AX11	1211A	174.5-177.5	1.13 ± 0.06	0.80 ± 0.04	2.61 ± 0.13
AX11	1211B	177.5-181.5	1.16 ± 0.06	0.94 ± 0.05	3.11 ± 0.16
AX11	1211C	201.5-203.5	1.25 ± 0.06	0.88 ± 0.04	2.99 ± 0.15
AX11	1211D	203.5-206.5	1.32 ± 0.07	0.86 ± 0.04	2.85 ± 0.14
AX11	1211E	208.5-212.5	1.60 ± 0.08	1.46 ± 0.07	5.26 ± 0.26
AC07	1768A	76	2.30 ± 0.16	2.79 ± 0.20	10.41 ± 0.73
AC07	1768E	143	1.54 ± 0.11	2.16 ± 0.15	7.03 ± 0.49
AC07	1768G	268.5	1.44 ± 0.10	2.72 ± 0.19	8.78 ± 0.61
VC09	1770A	44	1.51 ± 0.11	2.42 ± 0.17	8.43 ± 0.59

VC09	1770D	51	0.53 ± 0.04	1.37 ± 0.10	2.61 ± 0.18
VC09	1770G	72	0.98 ± 0.07	0.87 ± 0.06	2.76 ± 0.19
VC15	1772A	112.5	0.72 ± 0.05	0.96 ± 0.07	2.79 ± 0.20
VC15	1772D	133.5	0.79 ± 0.06	0.93 ± 0.07	2.86 ± 0.20

Table 4. Infinite matrix dose rates determined from ICP-MS and ICP-OES.

Core	Lab code	Depth in core / cm	ICP-OES and ICP-MS		
			Alpha, dry /mGy a^{-1}	Beta, dry /mGy a^{-1}	Gamma, dry /mGy a^{-1}
AX05	1207B	98-101	3.94 ± 0.14	0.90 ± 0.04	0.44 ± 0.01
AX05	1207C	103-105	8.35 ± 0.30	1.30 ± 0.05	0.74 ± 0.02
AX05	1207D	107-109	13.99 ± 0.5	1.76 ± 0.07	1.11 ± 0.03
AX05	1207E	111-113	14.12 ± 0.5	1.93 ± 0.08	1.18 ± 0.03
AX05	1207F	125-127	-	-	-
AX05	1207G	129-132	-	-	-
AX07	1209B	82.5-85.5	8.94 ± 0.32	1.45 ± 0.06	0.82 ± 0.02
AX07	1209C	85.5-89.5	10.04 ±0.36	1.58 ± 0.06	0.91 ± 0.03
AX07	1209D	89.5-93.5	8.92 ± 0.32	1.51 ± 0.06	0.84 ± 0.03
AX07	1209E	93.5-97.5	7.30 ± 0.26	1.49 ± 0.06	0.77 ± 0.02
AX07	1209F	98.5-100.5	-	-	-
AX11	1211A	174.5-177.5	4.16 ± 0.15	1.03 ± 0.05	0.50 ± 0.02
AX11	1211B	177.5-181.5	4.93 ± 0.17	1.08 ± 0.05	0.54 ± 0.02
AX11	1211C	201.5-203.5	4.66 ± 0.17	1.14 ± 0.05	0.55 ± 0.02
AX11	1211D	203.5-206.5	4.50 ± 0.16	1.19 ± 0.05	0.56 ± 0.02
AX11	1211E	208.5-212.5	7.95 ± 0.28	1.53 ± 0.06	0.81 ± 0.02
BB BE23 AC07	1768A	76	15.47 ± 0.77	2.22 ± 0.12	1.38 ± 0.06
BB BE23 AC07	1768E	143	11.23 ± 0.56	1.53 ± 0.08	0.96 ± 0.04
BB BE23 AC07	1768G	268.5	14.08 ± 0.70	1.57 ± 0.08	1.08 ± 0.04
BB SS23 VC09	1770A	44	12.99 ± 0.64	1.58 ± 0.08	1.05 ± 0.04
BB SS23 VC09	1770D	51	5.74 ± 0.30	0.61 ± 0.03	0.41 ± 0.02
BB SS23 VC09	1770G	72	4.48 ± 0.22	0.87 ± 0.05	0.47 ± 0.02
BB SS23 VC15	1772A	112.5	4.75 ± 0.24	0.07 ± 0.04	0.42 ± 0.02
BB SS23 VC15	1772D	133.5	4.72 ± 0.23	0.75 ± 0.04	0.44 ± 0.02

Table 5. Total environmental dose rates: [a]Effective beta dose rate combining water content corrections with inverse grain size attenuation factors obtained by Mejdahl (1979) for K, U, and Th; [b] gamma dose rates reconciled using a distance-weigthed contribution; [c]cosmic dose contribution.

Core	Lab code	Depth in core / cm	Water content	[c]Cosmic dose / mGy a^{-1}	Effective dose rates, wet / mGy a^{-1}		
					[a]Beta $\dot{D}_\beta$ / mGy a^{-1}	[b]Gamma $\dot{D}_\gamma$ / mGy a^{-1}	Total dose $\dot{D}_{eff}$ / mGy a^{-1}
AX05	1207B	98-101	15 ± 5	0.04 ± 0.01	0.43 ± 0.03	0.45 ± 0.03	0.92 ± 0.04
AX05	1207C	103-105	15 ± 4	0.04 ± 0.01	0.74 ± 0.04	0.52 ± 0.03	1.29 ± 0.05
AX05	1207D	107-109	19 ± 6	0.04 ± 0.01	1.06 ± 0.06	0.57 ± 0.03	1.68 ± 0.06
AX05	1207E	111-113	25 ± 7	0.04 ± 0.01	1.51 ± 0.12[d]	0.57 ± 0.04	2.13 ± 0.12
AX05	1207F	125-127	21 ± 7	0.04 ± 0.01	0.80 ± 0.07[c]	0.57 ± 0.08	1.41 ± 0.10
AX05	1207G	129-132	24 ± 7	0.04 ± 0.01	0.86 ± 0.07[c]	0.57 ± 0.09	1.47 ± 0.12
AX07	1209B	82.5-85.5	15 ± 5	0.14 ± 0.01	0.73 ± 0.04	0.58 ± 0.03	1.45 ± 0.05
AX07	1209C	85.5-89.5	21 ± 6	0.14 ± 0.01	0.87 ± 0.05	0.59 ± 0.03	1.60 ± 0.06

AX07	1209D	89.5-93.5	24 ± 7	0.14 ± 0.01	0.78 ± 0.05	0.57 ± 0.03	1.48 ± 0.06
AX07	1209E	93.5-97.5	25 ± 7	0.14 ± 0.01	0.67 ± 0.05	0.55 ± 0.03	1.35 ± 0.06
AX07	1209F	98.5-100.5	20 ± 7	0.14 ± 0.01	0.49 ± 0.05[c]	0.55 ± 0.03	1.18 ± 0.06
AX11	1211A	174.5-177.5	17 ± 5	0.12 ± 0.01	0.49 ± 0.03	0.34 ± 0.04	0.96 ± 0.05
AX11	1211B	177.5-181.5	18 ± 5	0.12 ± 0.01	0.46 ± 0.03	0.35 ± 0.04	0.94 ± 0.05
AX11	1211C	201.5-203.5	18 ± 5	0.12 ± 0.01	0.54 ± 0.03	0.38 ± 0.03	1.04 ± 0.05
AX11	1211D	203.5-206.5	18 ± 5	0.12 ± 0.01	0.60 ± 0.04	0.38 ± 0.03	1.11 ± 0.05
AX11	1211E	208.5-212.5	23 ± 7	0.12 ± 0.01	0.80 ± 0.05	0.43 ± 0.04	1.35 ± 0.06
BB BE23 AC07	1768A	76	27 ± 7	-	1.71 ± 0.14	1.06 ± 0.07	2.77 ± 0.16
BB BE23 AC07	1768E	143	22 ± 5	-	1.23 ± 0.09	0.77 ± 0.06	2.00 ± 0.11
BB BE23 AC07	1768G	268.5	22 ± 5	-	1.26 ± 0.09	0.87 ± 0.06	2.13 ± 0.11
BB SS23 VC09	1770A	44	16 ± 4	-	1.33 ± 0.09	0.64 ± 0.05	1.97 ± 0.10
BB SS23 VC09	1770D	51	11 ± 3	-	0.54 ± 0.03	0.40 ± 0.04	0.94 ± 0.05
BB SS23 VC09	1770G	72	19 ± 5	-	0.71 ± 0.05	0.39 ± 0.05	1.11 ± 0.07
BB SS23 VC15	1772A	112.5	15 ± 4	-	0.60 ± 0.04	0.36 ± 0.05	0.95 ± 0.07
BB SS23 VC15	1772D	133.5	20 ± 5	-	0.61 ± 0.05	0.36 ± 0.06	0.97 ± 0.07

3. Mineral preparation of quartz enriched 4-11 fraction, BE23-19_AC07 (cersa1768)

Mineral preparation. All sample handling and preparation was conducted under red-light conditions at the luminescence laboratories at the School of Earth and Environmental Sciences, University of St Andrews. Standardised protocols were followed: on receipt of the samples in St Andrews, the samples were weighed, saturated and dried to determine the range of water contents (Kinnaird et al., 2025; Srivastava et al., 2023). Preliminary tests were then undertaken to determine the most suitable dosimeter and grain-size for dating purposes: it was found that the sediment did not contain sufficient >90 µm grains for conventional small aliquot OSL dating, and so, the polymineral fine fraction was explored for this purpose. All samples were sieved to isolate the <90 µm fraction. After settling, this fraction was treated with hydrochloric acid (HCl) to remove carbonate (until there was no visible reaction, < 2 days), then a week-long treatment in hydrogen peroxide to remove organic matter. To enrich the polymineral fine-grained fraction in quartz, samples were treated in fluorosilicic acid for two weeks, then 'rinsed' in HCl to dissolve any potential fluorites that might have precipitated in the prior step. To prepare aliquots, suspension of quartz enriched 4-11 µm fraction was isolated using Stokes' Law and then pipetted to settling tubes, containing a 10 mm diameter aluminium discs. These were then placed in an oven set to 50°C to evaporate.

4. K feldspar pIR IRSL225 equivalent dose determinations

For AX05 both quartz OSL and feldspar pIRIR analysis was explored to obtain burial ages as it was implied that the quartz system would be close to saturation. The Feldspar pIRIR may be used to date older samples as the pIRIR signals saturate at greater doses (e.g. Wallinga & Cunningham, 2015). Equivalent doses were also determined using an elevated temperature post-IR IRSL SAR approach (Waajen et al., 2024; Zhang and Li, 2020) (Table 6). Fading tests have been initiated, but have not been completed. As obtained results using this method are less robust than unsaturated quartz ages, these ages were not used for interpretations.

Table 6. Measurement procedure used in K feldspar pIR IRSL225 SAR dating.

Step	Action	Measured
1	Natural dose (or regenerative beta dose)	
2	preheat discs to 250 °C at rate of 5 °C/s, held for 60 s	

3	60s infra-red stimulation at 50 °C, 230 channels, 10 channels background either side of stimulation	
4	60s infra-red stimulation at 225 °C, 230 channels, 10 channels background either side of stimulation	Ln, Li
4	Beta test dose	
5	preheat discs to 250 °C at rate of 5 °C/s, held for 60 s	
6	60s infra-red stimulation at 50 °C, 230 channels, 10 channels background either side of stimulation	
7	60s infra-red stimulation at 225 °C, 230 channels, 10 channels background either side of stimulation	Tn, Ti
8	60s infra-red stimulation at 225 °C	
9	Repeat step 1-8 for a range of doses (incl. zero and repeat)	

Again, equivalent distributions were appraised for homogeneity at each investigated depth, and, when warranted, different combinations of merged datasets explored (Figure 1, Table 7).

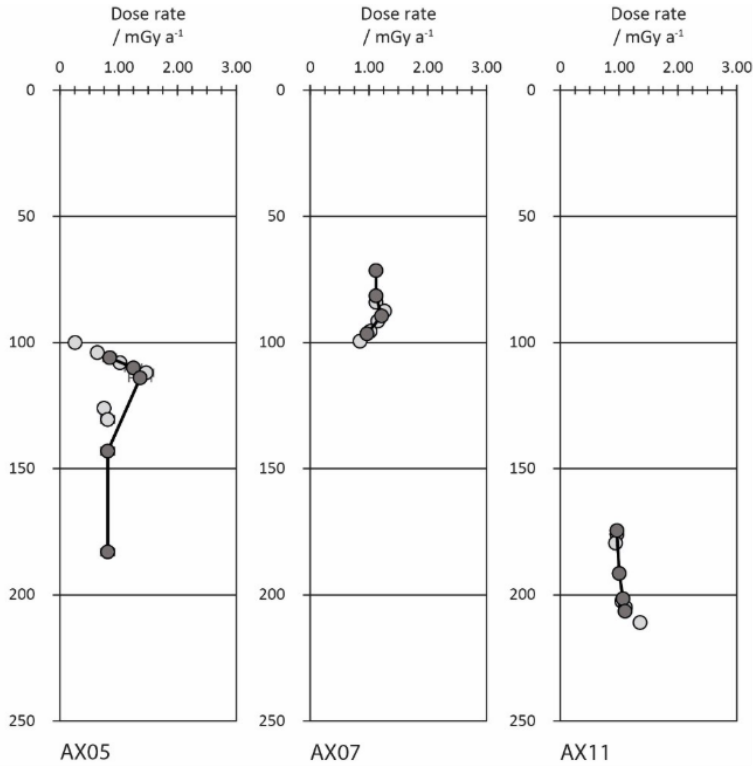


Figure 1. Dose rates to the HF etched quartz fraction at each of the dating positions - measured (dark grey) vs modelled (light grey).

Table 7. Total environmental dose rates to the quartz and feldspar fractions at the position of the dating sample (see Figure 1).

Core	Dating sample / CERSA#	Depth /cm	Dose rate to HF etched quartz / mGy a-1	Dose rate to K feldspar / mGy a-1
AX05	1206/12	106	1.50 ± 0.11	-
	1206/13	110	1.91 ± 0.14	-
	1206/14	114	2.02 ± 0.19	-
	1206/16	133	-	2.00 ± 0.29

	1206/17	143	1.47 ± 0.12	-
	1206/18	163	-	2.00 ± 0.29
	1206/19	183	1.47 ± 0.12	-
AX07	1208/9	71.5	1.45 ± 0.05	-
	1208/10	81.5	1.45 ± 0.05	-
	1208/11	89.5	1.54 ± 0.10	-
	1208/12	96.5	1.30 ± 0.09	-
AX11	1210/18	174.5	0.96 ± 0.05	-
	1210/20	191.5	1.00 ± 0.07	-
	1210/22	201.5	1.07 ± 0.08	-
	1210/23	206.5	1.10 ± 0.07	-

5. Age determinations

Burial doses, environmental dose rates and corresponding depositional ages are listed in Table 8. The equivalent dose distributions are shown in Figure 2 to Figure 8. Given the uncertainty regarding depositional environment and/or complex burial history of certain units, ages are presented with and without contributions from the cosmic dose included in the dose rate calculation.

Table 8. Burial doses, total effective environmental dose rates and corresponding depositional ages. Ages in blue are ages with contribution of cosmic dose rate.

Core	CERSA#	Depth / cm	Palaeo-dose / Gy	Aliquots / n	Over-dispersion / %	Dose rate / mGy a-1	Age / ka	Age range / BP	Comment
Quartz OSL									
AX05	1206/12	97	7.2 ± 1.0	17	57.5 ± 9.9	1.50 ± 0.11	4.8 ± 0.8	4000-5600	outlier (reversal)
	1206/13	101	4.7 ± 0.4	17	31.7 ± 6.0	1.91 ± 0.14	2.5 ± 0.3	2200-2800	reliable
	1206/14	105	4.7 ± 0.3	17	24.3 ± 5.4	2.02 ± 0.19	2.3 ± 0.3	2000-2600	reliable
	1206/17	134	109.0 ± 15.5	5	-	1.47 ± 0.12	74.1 ± 12.2	61900-86300	best-estimate
	1206/19	174	175.2 ± 22.8	12	32.3 ± 11.1	1.47 ± 0.12	119.1 ± 18.3	100800-137400	outlier (saturation)
AX07	1208/9	72	78.4 ± 4.0	19	20.7 ± 3.8	1.45 ± 0.05	54.0 ± 3.4	50600-57400	reliable
	1208/10	82	81.0 ± 1.3	21	5.5 ± 1.6	1.45 ± 0.05	55.7 ± 2.2	53500-57900	reliable
	1208/11	90	82.7 ± 2.3	16	8.8 ± 2.4	1.54 ± 0.10	53.5 ± 3.8	49700-57300	reliable
	1208/12	97	70.9 ± 2.4	24	13.7 ± 2.6	1.30 ± 0.09	54.6 ± 4.0	50600-58600	reliable
AX11	1210/18	175	58.6 ± 2.1	20	15.1 ± 2.6	0.96 ± 0.05	69.9 ± 4.8 61.0 ± 3.9	65100-74700 57100-64900	reliable
	1210/20	192	88.0 ± 8.8	18	36.9 ± 8.0	1.00 ± 0.07	99.8 ± 12.6 87.9 ± 10.7	87200-112400 77200-98600	outlier (reversal)
	1210/22	202	62.1 ± 2.2	23	16.4 ± 2.6	1.07 ± 0.08	65.6 ± 5.6 58.3 ± 4.6	60000-71200 53700-62900	reliable
	1210/23	207	61.0 ± 1.7	21	11.6 ± 21.1	1.10 ± 0.07	62.3 ± 4.8 55.6 ± 4.0	57500-67100 51600-59600	reliable
AC07	1768A	76	87.2 ± 2.0	18	7.3 ± 2.2	2.77 ± 0.16	31.54 ± 1.93 29.54 ± 1.93	29600 - 33470	*fines
	1768E	143	66.9 ± 1.4	20	7.8 ± 1.6	2.00 ± 0.11	33.44 ± 1.99 31.54 ± 1.99	31450 - 35430	*fines

	1768G	269	61.7 ± 0.9	20	5.1 ± 2.1	2.13 ± 0.11	28.93 ± 1.57 26.54 ± 1.57	27360 - 30500	*fines
VC09	1770A	44	138.7 ± 7.1	18	18.7 ± 4.0	1.97 ± 0.10	70.23 ± 5.07 65.23 ± 5.07	65150 - 75300	best-estimate
	1770D	51	104.3 ± 5.3	18	19.2 ± 4.0	0.94 ± 0.05	110.53 ± 8.37 94.53 ± 8.37	102170 - 118900	reliable
	1770G	72	300.5 ± 15.7	18	22.7 ± 4.2	1.11 ± 0.07	271.26 ± 23.10 236.26 ± 23.10	248160 - 294350	minimum-estimate
VC15	1772A	113	116.7 ± 5.6	19	19.5 ± 3.6	0.95 ± 0.07	122.16 ± 10.26 117.16 ± 10.26	111900 - 132420	reliable
	1772D	134	162.3 ± 10.6	18	26.1 ± 4.9	0.97 ± 0.07	166.84 ± 16.64 144.84 ± 16.64	150200 - 183490	reliable
K feldspar pIR IRSL225									
AX05	1206/16	124	94.3 ± 3.1	19	7.4 ± 4.3	2.00 ± 0.29	47.1 ± 7.0	40100 - 54100	uncorrected fading
	1206/18	154	118.4 ± 8.3	24	32.0 ± 5.3	2.00 ± 0.29	59.6 ± 9.6	50000-69200	uncorrected fading

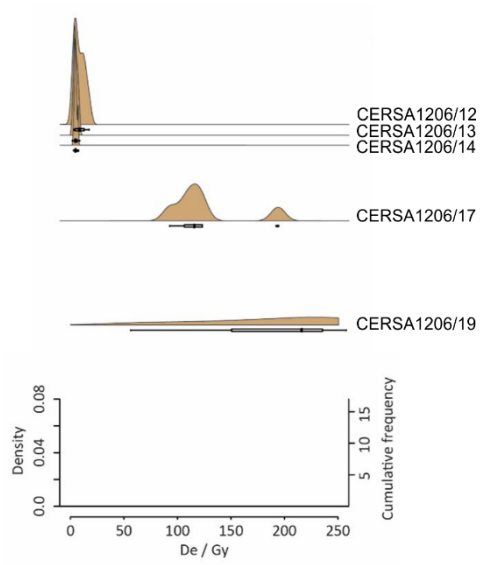


Figure 2. Equivalent dose distributions for CERSA1206/12, CERSA1206/13, CERSA1206/14, CERSA1206/17 and CERSA1206/19 (core AX05)

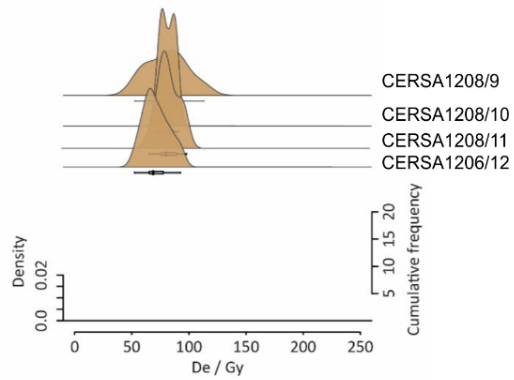


Figure 3. Equivalent dose distributions for CERSA1208/9, CERSA1208/10, CERSA1208/11 and CERSA1208/12 (core AX07).

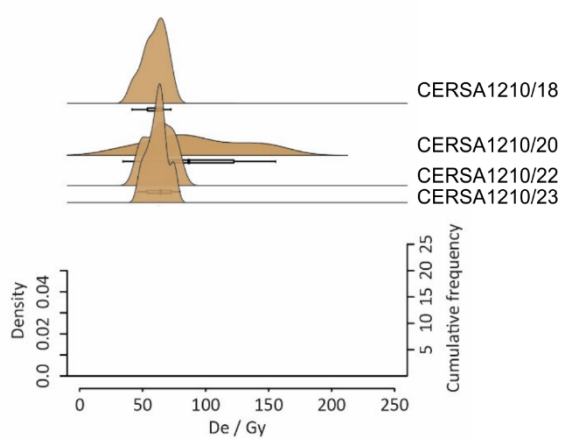


Figure 4. Equivalent dose distributions for CERSA1210/18, CERSA1210/20, CERSA1210/22, and CERSA1210/23 (core AX11).

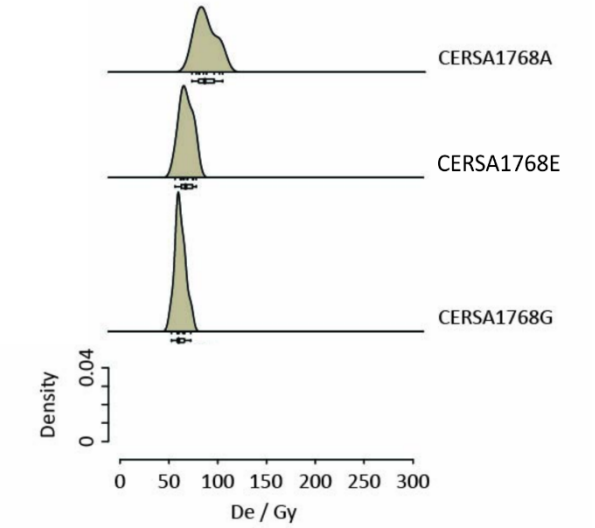


Figure 5. Equivalent dose distributions for CERSA1768A, CERSA1768E and CERSA1768G (core AC07).

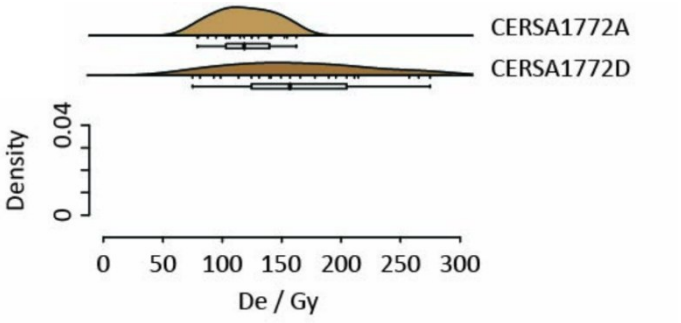


Figure 6. Equivalent dose distributions for CERSA1772A and CERSA1772D (core VC15).

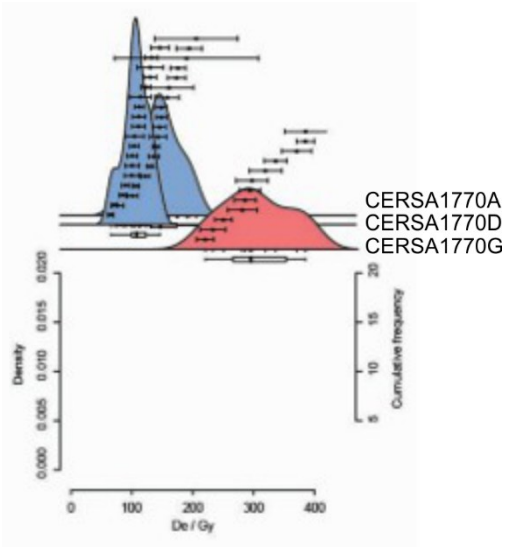


Figure 7. Equivalent dose distributions for CERSA1770A, CERSA1770D and CERSA1770G (core VC09).

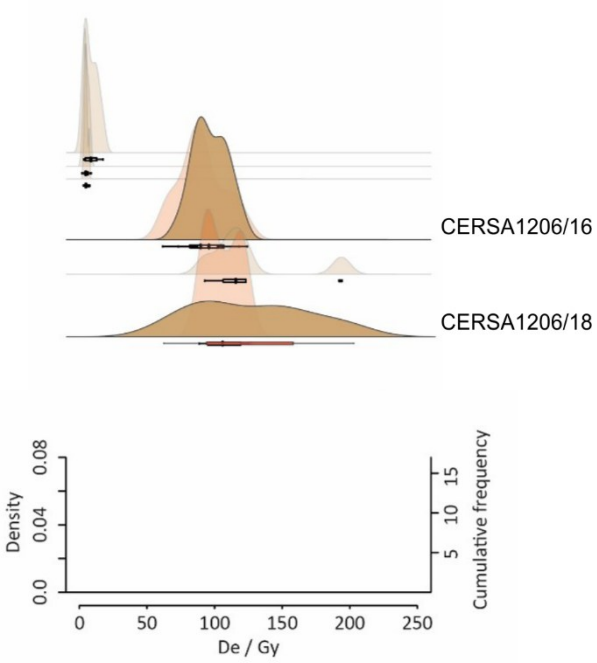
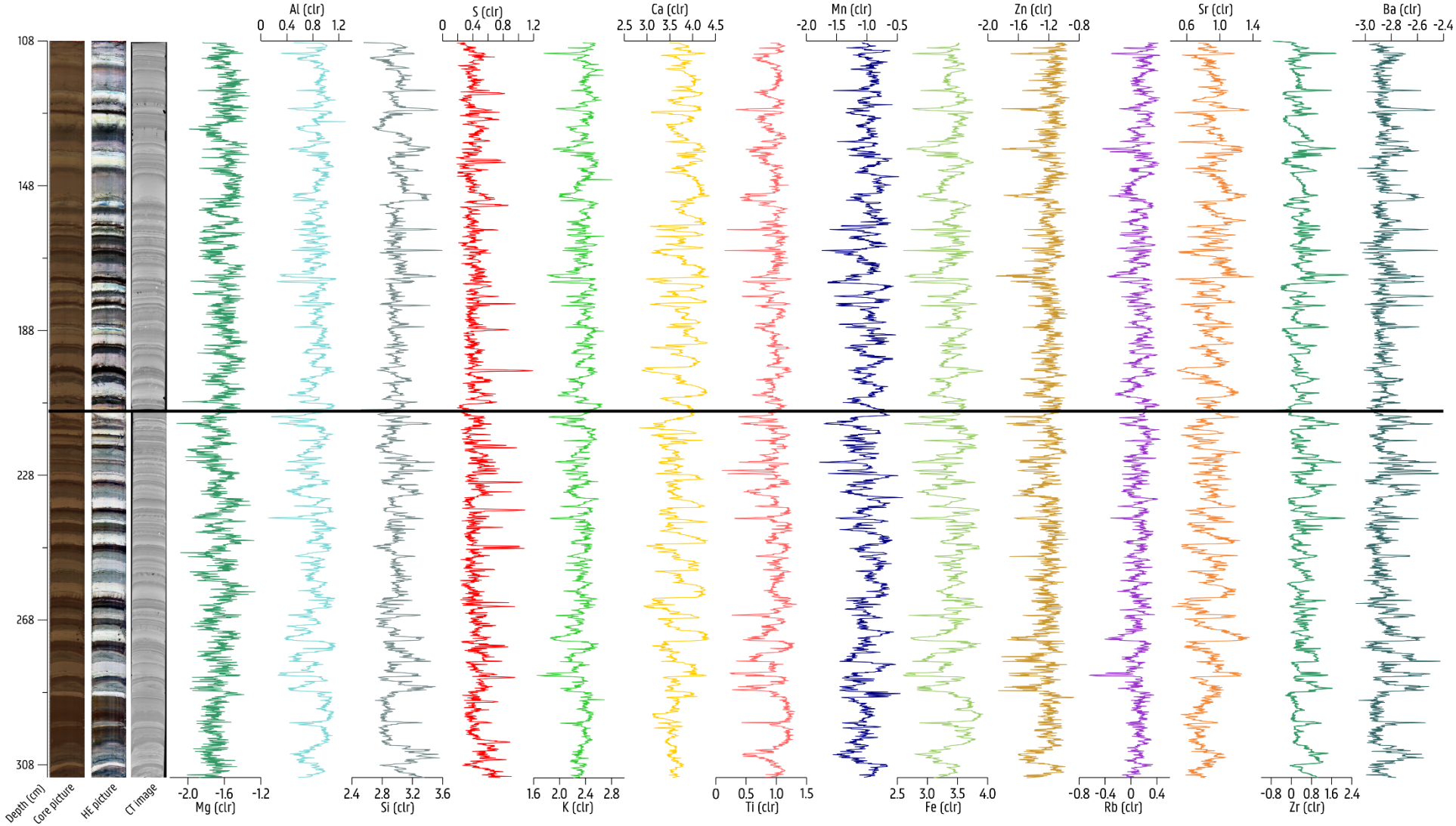


Figure 8. pIR IRS225 equivalent dose distributions for CERSA1206/16 and CERSA 1206/18 (core AX05)

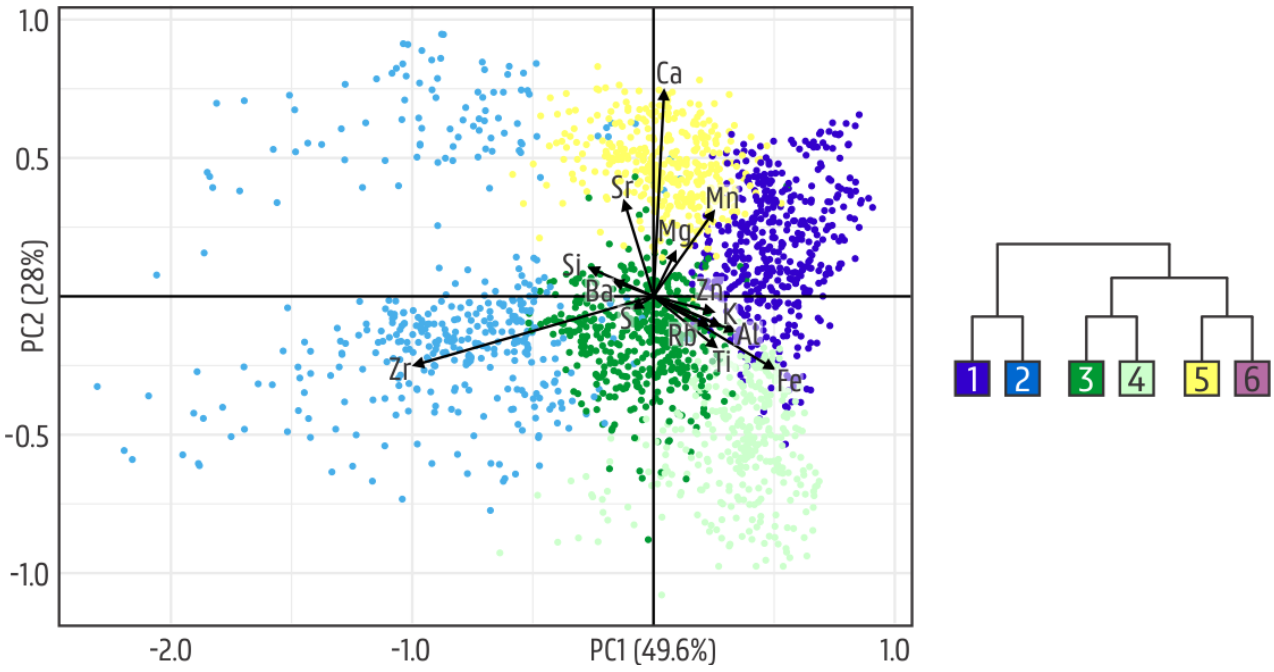
Supplementary Figure S10

XRF core scanning elemental composition (clr-values of Mg, Al, Si, S, K, Ca, Ti, Mn, Fe, Zn, Rb, Sr, Zr, Ba) plots along core AC07 (Chapter 5).



Supplementary Figure S11

PCA clustering results of XRF data from core AC07.



REFERENCES

Agentschap Maritieme Dienstverlening en Kust, 2024. Vergelijkingsvlak ALAT naar approximate MSL vlak (ETRS89 - N31).

Amkreutz, L., Vaart-Verschoof, S. van der, 2021. Doggerland: verdwenen wereld in de Noordzee, Derde herziene druk. ed. Sidestone Press, Leiden.

Arfai, J., Franke, D., Lutz, R., Reinhardt, L., Kley, J., Gaedicke, C., 2018. Rapid Quaternary subsidence in the northwestern German North Sea. Sci. Rep. 8, 11524. https://doi.org/10.1038/s41598-018-29638-6

Arosio, R., Collier, J.S., Hawes, J., Gupta, S., Sperry, J., 2021. New perspectives on the English Channel megaflood hypothesis: High-resolution multibeam and seabed camera imaging of submarine landforms in the Northern Palaeovalley. Geomorphology 382, 107692. https://doi.org/10.1016/j.geomorph.2021.107692

Bakker, M.A.J., Van Der Meer, J.J.M., 2003. Structure of a Pleistocene push moraine revealed by GPR: the eastern Veluwe Ridge, The Netherlands. Geol. Soc. Lond. Spec. Publ. 211, 143–151. https://doi.org/10.1144/GSL.SP.2001.211.01.12

Balson, P.S., D'Olier, B., 1990. Thames Estuary Sheet 51 N - 00 Sea Bed Sediments and Quaternary. 1:250 000 UTM series of the United Kingdom and continental shelf.

Balson, P.S., Laban, C., Schüttenhelm, R.T.E., Paepe, R., Baeteman, C., 1991. Ostend Sheet 51 N - 3 E Sea Bed Sediments and Holocene. 1:250 000 UTM series of the United Kingdom and continental shelf.

Batchelor, C.L., Margold, M., Krapp, M., Murton, D.K., Dalton, A.S., Gibbard, P.L., Stokes, C.R., Murton, J.B., Manica, A., 2019. The configuration of Northern Hemisphere ice sheets through the Quaternary. Nat. Commun. 10, 3713. https://doi.org/10.1038/s41467-019-11601-2

Beets, C.J., Beets, D.J., 2003. A high resolution stable isotope record of the penultimate deglaciation in lake sediments below the city of Amsterdam, The Netherlands. Quat. Sci. Rev. 22, 195–207. https://doi.org/10.1016/S0277-3791(02)00089-6

Beets, D.J., Meijer, T., Beets, C.J., Cleveringa, P., Laban, C., Van Der Spek, A.J.F., 2005. Evidence for a Middle Pleistocene glaciation of MIS 8 age in the southern North Sea. Quat. Int. 133–134, 7–19. https://doi.org/10.1016/j.quaint.2004.10.002

Behre, K.-E., Lade, U., 1986. Eine Folge von Eem und 4 Weichsel-Interstadialen in Oerel/Niedersachsen und ihr Vegetationsablauf. EG Quat. Sci. J. 36, 11–36. https://doi.org/10.3285/eg.36.1.02

Bell, F.G., Dickinson, C.A., 1971. The Barnwell Station Artic Flora: a reappraisal of some Plant Identifications. New Phytol. 70, 627–638.

Bell, W.T., Zimmerman, D.W., 1978. The effect of HF acid etching on the morphology of quartz inclusions for thermoluminescence dating. Archaeometry 20, 63–65. https://doi.org/10.1111/j.1475-4754.1978.tb00213.x

Bendixen, C., Lamb, R.M., Huuse, M., Boldreel, L.O., Jensen, J.B., Clausen, O.R., 2018. Evidence for a grounded ice sheet in the central North Sea during the early Middle Pleistocene Donian Glaciation. J. Geol. Soc. 175, 291–307. https://doi.org/10.1144/jgs2017-073

Bennett, K.D., 1994. Annotated catalogue of pollen and pteridophyte spore types of the British Isles.

Bennett, K.D., Whittington, G., Edwards, K.J., 1994. Recent plant nomenclatural changes and pollen morphology in the British Isles. Quat. Newsl. 73, 1–6.

Bennett, M.R., Glasser, N.F., 2009. Glacial geology: ice sheets and landforms, 2nd ed. ed. Wiley-Blackwell, Hoboken, NJ.

Bertrand, S., Tjallingii, R., Kylander, M.E., Wilhelm, B., Roberts, S.J., Arnaud, F., Brown, E., Bindler, R., 2024. Inorganic geochemistry of lake sediments: A review of analytical techniques and guidelines for data interpretation. Earth-Sci. Rev. 249, 104639. https://doi.org/10.1016/j.earscirev.2023.104639

Beug, H.-J., 1961. Leitfaden der Pollenbestimmung: Für Mitteleuropa und angrenzende Gebiete. Verlag Dr. Friedrich Pfeil, München.

BGS, 2026a. GeoIndex Offshore: Borehole Activity & scan - BH81/01A [WWW Document]. URL http://marinedata.bgs.ac.uk/Samples/WEB/52N002E/52N002E_470.pdf (accessed 1.29.26).
BGS, 2026b. GeoIndex Offshore: Borehole Activity & scan - BH81/53 [WWW Document]. URL http://marinedata.bgs.ac.uk/Samples/WEB/52N002E/52N002E_469.pdf (accessed 1.29.26).
BGS, 2026c. GeoIndex Offshore: Borehole Activity & scan - BH81/50A [WWW Document]. URL http://marinedata.bgs.ac.uk/Samples/WEB/52N002E/52N002E_467.pdf (accessed 1.29.26).
BGS, 2026d. GeoIndex Offshore: Borehole Activity & scan - BH79/01 [WWW Document]. URL http://marinedata.bgs.ac.uk/Samples/WEB/52N002E/52N002E_59.pdf (accessed 1.29.26).
BGS, 2000. 1:250 000 UTM series of the United Kingdom and continental shelf.
Bijlsma, S., 1981. Fluvial sedimentation from the Fennoscandian area into the Norh-West European Basin during the Late Cenozoic. Geol. En Mijnb. 8, 337–345.
Björck, S., Bennike, O., Ingólfsson, Ó., Barnekow, L., Penney, D.N., 1994. Lake Boksehandsken's earliest postglacial sediments and their palaeoenvironmental implications, Jameson Land, East Greenland. Boreas 23, 459–472. https://doi.org/10.1111/j.1502-3885.1994.tb00613.x
Blackmore, S., Steinmann, J.A.J., Hoen, P.P., Punt, W., 2003. BETULACEAE and CORYLACEAE. Rev. Palaeobot. Palynol. 123, 71–98. https://doi.org/10.1016/S0034-6667(02)00156-2
Blott, S.J., Pye, K., 2001. GRADISTAT: a grain size distribution and statistics package for the analysis of unconsolidated sediments. Earth Surf. Process. Landf. 26, 1237–1248. https://doi.org/10.1002/esp.261
Böse, M., Lüthgens, C., Lee, J.R., Rose, J., 2012. Quaternary glaciations of northern Europe. Quat. Sci. Rev. 44, 1–25. https://doi.org/10.1016/j.quascirev.2012.04.017
Bridgland, D.R., D'Olier, B., 1995. The Pleistocene evolution of the Thames and Rhine drainage systems in the southern North Sea. Geol. Soc. Spec. Publ. 27–45.
Busschers, F., Cohen, K., Wesselingh, F., Bakker, M., Schokker, J., Van Balen, R., Van Heteren, S., 2025. Quaternary, in: Geology of the Netherlands. Amsterdam University Press, Nieuwe Prinsengracht 89 1018 VR Amsterdam Nederland. https://doi.org/10.5117/9789463728362_ch10
Busschers, F.S., Kasse, C., Van Balen, R.T., Vandenberghe, J., Cohen, K.M., Weerts, H.J.T., Wallinga, J., Johns, C., Cleveringa, P., Bunnik, F.P.M., 2007. Late Pleistocene evolution of the Rhine-Meuse system in the southern North Sea basin: imprints of climate change, sea-level oscillation and glacio-isostacy. Quat. Sci. Rev. 26, 3216–3248. https://doi.org/10.1016/j.quascirev.2007.07.013
Busschers, F.S., Van Balen, R.T., Cohen, K.M., Kasse, C., Weerts, H.J.T., Wallinga, J., Bunnik, F.P.M., 2008. Response of the Rhine–Meuse fluvial system to Saalian ice-sheet dynamics. Boreas 37, 377–398. https://doi.org/10.1111/j.1502-3885.2008.00025.x
Bynoe, R., 2018. The submerged archaeology of the North Sea: Enhancing the Lower Palaeolithic record of northwest Europe. Quat. Sci. Rev. 191, 1–14. https://doi.org/10.1016/j.quascirev.2018.05.002
Cameron, T.D.J., Crosby, A., Balson, P.S., Jeffery, D.H., Lott, G.K., Bulat, J., Harrison, D.J. (Eds.), 1992. The Geology of the southern North Sea, United Kingdom Offshore Regional Reports. H.M.S.O for the British Geological Survey, London.
Cameron, T.D.J., Laban, C., Schüttenhelm, R.T.E., 1989. Upper Pliocene and Lower Pleistocene stratigraphy in the Southern Bight of the North Sea, in: Henriet, J.P., De Moor, G. (Eds.), The Quaternary and Tertiary Geology of the Southern Bight, North Sea. Ministry of Economic Affairs & Belgian Geological Survey, pp. 97–110.
Cameron, T.D.J., Laban, C., Schüttenhelm, R.T.E., 1984a. Flemish Bight Sheet 52 N - 02 E Quaternary Geology. 1:250 000 UTM series of the United Kingdom and continental shelf.
Cameron, T.D.J., Laban, C., Schüttenhelm, R.T.E., 1984b. Flemish Bight Sheet 52 N - 02 E Sea Bed Sediments and Holocene. 1:250 000 UTM series of the United Kingdom and continental shelf.
Carr, S.J., Holmes, R., Van Der Meer, J.J.M., Rose, J., 2006. The Last Glacial Maximum in the North Sea Basin: micromorphological evidence of extensive glaciation. J. Quat. Sci. 21, 131–153. https://doi.org/10.1002/jqs.950

Carrivick, J.L., Tweed, F.S., 2013. Proglacial lakes: character, behaviour and geological importance. Quat. Sci. Rev. 78, 34–52. https://doi.org/10.1016/j.quascirev.2013.07.028

Cartelle, V., Barlow, N.L.M., Hodgson, D.M., Busschers, F.S., Cohen, K.M., Meijninger, B.M.L., Van Kesteren, W.P., 2021. Sedimentary architecture and landforms of the late Saalian (MIS 6) ice sheet margin offshore of the Netherlands. Earth Surf. Dyn. 9, 1399–1421. https://doi.org/10.5194/esurf-9-1399-2021

Clark, C.D., Ely, J.C., Hindmarsh, R.C.A., Bradley, S., Ignéczi, A., Fabel, D., Ó Cofaigh, C., Chiverrell, R.C., Scourse, J., Benetti, S., Bradwell, T., Evans, D.J.A., Roberts, D.H., Burke, M., Callard, S.L., Medialdea, A., Saher, M., Small, D., Smedley, R.K., Gasson, E., Gregoire, L., Gandy, N., Hughes, A.L.C., Ballantyne, C., Bateman, M.D., Bigg, G.R., Doole, J., Dove, D., Duller, G.A.T., Jenkins, G.T.H., Livingstone, S.L., McCarron, S., Moreton, S., Pollard, D., Praeg, D., Sejrup, H.P., Van Landeghem, K.J.J., Wilson, P., 2022. Growth and retreat of the last British–Irish Ice Sheet, 31 000 to 15 000 years ago: the BRITICE-CHRONO reconstruction. Boreas 51, 699–758. https://doi.org/10.1111/bor.12594

Clark, P.U., Archer, D., Pollard, D., Blum, J.D., Rial, J.A., Brovkin, V., Mix, A.C., Pisias, N.G., Roy, M., 2006. The middle Pleistocene transition: characteristics, mechanisms, and implications for long-term changes in atmospheric pCO2. Quat. Sci. Rev. 25, 3150–3184. https://doi.org/10.1016/j.quascirev.2006.07.008

Clark, R.L., 1982. Point Count Estimation of Charcoal in Pollen Preparation and Thin Sections of Sediments. Pollen Spores 24, 523–535.

Cnudde, V., Cnudde, J.P., Dupuis, C., Jacobs, P.J.S., 2004. X-ray micro-CT used for the localization of water repellents and consolidants inside natural building stones. Mater. Charact. 53, 259–271. https://doi.org/10.1016/j.matchar.2004.08.011

Cohen, K.M., Cartelle, V., Barnett, R., Busschers, F.S., Barlow, N.L.M., 2022. Last Interglacial sea-level data points from Northwest Europe. Earth Syst. Sci. Data 14, 2895–2937. https://doi.org/10.5194/essd-14-2895-2022

Cohen, K.M., Gibbard, P.L., 2019. Global chronostratigraphical correlation table for the last 2.7 million years, version 2019 QI-500. Quat. Int. 500, 20–31. https://doi.org/10.1016/j.quaint.2019.03.009

Cohen, K.M., Gibbard, P.L., Weerts, H.J.T., 2014. North Sea palaeogeographical reconstructions for the last 1 Ma. Neth. J. Geosci. - Geol. En Mijnb. 93, 7–29. https://doi.org/10.1017/njg.2014.12

Cohen, K.M., Westley, K., Erkens, G., Hijma, M.P., Weerts, H.J.T., 2017. The North Sea, in: Flemming, N.C., Harff, J., Moura, D., Burgess, A., Bailey, G.N. (Eds.), Submerged Landscapes of the European Continental Shelf. Wiley & Sons Ltd., pp. 147–186. https://doi.org/10.1002/9781118927823.ch7

Collier, J.S., Oggioni, F., Gupta, S., García-Moreno, D., Trentesaux, A., De Batist, M., 2015. Streamlined islands and the English Channel megaflood hypothesis. Glob. Planet. Change 135, 190–206. https://doi.org/10.1016/j.gloplacha.2015.11.004

Cotterill, C., Phillips, E., James, L., Forsberg, C., Tjelta, T.I., 2017. How understanding past landscapes might inform present-day site investigations: a case study from Dogger Bank, southern central North Sea. Surf. Geophys. 15, 403–414. https://doi.org/10.3997/1873-0604.2017032

Cotterill, C.J., Phillips, E., James, L., Forsberg, C.F., Tjelta, T.I., Carter, G., Dove, D., 2017. The evolution of the Dogger Bank, North Sea: A complex history of terrestrial, glacial and marine environmental change. Quat. Sci. Rev. 171, 136–153. https://doi.org/10.1016/j.quascirev.2017.07.006

Cresswell, A.J., Carter, J., Sanderson, D.C.W., 2018. Dose rate conversion parameters: Assessment of nuclear data. Radiat. Meas. 120, 195–201. https://doi.org/10.1016/j.radmeas.2018.02.007

Croudace, I.W., Rothwell, R.G. (Eds.), 2015. Micro-XRF Studies of Sediment Cores: Applications of a non-destructive tool for the environmental sciences, Developments in Paleoenvironmental Research. Springer Netherlands, Dordrecht. https://doi.org/10.1007/978-94-017-9849-5

Dakin, N., Dove, D., Lee, J., MacDonald, C., 2026. The shallow subsurface geology of the southern North Sea (UK): an updated assessment using data from offshore wind farms (British Geological Survey Open Report No. OR/26/0055). British Geological Survey.

Davies, B.J., Roberts, D.H., Bridgland, D.R., Cofaigh, C.Ó., Riding, J.B., 2011. Provenance and depositional environments of Quaternary sediments from the western North Sea Basin. J. Quat. Sci. 26, 59–75. https://doi.org/10.1002/jqs.1426

De Clercq, M., Chademenos, V., Van Lancker, V., Missiaen, T., 2016. A high-resolution DEM for the Top-Palaeogene surface of the Belgian Continental Shelf. J. Maps 12, 1047–1054. https://doi.org/10.1080/17445647.2015.1117992

De Clercq, M., Missiaen, T., Wallinga, J., Zurita Hurtado, O., Versendaal, A., Mathys, M., De Batist, M., 2018. A well-preserved Eemian incised-valley fill in the southern North Sea Basin, Belgian Continental Shelf - Coastal Plain: Implications for northwest European landscape evolution. Earth Surf. Process. Landf. 43, 1913–1942. https://doi.org/10.1002/esp.4365

De Gans, W., Beets, D.J., Centineo, M.C., 2000. Late Saalian and Eemian deposits in the Amsterdam glacial basin. Neth. J. Geosci. 79, 147–160. https://doi.org/10.1017/S0016774600021685

Dingwall, R.G., 1975. Sub-bottom infilled channels in an area of the eastern English Channel. Philos. Trans. R. Soc. Lond. Ser. Math. Phys. Sci. 279, 233–241. https://doi.org/10.1098/rsta.1975.0055

Dix, J., Sturt, F., 2011. The Relic Palaeo-landscapes of the Thames Estuary Final Report (No. MEPF 09/P126). Marine Aggregate Levy Sustainability Fund (MALSF).

Eaton, S., Barlow, N.L.M., Hodgson, D.M., Mellett, C.L., Emery, A.R., 2024. Landscape evolution during Holocene transgression of a mid-latitude low-relief coastal plain: The southern North Sea. Earth Surf. Process. Landf. 49, 3139–3157. https://doi.org/10.1002/esp.5880

Eaton, S.J., Hodgson, D.M., Barlow, N.L.M., Mortimer, E.E.J., Mellett, C.L., 2020. Palaeogeographical changes in response to glacial–interglacial cycles, as recorded in Middle and Late Pleistocene seismic stratigraphy, southern North Sea. J. Quat. Sci. 35, 760–775. https://doi.org/10.1002/jqs.3230

Ekman, S.R., 1998. Pleistocene pollen stratigraphy from borehole 81/34, devil's hole area, central north sea. Quat. Sci. Rev. 17, 855–869. https://doi.org/10.1016/S0277-3791(98)00022-5

Emery, A.R., 2020. Glacial and postglacial landscape evolution at Dogger Bank since the Last Glacial Maximum (PhD). University of Leeds, School of Earth and Environment.

Emery, A.R., Hodgson, D.M., Barlow, N.L.M., Carrivick, J.L., Cotterill, C.J., Phillips, E., 2019. Left High and Dry: Deglaciation of Dogger Bank, North Sea, Recorded in Proglacial Lake Evolution. Front. Earth Sci. 7, 234. https://doi.org/10.3389/feart.2019.00234

Emery, A.R., Hodgson, D.M., Barlow, N.L.M., Carrivick, J.L., Cotterill, C.J., Richardson, J.C., Ivanovic, R.F., Mellett, C.L., 2020. Ice sheet and palaeoclimate controls on drainage network evolution: an example from Dogger Bank, North Sea. Earth Surf. Dyn. 8, 869–891. https://doi.org/10.5194/esurf-8-869-2020

EMODnet Bathymetry Consortium, 2022. EMODnet Digital Bathymetry (DTM 2022). https://doi.org/https://doi.org/10.12770/ff3aff8a-cff1-44a3-a2c8-1910bf109f85

EU Copernicus Marine Service, 2024. European Seas Gridded L 4 Sea Surface Heights And Derived Variables Nrt. https://doi.org/10.48670/MOI-00142

European Comission, 2020. An EU Strategy to harness the potential of offshore renewable energy for a climate neutral future (No. COM/2020/741). European Comission, Brussels.

European Union-Copernicus Marine Service, 2019. EUROPEAN SEAS GRIDDED L4 SEA SURFACE HEIGHTS AND DERIVED VARIABLES NRT. https://doi.org/10.48670/MOI-00142

Francescangeli, F., Bouchet, V.M.P., Trentesaux, A., Armynot Du Chatelet, E., 2017. Does elevation matter? Living foraminiferal distribution in a hyper tidal salt marsh (Canche Estuary, Northern France). Estuar. Coast. Shelf Sci. 194, 192–204. https://doi.org/10.1016/j.ecss.2017.06.023

Francescangeli, F., Milker, Y., Bunzel, D., Thomas, H., Norbisrath, M., Schönfeld, J., Schmiedl, G., 2021. Recent benthic foraminiferal distribution in the Elbe Estuary (North Sea, Germany): A response to environmental stressors. Estuar. Coast. Shelf Sci. 251, 107198. https://doi.org/10.1016/j.ecss.2021.107198

Frontalini, F., Francescangeli, F., Du Chatelet, E.A., 2018. Significance of replicates: Environmental and paleoenvironmental studies on benthic foraminifera and testate amoebae. Micropaleontology 63, 257–274. https://doi.org/10.47894/mpal.63.5.01

Gaffney, V., Thomson, K., Fitch, S. (Eds.), 2007. Mapping Doggerland: The Mesolithic Landscapes of the Southern North Sea. Archaeopress Publishing Ltd. https://doi.org/10.2307/j.ctv1pzk1w9
Galbraith, R.F., Roberts, R.G., Laslett, G.M., Yoshida, H., Olley, J.M., 1999. Optical Dating of Single and Multiple Grains of Quartz from Jinmium Rock Shelter, Northern Australia: Part I, Expirimental Design and Statistical Models. Archaeometry 41, 339–364. https://doi.org/10.1111/j.1475-4754.1999.tb00987.x
García-Moreno, D., 2017. Origin and geomorphology of Dover Strait and southern North Sea palaeovalleys and palaeo-depressions. (PhD). Ghent University.
García-Moreno, D., Gupta, S., Collier, J.S., Oggioni, F., Vanneste, K., Trentesaux, A., Verbeeck, K., Versteeg, W., Jomard, H., Camelbeeck, T., De Batist, M., 2019. Middle–Late Pleistocene landscape evolution of the Dover Strait inferred from buried and submerged erosional landforms. Quat. Sci. Rev. 203, 209–232. https://doi.org/10.1016/j.quascirev.2018.11.011
García-Moreno, D., Vandorpe, T., De Clercq, M., Roche, M., Vertino, A., Missiaen, T., 2021. Characterisation of Middle–Late Pleistocene groove-and-ridge landforms incised across the Dover Strait. Geomorphology 376, 107517. https://doi.org/10.1016/j.geomorph.2020.107517
Geophysical Services Offshore BV, n.d. GSO 360 Tip Sparker Source.
Geotek Ltd., n.d. Multi-Sensor Core Logger (MSCL-s) [WWW Document]. URL British Crown Copyright 2024. All rights reserved (accessed 7.19.24).
Gibbard, P., 2007. Europe cut adrift. Nature 448, 259–260. https://doi.org/10.1038/448259a
Gibbard, P.L., 1995. The formation of the Strait of Dover, in: Preece, R.C. (Ed.), Island Britain: A Quaternary Perspective. Geological Society, London, Special Publication, pp. 15–26.
Gibbard, P.L., Cohen, K.M., 2015. Quaternary evolution of the North Sea and the English Channel, in: Proceedings of the Open University Geological Society. Godalming, Surrey, pp. 63–74.
Gibbard, P.L., Hughes, P.D., Clark, C.D., Glasser, N.F., Tomkins, M.D., 2022. Britain and Ireland: glacial landforms prior to the Last Glacial Maximum, in: Palacios, D., Hughes, P.D., García-Ruiz, J.M., Andrés, N. (Eds.), European Glacial Landscapes. Elsevier, pp. 245–253. https://doi.org/10.1016/B978-0-12-823498-3.00050-9
Gibbard, P.L., Lewin, J., 2016. Filling the North Sea Basin: Cenozoic sediment sources and river styles. Geol. Belg. 19, 201–217. https://doi.org/10.20341/gb.2015.017
Gibbard, P.L., Rose, J., Bridgland, D.R., 1988. The history of the great northwest European rivers during the past three million years. Philos. Trans. R. Soc. Lond. Biol. Sci. 318, 559–602. https://doi.org/10.1098/rstb.1988.0024
Godwin, H., 1975. History of the British Flora. A factual basis for phytogeography. Cambridge University Press, Cambridge.
Gonzalez, R.C., Woods, R.E., 2002. Digital image processing, 2. ed., internat. ed. ed. Prentice-Hall, Upper Saddle River, NJ.
Gosling, W.D., Bush, M.B., Hanselman, J.A., Chepstow-Lusty, A., 2008. Glacial-interglacial changes in moisture balance and the impact on vegetation in the southern hemisphere tropical Andes (Bolivia/Peru). Palaeogeogr. Palaeoclimatol. Palaeoecol. 259, 35–50. https://doi.org/10.1016/j.palaeo.2007.02.050
Gowan, E.J., Zhang, X., Khosravi, S., Rovere, A., Stocchi, P., Hughes, A.L.C., Gyllencreutz, R., Mangerud, J., Svendsen, J.-I., Lohmann, G., 2021. A new global ice sheet reconstruction for the past 80 000 years. Nat. Commun. 12, 1199. https://doi.org/10.1038/s41467-021-21469-w
Graham, A.G.C., Stoker, M.S., Lonergan, L., Bradwell, T., Stewart, M.A., 2011. The Pleistocene Glaciations of the North Sea Basin, in: Ehlers, J., Gibbard, P.L., Hughes, P.D. (Eds.), Quaternary Glaciations - Extent and Chronology: A Closer Look. Elsevier, pp. 261–278. https://doi.org/10.1016/B978-0-444-53447-7.00021-0
Grant, M., Marshall, P., 2025. Scientifique Dating of Pleistocene Sites: Guiedlines for Best Practice (No. HEAG0325), Historic England Advice and Guidance. Historic England, London.
Grimm, E.C., 1991. TILIA and TILIA GRAPH.
Gupta, S., Collier, J.S., Garcia-Moreno, D., Oggioni, F., Trentesaux, A., Vanneste, K., De Batist, M., Camelbeeck, T., Potter, G., Van Vliet-Lanoë, B., Arthur, J.C.R., 2017. Two-stage opening of the

Dover Strait and the origin of island Britain. Nat. Commun. 8, 15101. https://doi.org/10.1038/ncomms15101
Gupta, S., Collier, J.S., Palmer-Felgate, A., Potter, G., 2007. Catastrophic flooding origin of shelf valley systems in the English Channel. Nature 448, 342–345. https://doi.org/10.1038/nature06018
Haque, R.A.I., Mitra, A.J., Tarafdar, S., Dutta, T., 2023. Evolution of polygonal crack patterns in mud when subjected to repeated wetting–drying cycles. Chaos Solitons Fractals 174, 113894. https://doi.org/10.1016/j.chaos.2023.113894
Harrison, D.J., Hopson, P.M., 1991. East Anglia Sheet 52 N - 00 Quaternary Geology. 1:250 000 UTM series of the United Kingdom and continental shelf.
Henriet, J.P., Moor, G.D. (Eds.), 1989. The Quaternary and Tertiary Geology of the Southern Bight, North Sea. Ministry of Economic Affairs & Belgian Geological Survey.
Heyse, I., Demoulin, A., 2018. The Flemish Valley: Response of the Scheldt Drainage System to Climatic and Glacio-Eustatic Oscillations, in: Demoulin, A. (Ed.), Landscapes and Landforms of Belgium and Luxembourg, World Geomorphological Landscapes. Springer International Publishing, Cham, pp. 297–311. https://doi.org/10.1007/978-3-319-58239-9_18
Hijma, M.P., Bradley, S.L., Cohen, K.M., Van Der Wal, W., Barlow, N.L.M., Blank, B., Frechen, M., Hennekam, R., Van Heteren, S., Kiden, P., Mavritsakis, A., Meijninger, B.M.L., Reichart, G.-J., Reinhardt, L., Rijsdijk, K.F., Vink, A., Busschers, F.S., 2025. Global sea-level rise in the early Holocene revealed from North Sea peats. Nature 639, 652–657. https://doi.org/10.1038/s41586-025-08769-7
Hijma, M.P., Cohen, K.M., Roebroeks, W., Westerhoff, W.E., Busschers, F.S., 2012. Pleistocene Rhine–Thames landscapes: geological background for hominin occupation of the southern North Sea region. J. Quat. Sci. 27, 17–39. https://doi.org/10.1002/jqs.1549
Hjelstuen, B.O., Sejrup, H.P., Valvik, E., Becker, L.W.M., 2018. Evidence of an ice-dammed lake outburst in the North Sea during the last deglaciation. Mar. Geol. 402, 118–130. https://doi.org/10.1016/j.margeo.2017.11.021
Huang, X., Xiang, L., Lei, G., Sun, M., Qiu, M., Storozum, M., Huang, C., Munkhbayar, C., Demberel, O., Zhang, Jun, Zhang, Jiawu, Chen, X., Chen, J., Chen, F., 2021. Sedimentary Pediastrum record of middle–late Holocene temperature change and its impacts on early human culture in the desert-oasis area of northwestern China. Quat. Sci. Rev. 265, 107054. https://doi.org/10.1016/j.quascirev.2021.107054
Hughes, P.D., Gibbard, P.L., Ehlers, J., 2020. The “missing glaciations” of the Middle Pleistocene. Quat. Res. 96, 161–183. https://doi.org/10.1017/qua.2019.76
Huuse, M., Lykke-Andersen, H., 2000. Overdeepened Quaternary valleys in the eastern Danish North Sea: morphology and origin. Quat. Sci. Rev. 19, 1233–1253. https://doi.org/10.1016/S0277-3791(99)00103-1
Innomar Technologie GmbH, n.d. Innomar Quattro Parametric Sub-Bottom Profiler.
Issa, B.M., 2024. First record of the species Aubignyna perlucida in Basra marshlands sediments/ southern Iraqi. Basrah Res. Sci. 50, 239–246. https://doi.org/10.56714/bjrs.50.2.20
Jankovská, V., Komárek, J., 2000. Indicative value ofPediastrum and other coccal green algae in palaeoecology. Folia Geobot. 35, 59–82. https://doi.org/10.1007/BF02803087
Johnson, M.A., Kenyon, N.H., Belderson, R.H., Stride, A.H., 1982. Sand transport, in: Stride, A.H. (Ed.), Offshore Tidal Sands: Processes and Deposits. Chapman and Hall Ltd, New York, USA, pp. 58–96.
Kasse, C., Van Der Woude, J.D., Woolderink, H.A.G., Schokker, J., 2022. Eemian to Early Weichselian regional and local vegetation development and sedimentary and geomorphological controls, Amersfoort Basin, The Netherlands. Neth. J. Geosci. 101, e7. https://doi.org/10.1017/njg.2022.4
Kinnaird, T.C., Abellán Santisteban, J., Brandolini, F., Carlton, R., Carrer, F., Civantos, J.M.M., Duggan, M., Holcomb, J.A., Lekakis, S., Ramos Rodríguez, B., Salazar Ortiz, N., Sánchez-Pardo, J.C., Sevara, C., Snyder, J.R., Shillito, L., Silva Sanchez, N., Srivastava, A., Turner, A., Turner, S., 2025. Unearthing the Histories of Agrarian Landscapes: A Research Framework for Terraces

as Sustainable Environments. Geoarchaeology 40, e70004. https://doi.org/10.1002/gea.70004
Kirkham, J.D., Hogan, K.A., Larter, R.D., Arnold, N.S., Ely, J.C., Clark, C.D., Self, E., Games, K., Huuse, M., Stewart, M.A., Ottesen, D., Dowdeswell, J.A., 2024. Tunnel valley formation beneath deglaciating mid-latitude ice sheets: Observations and modelling. Quat. Sci. Rev. 323, 107680. https://doi.org/10.1016/j.quascirev.2022.107680
Knox, R.W.O.B., Bosh, J.H.A., Rasmussen, E.S., Heilmann-Clausen, C., Hiss, M., De Lugt, I.R., Kasinski, J., King, C., Köthe, A., Slodkowska, B., Standke, G., Vandenberghe, N., 2010. Cenozoic, in: Petroleum Geological Atlas of the Southern Permian Basin Area. EAGE Publications b.v., Houten, pp. 211–223.
Kongsberg Geoacoustics ltd., 2019. TOPAS PS18.
Kristensen, T.B., Huuse, M., Piotrowski, J.A., Clausen, O.R., 2007. A morphometric analysis of tunnel valleys in the eastern North Sea based on 3D seismic data. J. Quat. Sci. 22, 801–815. https://doi.org/10.1002/jqs.1123
Küster, H., 1988. Vom Werden einer Kulturlandschaft: Vegetationsgeschichtliche Studien am Auerberg (Südbayern), Quellen und Forschungen zur prähistorischen und provinzialrömischen Archäologie. VCH, Acta humaniora, Weinheim.
Kyriakoudi, D., De Batist, M., Vervoort, M., Mestdagh, T., Missiaen, T., Grant, M., Hill, T., Kinnaird, T., Plets, R., 2026. Evidence of a Weichselian MIS 3 proglacial lake south of Dogger Bank (southern North Sea). Quat. Sci. Rev. 390, 110190. https://doi.org/10.1016/j.quascirev.2026.110190
Laban, C., 1995. The Pleistocene glaciations in the Dutch sector of the North Sea (PhD). University of Amsterdam.
Laban, C., Cameron, T.D.J., Schüttenhelm, R.T.E., 1984. Geologie van het Kwartair in de zuidelijke bocht van de Noordzee. Meded Werkgr Tert Kwart Geol 21, 139–154.
Laban, C., Schüttenhelm, R.T.E., Balson, P.S., Baeteman, C., Paepe, R., 1992. Ostend Sheet 51 N - 02 E Quaternary. 1:250 000 UTM series of the United Kingdom and continental shelf.
Laban, C., van der Meer, J.J.M., 2011. Pleistocene Glaciation in The Netherlands, in: Quaternary Glaciatipns - Extent and Chronology: A Closer Look, Developments in Quaternary Science. Elsevier, pp. 247–260. https://doi.org/10.1016/B978-0-444-53447-7.00020-9
Lamb, R.M., Harding, R., Huuse, M., Stewart, M., Brocklehurst, S.H., 2018. The early Quaternary North Sea Basin. J. Geol. Soc. 175, 275–290. https://doi.org/10.1144/jgs2017-057
Lambeck, K., 1995. Late Devensian and Holocene shorelines of the British Isles and North Sea from models of glacio-hydro-isostatic rebound. J. Geol. Soc. 152, 437–448. https://doi.org/10.1144/gsjgs.152.3.0437
Limpenny, S.E., Barrio Froján, C., Foster-Smith, R.L., Pearce, B., Tizzard, L., Limpenny, D.L., Long, D., Walmsley, S., Kirby, S., Meadows, W.J., Rees, J., Hill, J., Wilson, C., Leivers, M., Churchley, S., Russell, J., Birchenough, A.C., Green, S.L., Law, R.J., 2011. The East Coast Regional Environmental Characterisation (Cefas Open report No. 08/04). Marine Aggregate Levy Sustainibility Fund (MALSF).
Lisiecki, L.E., Raymo, M.E., 2005. A Pliocene-Pleistocene stack of 57 globally distributed benthic δ^{18}O records. Paleoceanography 20, 2004PA001071. https://doi.org/10.1029/2004PA001071
Liu, A.C., De Batist, M., Henriet, J.P., Missiaen, T., 1993. Plio-Pleistocene scour hollows in the Southern Bight of the North Sea. Geol. En Mijnb. 71, 195–204.
Liu, A.C., Missiaen, T., Henriet, J.P., 1992. The morphology of the top-Tertiary erosion surface in the Belgian sector of the North Sea. Mar. Geol. 105, 275–284. https://doi.org/10.1016/0025-3227(92)90193-L
Lonergan, L., Maidment, S.C.R., Collier, J.S., 2006. Pleistocene subglacial tunnel valleys in the central North Sea basin: 3-D morphology and evolution. J. Quat. Sci. 21, 891–903. https://doi.org/10.1002/jqs.1015
Long, D., Laban, C., Streif, H., Cameron, T.D.J., Schüttenhelm, R.T.E., 1988. The sedimentary record of climatic variation in the southern North Sea. Philos. Trans. R. Soc. Lond. B Biol. Sci. 318, 523–537. https://doi.org/10.1098/rstb.1988.0022

Mahan, S.A., Rittenour, T.M., Nelson, M.S., Ataee, N., Brown, N., DeWitt, R., Durcan, J., Evans, M., Feathers, J., Frouin, M., Guérin, G., Heydari, M., Huot, S., Jain, M., Keen-Zebert, A., Li, B., López, G.I., Neudorf, C., Porat, N., Rodrigues, K., Sawakuchi, A.O., Spencer, J.Q.G., Thomsen, K., 2022. Guide for interpreting and reporting luminescence dating results. GSA Bull. https://doi.org/10.1130/B36404.1

Maizels, J.K., 1977. Experiments on the Origin of Kettle-holes. J. Glaciol. 18, 291–303. https://doi.org/10.3189/S0022143000021365

Martin, A.C., Harvey, W.J., 2017. The Global Pollen Project: a new tool for pollen identification and the dissemination of physical reference collections. Methods Ecol. Evol. 8, 892–897. https://doi.org/10.1111/2041-210X.12752

Martin-Puertas, C., Tjallingii, R., Bloemsma, M., Brauer, A., 2017. Varved sediment responses to early Holocene climate and environmental changes in Lake Meerfelder Maar (Germany) obtained from multivariate analyses of micro X-ray fluorescence core scanning data. J. Quat. Sci. 32, 427–436. https://doi.org/10.1002/jqs.2935

Mathys, M., 2009. The Quaternary geological evolution of the Belgian Continental Shelf, southern North Sea (PhD). Ghent University.

McCave, I.N., 1971. Sand waves in the North Sea off the coast of Holland. Mar. Geol. 10, 199–225. https://doi.org/10.1016/0025-3227(71)90063-6

McGuire, A.M., 2020. Resolving abrupt palaeoenvironmental changes in a lake sediment sequence from Ioannina, northwest Greece (PhD). University of Cambridge.

McGuire, A.M., Cartelle, V., Rush, G., Busschers, F.S., Cohen, K.M., Hodgson, D.M., Barlow, N.L.M., 2025. The RISeR cores: unexpected and extensive Middle Pleistocene terrestrial stratigraphy in the southern North Sea. Sci. Drill. 34, 29–39. https://doi.org/10.5194/sd-34-29-2025

Medina-Elizalde, M., 2013. A global compilation of coral sea-level benchmarks: Implications and new challenges. Earth Planet. Sci. Lett. 362, 310–318. https://doi.org/10.1016/j.epsl.2012.12.001

Meijer, T., Preece, R.C., 1995. Malacological evidence relating to the insularity of the British Isles during the Quaternary. Geol. Soc. Lond. Spec. Publ. 96, 89–110. https://doi.org/10.1144/GSL.SP.1995.096.01.08

Meijs, E.P.M., Van Peer, Ph., De Warrimont, J.P.L.M.N., 2013. Geomorphologic context and proposed chronostratigraphic position of Lower Palaeolithic artefacts from the Op de Schans pit near Kesselt (Belgium) to the west of Maastricht. Neth. J. Geosci. - Geol. En Mijnb. 91, 137–157. https://doi.org/10.1017/S0016774600001554

Mejdahl, V., 1979. Thermoluminescence dating: Beta-dose attenuation in quartz grains. Archaeometry 21, 61–72. https://doi.org/10.1111/j.1475-4754.1979.tb00241.x

Mellett, C.L., Hodgson, D.M., Plater, A.J., Mauz, B., Selby, I., Lang, A., 2013. Denudation of the continental shelf between Britain and France at the glacial–interglacial timescale. Geomorphology 203, 79–96. https://doi.org/10.1016/j.geomorph.2013.03.030

Mellett, C.L., Phillips, E., Lee, J.R., Cotterill, C.J., Tjelta, T.I., James, L., Duffy, C., 2020. Elsterian ice-sheet retreat in the southern North Sea: antecedent controls on large-scale glaciotectonics and subglacial bed conditions. Boreas 49, 129–151. https://doi.org/10.1111/bor.12410

Missiaen, T., 2010. The potential of seismic imaging in marine archaeological site investigations. Relicta Archeol. Monum.- En Landschapsonderzoek Vlaan. 219–236. https://doi.org/10.55465/EAIE7018

Missiaen, T., Fitch, S., Harding, R., Muru, M., Fraser, A., De Clercq, M., Moreno, D.G., Versteeg, W., Busschers, F.S., Van Heteren, S., Hijma, M.P., Reichart, G.-J., Gaffney, V., 2021. Targeting the Mesolithic: Interdisciplinary approaches to archaeological prospection in the Brown Bank area, southern North Sea. Quat. Int. 584, 141–151. https://doi.org/10.1016/j.quaint.2020.05.004

Mitchum, R.M., Vail, P.R., Sangree, J.B., 1977. Seismic Stratigraphy and Global Changes of Sea Level, Part 6Stratigraphic Interpretation of Seismic Reflection Patterns in Depositional Sequences, in: Seismic Stratigraphy — Applications to Hydrocarbon Exploration. American Association of Petroleum Geologists. https://doi.org/10.1306/M26490C8

Moore, P.D., Webb, J.A., Collinson, M.E., 1991. Pollen analysis. Blackwell, Oxford.

Moreau, J., Huuse, M., Janszen, A., Van Der Vegt, P., Gibbard, P.L., Moscariello, A., 2012. The glaciogenic unconformity of the southern North Sea. Geol. Soc. Lond. Spec. Publ. 368, 99–110. https://doi.org/10.1144/SP368.5

Munyikwa, K., Kinnaird, T.C., Sanderson, D.C.W., 2021. The potential of portable luminescence readers in geomorphological investigations: a review. Earth Surf. Process. Landf. 46, 131–150. https://doi.org/10.1002/esp.4975

Murray, A.S., Wintle, A.G., 2000. Luminescence dating of quartz using an improved single-aliquot regenerative-dose protocol. Radiat. Meas. 32, 57–73. https://doi.org/10.1016/S1350-4487(99)00253-X

Murray, J.W., Whittaker, J.E., Alve, E., 2000. On the type species of Aubignyna and a description of A. hamblensis, a new microforaminifer from temperate shallow waters. J. Micropalaeontology 19, 61–67. https://doi.org/10.1144/jm.19.1.61

Murton, D.K., Murton, J.B., 2012. Middle and Late Pleistocene glacial lakes of lowland Britain and the southern North Sea Basin. Quat. Int. 260, 115–142. https://doi.org/10.1016/j.quaint.2011.07.034

Murton, J.B., Evans, D.J.A., Gupta, S., 2026. Enigmatic lineations in the Strait of Dover may be glacial. Proc. Geol. Assoc. 137, 101186. https://doi.org/10.1016/j.pgeola.2026.101186

Nanda, N.C., 2021. Seismic Data Interpretation and Evaluation for Hydrocarbon Exploration and Production: A Practitioner's Guide, Advances in Oil and Gas Exploration & Production. Springer International Publishing, Cham. https://doi.org/10.1007/978-3-030-75301-6

Nichols, G., 2010. Sedimentology and stratigraphy, 2. ed., [Nachdr.]. ed. Wiley-Blackwell, Chichester.

Nielsen, H., Sørensen, I., 1992. Taxonomy and stratigraphy of late-glacial Pediastrum taxa from Lysmosen, Denmark — a preliminary study. Rev. Palaeobot. Palynol. 74, 55–75. https://doi.org/10.1016/0034-6667(92)90138-7

OBIS, 2026. Ocean Biodiversity Information System [WWW Document]. URL https://obis.org/data/access/

Ottesen, D., Batchelor, C.L., Dowdeswell, J.A., Løseth, H., 2018. Morphology and pattern of Quaternary sedimentation in the North Sea Basin (52–62°N). Mar. Pet. Geol. 98, 836–859. https://doi.org/10.1016/j.marpetgeo.2018.08.022

Ottesen, D., Stewart, M., Brönner, M., Batchelor, C.L., 2020. Tunnel valleys of the central and northern North Sea (56°N to 62°N): Distribution and characteristics. Mar. Geol. 425, 106199. https://doi.org/10.1016/j.margeo.2020.106199

Overeem, I., Weltje, G.J., Bishop-Kay, C., Kroonenberg, S.B., 2001. The Late Cenozoic Eridanos delta system in the Southern North Sea Basin: a climate signal in sediment supply? Basin Res. 13, 293–312. https://doi.org/10.1046/j.1365-2117.2001.00151.x

Parfitt, S.A., Ashton, N.M., Lewis, S.G., Abel, R.L., Coope, G.R., Field, M.H., Gale, R., Hoare, P.G., Larkin, N.R., Lewis, M.D., Karloukovski, V., Maher, B.A., Peglar, S.M., Preece, R.C., Whittaker, J.E., Stringer, C.B., 2010. Early Pleistocene human occupation at the edge of the boreal zone in northwest Europe. Nature 466, 229–233. https://doi.org/10.1038/nature09117

Peeters, J., Busschers, F.S., Stouthamer, E., Bosch, J.H.A., Van Den Berg, M.W., Wallinga, J., Versendaal, A.J., Bunnik, F.P.M., Middelkoop, H., 2016. Sedimentary architecture and chronostratigraphy of a late Quaternary incised-valley fill: A case study of the late Middle and Late Pleistocene Rhine system in the Netherlands. Quat. Sci. Rev. 131, 211–236. https://doi.org/10.1016/j.quascirev.2015.10.015

Periplus Archeomare, 2023. Archeological Assessment of Paleolandscapes: Ijmuiden Ver Alpha and Beta (No. 20A034- 02).

Phillips, E., Cotterill, C., Johnson, K., Crombie, K., James, L., Carr, S., Ruiter, A., 2018. Large-scale glacitectonic deformation in response to active ice sheet retreat across Dogger Bank (southern central North Sea) during the Last Glacial Maximum. Quat. Sci. Rev. 179, 24–47. https://doi.org/10.1016/j.quascirev.2017.11.001

Praeg, D., 2003. Seismic imaging of mid-Pleistocene tunnel-valleys in the North Sea Basin—high resolution from low frequencies. J. Appl. Geophys. 53, 273–298. https://doi.org/10.1016/j.jappgeo.2003.08.001

Reid, E.M., 1949. The Late-Glacial Flora of the Lea Valley. New Phytol. 48, 245–252.
Reynolds, J.M., 2011. An introduction to applied and environmental geophysics, 2nd edition. ed. Wiley-Blackwell, Oxford Chichester, West Sussex Hoboken, NJ.
Richter, T.O., Van Der Gaast, S., Koster, B., Vaars, A., Gieles, R., De Stigter, H.C., De Haas, H., Van Weering, T.C.E., 2006. The Avaatech XRF Core Scanner: technical description and applications to NE Atlantic sediments. Geol. Soc. Lond. Spec. Publ. 267, 39–50. https://doi.org/10.1144/GSL.SP.2006.267.01.03
Rieu, R., Van Heteren, S., Van Der Spek, A.J.F., De Boer, P.L., 2005. Development and Preservation of a Mid-Holocene Tidal-Channel Network Offshore the Western Netherlands. J. Sediment. Res. 75, 409–419. https://doi.org/10.2110/jsr.2005.032
Rijsdijk, K.F., Passchier, S., Weerts, H.J.T., Laban, C., Van Leeuwen, R.J.W., Ebbing, J.H.J., 2005. Revised Upper Cenozoic stratigraphy of the Dutch sector of the North Sea Basin: towards an integrated lithostratigraphic, seismostratigraphic and allostratigraphic approach. Neth. J. Geosci. 84, 129–146. https://doi.org/10.1017/S0016774600023015
Roberts, D.H., Evans, D.J.A., Callard, S.L., Clark, C.D., Bateman, M.D., Medialdea, A., Dove, D., Cotterill, C.J., Saher, M., Cofaigh, C.Ó., Chiverrell, R.C., Moreton, S.G., Fabel, D., Bradwell, T., 2018. Ice marginal dynamics of the last British-Irish Ice Sheet in the southern North Sea: Ice limits, timing and the influence of the Dogger Bank. Quat. Sci. Rev. 198, 181–207. https://doi.org/10.1016/j.quascirev.2018.08.010
Ronchi, L., Fontana, A., Correggiari, A., Asioli, A., 2018. Late Quaternary incised and infilled landforms in the shelf of the northern Adriatic Sea (Italy). Mar. Geol. 405, 47–67. https://doi.org/10.1016/j.margeo.2018.08.004
Royal Netherlands Navy, Hydrographic Service, 2023. NLLAT2018.
Rundgren, M., 1995. Biostratigraphic Evidence of the Allerød-Younger Dryas-Preboreal Oscillation in Northern Iceland. Quat. Res. 44, 405–416. https://doi.org/10.1006/qres.1995.1085
Sanderson, D.C.W., Murphy, S., 2010. Using simple portable OSL measurements and laboratory characterisation to help understand complex and heterogeneous sediment sequences for luminescence dating. Quat. Geochronol. 5, 299–305. https://doi.org/10.1016/j.quageo.2009.02.001
Sarmaja-Korjonen, K., Seppänen, A., Bennike, O., 2006. Pediastrum algae from the classic late glacial Bølling Sø site, Denmark: Response of aquatic biota to climate change. Rev. Palaeobot. Palynol. 138, 95–107. https://doi.org/10.1016/j.revpalbo.2005.12.003
Sejrup, H.P., Clark, C.D., Hjelstuen, B.O., 2016. Rapid ice sheet retreat triggered by ice stream debuttressing: Evidence from the North Sea. Geology 44, 355–358. https://doi.org/10.1130/G37652.1
Selvam, P., Ramakrishnan, Y., Srinivasan, N., Maxwalt, S., 2025. A review of species diversity and distribution concerning environmental variables of Benthic Foraminifera around Marine Ecosystems Worldwide. Oeil Res. J. 23, 50–84. https://doi.org/10.14148.ORJ.2025.V23.I3.05
Slupik, A.A., Wesselingh, F.P., Mayhew, D.F., Janse, A.C., Dieleman, F.E., Van Strydonck, M., Kiden, P., Burger, A.W., Reumer, J.W.F., 2013. The role of a proto-Schelde River in the genesis of the southwestern Netherlands, inferred from the Quaternary successions and fossils in Moriaanshoofd Borehole (Zeeland, the Netherlands). Neth. J. Geosci. - Geol. En Mijnb. 92, 69–86. https://doi.org/10.1017/S0016774600000299
Smith, N.D., Ashley, G.M., 1985. Proglacial lacustrine environment, in: Ashley, Gail M., Shaw, J., Smith, Norman D. (Eds.), Glacial Sedimentary Environments. SEPM (Society for Sedimentary Geology), pp. 135–216.
Spagnolo, M., Clark, C.D., Ely, J.C., Stokes, C.R., Anderson, J.B., Andreassen, K., Graham, A.G.C., King, E.C., 2014. Size, shape and spatial arrangement of mega-scale glacial lineations from a large and diverse dataset. Earth Surf. Process. Landf. 39, 1432–1448. https://doi.org/10.1002/esp.3532
Spratt, R.M., Lisiecki, L.E., 2016. A Late Pleistocene sea level stack. Clim. Past 12, 1079–1092. https://doi.org/10.5194/cp-12-1079-2016

Srivastava, A., Kinnaird, T., Sevara, C., Holcomb, J.A., Turner, S., 2023. Dating Agricultural Terraces in the Mediterranean Using Luminescence: Recent Progress and Challenges. Land 12, 716. https://doi.org/10.3390/land12030716

Stace, C.A., 2010. New flora of the British Isles, 3rd ed. ed. Cambridge university press, Cambridge.

Stewart, M.A., Lonergan, L., 2011. Seven glacial cycles in the middle-late Pleistocene of northwest Europe: Geomorphic evidence from buried tunnel valleys. Geology 39, 283–286. https://doi.org/10.1130/G31631.1

Stockmar, J., 1971. Tablets with spores used in absolute pollen analysis. Pollen Spores 13, 615–621.

Stoker, M.S., Balson, P.S., Long, D., Tappin, D.R., 2011. An overview of the lithostratigraphical framework for the Quaternary deposits on the United Kingdom continental shelf (Research Report No. RR/11/03). British Geological Survey.

Sturt, F., Dix, J.K., EMU ltd, 2009. The Outer Thames Estuary Regional Environmental Characterisation (Technical Report No. 09/J/1/06/1305/0870). Marine Aggregate Levy Sustainability Fund (MALSF), London, GB.

Sturt, F., Garrow, D., Bradley, S., 2013. New models of North West European Holocene palaeogeography and inundation. J. Archaeol. Sci. 40, 3963–3976. https://doi.org/10.1016/j.jas.2013.05.023

Thorne, J.A., Watts, A.B., 1989. Quantitative analysis of North Sea subsidence. Am. Assoc. Pet. Geol. Bull. 73, 88–116.

Tizzard, L., Bicket, A.R., Benjamin, J., Loecker, D.D., 2014. A Middle Palaeolithic site in the southern North Sea: investigating the archaeology and palaeogeography of Area 240. J. Quat. Sci. 29, 698–710. https://doi.org/10.1002/jqs.2743

TNO-GDN, 2026a. Boven-Noordzee Groep [WWW Document]. Startigraphic Nomencl. Neth. URL https://www.dinoloket.nl/en/stratigraphic-nomenclature (accessed 11.19.25).

TNO-GDN, 2026b. Borehole lithology, stratigraphic data and core photographs [WWW Document]. URL https://www.dinoloket.nl/en/subsurface-data (accessed 1.29.26).

TNO-GDN, 2026c. Eem Formation [WWW Document]. Stratigr. Nomencl. Neth. TNO - Geol. Surv. Neth. URL http://www.dinoloket.nl/en/stratigraphic-nomenclature/eem-formation.

Törnqvist, T.E., Wallinga, J., Murray, A.S., De Wolf, H., Cleveringa, P., De Gans, W., 2000. Response of the Rhine–Meuse system (west-central Netherlands) to the last Quaternary glacio-eustatic cycles: a first assessment. Glob. Planet. Change 27, 89–111. https://doi.org/10.1016/S0921-8181(01)00072-8

Toucanne, S., Rodrigues, T., Menot, G., Soulet, G., Cheron, S., Billy, I., Eynaud, F., Antoine, P., Sinninghe Damste, J.S., Bard, E., Sanchez Goñi, M.-F., 2023. Marine Isotope Stage 4 (71–57 ka) on the Western European margin: Insights to the drainage and dynamics of the Western European Ice Sheet. Glob. Planet. Change 229, 104221. https://doi.org/10.1016/j.gloplacha.2023.104221

Toucanne, S., Zaragosi, S., Bourillet, J.F., Cremer, M., Eynaud, F., Van Vliet-Lanoë, B., Penaud, A., Fontanier, C., Turon, J.L., Cortijo, E., 2009a. Timing of massive 'Fleuve Manche' discharges over the last 350kyr: insights into the European ice-sheet oscillations and the European drainage network from MIS 10 to 2. Quat. Sci. Rev. 28, 1238–1256. https://doi.org/10.1016/j.quascirev.2009.01.006

Toucanne, S., Zaragosi, S., Bourillet, J.F., Gibbard, P.L., Eynaud, F., Giraudeau, J., Turon, J.L., Cremer, M., Cortijo, E., Martinez, P., Rossignol, L., 2009b. A 1.2Ma record of glaciation and fluvial discharge from the West European Atlantic margin. Quat. Sci. Rev. 28, 2974–2981. https://doi.org/10.1016/j.quascirev.2009.08.003

Toucanne, S., Zaragosi, S., Bourillet, J.-F., Marieu, V., Cremer, M., Kageyama, M., Van Vliet-Lanoë, B., Eynaud, F., Turon, J.-L., Gibbard, P.L., 2010. The first estimation of Fleuve Manche palaeoriver discharge during the last deglaciation: Evidence for Fennoscandian ice sheet meltwater flow in the English Channel ca 20–18 ka ago. Earth Planet. Sci. Lett. 290, 459–473. https://doi.org/10.1016/j.epsl.2009.12.050

Turner, F., Pott, R., Schwarz, A., Schwalb, A., 2014. Response of Pediastrum in German floodplain lakes to Late Glacial climate changes. J. Paleolimnol. 52, 293–310. https://doi.org/10.1007/s10933-014-9794-2

Udden, J., 1914. Mechanical composition of clastic sediments. Geol. Soc. Am. Bull. 25, 655–744.

Van Daele, M., Bertrand, S., Meyer, I., Moernaut, J., Vandoorne, W., Siani, G., Tanghe, N., Ghazoui, Z., Pino, M., Urrutia, R., De Batist, M., 2016. Late Quaternary evolution of Lago Castor (Chile, 45.6°S): Timing of the deglaciation in northern Patagonia and evolution of the southern westerlies during the last 17 kyr. Quat. Sci. Rev. 133, 130–146. https://doi.org/10.1016/j.quascirev.2015.12.021

Van Der Veen, H.H., Hulscher, S.J.M.H., Knaapen, M.A.F., 2006. Grain size dependency in the occurrence of sand waves. Ocean Dyn. 56, 228–234. https://doi.org/10.1007/s10236-005-0049-7

Van Geel, B., 2002. Non-Pollen Palynomorphs, in: Smol, J.P., Birks, H.J.B., Last, W.M., Bradley, R.S., Alverson, K. (Eds.), Tracking Environmental Change Using Lake Sediments, Developments in Paleoenvironmental Research. Springer Netherlands, Dordrecht, pp. 99–119. https://doi.org/10.1007/0-306-47668-1_6

Van Veen, J., 1935. Sand waves in the North Sea. Hydrogr. Rev. 12, 21–29.

Vervoort, M., Plets, R., Kyriakoudi, D., Missiaen, T., De Batist, M., 2026. Geomorphology of the Axial Channel (Southern Bight, North Sea). J. Maps 22, 2620910. https://doi.org/10.1080/17445647.2026.2620910

Verweirder, L., Georgiopoulou, A., Langedock, K., Fourie, F., White, M., Benetti, S., Sacchetti, F., Boone, W., Van Rooij, D., 2026. Variations in downslope activity and bottom current dynamics in a land-detached submarine channel system since the Last Glacial Maximum. Sedimentology 73, 620–644. https://doi.org/10.1111/sed.70077

Waajen, I.M., Busschers, F.S., Donders, T.H., Van Heteren, S., Plets, R., Wallinga, J., Hennekam, R., Reichart, G., Kinnaird, T., Wagner-Cremer, F., 2024. Late MIS5a in the southern North Sea: new chronostratigraphic insights from the Brown Bank Formation. J. Quat. Sci. 39, 408–420. https://doi.org/10.1002/jqs.3592

Waajen-Labee, I., 2025. Cooling of the North Sea: Palaeoenvrionmental response to climate instability during the last glacial inception (MIS 5 - MIS 4 transition) (PhD). Utrecht University, Studies in Earth Sciences.

Waajen-Labee, I., Plets, R., Cartelle, V., Cuperus, M., Donders, T., Van Heteren, S., Mestdagh, T., Wagner-Cremer, F., Wallinga, J., Wesselingh, F., Busschers, F., 2025. Sedimentary architecture of the Brown Bank Formation (Dutch sector of the North Sea) reveals consecutive shallow marine depositional phases during the MIS 5-4 transition. Quat. Sci. Rev. 365, 109442. https://doi.org/10.1016/j.quascirev.2025.109442

Wallinga, J., Cunningham, A.C., 2015. Luminescence Dating, Uncertainties and Age Range, in: Jack Rink, W., Thompson, J.W. (Eds.), Encyclopedia of Scientific Dating Methods, Encyclopedia of Earth Sciences Series. Springer Netherlands, Dordrecht, pp. 440–445. https://doi.org/10.1007/978-94-007-6304-3_197

Watts, W.A., 1977. The Late Devensian Vegetation of Ireland. Philos. Trans. R. Soc. Lond. B Biol. Sci. 280, 273–293.

Wentworth, C., 1922. A scale of grade and class terms for clastic sediments. J. Geol. 30, 377–394.

Wessex Archaeology, 2018a. Norfolk Boreas Offshore Wind Farm: Archeological Assesment of Geophysical Data (No. 117120.03). Wessex Archeology.

Wessex Archaeology, 2018b. East Anglia ONE North Offshore Windfarm: Archeological Assessment of Geophysical Data (No. 117810.03). Wessex Archeology.

Wessex Archaeology, 2018c. East Anglia TWO Offshore Windfarm: Archeological Assessment of Geophysical Data (No. 117810.01). Wessex Archeology.

Wessex Archaeology, 2017. Norfolk Vanguard Offshore Wind Farm: Marine Archeological Technical Report (No. 112380.03). Wessex Archeology.

Wessex Archaeology, 2015. Understanding submerged palaeo-environments in the southern North Sea: Pathways and timescales of hominin colonisation (No. 102771.02).

Wessex Archaeology, 2014. East Anglia THREE Volume 3 Chapter 17: Offshore Archeology and Cultural Heritage Appendicex 17.1.
West, R., 2000. Plant life of the Quaternary cold stages. Evidence from the British Isles. Cambridge University Press, Cambridge.
West, R.G., 1980. The pre-glacial Pleistocene of the Norfolk and Suffolk coasts. Cambridge University Press, Cambridge.
White, M.J., Schreve, D.C., 2000. Island Britain – Peninsula Britain: Palaeogeography, Colonisation, and the Lower Palaeolithic Settlement of the British Isles. Proc. Prehist. Soc. 66, 1–28. https://doi.org/10.1017/S0079497X00001742
Wintle, A.G., Murray, A.S., 2006. A review of quartz optically stimulated luminescence characteristics and their relevance in single-aliquot regeneration dating protocols. Radiat. Meas. 41, 369–391. https://doi.org/10.1016/j.radmeas.2005.11.001
Zagwijn, W., van Staalduinen, C., 1975. Toelichting bij geologische overzichtskaarten van Nederland. Rijks Geologische Dienst, Haarlem.
Zagwijn, W.H., 1983. Sea-level changes in the Netherlands during the Eemian. Geol. En Mijnb. 62, 437–450.
Zagwijn, W.H., 1961. Vegetation, climate and radiocarbon datings in the Late Pleistocene of the Netherlands. Part I: Eemian and Early Weichselian. Meded. Van Geol. Sticht. Nieuwe Ser. 14, 15–40.
Zhang, J., Li, S.-H., 2020. Review of the Post-IR IRSL Dating Protocols of K-Feldspar. Methods Protoc. 3, 7. https://doi.org/10.3390/mps3010007
Zolitschka, B., Francus, P., Ojala, A.E.K., Schimmelmann, A., 2015. Varves in lake sediments – a review. Quat. Sci. Rev. 117, 1–41. https://doi.org/10.1016/j.quascirev.2015.03.019



GHENT
UNIVERSITY